A SINGLE-CRYSTAL EPR STUDY OF RADIATION-INDUCED DEFECTS IN SELECTED SILICATES

A Thesis Submitted to the College of

Graduate Studies and Research

In Partial Fulfillment of the Requirements

For the Degree of Doctor of Philosophy

In the Department of Geological Sciences

University of Saskatchewan

Saskatoon

By

Mao Mao

Permission to Use

In presenting this thesis in partial fulfilment of the requirements for a Doctor of Philosophy degree from the University of Saskatchewan, I agree that the Libraries of this University may make it freely available for inspection. I further agree that permission for copying of this thesis in any manner, in whole or in part, for scholarly purposes may be granted by the professor or professors who supervised my thesis work or, in their absence, by the Head of the Department or the Dean of the College in which my thesis work was done. It is understood that any copying or publication or use of this thesis or parts thereof for financial gain shall not be allowed without my written permission. It is also understood that due recognition shall be given to me and to the University of Saskatchewan in any scholarly use which may be made of any material in my thesis.

Requests for permission to copy or to make other use of material in this thesis in whole or part should be addressed to:

Head of the Department of Geological Sciences

114 Science Place

University of Saskatchewan

Saskatoon, Saskatchewan

S7N5E2, Canada

Abstract

This thesis presents a series of single-crystal electron paramagnetic resonance (EPR) studies on radiation-induced defects in selected silicate minerals, including apophyllites, prehnite, and hemimorphite, not only providing new insights to mechanisms of radiation-induced damage in minerals but also having direct relevance to remediation of heavy metalloid contamination and nuclear waste disposal.

The NH_2 free radical, which is one of the most studied triatomic molecules and is widely used as spin labels in biophysical and biomedical research, in fluorapophyllite has been observed and characterized by single-crystal EPR spectra. Fourier-transform infrared (FTIR) spectrum supports electron-microprobe analyses that fluorapophyllite on the cavity walls in a phonolite (North Bohemia, Czech Republic) contains ammonium NH_4^+. The spin-Hamiltonian parameters of the NH_2 free radical show that this molecule is oriented parallel to (and rapidly rotated about) the crystallographic **c** axis. The NH_2 free radical in fluorapophyllite, most likely formed from radiolysis of the NH_4^+ ion, remains stable after annealing at 300°C, but is bleached at 340°C. This is the first report of the NH_2 free radical in a mineral lattice.

An O^- center and its biradicals in hydroxylapophyllite have been investigated by use of single-crystal and powder EPR spectroscopy at 290 and 90 K and three-pulse electron spin echo envelope modulation (ESEEM) spectroscopy at 25 K. The spin-Hamiltonian parameters show that the O^- center (σ-type) represents an unpaired electron in the $2p_z$ orbital of the hydroxyl oxygen atom. A series of weak

satellite peaks accompanying the main lines have been attributed to four geometrically distinct pairs of neighboring O^- centers (*i.e.*, biradicals). These biradicals have a point-dipole character and further support the O^- model and its location. The O^- center in hydroxylapophyllite is most likely produced by natural radiation and can be enhanced by gamma-ray irradiation. It is bleached at 300°C but can be restored readily by gamma-ray irradiation.

An Al-O^- center in gamma-ray-irradiated prehnite has been investigated by single-crystal EPR spectroscopy at 298 and 160 K. The spin-Hamiltonian parameters **g** and **A**(^{27}Al) at 298 K show that the hole traps on an apical hydroxyl oxygen of the octahedral $O_4Al(OH)_2$ group, after removal of the proton. Pulsed electron nuclear double resonance (ENDOR) spectra measured at 25 K further confirm the structural model of the Al-O^- center. Isothermal and isochronal annealing experiments show that the Al-O^- center exhibits second-order decay kinetics. The Al-O^- center is bleached after annealing at 375°C but can be restored by gamma-ray irradiation. These results from the Al-O^- center in prehnite provide support for and new insights into Clozel *et al*. (1995)'s $^{VI}Al–O^––^{VI}Al$ model for the B center in kaolinite.

Two arsenic-centered oxyradicals ($[AsO_4]^{4-}$ and $[AsO_4]^{2-}$) in gamma-ray irradiated hemimorphite (Mapimi, Durago, Mexico) have been observed and characterized by single-crystal EPR at ~295 K. The spin-Hamiltonian parameters suggest that the $[AsO_4]^{4-}$ radical is produced from electron trapping by a locally uncompensated $[AsO_4]^{3-}$ group substituting for the $[SiO_4]^{4-}$ group. The spin-Hamiltonian parameters of the $[AsO_4]^{2-}$ radical, including its ^{29}Si and ^{1}H

superhyperfine coupling constants, suggest hole trapping on the bridging oxygen linked to a Si^{4+} ion. Hydrothermal experiments at 200 °C and ~9.5 MPa show that hemimorphite is able to accommodate up to 2.5 wt% As_2O_5. These results demonstrate that hemimorphite is capable of sequestering arsenate in its crystal lattice, so it is a natural sink for attenuating As in supergene non-sulfide Zn deposits and Zn mine tailings.

Hemimorphite commonly contains elevated contents of heavy metalloids such as As, Cu, Cd, and Pb. Cation-exchange experiments of hemimorphite with 0.1M $CaCl_2$ solution at 110°C show that As and Cu are retained, whereas Cd and Pb are readily exchanged. This exchange behavior of Cd and Pb suggests that they may reside in the channel. Single-crystal EPR results at 295 and 120 K show that Cu^{2+} resides at the tetrahedral Zn site, not in the channel as previously suggested by the powder EPR study of Gallegos *et al*. (2009). These results suggest that hemimorphite is potentially useful for the remediation of heavy metalloid contamination.

Single-crystal EPR spectra of gamma-ray-irradiated hemimorphite after storage at room temperature for three months reveal a hydroperoxy radical HO_2 with complex proton hyperfine and superhyperfine structures. The single-crystal EPR spectra of this HO_2 radical, measured from 4 K to 275 K, confirm two reversible phase transitions at ~98 K and ~21 K. Spin-Hamiltonian parameters show that the HO_2 radical at 110 K forms from the H_2O molecule in the channel and interacts with two equivalent protons of the nearest hydroxyl groups. The HO_2 radical changes in site symmetry from monoclinic to triclinic across the ~98 K phase transitions and

confirms dynamic ordering and rotation of its precursor water molecule in the channel at <98 K. The EPR spectra of the HO_2 radical at <21 K and results from density functional theory (DFT) calculations suggest that hemimorphite adopts the monoclinic space group *Im* with completely ordered O−H systems at low temperature.

Acknowledgements

I would have never completed this research without my supervisor Dr. Yuanming Pan. He has taught me the way to do research and pushed me to work hard. I am grateful to him for the time and patience that he has generously spent on my research in these years. I also thank the members of my advisory committee: Dr. Kevin Ansdell, Dr. Jim Merriam, Dr. Ingrid Pickering, Dr. Robin W. Renaut, and Dr. Robert Scott, as well as my external examiner Dr. Mostafa Fayek, for incisive criticisms and helpful suggestions.

Special thanks to Dr. Mark J. Nilges for the collaborative work with ESEEM and ENDOR experiments at Illinois EPR Research Center, and Dr. Ramaswami Sammynaiken of Saskatchewan Structural Science Centre for his assistance on the X-band EPR experiments. I am very grateful to Mr. T. Bonli, Dr. J. Fan, Dr. Z. Li, and Mr. B. Novakovski of the Department of Geological Science for their assistance with electron microprobe analysis, inductively-coupled plasma mass spectroscopy analysis, DFT calculations, and sample preparation, respectively.

I also want to express my gratitude to my family for their support and encouragements. They have been always proud of my achievement and encouraged me when I faced problems on research. At last, I gratefully thank Natural Science and Engineering Research Council of Canada, Areva Resources Canada Scholarship, and University of Saskatchewan Graduate Teaching Fellowship for financial support to my research.

TABLE OF CONTENTS

LIST OF TABLES

LIST OF FIGURES

Chapter 1

Introduction and objectives

1.1 Study overview

Defects are known to exert important controls on physical and chemical properties of minerals, which are supported by the research focused on the colours of gemstones and semiconductor crystals. Based on radiation sensitivity of many defects, minerals with these defects have also been widely applied in archeology, geochronology, gemstone enhancement, nuclear waste disposal and mineral exploration (Nassau, 1983, 1984; Ikeya, 1993; Rossman, 1994; Marfunin, 1994; Rink, 1997; Pan *et al*., 2006).

1.1.1 Defects

In early mineral researches, the defects of minerals have been studied as "color centers", which are paramagnetic point defects in minerals, based on the studies dating back to 1920s of various materials such as halides (see also Marfunin 1979). For example, the F-center, which is an electron trapped at an anion vacancy, was first studied by Pohl (1925, 1937) and de Boer (1937). Since the F-center in some transparent materials produces an absorption in the visible range of the electromagnetic spectrum, it is called a "colour center". Because the electron at the vacancy is unpaired (*i.e.,* without a counteracting spin), it can be analyzed by electron

paramagnetic resonance (EPR) spectroscopy. After the F-center was found, many other colour centers have been detected by EPR. Although only some of the known colour centers absorb wavelengths in the visible band of optical spectrum, the term "colour center" has been retained and widely used in the literature (Marfunin, 1979).

The types of point defects include: (1) anion and cation vacancies, (2) interstitial atoms and molecules, (3) impurity ions (isomorphous or interstitial), (4) atoms in disordered solid solution, and (5) vacancy and impurity aggregates (Marfunin, 1979).

Since the discovery of paramagnetic defects, they have received more and more studies related to alteration of the physical properties of their host. For example, many desirable colors in gemstone are actually produced by their crystal defects (Nassau *et al*. 1976; Solntsev *et al*., 1981; Blak *et al*. 1982; Krambrock *et al*. 2002, 2007; Isotani *et al*. 2010). Within these minerals, the isomorphous impurity ions (*i.e*., foreign ions at regular lattice sites in a crystal), which do not have identical sizes and/or valence states to the lattice ions, may control the colours in their host minerals, because they commonly cause a local distortion and influence the local crystal field in the crystal. Similarly, when anions or cations are not present in their "correct" lattice sites, vacancies are produced and resulting the variation of their local crystal field (Fowler 1968). Due to the crystal field changes, the energy levels will be different from those of lattice atoms, so additional energy levels appear in the band gap, and produce extra absorption peaks in electromagnetic spectra, thus affecting the colour of the host mineral if the absorption energy is in the visible range (~400 – 700 nm).

One of the main methods to produce paramagnetic centers is irradiation by γ-ray, X-ray, electron, and neutron sources. Such radiation excites electrons to excited orbitals to form paramagnetic defects in minerals. The radiation dose required depends on the radiation source and exposure time, but the radiation-induced defects are usually small in absolute numbers (*i.e*., in a very low concentration). Radiation-induced defects usually can be removed ("bleached") at different annealing temperatures. By using of this property of defects, various minerals can be applied as natural dosimeters, geothermometers, and geochronometers (Ikeya 1993). Therefore, it is necessary to establish the relations among the EPR signal intensity of the specific center, radiation dose, and annealing temperature and time. By identifying the type of defect centers and their formational mechanisms it is possible to use them as markers for past geological events (Pan *et al*. 2006).

Consequently, the studies of defect centers straddle the boundaries of physical chemistry, material sciences, archaeology, gemology, mineralogy and geology, and have contributed the knowledgebase of all these areas (Marfunin 1979; Nassau 1983, 1984; Ikeya 1993; Rink 1997; Allard *et al*. 2003; Pan *et al*. 2006).

To investigate defect centers, X-ray electron spectroscopy, UV-Vis-NIR absorption spectroscopy, Fourier-transform infrared spectroscopy (FTIR), Raman spectroscopy, nuclear magnetic resonance (NMR), and EPR spectroscopy have been employed by previous studies. However, the EPR spectroscopy have been proven to be the most effective technique to study defect centers, because of the excellent sensitivity of EPR spectroscopy (down to 0.0001%) (Weil & Bolton, 2007) and very

fine linewidth (some cases < 0.1 mT). These distinctive features make EPR suitable for investigating the electronic structure and local symmetry of paramagnetic species. As a limitation of EPR spectroscopy, it is only able to detect paramagnetic defects and diamagnetic defects are not detectable by EPR. Nevertheless, this limitation can be easily overcome because many defects are paramagnetic or can transfer to paramagnetic after artificial irradiation. Therefore, EPR is the most powerful method to investigate defects in minerals.

1.1.2 The selected silicates

Silicate minerals are the most abundant group of minerals and the most important rock-forming minerals in Earth's crust (Nesse 2012), so they actually contain much information about the history of Earth. Some silicates, such as beryl and garnets are used as gemstones. A few silicates, such as spodumene and zircon, are actively mined for extracting Li and Zr respectively. Many silicates have been used as industrial materials due to their physical and chemical properties (Klein 2002; Nesse 2012).

Clay minerals are an important group of phyllosilicates that are widely distributed in sedimentary rocks and occur in igneous and metamorphic rocks as alteration products. Clay minerals have many specific and unique properties, some of which are useful in a number of industrial and technological applications, such as the manufacture of ceramics, as filling materials, as catalysts, as geologically datable material, and dosimeter. Therefore, studies on paramagnetic defects in clay minerals

have many important applications (Friedlander & Saldick, 1963; Pinnavaia, 1982; Michael & McWhinnie, 1989; Balan *et al*., 1999; Götze *et al.,* 2002).

Kaolinite-group minerals (*e.g*., kaolinite and dickite) are the most common clay minerals. Since kaolinite-group minerals are widely distributed as secondary mineral in sedimentary beds (Murray, 1988), and because they are very stable under most environmental conditions, these minerals have been used as natural dosimeters to trace past radionuclide migration in uranium exploration (Mosser *et al.,* 1996; Allard *et al.,* 1998, 2003). The EPR signal of kaolinite mainly appears at the $g \approx 4$ and $g \approx 2$ regions which have been produced by Fe^{3+} ion and some hole-like centers respectively (Allard *et al.* 2003).

Apophyllites as a phyllosilicate is an analogue of clay mineral have been developed as a nanocomposite (Aldushin *et al*. 2004; Chen *et al*. 2007). Moreover, a several studies on defects have been done on apophyllites due to the fact that it occurs as large crystals and is used as a semi-precious gemstone, and is thus amenable to single-crystal EPR studies. Bershov and Marfunin (1965, 1970) investigated the Ti^{3+} and Mn^{2+} centers in apophyllites. Bershov and Marfunin (1966), Vassilikou-Dova (1988) and Ramakrishnan (1991) studied two different VO^{2+} centers in apophyllites in detail. Bershov and Marfunin (1966) also reported the oxygen-related hole-like center in apophyllites to have $g_1 = 2.0041$, $g_2 = 2.0106$, $g_3 = 2.04511$ without any other detail.

Another phyllosilicate mineral, prehnite, is also used as a semi-precious gemstone, because of its brilliant green color. EPR and other studies of prehnite have

focused on the origin of its color, as related to the Fe^{3+} ion (Nazarova *et al.* 1991; Gangi Reddy *et al.* 2005). The Mn^{2+} center was found by Narasimha Reddy *et al.* (2001) through the EPR spectroscopy. Nazarova *et al.* (1991) detected a VO^{2+} center in prehnite, but concluded that it is not the cause of the green color. After γ-ray irradiation, a center with $g_{//} = 2.0196$ and $g_{\perp} = 2.0050$ was detected, and a brownish color was produced; it was attributed to the O^-−bridge associated to Fe^{3+} ion. The brownish color vanished after heating, and the O^- center faded at 100˚C (Nazarova *et al.* 1991).

Hemimorphite, a framework silicate, is also investigated in this study. It is a refractory mineral in surface environments and commonly presents in zinc mine tailings. Hemimorphite has attracted many studies because of its catalytic applications (Breuer *et al.*, 1999; Yurieva *et al.*, 2001; Catillon-Mucherie *et al.*, 2007) and its interesting features related to its zeolite-like crystal structure containing confined water molecules in the channel (Libowitzky *et al.*, 1997, 1998; Kolesov, 2006; Frost *et al.*, 2007; Geiger & Dachs, 2009; Dachs & Geiger, 2009). A Mn^{2+} center in hemimorphite was studied by Vassilikou-Dova & Eftaxias (1992). Gallegos *et al.* (2009) investigated powder EPR spectra of hemimorphite, disclosed Cu^{2+} and Fe^{3+}, and also proposed the existence of Al—O^-, E_1', and Pb^+—Pb^{3+} centers. However, the detailed structure models for these centers are not clear owing to limited information from the powder EPR spectra.

1.2 Research objectives and rationale

Kaolinite-group minerals and other clay minerals such as illite and montmorillonite have been widely used as natural dosimeters (Mosser *et al.* 1996; Allard *et al.* 1998, 2003; Morichon *et al.* 2008), because of the radioactivity-sensitive centers at the g ≈ 2 region (Angel *et al.* 1974). However, the structural models for these centers remain controversial. Because these minerals almost invariably occur in sizes of micrometers or less, EPR studies of kaolinite-group minerals have all been done with powder samples. Therefore, all the clay mineral studies and the explanations of centers noted above have been based on powder EPR spectra. Clozel *et al.* (1994), Sorieul *et al.* (2005), and Morichon *et al.* (2008) oriented kaolinite, montmorillonite, and illite respectively by the preferential development of platy particles through compression and sedimentation. Clozel *et al.* (1994) characterized the order/disorder of the grain orientation of kaolinite samples by using of the X-ray powder diffraction (XRD) and FTIR spectroscopy. However, the disorder indices of XRD (0.85−1.18) show that the kaolinite did not accumulate perfectly aligning along its **c** axis. Furthermore, Aparicio & Galán (1999) and Aparicio *et al.* (2006) indicate that the XRD method to determine the disorder indices of kaolinite presents problems due to peak overlapping effects from other minerals.

The main controversial points include: 1. the origins of the A and B centers; 2. the existence of the A' center (Clozel *et al.* 1994); 3. structural models for all centers at the g ≈ 2 region.

The A center does not have any visible hyperfine structure. Therefore, its g values are the only piece of information for identifying this center. However, the g values of the O_2^- and those of the SiO_4^{3-} centre are all close to the reported g values for the A center in kaolinite (Kasai 1965; Symon 1971; and Marfunin 1979), thus additional information is required to better establish the structural model and origin of this center.

Although a hyperfine structure with $A/g_e\beta_e$ = ~0.76 mT is resolved for the B center at liquid-nitrogen temperatures (Meads & Malden, 1975; Hall 1980; Clozel *et al.* 1994; Götze *et al.* 2002; Köksal *et al.* 2004), and all studies agreed that the B center is related to aluminum, the disputes focus on the position of the O^- ion and the number (one or two) of neighboring Al nuclei (Hall 1980; Clozel *et al.* 1994; Götze *et al.* 2002; Köksal *et al.* 2004). The reliance on only powder EPR spectra makes it difficult to resolve this dispute.

One possible solution to these problems is a single-crystal EPR study, which is far more sensitive and informative than its powder counterpart. Accordingly, a single-crystal EPR study was initiated to investigate radiation-induced defects in apophyllites, prehnite, and hemimorphite, which usually occur as large crystals that are amenable to single-crystal EPR studies. Therefore, detailed structural information for radiation-induced defects in apophyllites obtainable from single-crystal EPR studies can be used for better understanding of similar defects in other phyllosilicates.

Apophyllites and prehnite are layer silicates, structurally similar to clay minerals. Hemimorphite is a sorosilicate with a framework structure built from zinc

and silicon tetrahedra, and aluminum is a common impurity in the structure. Therefore, radiation-induced defects in apophyllites, prehnite, and hemimorphite are expected to be close analogues for those in common clay minerals. If this assumption is correct, quantitative information for radiation-induced defects in apophyllites, prehnite, and hemimorphite determined by the single-crystal EPR technique can then be used to provide insights into their counterparts (*e.g*., A, A', and B centers) in clay minerals.

Hemimorphite has been studied as a sink for As and heavy metals (Cd, Cu and Pb) in mine tailings and soils surrounding smelters (Walder & Chavez 1995; Day & Bowell 2005; Espiari *et al*. 2006; Schaider *et al*. 2007; Cabala *et al*. 2009). But the study based on powder EPR spectra can not provide unambiguous positions of these heavy metals in hemimorphite (Gallegos *et al*., 2009). Therefore, one purpose of the present study is to understand the local structure of these heavy metals in hemimorphite.

In addition, Libowisky *et al.* (1997) reported a phase transition present in hemimorphite at ~98(2) K, and studied the crystal structure of hemimorphite at 20 K by neutron diffraction (Libowisky *et al*., 1998). Kolesov (2006) reported another phase transition at ~20 – 30 K. However, the two reversible phase transitions (~98 K and ~20 – 30 K) are not observed in dehydrated hemimorphite, suggesting that these phase transitions are related to the H_2O molecules (Libowisky & Rossman, 1997; Libowisky *et al*., 1997, 1998; Kolesov, 2006). A question that arises is: What is the space group of hemimorphite below the phase transition at 20 K? Therefore, another

purpose of the current study is to resolve this question, through studies on the center that is sensitive to phase transitions of hemimorphite.

1.3 Thesis outline

Aiming to solve the problems proposed above, this research has focused on paramagnetic defects in apophyllites, prehnite, and hemimorphite, by using single-crystal EPR spectroscopy and other techniques. The main body of this thesis is composed of six chapters. Chapters 2, 3, 4, 5 and 6 have already been published as separate articles in peer reviewed journals, and Chapter 7 is a manuscript submitted to a peer reviewed journal.

Chapter 2, derived from a paper published in European Journal of Mineralogy (Mao & Pan, 2009), presents the investigation of the NH_2 free radical in fluorapophyllite. The study disclosed the presence of NH_4^+ group and NH_2 free radical in a natural fluorapophyllite through FTIR and EPR spectroscopy, and determined the spin-Hamiltonian parameters of the NH_2 free radical by single-crystal EPR data. The results showed that the NH_2 free radical resides in the crystal lattice. The NH_2 free radical can be produced by gamma-ray radiation on fluorapophyllite and bleached at 340 °C.

Chapter 3, published in European Journal of Mineralogy (Mao, Nilges & Pan, 2010), investigates a σ-type O^- center and its biradicals in natural hydroxylapophyllite by use of single-crystal EPR at 290 and 90 K. This center is annealed out at 300°C and can be restored easily by gamma-ray irradiation. To provide more detailed

structural information, data from three-pulse electron spin echo envelope modulation (ESEEM) spectroscopy at 25 K has been acquired and analyzed by Dr. Mark J. Nilges (Assistant Director and Lab Manager, Illinois EPR research center) who was included as a co-author of a paper that stemmed from this chapter.

Chapter 4, published in European Journal of Mineralogy (Mao, Nilges & Pan, 2010), is aimed at comparing an $Al\text{-}O^-$ center in gamma-irradiated natural prehnite with the B center in kaolinite. Single-crystal EPR measurements of gamma-ray-irradiated natural prehnite, including those after isothermal and isochronal annealing, have been made at 298 and 160 K. Data from pulsed electron nuclear double resonance (ENDOR) spectroscopy had been analyzed by Dr. Mark J. Nilges and further confirmed the structural model of the $Al\text{-}O^-$ center. Results from prehnite clarified the structural model of the B center in kaolinite.

To study the site occupancies and local structures of heavy metals in natural hemimorphite, two arsenic-related centers ($[AsO_4]^{4-}$ and $[AsO_4]^{2-}$) and a Cu^{2+} center have been investigated by single-crystal EPR in Chapters 5 (Mao, Lin & Pan, 2010) and 6 (Mao & Pan, 2012), respectively. Hydrothermal experiments that had been done by Ms. Jinru Lin (Ph.D. student, University of Saskatchewan) were also included in Chapter 5. Chapter 6 includes a series of cation-exchange experiments at 110 °C to evaluate the behavior of As, Cd, Cu and Pb as well.

Chapter 7, stemming from a manuscript (Mao, Li, & Pan, submitted to Physics and Chemistry of Minerals), reports on a single-crystal EPR study of an HO_2 center in gamma-ray-irradiated hemimorphite from 4 K to 275 K. EPR spectra, incuding proton

hyperfine and superhyperfine coupling constants determined at 110 K, 85 K, 40 K and 7 K, confirm two second-order, reversible phase transitions at ~98 K and ~21 K (Libowitzky & Rossman 1997; Kolesov 2006), provide new insights into the origins of these phase transitions (*i.e.*, proton ordering), and allow us to propose a new monoclinic structure for hemimorphite at <21 K. Dr. Zucheng Li (Postdoctoral Fellow, University of Saskatchewan), who performed first-principles calculations to optimize the monoclinic structures of hemimorphite deduced from EPR spectra at <21 K, is a co-author of the manuscript stemming from this chapter.

1.4 References

ALDUSHIN, K., JORDAN, G., RAMMENSEE, W., SCHMAHL, W.W. & BECKER, H.-W. (2004): Apophyllite (001) surface alteration in aqueous solutions studied by HAFM. *Geochim. Cosmochim. Acta* **68**, 217-226.

ALLARD, T., ILDEFONSE, P., PEREZ DEL VILLAR, L., SORIEUL, S., PELAYO, M., BOIZOT, B., BALAN, E., & CALAS, G. (2003) Radiation-induced defects in dickites from the EL Berrocal granitic system (Spain): relation with past occurrence of natural radioelements. *Eur. J. Mineral*. **15**, 629-640.

ALLARD, T., & MULLER J. (1998): Kaolinite as an in situ dosimeter for past radionuclide migration at the Earth's surface. *Applied Geochemistry.* **13**, 751-765.

ANGEL, B. R., JONES, J. P. E., & HALL, P. L. (1974): Electron spin resonance studies of doped synthetic kaolinite. I. *Clay Minerals*. **10**, 247-255.

APARICIO, P, & GALÁN, E. (1999): Mineralogical interference on kaolinite crystallinity index measurements. *Clays and Clay Minerals*, **47**, 12-27.

APARICIO, P, GALÁN, E, FERRELL, R.E. (2006): A new kaolinite order index based on XRD profile fitting. *Clay Minerals*, **41**, 811-817.

BALAN, E., ALLARD, T., BOIZOT, B., MORIN, G., & MULLER, J. P. (1999): Structural Fe^{3+} in natural kaolinites: new insights from electron paramagnetic resonance spectra fitting at X and Q-band frequencies. *Clays and Clay Minerals*. **47**, 605-616.

BERSHOV, L.V. (1970): Isomorphism of titanium in minerals. *Izv. Akad. Nauk*. **12**, 47-54.

BERSHOV, L. V. & MARFUNIN, A. S. (1965): Vanadyl ion in minerals; features of electron paramagnetic resonance of initial elements. *International geology reviews*. **9**, 42-52.

BERSHOV, L. V. & MARFUNIN, A. S. (1966): Electron-spin resonance of electron-hole centers in minerals. *Doklady Akademii Nauk SSSR*. **173**, 91-93.

BLAK, A. R., ISOTANI, S., & WATANABE, S. (1982): Optical absorption and electron paramagnetic resonance studies of colorless and pin beryl. *Revista Brasileira de Física*. **12**, 285-292.

BREUER, K., TELES, J.H., DEMUTH, D., HIBST, H., SCHÄFER, A., BRODE, S. & DOMGÖRGEN, H. (1999): Zinc silicates: very efficient heterogeneous catalysts for the addition of primary alcohols to alkynes and allenes. *Angew. Chem. Int. Ed*. **38**, 1401–1405.

CABALA J., KRUPA P., & MISZ-KENNAN M. (2009) Heavy metals in mycorrhizal rhizospheres contaminated by Zn-Pb mining and smelting around Olkusz in southern Poland. *Water Air Soil Pollution,* **199**, 139-149.

CATILLON-MUCHERIE, S., AMMARI, F., KRAFFT, J.-M., LAURON-PERNOT, H., TOUROUDE, R. & LOUIS, C. (2007): Preparation of coimpregnated Cu–Zn/SiO_2 catalysts: Influence of the drying step on metallic particle size and on Cu0–ZnII interactions. *J. Phys. Chem. C* **111**, 11619–11626.

CHEN, C.G., YEBASSA, D. & RAGHAVAN, D. (2007): Synthesis, characterization, and mechnical properties of evaluation of thermally stable apophyllite vinyl ester nanocomposites. *Polym. Advan. Technol.* **18**, 574-581.

CLOZEL, B., ALLARD, T., & MULLER, J. P. (1994): Nature and stability of radiation-induced defects in natural Kaolinite: new results and a reappraisal of published works. *Clays and clay minerals*. **42**, 657-666.

CLOZEL, B., GAITE, J. M., & MULLER, J. P. (1995): Al-O^--Al paramagnetic defects in kaolinite. *Physics and chemistry in minerals*. **22**, 351-356.

Dachs, E. & Geiger, C.A. (2009): Heat-capacity behaviour of hemimorphite, $Zn_4Si_2O_7(OH)_2 \cdot H_2O$, and its dehydrated analogue $Zn_4Si_2O_7(OH)_2$: a calorimetric and thermodynamic investigation of their phase transitions. *Eur. J. Mineral*. **21**, 971–988.

DAY S.J., & BOWELL R.J. (2005) Atypical and typical zinc geochemistry in a carbonate setting, Sä Dena Hes Mine, Yukon Territory, Canada. *Geochem. Explor. Environ. Analysis,* **5**, 255-266.

DE BOER J. H. (1937) Über die Nature der Farbzentren in Alkalihalogenid-Kristallen. *Recueil des Travaux Chimiques des Pays-Bas,* **56**, 301-309.

ESPIARI S., RASHCHI F., & SADRNEZHAAD S.K. (2006) Hydrometallurgical treatment of tailings with high zinc content. *Hydrometallurgy*. **82**, 54-62.

FOWLER, W. B. (1968): Physics of color centers. *New York, Academic Press*.

FRIEDLANDER, H. Z. & SALDICK, J. (1963): Electron spin resonance spectra in various clay minerals. *Nature*. **199**, 61-62.

FROST, R.L., BOUZAID, J.M. & REDDY, B.J. (2007): Vibrational spectroscopy of the sorosilicate mineral hemimorphite $Zn_4(OH)_2Si_2O_7 \bullet H_2O$. *Polyhedron,* **26**, 2405–2412.

GALLEGOS, E.A., CANO, N.F., WATANABA, S. & CHUBACI, J.D.F. (2009): Thermoluminescence, infrared reflectivity and electron paramagnetic resonance properties of hemimorphite. *Rad. Measur*. **44**, 11-17.

GANGI REDDY, N. C., FAYAZYDDIN, S. MD., RAMA SUBBA REDDY, R., SIVA REDDY, G., LAKSHMI REDDY, S., SAMBASIVA RAO, P., & JAGANNATHA REDDY, B. (2005): Charactersation of prehnite by EPMA, Mossbauer, optical absorption and EPR spectroscopic methods. *Spectrochimica Acta Part A*. **62**, 71-75.

GEIGER, C.A. & DACHS, E. (2009): Quasi-ice-like C_p behavior of molecular H_2O in hemimorphite $Zn_4Si_2O_7(OH)_2 \bullet H_2O$: C_p and entropy confined H_2O in microporous silicates. *American Mineralogists*. **94**, 634–637.

GÖTZE, J., PLÖTZE, M., GÖTTE, TH., NEUSER, R. D., & RICHTER, D. K. (2002): Cathodoluminescence and electron paramagnetic resonance studies of clay minerals. *Mineralogy and petrology*. **76**, 195-212.

HALL, P. L. (1980): The application of electron spin resonance spectroscopy to studies of clay minerals: I. isomorphous subsitutions and external surface properties. *Clay minerals*. **15**, 321-335.

IKEYA, M. (1993) New Application of Electron Spin Resonance-dating, Dosimetry and Microscopy. *World Scientific, Singapore*.

ISOTANI, S., BLAK, A. R., & WATANABE, S. (2010): UV optical absorption spectra analysis of beryl crystals from Brazil. *Physica B: Condensed matter*. **405**, 1501-1508.

JONES, J. P. E., ANGEL, B. R., & HALL, P. L. (1974): Electron spin resonance studies of doped synthetic kaolinite. II. *Clay Minerals*. **10**, 257-270.

KASAI, P. H. (1965): Electron spin resonance studies of γ- and X-ray-irradiated zeolites. *The journal of chemical physics*. **43**, 3322-3327.

KLEIN, C. (2002): The 22nd edition of the manual of mineral science. *Wiley*.

KOLESOV, B. (2006) Raman investigation of H_2O molecule and hydroxyl groups in the channels of hemimorphite. *American Mineralogist*, **91**, 1355-1362.

KÖKSAL, F., KOSEOGLU, R., SAKA, I., BASARAN, E., & SENER, F. (2004): Electron paramagnetic resonance of natural and gamma-irradiated alunite and kaolin mineral powders. *Radiation effects & Defects in solids*. **159**, 393-398.

KRAMBROCK, K., PINHEIRO, M. V. B., GUEDES, K. J., MEDEIROS, S. M., SCHWEIZER, S., & SPAETH J.-M. (2004): Correlation of irradiation-induced yellow color with the O^- hole center in tourmaline. *Physics and chemistry of minerals*. **31**, 168-175.

KRAMBROCK, K., RIBEIRO, L. G. M., PINHEIRO, M. V. B., LEAL, A. S., MENEZES, M. A., & SPAETH J.-M. (2007): Color centers in topaz: comparison between neutron and gamma irradiation. *Physics and chemistry of minerals*. **34**, 437-444.

LIBOWITZKY, E., KOHLER, T., ARMBRUSTER, T. & ROSSMAN, G.R. (1997): Proton disorder in dehydrated hemimorphite. IR spectroscopy and x-ray structure refinement at low and ambient temperatures. *Eur. J. Mineral*. **9**, 803-810.

LIBOWITZKY, E. & ROSSMAN, G.R. (1997): IR spectroscopy of hemimorphite between 82 and 373 K and optical evidence for a low-temperature phase transition. *Eur. J. Mineral*. **9**, 793-802.

LIBOWITZKY, E., SCHULTZ, A.J. & YOUNG, D.M. (1998): The low-temperature structure and phase transition of hemimorphite, $Zn_4Si_2O_7(OH)_2 \bullet H_2O$. *Zeit. Kristal*. **213**, 659-668.

MAO, M., LIN, J. & PAN, Y. (2010) Hemimorphite as a natural sink for arsenic in zinc deposits and related mine tailings: Evidence from single-crystal EPR spectroscopy and hydrothermal synthesis. *Geochim. Cosmochim. Acta* **74**, 2943–2956.

MAO, M., NILGES, M.J. & PAN, Y. (2010) Radiation-induced defects in apophyllites. II. An O^- center and its related biradicals in hydroxylapophyllite. *Eur. J. Mineral.* **22**, 89–102.

MAO, M., NILGES, M.J. & PAN, Y. (2010) Single-crystal EPR and ENDOR study of an Al-O^- center in prehnite: implications for aluminum-associated oxyradicals in layer silicates. *Eur. J. Mineral.* **22**, 381–392.

Mao, M. and Pan Y. (2009) Radiation-induced defects in apophyllites. I. The NH_2 radical in fluorapophyllite. *Eur. J. Mineral.* **21**, 317–324

MAO, M. & PAN, Y. (2010) (2012) Nature of heavy metals in hemimorphite: A cation-exchange and single-crystal EPR study. *Can. Mineral.* **50**, 31-43.

MAO, M. & PAN, Y. (ms) Phase transitions and proton ordering in hemimorphite: New insights from single-crystal EPR experiments between 4 K and 275 K. *Phys. Chem. Minerals* (submitted)

MARFUNIN, A. S. (1979) Spectroscopy, luminescence and radiation centers in minerals. *Springer-verlag berlin Heidelberg New York*.

MARFUNIN, A. S. (1994) Composition, structure, and properties of mineral matter. *Springer-Verlag*.

MEADS, R. E. & MALDEN P. J. (1975): Electron spin resonance in natural kaolinites containing Fe^{3+} and other transition metal ions. *Clay minerals*. **10**, 313-345.

MICHAEL, P. J. & MCWHINNIE, W. R. (1989): Mossbauer and ESR studies of the thermochemistry of illite and montmorillonite. *Polyhedron*. **8**, 2709-2718.

MORICHON, E., ALLARD, T., BEAUFORT, D., & PATRIER, P. (2008): Evidence of native radiation-induced paramagnetic defects in natural illites from unconformity-type uranium deposits. *Physics and chemistry of minerals*. **35**, 339-346.

MOSSER, C., BOUDEULLE, M., WEBER, F., & PACQUET, A. (1996): Ferriferous and vanadiferous kaolinites from the hydrothermal alteration halo of the cigar lake uranium deposit (Canada). *Clay Minerals*. **31**, 291-299.

MULLER, J. P. (1989): Tracing kaolinites through their defect centers: kaolinite paragenesis in a laterite (Cameroon). *Economic geology*. **84**, 694-707.

MURRAY, H. H. (1988): Kaolin minerals: their genesis and occurrences. *Reviews in mineralogy*. **19**, 67-89.

NARASIMHA REDDY, S., RAO, P. S., RAVIKUMAR, R. V. S. S. N., & REDDY, B. J. (2001): EPMA, optical EPR and IR spectral studies of prehnite mineral. *Indian Journal of physics Part A*. **75**, 429-432.

NASSAU, K. (1984): Gemstone enhancement. *Butterworths*.

NASSAU, K. (1983): The physics and chemistry of color. *Wiley Interscience*.

NASSAU, K., PRESCOTT, B. E., & WOOD, D. L. (1976): The deep blue Maxixe-type color center in beryl. *American mineralogist*. **61**, 100-107.

NAZAROVA, G. S., OSTASHCHENKO, B. A., MITROFANOV, V. YA., SHILOVA, O. YU., & ZARIPOVA, L. D. (1991): Nature of the color of prehnite. *Zhurnal Prikladnoi Spektroskopii*. **53**, No. 2, 305-310.

NESSE, W. D. (2012): Introduction to mineralogy. Second edition. *Oxford University Press*.

PAN, Y., BOTIS, S. M., & NOKHRIN, S. (2006) Applications of Natural Radiation-Induced Paramagnetic Defects in Quartz to Exploration in Sedimentary Basins. *Journal of China University of Geoscience*, **17**, 258-271.

PINNAVAIA, T. J. (1982): Electron spin resonance studies of clay minerals. *Developments in Sedimentology*. **34**, 139-161.

RAMAKRISHNAN, G., SWAMY, M. B. V. L. N., RAO S. P., & SUBRAMANIAN S. (1991): EPR of vanadyl ion in a natural mineral, apophyllite. *Proceedings of chemistry sciences*. **103**, 613-619.

RINK, W. J. (1997): Electron spin resonance (ESR) dating and ESR applications in quaternary science and archaeometry. *Radiation measurements*, **27**, 975-1025.

ROSSMAN, G. R. (1994): Colored varieties of the silica minerals. Reviews in *Mineralogy and Geochemistry*, **29**, 433-467.

SCHAIDER L.A., SENN D.B., BRABANDER D.J., MCCARTHY K.D., & SHINE J.P. (2007): Characterization of zinc, lead, and cadmium mine waste: Implications for transport, exposure and bioavailability. *Environ. Sci. Tech*. **41**, 4164-4171.

SOLNTSEV, V. P., KHARCHENKO, E. I., LEBEDEV, A. S., KLYAKHIN, V. A., & IL'IN, A. G. (1981): Nature of color centers and EPR of a manganese-activated beryl. *Journal of applied spectroscopy*. **34**, 111-115.

SYMONS, M. C. R. (1971): Pramagnetic centers in or on various oxides. *The Journal of Physical Chemistry*. **76**, 3095-3098.

VASSILIKOU-DOVA, A.B. & EFTAXIAS, K. (1991): Electron spin resonance of Mn^{2+} in hemimorphite. *Crystal Res. Tech*. **27**, 117-120.

VASSILIKOU-DOVA, A. B., & LEHMANN, G. (1988): EPR of V^{4+} in apophyllite. *Physical Status Solidi B*. **147**, 691-697.

WALDER I.F., & CHAVEZ W.X. JR. (1995) Mineralogical and geochemical behavior of mill tailing material produced from lead-zinc skarn mineralization, Hanover, Grant County, New Mexico, USA. *Environ. Geol*. **26**, 1-18.

WAUCHOPE, R. D. & HAQUE, R. (1971): ESR in clay minerals. *Nature physical science*. **233,** 141-142.

WEIL, J. A., & BOLTON, J. R. (2007): Electron paramagnetic resonance, elementary theory and practical applications. *Wiley Interscience*.

YURIEVA, T.M., KUSTOVA, G.N., MINYUKOVA, T.P., POELS, E.K., BLIEK, A., DEMESHKINA, M.P., PLYASOVA, L.M., KRIEGER, T.K. & ZAIKOVSKII, V. I. (2001): Non-hydrothermal synthesis of copper-, zinc- and copper–zinc hydrosilicates. *Mater. Res. Innov*. **5**, 3–11.

Chapter 2

Radiation-induced defects in apophyllites. I. The NH_2 free radical in fluorapophyllite

The NH_2 free radical, which is one of the most studied triatomic molecules and is widely used as spin labels in biophysical and biomedical research, has not been reported in mineral lattices. Fourier-transform infrared (FTIR) spectrum supports electron microprobe analyses that fluorapophyllite on the cavity walls in a phonolite (North Bohemia, Czech Republic) contains ammonium NH_4^+. Powder and single-crystal electron paramagnetic resonance (EPR) spectra of this fluorapophyllite, with and without γ irradiation, disclose at least four paramagnetic defects, including two previously reported VO^{2+} centers, the NH_2 free radical and an oxygen-associated center. The spin-Hamiltonian parameters of the NH_2 free radical have been determined from single-crystal EPR data and show that this molecule is oriented parallel to (and rapidly rotated about) the crystallographic **c** axis. The NH_2 free radical in fluorapophyllite, most likely formed from radiolysis of the NH_4^+ ion, remains stable after annealing at 300 °C, but is bleached at 340 °C.

2.1 Introduction

Radiation-induced defects in layer silicates (*e.g.*, kaolinite, dickite, illite, and montmorillonite) have received considerable interests, because they are sensitive dosimeters for determining and monitoring the migration of radionuclides in the Earth's surface environments and have direct relevance to long-term nuclear waste disposal (*e.g.*, Clozel *et al.*, 1994; Allard & Muller, 1998; Götze *et al*., 2002; Allard *et al.*, 2003, 2007; Sorieul *et al*., 2005; Morichon *et al*., 2008). For example, Clozel *et al.* (1994), on the basis of a detailed powder electron paramagnetic resonance (EPR) spectroscopic study, distinguished three radiation-induced defects in kaolinite: Centers A and A' are trapped holes on apical oxygen from Si–O bonds, and Center B is a hole trapped on an oxygen shared by two Al octahedra. Clozel *et al.* (1994) used EPR spectra measured on oriented films to demonstrate that Centers A and A' have orthogonal orientations. They also showed that the hyperfine structure of Center B arises from interaction with two equivalent ^{27}Al nuclei (I = 5/2 and natural isotope abundance = 100 %). Confirmation of these structural models requires additional data: *e.g.*, (1) localization of the unpaired spin on a single oxygen atom, (2) characteristic hyperfine structures arising from interaction with a ^{29}Si nucleus (*i.e.*, Centers A and A'), and (3) defect orientations and their relationships to specific bond and other symmetrical directions in the ideal structures. All of these data can be obtained by analysis of single-crystal EPR spectra but are missing for radiation-induced defects in layer silicates, because of the fact that these minerals invariably occur in ‘‘clay’’ sizes.

Apophyllites [$(K,Na)Ca_4Si_8O_{20}(F,OH)\bullet 8H_2O$, *P4/mnc*] consist of tetrahedral SiO_4 sheets alternating with layers of K, Ca, F and H_2O (Colville *et al.*, 1971; Rouse *et al.*, 1978; Pechar, 1987) and are analogues of layer silicates (Aldushin *et al.*, 2004; Chen *et al.*, 2007). Apophyllites usually occur as large crystals that are amenable to single-crystal EPR studies. Therefore, detailed structural information for radiation-induced defects in apophyllites obtainable from single-crystal EPR studies can be used for better understanding of similar defects in other layer silicates. Accordingly, we initiated a single-crystal EPR study on a suite of natural apophyllites with or without γ irradiation. Results reported herein show that a specimen of ammonian fluorapophyllite contains at least four paramagnetic centers. These centers correspond to two previously reported VO^{2+} centers (Bershov & Marfunin, 1965; Vassilikou-Dova & Lehmann, 1988), a new NH_2 free radical and a new oxygen-associated center. This contribution focuses on the quantitative characterization, formation, and thermal stability of the NH_2 free radical, which has never been reported to occur in mineral lattices. The oxygen-associated center, which is particularly relevant to radiation-induced defects in layer silicates (Clozel *et al.*, 1994; Allard *et al.*, 2003), is better resolved in a sample of hydroxylapophyllite and will be dealt with in a subsequent contribution.

2.2 Sample and experimental techniques

A sample of short prismatic fluorapophyllite crystals of ~ 1–2 mm long on the cavity walls in a phonolite (North Bohemia, Czech), from the University of

Saskatchewan reference mineral collection, was used in this study. Selected crystals were polished for electron microprobe analysis (EMPA) and pulverized for Fourier-transform infrared (FTIR) and powder electron paramagnetic resonance (EPR) spectroscopic analyses. Samples for EPR analyses have been subject to γ irradiation by use of a ^{60}Co source (a dose of ~ 5.4 Mrad) at room temperature. A γ irradiated powder sample has also been sequentially annealed in air from 100 to 460 °C, at an interval of 40 °C for 30 min each. EMPA was performed on a JEOL JXA-8600 superprobe equipped with three wavelength-dispersive spectrometers, at the Department of Geological Sciences, University of Saskatchewan. Analytical conditions included an accelerating voltage of 15 kV, beam current of 10 nA, beam diameter of ~ 5 μm and the following standards: quartz (Si), γ-Al garnet (Al), jadeite (Na), magnetite (Fe), diopside (Ca), sanidine (K), fluorite (F), and tugtupite (Cl).

Fluorapophyllite was mixed with KBr for FTIR measurements on a BIO-RAD FTS-40 spectrometer with a resolution of 4 cm^{-1}, at the Saskatchewan Structure Science Centre (SSSC), University of Saskatchewan. Powder and single-crystal EPR spectra were measured on a Brucker EMX spectrometer with an ER4119 cavity at SSSC. Experimental conditions for powder EPR measurements at room temperature included microwave frequencies from ~ 9.38 to ~ 9.75 GHz, modulation frequency of 100 kHz, modulation amplitude of 0.06 mT and microwave powers from 2 to 20 mW. Spectral resolutions were ~ 0.098 mT (*i.e.*, 2048 field data points over 200 mT) or 0.117 mT (1024 points over 120 mT). Calibration of the magnetic field was made by use of 2,2-diphenyl-1-picrylhydrazyl (DPPH).

Single-crystal EPR measurements at room temperature were made on a γ irradiated crystal of ~ 1 mm x 1 mm x 2 mm in size. Crystal alignment was accomplished by use of its prismatic form and the perfect {001} cleavage. Single-crystal spectra were collected for two orthogonal rotation planes: one perpendicular to the crystallographic axis **c** is denoted the xy plane, and the other containing both a and c is designated the xz plane. Experimental conditions for single-crystal EPR measurements included a microwave frequency of ~ 9.84 GHz, modulation frequency of 100 kHz, modulation amplitude of 0.06 mT and a microwave power of 20 mW. The spectral resolutions were ~ 0.012 mT (*i.e.*, 1024 field data points over 13 mT), and the angle interval of each measurement was 5° for both planes.

Data analyses of powder and single-crystal EPR spectra, including angle correction, fitting of spin-Hamiltonian parameters and spectral simulations, were all made by use of the EPR–NMR software package of Mombourquette *et al*. (1996).

2.3 Results

2.3.1 Chemical composition and FTIR spectrum

Table 2.1 lists six electron microprobe analyses of the sample investigated in this study. Chemical formulas calculated on the basis of Σ(Si + Al) = 8 atoms show that this sample approaches the endmember fluorapophyllite but has a significant deficiency in the K site. We interpret this deficiency to arise from a substitution of NH_4^+ for K^+ (Marriner *et al*., 1990; Cave, 2002). This interpretation is supported by

the characteristic ~1460 cm^{-1} band in the FTIR spectrum (Figure 2.1; Marriner *et al*., 1990), which is in fact a doublet consisting of two Gaussian bands at ~ 1460 cm^{-1} and ~ 1440 cm^{-1}. The latter is close to the 1430–1435 cm^{-1} band that has been assigned to the bending mode of NH_4^+ in other silicates (Solomon & Rossman, 1988; Vonckenet al., 1993). However, the stretching vibration and combination bands between 3300 cm^{-1} and 2800 cm^{-1} (Voncken *et al*., 1993) are not resolved owing to pronounced O–H bands (Figure 2.1; Matsueda *et al*., 1981). Also, quantitative analysis on the absolute amount of NH_4^+ in fluorapophyllite was not attempted.

2.3.2 Single-crystal EPR spectra

Single-crystal EPR spectra of the γ irradiated fluorapophyllite (Figure 2.2) disclose at least four paramagnetic defects: two V^{4+} centers (Bershov &Marfunin, 1965; Vassilikou-Dova & Lehmann, 1988); an oxygen-associated center and a NH_2 free radical (see below). Additional weak absorption lines, which are detectable only at a few orientations (Figure 2.2b) but do not correspond to the previously reported Mn^{2+} or Ti^{3+} centers in apophyllites (Bershov *et al*., 1965; Bershov, 1970), are not discussed further here.

The two previously reported V^{4+} centers (Bershov & Marfunin, 1965; Vassilikou-Dova & Lehmann, 1988) are readily identified by their characteristic ^{51}V hyperfine structures (I = 7/2 and natural isotope abundance = 100 %). Spectral simulations for selected orientations show that the spin-Hamiltonian parameters reported by Vassilikou-Dova & Lehmann (1988) give excellent predictions for the

observed line positions of these two centers. These V^{4+} centers in apophyllites have been interpreted by Vassilikou-Dova & Lehmann (1988) to be VO^{2+} radicals at the K and Ca sites.

Table 2.1 Chemical composition of fluorapophyllite from North Bohemia, Czech Republic.

Analysis	1	2	3	4	5	6	Average	Std
SiO_2(wt.%)	54.1	54.7	55.2	54.9	54.9	54.1	54.6	0.45
Al_2O_3	0.18	0.23	0.20	0.19	0.19	0.11	0.18	0.04
FeO	0.00	0.03	0.00	0.01	0.01	0.00	0.01	0.01
CaO	24.60	24.78	24.56	24.51	24.56	24.60	24.60	0.09
Na_2O	0.08	0.11	0.10	0.10	0.10	0.07	0.09	0.02
K_2O	3.21	3.13	3.22	3.16	3.20	3.27	3.20	0.05
F	2.09	2.17	2.13	2.08	2.13	2.09	2.12	0.03
Cl	0.00	0.00	0.00	0.01	0.02	0.01	0.01	0.01
-O≡F,Cl	0.88	0.91	0.89	0.88	0.89	0.88	0.89	
Total	83.3	84.2	84.5	84.0	84.2	83.4	83.9	0.49
Structural formula on the basis of ∑(Si + Al) = 8								
Si	7.969	7.961	7.967	7.968	7.968	7.981	7.969	
Al	0.031	0.039	0.033	0.032	0.032	0.019	0.031	
Ca	3.883	3.868	3.799	3.815	3.819	3.891	3.845	
Na	0.022	0.030	0.028	0.028	0.030	0.019	0.026	
K	0.603	0.581	0.593	0.585	0.593	0.614	0.595	
F	0.976	0.999	0.975	0.957	0.976	0.976	0.977	
Cl	0.000	0.000	0.000	0.003	0.004	0.003	0.002	

The single-crystal EPR spectra of a third center are characterized by a single broad absorption line (with an average linewidth of ~ 0.4 mT) in both xy and xz planes (Figure 2.2a), indicative of a center of a single unpaired electron (S = 1/2 and

axial symmetry. The fitted spin-Hamiltonian parameters for this center include $g_{//}$ = 2.00214(1) and $g_{\perp}$ = 2.04438(1), with the former axis approximately along the crystallographic axis **c** (Figure 2.2b). This center is closely comparable in the principal *g* values to Centers A [$g_{//}$ = 2.049(2) and $g_{\perp}$ = 2.007(1)] and A' [$g_{//}$ = 2.039(2) and $g_{\perp}$ = 2.008(1)] in kaolinite (Clozel *et al.*, 1994) and is shown by single-crystal EPR spectra of a hydroxylapophyllite to possess complex satellite peaks arising from several defect pairs (*i.e.*, biradicals; Part II).

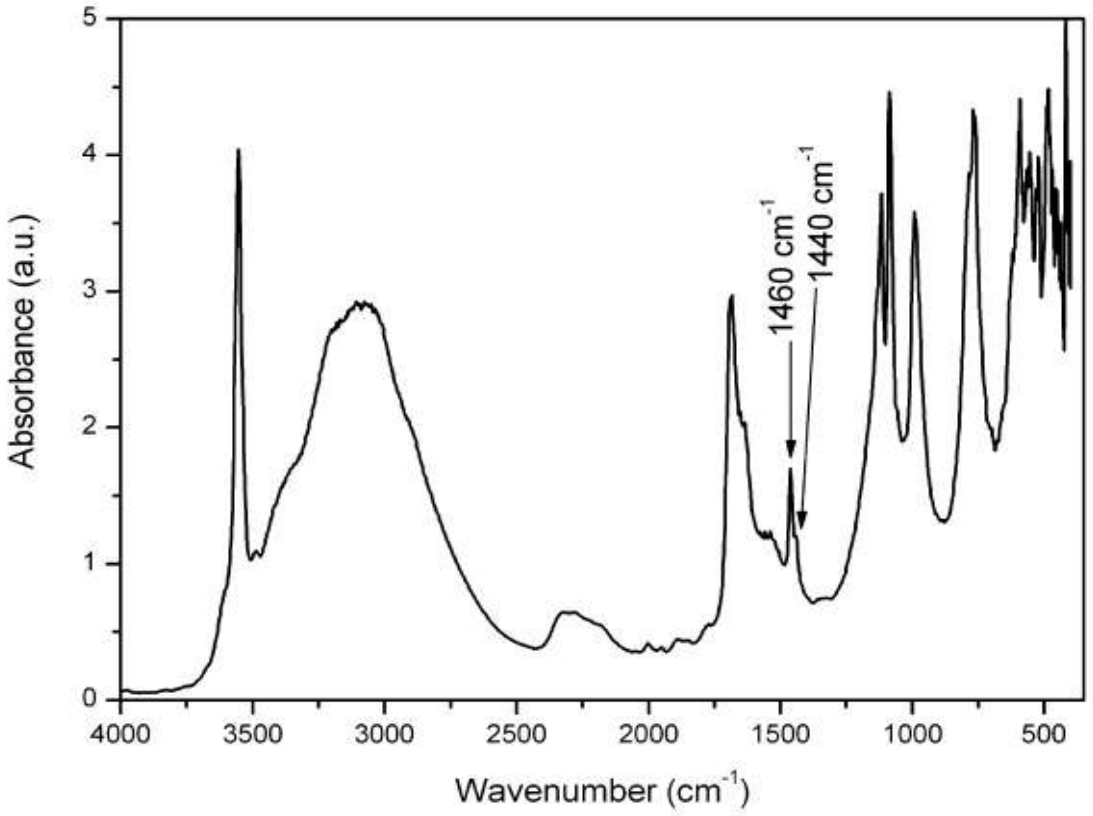

Figure 2.1 FTIR spectrum of fluorapophyllite from North Bohemia, Czech Republic. The 1460 cm^{-1} band and its shoulder at 1440 cm^{-1} are marked by arrows.

The single-crystal EPR spectra of the forth center consist of at most 18 and 24 absorption lines in the *xy* and *xz* planes, respectively, although the number of lines at

most orientations are usually less owing to peak overlapping (Figure 2.3). For example, the spectrum with **B**//**a** contains 3 sets of 3 equally-spaced peaks with intensity ratios of approximately 1:1:1:2:2:2:1:1:1 for a total of 12 equal-intensity lines (Figure 2.2a). Similarly, the spectrum with **B**//**c** has 7 peaks with intensity ratios of 1:2:2:2:2:2:1 for a total of 12 equal-intensity lines (Figure 2.2b). This type of spectra is indicative of an $S = 1/2$ center that has an axial symmetry and a hyperfine structure arising from interaction with one nucleus of $I = 1$ and two equivalent nuclei of $I = 1/2$, and all three nuclei have natural isotope abundances of ~ 100 %. Together with the presence of NH_4^+ as suggested by EMPA results and the FTIR spectrum, we interpret this center to be the NH_2 free radical.

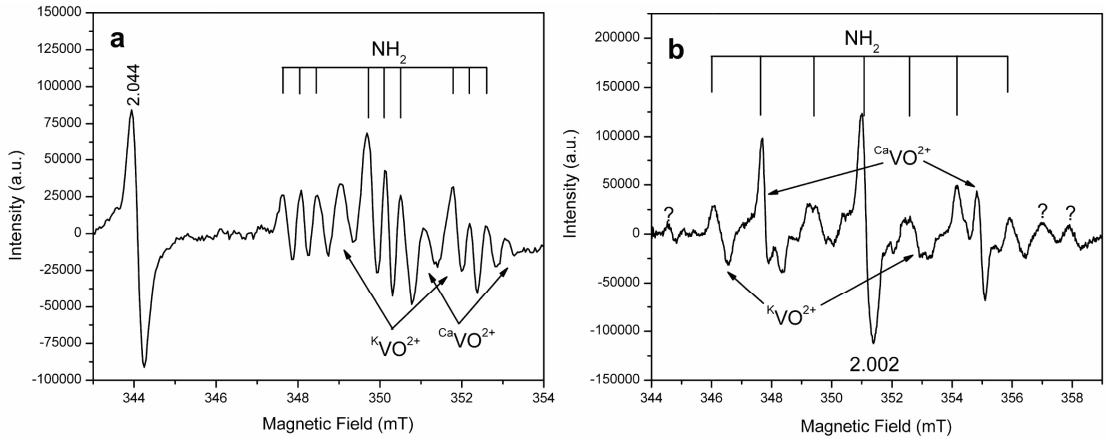

Figure. 2.2 Representative single-crystal EPR spectra of γ irradiated fluorapopphyllite: (a) magnetic field **B** approximately parallel to **a** and (b) **B** approximately parallel to **c**, illustrating the two VO^{2+} centers at the Ca and K sites (*i.e.*, labelled as $CaVO^{2+}$ and KVO^{2+}, respectively; Vassilikou-Dova & Lehmann, 1988), the oxygen-associated center ($g_{\perp}$ = ~ 2.044 and $g_{//}$ = ~ 2.002) and the NH_2 free radical. Unidentified peaks are highlighted by question marks.

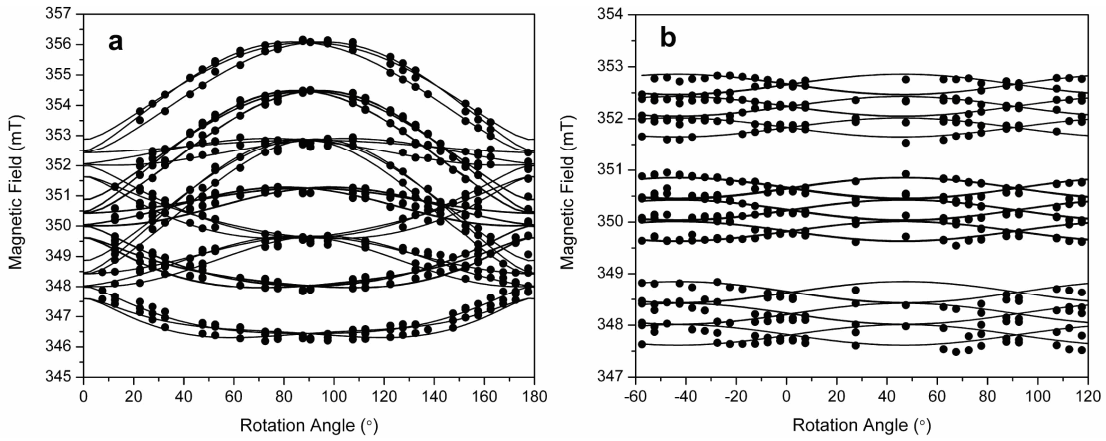

Figure 2.3 The angle dependence of line position data (*i.e.*, roadmap) of the NH_2 free radical in: (a) approximately the *xz* plane and (b) approximately the *xy* plane. Rotation angle 0° in both planes corresponds approximately to an **a** axis. Solid circles represent experimental data points, and solid lines predicted by the fitted spin-Hamiltonian parameters (**Table 2.2**).

The single-crystal EPR spectra of the NH_2 free radical can be described by a spin-Hamiltonian of the form:

$$H = \beta_e \mathbf{S \bullet g \bullet B} + \Sigma \, (\mathbf{S \bullet A_i \bullet I_i} + \mathbf{I_i \bullet P_i \bullet I_i} - \beta_n \mathbf{I_i \bullet g_i \bullet B}) \quad \text{……..……..(2.1)}$$

where β_e and β_n are the electron and nuclear magneton, respectively, and **i** denotes the ^{14}N and two equivalent ^{1}H nuclei. The parameters to be optimized are matrices **g**, **A**(^{14}N) and **P**(^{14}N) and **A**(^{1}H). The total number of line-position points used for optimization was 1982, of which 17 were assigned a weighing factor of 0.1 owing to peak overlapping. The final value of the root-mean squares of weighted differences (RMSD) between the calculated and observed line positions was 0.08 mT, which is less than half of the average linewidth (~ 0.21 mT) for the NH_2 free radical. The signs of the hyperfine matrices **A** and **P** cannot be determined from EPR data alone. Following theoretical studies (Michaut *et al*., 1975; Austen *et al*., 1994), we adopted a

negative sign and a positive sign for the isotropic parts of **A** for ^{1}H and ^{14}N, respectively (Table 2.2). The quadrupole matrix **P**(^{14}N) was fitted but not included in Table 2.2, because it has a negligible effect (i.e., its inclusion in the optimization did not result in any notable change in the RMSD value).

Table 2.2 Spin-Hamiltonian parameters of the NH_2 free radical in γ irradiated fluorapophyllite.

		Matrix **Y**		k	Principal value (Y_k)	Principal direction θ (°)	φ (°)
G	2.00786(2)	0.00112(1)	0.00081(2)	1	2.00923(2)	80.9(2)	46.3(4)
		2.00798(2)	0.00077(1)	2	2.00679(2)	89.4(1)	316.2(1)
			2.00215(1)	3	2.00197(2)	170.9(2)	42(2)
A(^{14}N)/$g_e\beta_e$	-0.416(5)	-0.006(4)	-0.031(8)	1	3.221(4)	0.6(1)	224(10)*
(mT)		-0.412(5)	-0.030(8)	2	-0.408(5)	90.6(1)	234(19)
			3.221(4)	3	-0.421(8)	89.8(2)	324(19)
A(^{1}H)/$g_e\beta_e$	-2.01(1)	-0.01(1)	0.00(1)	1	-2.02(2)	90(1)	53(40)
(mT)		-2.02(1)	0.00(1)	2	-2.01(2)	90(2)	323(40)
			-1.59(1)	3	-1.59(1)	0(1)	43(178)*
A(^{1}H)/$g_e\beta_e$	-2.01(1)	-0.00(1)	0.01(1)	1	-2.02(1)	87(2)	241(58)
(mT)		-2.01(1)	0.01(1)	2	-2.00(1)	89(3)	151(57)
			-1.59(1)	3	-1.59(1)	2(1)	43(53)*

*φ (tilting angle from the crystallographic axis **a**) is meaningless, when θ (tilting angle from **c**) is close to the **c** axis.

2.3.3 Powder EPR spectra

Powder EPR spectra of fluorapophyllite without γ irradiation also disclose the two VO^{2+} centers (Bershov & Marfunin, 1965; Vassilikou-Dova & Lehmann, 1988) and the NH_2 free radical established by the single-crystal EPR spectra. Powder EPR spectra of this fluorapophyllite after γ irradiation show significant increases in intensity of these three centers and disclose the oxygen-associated center as well (Figure 2.4a). Isochronal annealing experiments show that fluorapophyllite exhibits

only a minor weight lost (< 1 wt.%) before 300 °C but a major dehydration (~ 10 wt.%) between 420 °C and 460 °C. The oxygen-associated hole-like center decreases significantly in intensity at 220 °C and disappears completely at 300 °C (Figure 2.4b). The NH_2 free radical remains stable to at least 300 °C but is bleached completely at 340 °C (Figure 2.4b). The VO^{2+} radical at the K site shows a major decrease in intensity between 300 °C and 340 °C and disappears completely at 420 °C (Figure 2.4b).

2.4 Discussion

2.4.1 Identification and spin-Hamiltonian parameters of the NH_2 free radical

The NH_2 free radical with 7 valence electrons has a bent configuration of point symmetry C_{2v} and a HNH bond angle of ~ 104° (Austen *et al.*, 1994). It is one of the most studied triatomic molecules (*e.g.*, Foner *et al.*, 1958; Hills & Cook, 1982; Funken *et al.*, 1990; Austen *et al.*, 1994; Tonooka *et al.*, 1997; Airne & Brill, 2001) and is widely used as spin labels in biophysical and biomedical research (Eaton *et al.*, 2005). However, significant differences in the reported spin-Hamiltonian parameters, particularly the ^{14}N hyperfine constants, were apparent among the early EPR studies of this radical (Table 2.3; Foner *et al.*, 1958; Morton & Smith, 1966; Rao & Symons, 1971; Michaut *et al.*, 1975). These differences have since been shown by theoretical studies (Michaut *et al.*, 1975; Austen *et al.*, 1994; Airne & Brill, 2001) to originate from the motions of this molecule in various matrices. For example, Michaut *et al.*

(1975) noted that **g**, **A**(^{14}N) and **A**(^{1}H) in NH_3 crystals are all axially symmetric about the C_2 axis (*i.e.*, the bisector of the HNH angle) and interpreted them to arise from a free rotation of the radical in the NH_3 lattice during the time-scale of their EPR experiments. Similarly, Foner *et al.* (1958) noted that the NH_2 radical in the argon gas rotates freely, even at 4.2 K, which gives rise to a total hyperfine splitting of ~ 6.8 mT. Significantly wider hyperfine structures have been reported for the NH_2 radical in other matrices. For example, the NH_2 radicals in KNH_2SiO_3 crystals and ammoniated zeolites have the total hyperfine splittings of ~ 13 mT and ~ 12 mT, respectively (Morton & Smith, 1966; Vantsand & Lunsford, 1972).

The fitted spin-Hamiltonian parameters of the NH_2 free radical in fluorapophyllite (Table 2.2) are broadly comparable to those of its counterparts in the literature (Table 2.3). The negligible quadrupole matrix **P**(^{14}N) is consistent with those reported by Hills & Cook (1982) and Tonooka *et al*. (1997), who showed that the ^{14}N quadrupole parameters of the NH_2 radical in the ground state $^2B_1$ are two orders of magnitude less than their corresponding hyperfine constants. The axial symmetries of all matrices **g**, **A**(^{14}N) and **A**(^{1}H) (Table 2.2) indicate that the NH_2 radical in fluorapophyllite also rotates rapidly (*cf*., Michaut *et al*., 1975). Moreover, **g**, **A**(^{14}N) and **A**(^{1}H) all have their unique principal axes approximately along the crystallographic c axis, suggesting a rotation of the NH_2 radical about this axis. It is unclear, however, why the isotropic part of the proton hyperfine (1.87 mT) for the NH_2 free radical in fluorapophyllite is notably smaller than the average value of ~ 2.4 mT in the literature (Table 2.3).

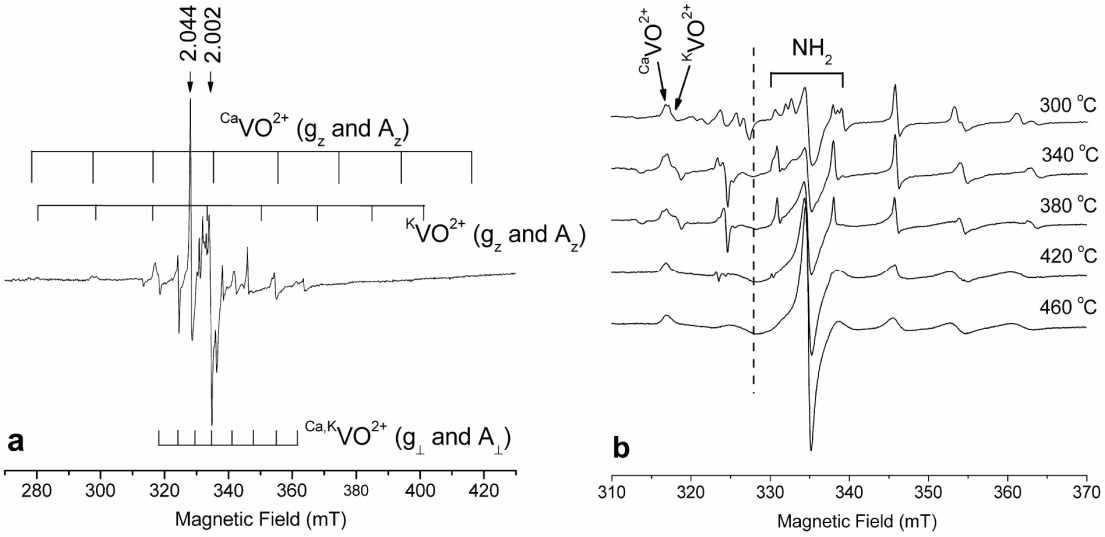

Figure 2.4 Comparison of powder EPR spectra of γ irradiated fluorapophyllite: (a) without annealing illustrating the two VO^{2+} centers at the Ca and K sites [*i.e.*, $^{Ca}VO^{2+}$ and $^{K}VO^{2+}$, which are readily distinguished by their distinct g_z and A_z values (marked) but share similar g_x, g_y, A_x and A_y values (hence marked together as $^{Ca,K}VO^{2+}$($g_\perp$ and $A_\perp$)] and the oxygen-associated center ($g_\perp$ = ~ 2.044 and $g_{//}$ = ~ 2.002); the NH_2 free radical is visible but overshadowed by the VO^{2+} centers and the oxygen-associated center; and (b) annealed between 300 °C and 460 °C. Note that the NH_2 radical is visible in the 300 °C spectrum between 330 mT and 340 mT (outlined) but is bleached at 340 °C. Also note that the oxygen-associated center with $g_\perp$ = 2.044 (marked by the dashed line) is now bleached completely. Also the VO^{2+} center at the K site ($^{K}VO^{2+}$) decreases significantly in intensity between 300 °C and 340 °C and disappears completely at 420 °C.

The only previously reported occurrence of the NH_2 free radical in minerals is that of Yang *et al*. (2007), who suggested the observed NH_2 radical in green quartzite originated from radiolysis of NH_3 in fluid inclusions. Although the substitution of NH_4^+ for K^+ is not uncommon in feldspars [including the presence of buddingtonite $(NH_4)AlSi_3O_8$; Solomon & Rossman, 1988; Voncken *et al*., 1993] and other K-rich

minerals, the NH_2 radical has not been found in naturally or artificially irradiated feldspars (Petrov, 1994). Matyash *et al*. (1982) reported two N-associated paramagnetic defects (NH_3^+ and N^{2-}) inmicrocline from pegmatites, which have been shown by Petrov (1994) to be the CH_3 and NO_2 free radicals, respectively. To the best of our knowledge, the NH_2 free radical in fluorapophyllite is the first occurrence of this radical in mineral lattices.

Attempts to detect the NH_2 free radical in fluorapophyllite at 90 K have been made but were not successful. This result may be attributable to severe line broadening related to a restricted rotation of this molecule in the fluorapophyllite lattice at cryogenic temperatures.

2.4.2 Formation and thermal stability of the NH_2 free radical in fluorapophyllite

Extensive literature exists on the formation of the NH_2 freeradical from the dissociation of ammonia in (and on the surfaces of) various matrices via radiolysis or photolysis (Vantsand & Lunsford, 1972; Kartel *et al.*, 1978; Wolkow & Avouris, 1988)

$$NH_3 + H^+ + e \rightarrow NH_2 + H_2 \quad \text{..... (2.2)}$$

Also the reaction between NH_4^+ and NH_3 is well known

$$NH_4^+ \rightarrow NH_3 + H^+ \quad \text{..... (2.3)}$$

It is possibly, therefore, that the NH_2 free radical formed from the NH_4^+ ion via these two reactions, which can be combined as

$NH_4^+ + e \rightarrow NH_2 + H_2$ .....(2.4)

Reaction (3) for the formation of the NH_2 radical in fluorapophyllite can be rewritten as

$\equiv Si–OH_2–NH_4^+ + e \rightarrow \equiv Si–OH_2–NH_2 + H_2$ .....(2.5)

where ≡ represents three Si–O bonds and the NH_4^+ ion (and presumably the NH_2 radical as well) occupies the K site coordinated to eight water molecules (Colville *et al.*, 1971; Rouse *et al*., 1978; Pechar, 1987). Reaction (2.5) is closely comparable to the formation of the NH_2 free radical on the surfaces of γ irradiated ammonia silica (Kartel *et al.*, 1978). Other reactions such as $NH_4^+ \rightarrow NH_3^+ + H^0$ and $NH_3^+ + e \rightarrow NH_2 + H^0$ can be ruled out on the basis of the absence of the paramagnetic NH_3^+ and H^0 species in the EPR spectra. Reactions (2.4) and (2.5) also suggest that the NH_2 free radical may be common in K-feldspars and other ammonium-bearing minerals. However, detection of the NH_2 free radical in most minerals by conventional EPR techniques may be difficult owing to the motional effects.

The dehydration process of fluorapophyllite observed in our isochronal annealing experiments is similar to those reported by previous studies (Ståhl *et al*., 1987; Marriner *et al*., 1990; Ståhl, 1993; Wlodyka, 2002). For example, Marriner *et al*. (1990) observed two stages of dehydration for both fluorapophyllite (310–334 °C and 430–450 °C) and hydroxylapophyllite (300–310 °C and 400–422 °C). Marriner *et al*. (1990) noted that ammonium apophyllites dehydrate at slightly lower temperatures than their ammonium-free counterparts. Marriner *et al*. (1990) also reported that the NH_4^+ band at 1460 cm^{-1} disappears in the IR spectrum of a partially dehydrated

fluorapophyllite, but did not give the temperature value. The present study shows that the NH_2 free radical remains stable after annealing at 300 °C but is bleached completely at 340 °C (Figure 2.4b).

Table 2.3 Literature data of the NH_2 free radical in selected matrices.

Matrix	g	$\mathbf{A}(^{14}N)/g_e\beta_e$	$\mathbf{A}(^{1}H)/g_e\beta_e$	Experiment	Reference
Argon(gas)	2.0048	1.04	2.38	4.2 K	1
Ammonia(gas)	2.0046(3)	1.52	2.54	77 K	2
Water	2.003	4.1($_{//}$), 0($_{\perp}$)	2.4	77 K	3
KNH_2SO_3 (single crystal)		3.82	3.14	77 K	4
		0.14	2.55		
		0.03	2.50		
NH_3 (single crystal)	2.0047	1.67	-3.09	77 K	5
	2.0047	1.67	-2.15		
	2.0011	0	-2.10		
Zeolite (synthetic)	$g_{//}$=2.0022	+3.5	2.6	77 K	6
		±0.3			
		±0.3			

Reference 1, Foner et al. (1958); 2, Smith & Seddon (1970); 3, Rao & Symons (1971); 4, Morton & Smith (1966); 5, Michaut et al. (1975); and 6, Vantsand & Lunsford (1972).

Ståhl (1993) showed that the dehydration process of fluorapophyllite is diffusion controlled (*i.e.*, a kinetic effect) and occurs as a two steps reaction: the first step expels one of the eight water molecules in the K coordination sphere, and the second step destabilizes the K and Ca coordinations to form an amorphous phase. The observed thermal stabilities of the two VO^{2+} centers (Figure 2.4b) are in agreement with this two steps reaction. For example, the marked decrease in intensity of the VO^{2+} center at the K site between 300 °C and 340 °C (Figure 2.4b) is similar to the disappearance of this center after annealing of an India apophyllite at ~220 °C (Ramakrishnan *et al.*, 1991), supporting the first step involving the K site (*cf.*,

Vassilikou-Dova & Lehmann, 1988). The convergence of the two VO^{2+} centers at 420 °C corresponds to the collapse of both K and Ca sites and the formation of the amorphous phase (Ståhl, 1993; Wlodyka, 2002).

2.5 Conclusions

Single-crystal EPR spectra of γ-ray irradiated fluorapophyllite measured at room temperature revealed a NH_2 radical. The best-fit spin-Hamiltonian parameters indicate that the NH_2 radical occupies the K site and spins rapidly along the molecular C_2 axis that coincides with the crystallographic **c** axis. These data, together with results frm FTIR and electron microprobe analyses, suggest that the NH_2 radical most likely formed from the radiolysis of the NH_4^+ ion. This is the first report of the NH_2 radical in a mineral lattice.

2.6 References

AIRNE, A.R. & BRILL, A.S. (2001): Nuclear spin-state mixing in the NH_2 radical. *Phys. Rev. A* **63**, 052511-1-10.

ALDUSHIN, K., JORDAN, G., RAMMENSEE, W., SCHMAHL, W.W. & BECKER, H.-W. (2004): Apophyllite (001) surface alteration in aqueous solutions studied by HAFM. *Geochim. Cosmochim. Acta* **68**, 217-226.

ALLARD, T. & MULLER, J.P. (1998): Kaolinite as an in situ dosimeter for past radionuclide migration at the Earth's surface. *Appl. Geochem.* **13**, 751–765.

ALLARD, T., ILDEFONSE, P., PEREZ DEL VILLARD, L., SORIEUL, S., PELAYO, M., BOIZOT, B., BALAN, E. & CALAS, G. (2003): Radiation-induced defects in dickites from the El Berrocal granitic system (Spain): relation with past occurrence of natural radioelements. *Eur. J. Mineral.* **15**, 629–640.

ALLARD, T., CALAS, G. & ILDEFONSE, P. (2007): Reconstruction of past U migration in a sedimentary deposit (Coutras, France): Implications for a radwaste repository. *Chem. Geol.* **239**, 50-63.

AUSTEN, M.A., ERIKSSON, L.A. & BOYD, R.J. (1994): A density functional theory study of the free radicals NH_2, NF_2, NCl_2, PH_2, PF_2, and PCl_2. *Canad. J. Chem*. **72**, 698-704.

BERSHOV, L.V. (1970): Isomorphism of titanium in minerals. *Izv.Akad. Nauk SSSR*, **12**, 47-54.

BERSHOV, L.V. & MARFUNIN, A.S. (1965): Vanadyl ion in minerals. *Izv. Akad. Nauk SSSR Ser. Geol.*, **9**, 42-52.

BERSHOV, L.V., MARFUNIN, A.S., & MINEEVA, R.M. (1965): Vanadyl ion in minerals. *Izv. Akad. Nauk. Ser. Geol.* **9**, 42-52.

CAVE, L.C. (2002): Apophyllite weathering and the aqueous geochemistry of a Karoo breccia pipe. PhD thesis, Dept. Geological Sciences, University of Cape Town.

CHEN, C.G., YEBASSA, D. & RAGHAVAN, D. (2007): Synthesis, characterization, and mechnical properties of evaluation of thermally stable apophyllite vinyl ester nanocomposites. *Polym. Advan. Technol.* **18**, 574-581.

CLOZEL, B., ALLARD, T. & MULLER, J.P. (1994): Nature and stability of radiation-induced defects in natural kaolinites: new results and reappraisal of published works. *Clays Clay Minerals* **42**, 657–666.

COLVILLE, A.A., ANDERSON, C.P. & BLACK, P.M. (1971): Refinement of the crystal structure of apophyllite: I. X-ray diffraction and physical properties. *Amer. Mineral.* **56**, 1222-1233.

EATON, S.S., EATON, G.R. & BERLINER, L.J. (2005): Biomedical EPR – part B: methodology, instrumentation and dynamics. *Biol. Magn. Reson.* **24**, 472.

FONER, S.N., COCHRAN, E.L., BOWERS, V.A., Jen, C.K. (1958): Electron spin resonance spectra of the NH_2 and ND_2 free radicals at 4.2. K. *J. Phys. Lett.*, **1**, 91-92.

FUNKEN, K., ENGELS, B., PEYERIMHOFF, S.D. & GREIN, F. (1990): Study of the hyperfine coupling constants of the molecules NH_2, NHD and ND_2. *Chem. Phys. Lett.* **172**, 180-186.

GÖTZE, J., PLÖTZE, M., GÖTTE, TH., NEUSER, R.D., & RICHTER, D.K. (2002): Cathodoluminescence (CL) and electron paramagnetic resonance (EPR) studies of clay minerals. *Mineral. Petrol.*, **76**, 195-212.

HILLS, H.W. & COOK, J.M. (1982): Fine and hyperfine parameters for NH_2 in $X^2B_1(100)$. *J. Mol. Spec.* **94**, 456-460.

KARTEL, N.T., TSYBA, N.N., KABAKCHI, A.M., & STRELKO, V.V. (1978): A study of the products from the radiolysis of the gamma-irradiated ammonia–silica system. *J. Appl. Spectrosc.*, **28**, 339-343.

MARRINER, G.F., TARNEY, J. & LANGFORD, J.I. (1990): Apophyllite group: effects of chemical substitutions on dehydration behaviour, recrystallization products and cell parameters. *Mineral. Mag.* **54**, 567-577.

MATSUEDA, H., MIURA, Y., & RUCKLIDGE, J. (1981): Natroapophyllite, a new orthorhombic sodium analog of apophyllite; I, Description, occurrence, and nomenclature. *Am. Mineral.*, **66**, 410-415.

MATYASH, I.V., BAGMUT, N.N., LITOVCHENKO, A.S. & PROSHKO, V.YA (1982): Electron paramagnetic resonance study of new paramagnetic centers in microcline-perthites from pegmatites. *Phys. Chem. Minerals* **8**, 149-152.

MICHAUT, J.P., RONCIN, J. & MARX, R. (1975): NH_2 radicals trapped in NH_3 single crystals and various polycrystalline ammonia matrices. *Chem. Phys. Lett.* **36**, 599-605.

MOMBOURQUETTE, M.J., WEIL, J.A. & MCGAVIN, D. (1996): EPR-NMR ussers' manual. Department of Chemistry, University of Saskatchewan, Saskatoon, Saskatchewan.

MORICHON, E., ALLARD, T., BEAUFORT, D. & PATRIER, P. (2008): Evidence of native radiation-induced paramagnetic defects in natural illite from unconformity-type uranium deposits. *Phys. Chem. Minerals* (on line).

MORTON, J.R. & SMITH, D.R. (1966): Electron spin resonance spectra of ^{15}N-centered radicals at low temperatures. II. The radiolysis of potassium sulfamate. *Canad. J. Chem.* **44**, 1951-1955.

PECHAR, F. (1987): The X-ray diffraction refinement of the crystal structure of natural apophyllite. *Crystal. Res. Technol*. **22**, 1041-1046.

PETROV, I. (1994): Lattice-stabilized CH_3, C_2H_5, NO_2, and O^{1-} radicals in feldspar with different Al-Si order. *Amer. Mineral.* **79**, 221-239.

RAMAKRISHNAN, G., SWAMY, M.B.V.L.N., RAO, P.S., & SUBRAMANIAN, S. (1991): EPR of vanadyl ion in a natural mineral, apophyllite. *J. Chem. Sci.*, **103**, 613-619.

RAO, K.V.S. & SYMONS, M.C.R. (1971): Unstable intermediates. Part XCVI. The effect of hydrogen-bonding on the e.s.r. parameters for NH_2, NH_3^+, and H_2CN. *J. Chem. Soc. A*, 2163-2166.

ROUSE, R.C., PEACOR, D.R. & DUNN, P.J. (1978): Hydroxyapophyllite, a new mineral, and a redefinition of the apophyllite group. II, Crystal structure. *Amer. Mineral*. **63**, 199-202.

SMITH, D.R. & SEDDON, W.A. (1970): Electron spin resonance spectra of ^{15}N labeled amino radicals. *Canad J. Chem.* **48**, 1938-1942.

SOLOMON, G.C. & ROSSMAN, G.R. (1988): NH_4^+ in pegmatitic feldspars from the southern Black Hills, South Dakota. *Amer. Mineral*. **73**, 818-21.

SORIEUL, S., ALLARD, T., MORIN, G., BOIZOT, B., & CALAS, G. (2005): Native and artificial radiation-induced defects in montmorillonite. An EPR study. *Phys. Chem. Minerals*, **32**, 1-7.

STÅHL, K. (1993): A neutron powder diffraction study of partially dehydrated fluorapophyllite, $KCa_4(Si_8O_{20})F{\cdot}8H_2O$. *Eur. J. Mineral*. **5**, 845-849.

STÅHL, K. (1987): A neutron diffraction and thermogravimetric study of the hydrogen and dehydration behaviour in fluorapophyllite, $KCa_4(Si_8O_{20})F{\cdot}8H_2O$, and its partially dehydrated form. *Acta Cryst*. **B43**, 517-523.

TONOOKA, M., YAMAMOTO, S., KOBAYASHI, K., & SATO, S. (1997): The microwave spectrum of the NH_2 radical: the hyperfine structure of the $^2B_1$ pround electronic state. *J. Chem. Phys.*, **106**, 2563-2568.

VANTSAND, E.F. & LUNSFORD, J.H. (1972): Electron paramagnetic resonance spectra of NH_2 radicals formed by γ irradiation of ammoniazted zeolites. *J. Phys. Chem.* **76**, 2716-2718.

VASSILIKOU-DOVA, A.B. & LEHMANN, G. (1988): EPR of V^{4+} in apophyllite. *Phys. Stat.Sol.* **147**, 691-697.

VONCKEN, J.H.L., VAN ROERMUND, H.L.M., VAN DER EERDEN, A.M.J., JANSEN, J.B.H. & ERD, R.C. (1993): Holotype buddingtonite, an ammonium feldspar without zeolitic H_2O. *Amer. Mineral.* **78**, 204-209.

WLODYKA, R. (2002): Raman spectroscopic study of the dehydration behavior in fluorapophyllite. *Polsk. Towarz. Mineral*. **20**, 228-230.

WOLKOW, R. & AVOURIS, P. (1988): Atomic-resolved surface chemistry using scanning tunneling microscopy. *Phys. Rev. Lett.*, **60**, 1049-1052.

YANG, L., MASHKOVTSEV, R., BOTIS, S. & PAN, Y. (2007): Multi-spectroscopic study of green quartzite (Guizhou Jade) from the Qinglong antimony deposit, Guizhou Province, China. *J. China Univ. Geosci.* **18**, 383-386.

Chapter 3

Radiation-induced defects in apophyllites. II. An O^- centre and related O^--O^- pairs in hydroxylapophyllite

A hole-like centre present in natural hydroxylapophyllite without any artificial irradiation has been investigated by single-crystal and powder electron paramagnetic resonance (EPR) spectroscopy at 290 K and 90 K, and by three-pulse electron spin echo envelope modulation (ESEEM) spectroscopy at 25 K. Calculated matrices **g**, **A**(^{29}Si), **A**(^{1}H), **A**(^{39}K) and **P**(^{39}K) suggest it to be an O^- centre at the hydroxyl oxygen site and the unpaired electron in the $2p_z$ orbital. A series of weak satellite peaks accompanying the main absorption line in single-crystal EPR spectra have been shown to arise from four geometrically distinct pairs of neighbouring O^- centres (*i.e.*, biradicals). The spin Hamiltonian parameters of these O^--O^- pairs provide further support for the O^- model and its location at the hydroxyl oxygen site. The O^- centre in hydroxylapophyllite most likely formed from natural radiation and can be enhanced by gamma-ray irradiation. It is annealed out at 300°C but can be restored readily by gammaray irradiation. The presence of these O^--O^- pairs in the hydroxylapophyllite is probably attributable to a high abundance of the O^- centre in this sample.

3.1 Introduction

In Part I of this series (Mao & Pan, 2009), we investigated an NH_2 free radical in a gamma-ray-irradiated fluorapophyllite by electron paramagnetic resonance (EPR) spectroscopy. The single-crystal EPR spectra of the gamma-ray-irradiated fluorapophyllite also disclosed another simple spin (S = 1/2) centre with $g_{//}$ = ~2.002 and $g_{\perp}$ = ~2.044, which was not present before gamma-ray irradiation. Therefore, this centre apparently formed in this sample by gamma-ray irradiation as well (hence a radiation-induced defect) and is similar to the common O^- centre in various minerals and other materials (*e.g.*, Marfunin, 1979; Che & Tench, 1983; Murphy & Chiesa, 2004). This centre has also been observed in single-crystal and powder EPR spectra of a natural hydroxylapophyllite without any artificial irradiation, which have significantly higher signal-to-noise ratios than those of the gamma-ray-irradiated fluorapophyllite and disclose a series of weak satellite peaks accompanying the main absorption line. As part of our continuing efforts to better characterise oxygen-associated radiation-induced defects in layer silicates, we have analyzed this O^- centre in the natural hydroxylapophyllite by using both continuous-wave (CW) single-crystal EPR spectra and pulsed electron spin echo envelope modulation (ESEEM) spectra. Results reported herein confirm the O^- centre to reside at the hydroxyl oxygen site. Moreover, the satellite peaks are shown to arise from four geometrically distinct pairs of O^- centres (*i.e.*, biradicals; Mashkovtsev *et al*., 2007; Weil & Bolton, 2007).

Apophyllites ($KCa_4Si_8O_{20}(F,OH)•8H_2O$) are layer silicates with ‘‘puckered’’ Si_8O_{20} sheets alternating with layers of K^+, Ca^{2+}, F^-, OH^- and H_2O (Figure 3.1; Taylor & Náray-Szabó, 1931; Chao, 1971; Colville *et al*., 1971; Prince, 1971; Bartl & Pfeifer, 1976; Rouse *et al*., 1978; Pechar, 1987). The ‘‘puckered’’ Si_8O_{20} sheets form from 4- and 8-membered rings of SiO_4 tetrahedra. The interlayer K^+ cation is coordinated to eight water molecules in the form of a squat tetragonal prism, whereas Ca^{2+} is coordinated to 2 water molecules, $4O^{2-}$ ions and $1F^-$ or OH^- ion. In fluorapophyllite, the F^- ion at equipoint 2a (0,0,0) is surrounded by a planar group of $4Ca^{2+}$ ions. Prince (1971), on the basis of his neutron diffraction study of a ‘‘fluorapophyllite’’ crystal, suggested that the F^- ion is coordinated to a hydrogen H(3) to form an HF molecule. Bartl & Pfeifer (1976) showed that H(3) in intermediate fluorapophyllite and hydroxylapophyllite is not bonded to fluorine but to oxygen as an OH^- group. Dunn *et al*. (1978) noted that crystals from the locality investigated in Prince (1971) have intermediate compositions between hydroxylapophyllite and fluorapophyllite. Dunn *et al*. (1978) also showed that hydroxylapophyllite belongs to the space group *P4/mnc*, with a = 8.978(3) Å and c = 15.83(1) Å. Rouse *et al*. (1978) noted that X-ray data of hydroxylapophyllite do not provide unequivocal evidence for the expected positional disorder of the hydroxyl oxygen atom at equipoint 4e (*i.e.*, half at 0,0,z and half at 0,0,$\bar{z}$), which was then kept at 0,0,0 (Figure 3.1).

3.2 Samples and experimental techniques

A suite of apophyllite specimens from the University of Saskatchewan reference mineral collection has been investigated by reconnaissance single-crystal EPR experiments. Prismatic to platy hydroxylapophyllite crystals (~2 to ~15 mm long and ~4 to ~20 mm in diameter) from an unknown locality were then chosen for detailed single-crystal EPR and ESEEM measurements. Selected crystals of this specimen were also polished for electron microprobe analysis (EMPA) and pulverised for Fourier-transform infrared (FTIR) analysis, powder EPR analysis, and inductively coupled plasmamass spectrometry (ICP-MS) analysis. The sample used for powder EPR measurements was also subject to first a series of step-wise, isochronal annealing experiments from 100 °C to 300 °C, at an interval of 25 °C and a duration of 30 minutes each step, and then gamma-ray irradiation in a ^{60}Co source at room temperature for a dose of ~32 kGy. Another powder sample without annealing was also irradiated in the ^{60}Co source at room temperature for a dose of ~50 kGy.

Electron microprobe analysis was performed on a JEOL JXA-8600 superprobe equipped with three wavelength-dispersive spectrometers, at the Department of Geological Sciences, University of Saskatchewan. Analytical conditions included an accelerating voltage of 15 kV, beam current of 10 nA, beam diameter of ~5 μm and the following standards: quartz (Si), γ-Al garnet (Al), Jadeite (Na), magnetite (Fe), diopside (Ca), sanidine (K), fluorite (F) and tugtupite (Cl). ICP-MS analysis was made on a Perkin-Elmer Sciex Elan 5000 instrument, using the HF-HNO_3 acid-dissolution method. Powder sample of hydroxylapophyllite was mixed with KBr

for FTIR measurements on a BIO-RAD FTS-40 spectrometer with a resolution of 4 cm^{-1}, at the Saskatchewan Structure Science Centre (SSSC), University of Saskatchewan.

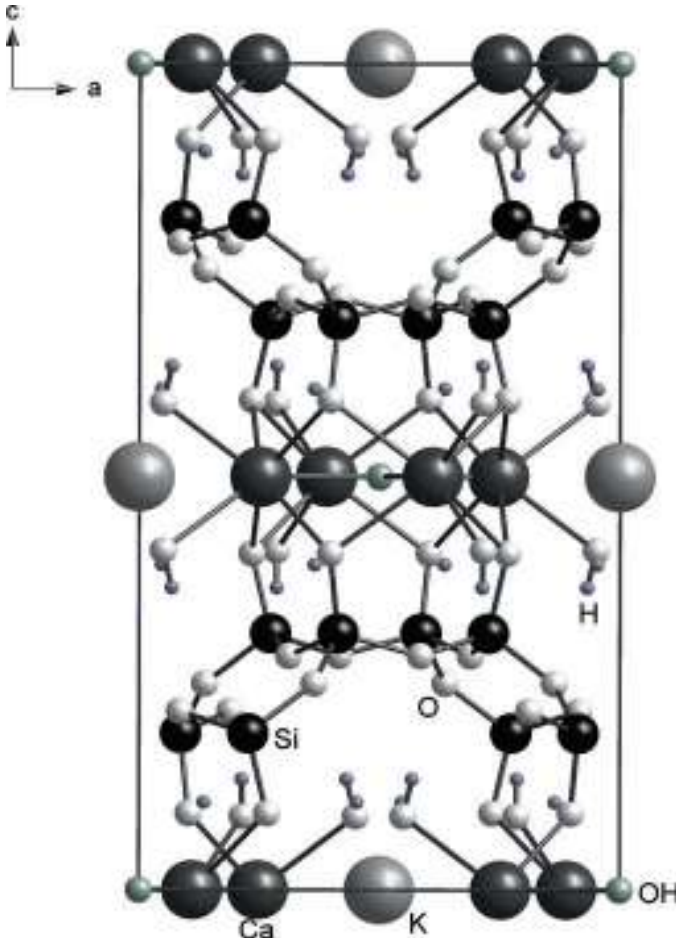

Figure 3.1 Projection of the hydroxylapophyllite structure on the (100) plane illustrating alternating Si_8O_{20} sheets and K,Ca sheets (data from Rouse *et al*., 1978). Note that the hydroxyl group is located at 0,0,0.

Powder and single-crystal EPR spectra were measured on a Bruker EMX spectrometer with an ER4119 cavity at SSSC. Experimental conditions for powder EPR measurements at room temperature (290 K) and 90 K included microwave frequencies of ~9.38 GHz and ~9.75 GHz, modulation frequency of 100 kHz,

modulation amplitude of 0.05 mT and microwave powers of ~2 mW. Spectral resolutions were ~0.015 mT (*i.e.*, 1024 field data points over 15 mT) or 0.014 mT (1024 points over 14 mT). Calibration of the magnetic field was made by use of the free radical 2,2-diphenyl-1-picrylhydrazyl (DPPH; g = 2.0036).

Reconnaissance single-crystal EPR measurements at 290 K and 90 K were made on several crystals. One crystal of ~1 mm x 1 mm x 2 mm in size was then selected for detailed single-crystal EPR measurements at these two temperatures in two orthogonal planes: with the magnetic field B parallel to (001) and (110) faces. Experimental conditions for single-crystal EPR measurements included a microwave frequency of ~9.38 GHz, modulation frequency of 100 kHz, modulation amplitude of 0.05 mT, and microwave power of 2 mW. The spectral resolutions were ~0.013 mT (1024 field data points over 13 mT). The angle interval of each measurement was 5° for both planes. The Bruker ER 218G1 goniometer used in this study has an angle uncertainty of ~0.2°.

ESEEM spectra at 25 K were collected on a Bruker E580-10 Elexsys with a liquid He Oxford CF935 cryostat. Spectra were obtained with a three-pulse scheme ($\pi/2–\tau–\pi/2–T–\pi/2–$echo) with four-step phase cycling (4096 points @ 8 ns steps). Time domain ESEEM spectra were baseline corrected, zero-filled, apodized, and Fourier transformed to give frequency domain spectra. Because three-pulsed ESEEM gives rise to blindspots that arise from an oscillating τ dependence, ESEEM spectra were also recorded as a function of τ and later summed (24 spectra @ 8 ns steps). Because of a finite dead time the absolute value spectra of Fourier transformed spectra

is usually presented. However, this results in distortions in the ESEEM spectra, especially at the lower frequencies, such those for ^{39}K and ^{29}Si. To minimize these effects, the data were reprocessed using cross term averaging (Van Doorslaer *et al*., 1999; 48 points @ 64 ns steps).

ESEEM spectra at a rotation angle of every 10° were collected on a crystal mounted with the rotation axis in the (001) face. As the CW EPR spectra do not show any site splitting, all eight symmetry related sites are excited simultaneously by the microwave pulse. As such, angle corrections (accurate to ~0.5°) had to be calculated directly from the fitting of the ^{29}Si ESEEM spectra, which were well resolved. Angle corrections indicated that the rotation axis was ~4.5° from the [110] direction. ESEEM spectra were then simulated using SIMEND (Nilges *et al*., 2009), with the addition of a routine to simulate dead-time effects using FFT (Keijzers *et al*., 1987) and a routine to simulate the additional effects of cross-term averaging. Because the observed modulations were very weak, the contributions from the various nuclei could be considered independently.

3.3 Results

3.3.1 Chemical composition and FTIR spectrum

The average of 12 EPMA analyses for the sample investigated in this study is given in Table 3.1. This sample approaches the hydroxylapophyllite end-member, except for a minor substitution of Ca for K (Table 3.1). This substitution is also evident in hydroxylapophyllite analyses listed in Dunn *et al*. (1978), where charge balance is maintained partly by a concomitant substitution of Al^{3+} for Si^{4+}. In

hydroxylapophyllite of this study, however, the amounts of Al^{3+} and Fe^{3+} are negligible. Two other plausible substitutions for maintaining charge balance involve O^{2-} for OH^- and vacancy at the K site (Table 3.1). The presence of impurity O^{2-} ions at the hydroxyl site can also explain the absence of X-ray diffraction evidence for the positional disorder (Rouse *et al.*, 1978). Unlike the ammonium-bearing fluorapophyllite reported in Part I (Mao & Pan, 2009), the characteristic N–H bands at ~1460 and ~1440 cm^{-1} are absent in the FTIR spectrum of hydroxylapophyllite (not shown). ICP-MS analysis of this sample yielded trace amounts of Rb (162 ppm), Fe (192), Mn (2) and V (3).

Table 3.1 Composition of hydroxylapophyllite.

Analysis	Average (n = 12)	Standard deviation
SiO_2 (wt%)	53.0	0.9
Al_2O_3	0.04	0.02
Fe_2O_3	0.01	0.01
CaO	25.5	0.3
Na_2O	0.05	0.01
K_2O	4.09	0.09
F	0.01	0.01
Cl	0.00	0.00
-O≡F, Cl	0.00	0.00
Total	82.8	1.1
∑(Si + Al + Fe) = 8		
Si	7.992	
Al	0.007	
Fe	0.001	
Ca	4.120	
Na	0.017	
K	0.788	
F	0.005	
Cl	0.000	

wt% is weight percent

3.3.2 Single-crystal EPR spectra

The single-crystal EPR spectra of hydroxylapophyllite are distinct from those of fluorapophyllite (Mao & Pan, 2009). For example, the two pronounced VO^{2+} centres and the radiation-induced NH_2 free radical observed in fluorapophyllite (Mao & Pan, 2009) are absent in hydroxylapophyllite, even after gamma-ray irradiation. The single-crystal EPR spectra of hydroxylapophyllite measured at 290 K disclose a single pronounced absorption line of ~0.4 mT wide at all orientations, which is accompanied by a series of poorly resolved satellite peaks. The main absorption line arises from the same centre that was observed in gamma-ray-irradiated fluorapophyllite (and tentatively interpreted to be an O^- centre in Mao & Pan, 2009). However, this centre in hydroxylapophyllite is visible without any artificial irradiation. Reconnaissance single-crystal EPR examinations also identified this centre (including its satellite peaks) in two other apophyllite specimens (*i.e.*, Gaspé, Quebec and Wasson's Bluff, Nova Scotia) without any artificial irradiation. However, the EPR spectra of the hydroxylapophyllite specimen are almost an order of magnitude higher in intensity than those of the Quebec and Nova Scotia samples.

This O^- centre is better resolved in the single-crystal EPR spectra measured at 90 K, with the main absorption line narrowed down to ~0.17 mT. Again, only one main absorption line is observed in both (001) and (110) planes, indicative of a single unpaired electron S = 1/2 and an axial symmetry. Moreover, the weak satellite peaks (~0.14 mT wide) accompanying the main absorption line are now clearly resolved at most orientations (Figure 3.3). Spectral simulations show that all satellite peaks are

approximately similar in intensity, except where two or more peaks overlap (Figure 3.2b). However, the intensity ratio of each satellite peak to the main absorption line in different crystals shows a wide variation from ~1:1500 to ~1:300, which confirms that these satellite peaks do not arise from hyperfine interactions with nuclei of non-zero nuclear spins. Instead, we have been able to distinguish these satellite peaks into four separate sets (I, II, III, and IV; Figure 3.3) and characterize them as geometrically distinct pairs of weakly interacting O^- centres (*i.e.*, biradicals; *cf.* Weil & Bolton, 2007; Mashkovtsev *et al.*, 2007).

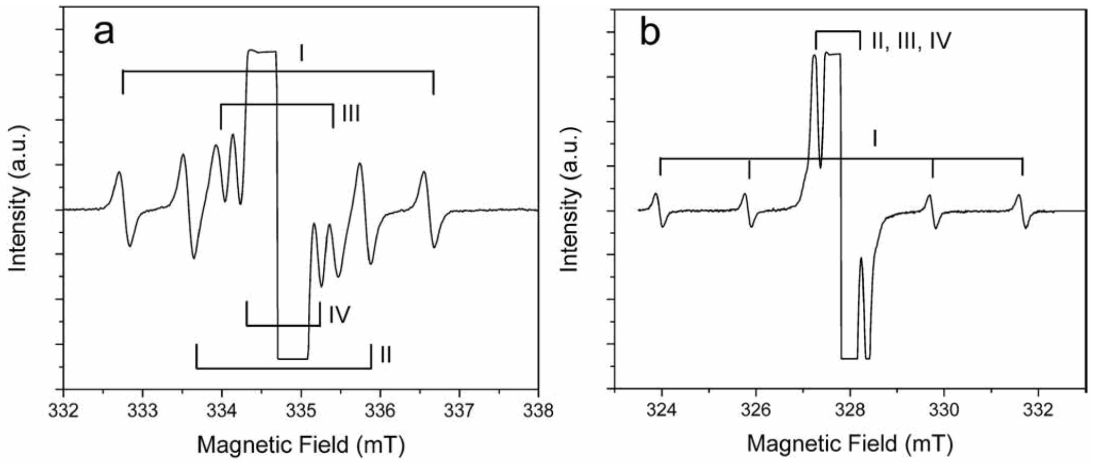

Figure 3.2 Single-crystal EPR spectra measured at ~90 K and microwave frequency of 9.379 GHz: a) magnetic field **B** parallel to the crystallographic axis **c** and b) B//a. Labels for the four sets of satellite peaks correspond to those in **Tables 3.3** and **3.5**.

The spin Hamiltonian to describe the main absorption line of this S = 1/2 centre is as follows:

$$H = \beta_e \mathbf{B}^T \bullet \mathbf{g} \bullet \mathbf{S} \quad \text{.....(3.1)}$$

where β_e is the electronic (Bohr) magneton. Matrix **g** has been fitted by use of the software EPR-NMR (Mombourquette *et al.*, 1996) for line-position data from the spectra measured at both 90 K and 290 K (Table 3.2). The total line-position data used for both temperatures are 296, and a uniform weighing factor of 1 was assigned to all lines. The final values of the root-mean-squares of weighted differences (RMSD) between calculated and measured line-position data at 90 K and 290 K are 0.01 and 0.02 mT, respectively, both of which are considerably less than half of their respective average linewidths. The most salient features of matrix **g** are: (1) axial symmetry and (2) the unique principal axis $g_{//}$ along the crystallographic **c**-axis (Table 3.2). The principal g values in Table 3.2 are similar to those obtained from the gamma-ray-irradiated fluorapophyllite (Mao & Pan, 2009).

The four sets of well-resolved satellite peaks (I, II, III and IV; Figure 3.3) can be interpreted in terms of a pair of interacting spins (Weil & Bolton, 2007; Mashkovtsev *et al.*, 2007):

$$H = \beta_e \mathbf{B}^T \bullet (g_1 \bullet S_1 + g_2 \bullet S_2^T) + [(S_1^T \bullet \mathbf{J} \bullet S_2 + S_2^T \bullet \mathbf{J} \bullet S_1)/2] \quad \text{.....(3.2)}$$

Here matrix $\mathbf{J} = J\mathbf{E} + {}^{II}\mathbf{D}$, where J is the scalar exchange energy and **E** is a 3 x 3 unit matrix (Mashkovtsev *et al*., 2007). Since the observed satellite peaks involve pairs of similar centres, the principal values of $\mathbf{g_1}$ are expected to be equal to those of $\mathbf{g_2}$. Depending upon the choice of possible centre pairs, the orientations of the two **g**-axis sets are expected to be either exactly the same or very similar. If $\mathbf{S_1} = \mathbf{S_2} = 1/2$ and $\mathbf{g_1} = \mathbf{g_2}$, the EPR transitions become independent of the exchange coupling, J, and the singlet-triplet mixing is zero. As such, the presence of the singlet state can be

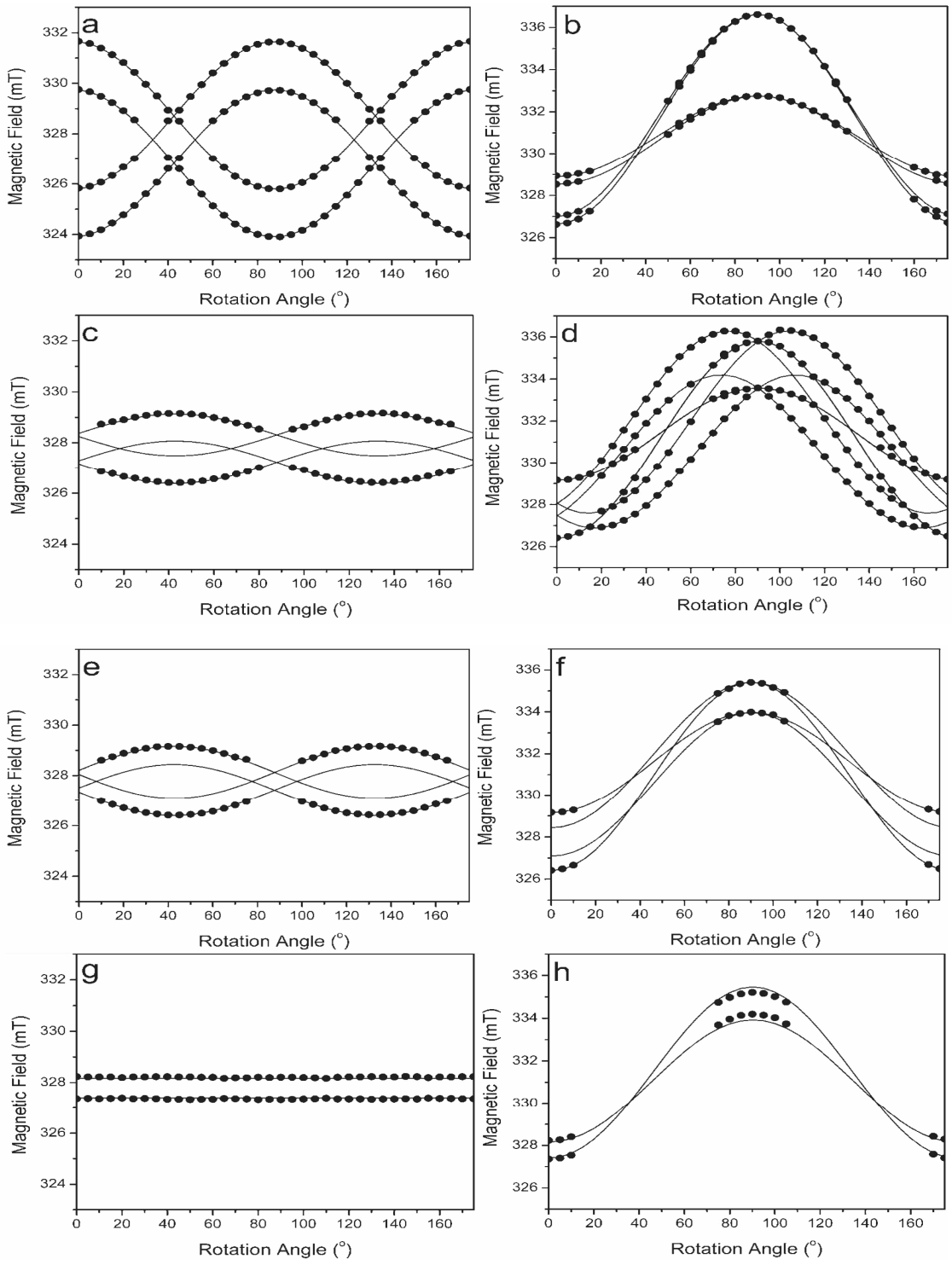

Figure 3.3 Angle-dependence of line-position data (*i.e.*, road maps) of four sets of satellite peaks I (a, b), II (c, d), III (e, f) and IV (g, h) in the (001) and (110) planes, microwave frequency = 9.379 GHz. Solid circles represent experimental data, and solid lines denote predictions from spin Hamiltonian parameters in Table 3.3. Note that the ranges of magnetic field are kept the same for each plane to facilitate comparison.

Table 3.2 Spin Hamiltonian parameters of the O^- centre in hydroxylapophyllite

		Matrix **Y**		k	Principal value Y_k	Principal directions		RMSD
						θ (º)	φ (º)	
Electronic Zeeman parameter from CW-EPR at 90 K and 290 K								
g	2.04442(1)	0.00000(1)	0.00000(1)	1	2.04442(1)	90.00(1)	309*	
		2.04442(1)	0.00000(1)	2	2.04442(1)	90.00(1)	39*	
(90 K)			2.00219(1)	3	2.00219(1)	0.00(1)	0*	0.01
g	2.04419(1)	0.00000(1)	0.00000(1)	1	2.04419(1)	90.01(2)	307*	
		2.04419(1)	0.00000(1)	2	2.04419(1)	90.00(2)	37*	
(290 K)			2.00309(1)	3	2.00309(1)	0	0*	0.02
		^{29}Si, ^{1}H and ^{39}K hyperfine parameters from ESEEM at 25 K						Distance(Å)
Si1 **A**/h	0.342	–0.130	–0.419	1	0.691	90.0	290.4	
		0.643	–0.156	2	0.654	51.1	200.4	
(MHz)			0.098	3	–0.262	38.8	20.4	3.71
Si2 **A**/h	0.028	–0.024	–0.032	1	0.04	61.9	189.2	
		–0.003	–0.058	2	0.04	62.9	295.1	
(MHz)			–0.035	3	–0.09	40.9	61.3	7.10
H1a	1.242	0.962	0.627	1	1.790	75.9	21.5	
A/h		–0.822	0.245	2	–1.051	14.2	204.2	
			–0.881	3	–1.201	90.6	291.6	4.35
H1b	1.211	0.923	0.553	1	1.707	77.2	21.3	
A/h		–0.790	0.213	2	–1.030	12.9	207.4	
			–0.895	3	–1.151	91.3	291.6	4.41
H2a	–0.405	0.646	0.357	1	1.409	63.3	65.0	
A/h		0.683	0.767	2	–0.697	26.7	247.0	
			–0.271	3	–0.706	90.8	335.4	4.84
H2b	–0.375	0.639	0.361	1	1.308	62.8	63.3	
A/h		0.573	0.717	2	–0.667	27.2	243.7	
			–0.254	3	–0.697	90.2	333.4	4.94
H3 **A**/h	0.783	–0.420	0.359	1	1.02	75.2	342.0	
		–0.373	–0.117	2	–0.51	14.8	162.0	
(MHz)			–0.410	3	–0.51	90	253	5.41
H4 **A**/h	–0.224	–0.299	0.089	1	0.66	74.3	290.1	
		0.484	–0.244	2	–0.33	15.7	110.1	
(MHz)			–0.260	3	–0.33	90	200.1	6.22
H5 **A**/h	–0.179	0.044	0.391	1	0.71	24.7	14.1	
		–0.343	0.098	2	–0.35	65.3	194.1	
(MHz)			0.521	3	–0.35	90	284.1	6.08
K1 **A**/h	0.0052	0.0222	–0.0005	1	0.028	89.0	225.7	
		0.0062	–0.0005	2	–0.017	23.8	133.4	
(MHz)			–0.0165	3	–0.017	66.2	316.1	6.32
K1 **A**/h	–0.063	–0.002	0.002	1	0.150	0.5	354.5	
		–0.087	–0.000	2	–0.063	90.5	354.6	
(MHz)			0.150	3	–0.087	89.9	84.6	NA

Matrices **g**, **A** and **P** are for one of eight symmetrically related sites via the rotation group D_4; matrices **g** fitted from the main absorption line in single-crystal EPR spectra; Hyperfine matrices **A**(^{29}Si), **A**(^{1}H), **A**(^{39}K) and **P**(^{39}K) from ESEEM spectra; * tilting angles relative to axis a (φ) are meaningless when one tilting angle relative to axis c (θ) is close to zero. The sets of (θ, φ) and (180° − θ, 180° + φ) are equivalent. RMSD is the root-mean-squares of weighted difference between calculated and experimental line-position data. Distance calculated from the point-dipole model. NA, not applicable.

Table 3.3 Spin Hamiltonian parameters of the four O^--O^- pairs in hydroxylapophyllite at 90 K.

	Matrix **Y**			k	Principal value Y_k	Principal direction θ (˚)	Principal direction φ (˚)	RMSD(mT)
					I			
g	2.04441(1)	0.00000(1)	0.00000(1)	1	2.04441(1)	90.0(2)	329(37)	
		2.04440(1)	0.00000(1)	2	2.04439(1)	90.0(2)	59(37)	
			2.00215(1)	3	2.00215(1)	0.0(2)	12*	
$^{I}\mathbf{D}/g_e\beta_e$	1.350(1)	0.008(1)	0.000(1)	1	1.350(1)	90(2)	180.1(2)	0.02
		−2.639(1)	0.000(1)	2	1.288(1)	0(2)	0*	
			1.288(1)	3	−2.639(1)	90.0(2)	90.1(2)	
					II			
g	2.04443(3)	0.00004(2)	0.00010(2)	1	2.04447(3)	90.0(1)	313(14)	
		2.04442(3)	0.00006(2)	2	2.04438(1)	89.8(1)	43(14)	
			2.00215(2)	3	2.00215(2)	0.2(2)	59(15)	
$^{I}\mathbf{D}/g_e\beta_e$	0.369(2)	−0.569(1)	−0.976(3)	1	0.949(2)	105(1)	333(2)	0.03
		0.372(2)	−0.928(3)	2	0.895(3)	54.6(8)	254(3)	
			−0.742(2)	3	−1.845(2)	39.3(1)	44.1(1)	
					III			
g	2.04443(7)	0.00004(8)	0.00000(1)	1	2.04447(14)	90.0(1)	319(18)	
		2.04442(7)	0.00000(1)	2	2.04438(2)	90.1(1)	49(18)	
			2.00211(4)	3	2.00214(2)	0.0(2)	39*	
$^{I}\mathbf{D}/g_e\beta_e$	−0.238(3)	0.700(2)	0.00(1)	1	0.481(2)	90(30)	315.0(1)	0.03
		−0.242(3)	0.00(1)	2	0.459(3)	0(30)	45*	
			0.481(2)	3	−0.941(2)	90.0(1)	45.0(1)	
					IV			
g	2.04438(6)	0.00000(4)	0.0000(2)	1	2.04438(5)	90.0(3)	324.4*	
		2.04438(6)	0.0000(2)	2	2.04438(5)	90.0(3)	44*	
			2.00214(8)	3	2.00214(4)	0.1(4)	16.6*	
$^{I}\mathbf{D}/g_e\beta_e$	0.272(3)	0.00 (2)	0.0 (1)	1	0.272(3)	90(36)	63*	0.09
		0.272(3)	0.0 (1)	2	0.272(3)	90(21)	333*	
			−0.544(3)	3	−0.544(3)	0(2)	217*	

Matrices **g** and $^{I}\mathbf{D}$ are for one of eight symmetrically related sites by the rotation group D_4. Note that $^{II}\mathbf{D}$ is exactly twice that of $^{I}\mathbf{D}$ (Mashkovtsev *et al.*, 2007). * tilting angles relative to an **a** axis (φ) are meaningless when one tilting angle relative to the **c** axis (θ) is close to zero. The sets of (θ, φ) and (180° −θ, 180° + φ) are equivalent. RMSD is the root-mean-squares of weighted difference between calculated and experimental line-position data.

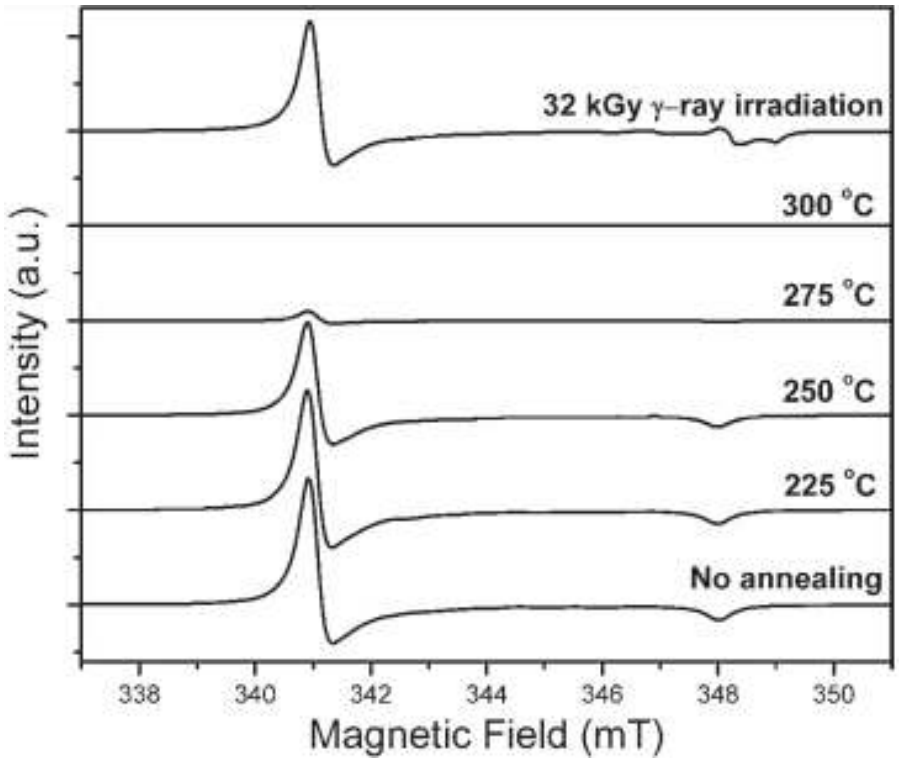

Figure 3.4 Room-temperature powder EPR spectra (microwave frequency = 9.38 GHz) of hydroxylapophyllite before and after isochronal annealing show that the O^- centre starts to decrease in intensity at 225 °C and is bleached at 300 °C. The spectrum of the thermally bleached sample after a ~32 kGy gamma-ray irradiation shows ~80 % restoration of the O^- centre.

neglected, and the spin system can be described by an effective triplet-state Hamiltonian with **S** = 1.

$$H = \beta_e \mathbf{B}^T \bullet \mathbf{g} \bullet \mathbf{S} + \mathbf{S}^T \bullet {}^{I}\mathbf{D} \bullet \mathbf{S} \quad \text{.....(3.3)}$$

Indeed, fitting using equation 2 but forcing $\mathbf{g_1} = \mathbf{g_2}$ gave exactly the same results as those of fitting with equation 3, except that the values of the triplet-state ${}^{I}\mathbf{D}$ tensor are one-half those of ${}^{II}\mathbf{D}$ (Mashkovtsev *et al*., 2007). Fitting using equation 2 but allowing independent $\mathbf{g_1}$ and $\mathbf{g_2}$ yielded generally equivalent $\mathbf{g_1}$ and $\mathbf{g_2}$ in each case, except that the **g**-maximum and **g**-minimum axes are always interchanged (see also

Mashkovtsev *et al*., 2007). We will show below that $^{II}\mathbf{D}$ is determined almost entirely by the distant dipole–dipole coupling. Therefore, it is highly unlikely that such a large rotation of axes occurs. Moreover, in the case of biradical IV, where the internuclear axis is parallel to the symmetry axis, no rotation should be expected. These considerations led us to report only spin Hamiltonian parameters **g** and $^{I}\mathbf{D}$ from the simpler equation 3 (Table 3.3).

The total line-position data used for fitting of I, II, III and IV are 448, 324, 204 and 404 (and corresponding sum of weighing factors = 448, 322, 200 and 404), respectively. The final RMSD values for I, II and III are between 0.02 and 0.03 mT (Table 3.3), smaller than half of their average linewidths. The larger RMSD value of 0.09 mT for IV (Table 3.3) is attributable to peak overlapping in the (001) plane. The principal **g** values from these four biradicals are within analytical uncertainties to one another and are indistinguishable from those obtained from the main absorption line at 90 K (Table 3.2). Matrices $^{I}\mathbf{D}$ for all four biradicals are approximately axial in symmetry (Table 3.3). The sign of $^{I}\mathbf{D}$ can not be determined from fitting of the EPR data, but the unique principal value of $^{I}\mathbf{D}$ is taken to be negative based upon the point-dipole model (Abraham *et al*., 1987).

3.3.3 Powder EPR spectra and thermal stability

The powder EPR spectra of the as-is hydroxylapophyllite show the O^- centre (Figure 3.4) and biradicals I and II at 90 K as well. A ~50 kGy γ-ray irradiation of this sample results in a ~60 % increase in the intensity of the O^- centre. The powder EPR

spectra of isochronally annealed hydroxylapophyllite show that the O^- centre remains essentially unchanged to 200 °C but starts to decrease in intensity at 225 °C and is bleached at 300 °C (Figure 3.4). A ~32 kGy gamma-ray irradiation of the thermally bleached sample restores the O^- centre to ~80 % of its original intensity (Figure 3.4).

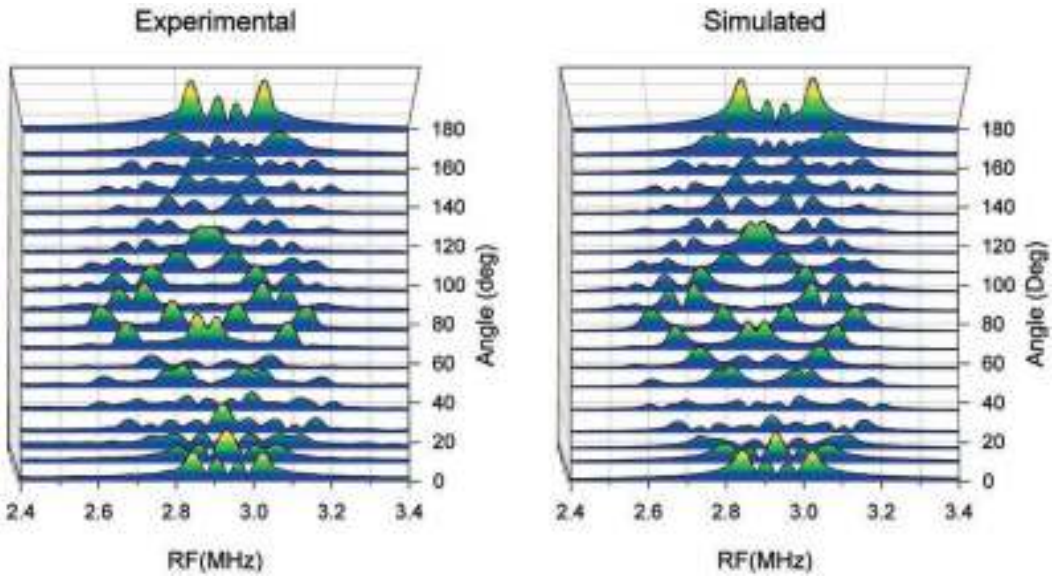

Figure 3.5 Stacked plots of the ^{29}Si portion of the experimental and simulated three-pulse ESEEM spectra as a function of rotation angles. Intensity in the vertical axis unlabelled (arbitrary unit).

3.3.4 ESEEM spectra

While the CW spectra for the hydroxylapophyllite sample are strong, spin echo spectra were not readily observed unless temperature was lowered significantly below 77 K. The short relaxation times appear to be the result of concentration induced dipolar coupling. Davies ENDOR of the crystal at 25 K yielded no discernible spectral features, while Mims ENDOR showed the presence of a single proton matrix peak at ~14.6 MHz. ESEEM spectra did show very weak modulation at

frequencies very close to those of ^{29}Si and ^{1}H at 2.9 MHz and 14.6 MHz. respectively (Figure 3.5–3.7). Also observed are a number of other frequencies below 1 MHz (Figure 3.8).

The ^{29}Si ‘‘matrix’’ peak is actually split into three to eight pairs depending on orientation (Figure 3.5). Spectral fittings show that these spectra can be readily accounted for by one ^{29}Si with a hyperfine splitting on the order of 0.5 MHz (Table 3.2). The anisotropic component of the ^{29}Si hyperfine is equal to –0.62 MHz, which corresponds to a distance (r) of 3.71 Å on the basis of the point-dipole model:

$$T_z = (2\mu_0/4\pi)(g\beta_e g_n \beta_n / r^3) \quad \text{.....(3.4)}$$

where T_z is the traceless part of hyperfine interaction ($T_x = T_y = -T_z/2$) and g_n is equal to –1.1097 for ^{29}Si. This value is the same as that between the hydroxyl oxygen atom and the nearest neighbor Si, while the orientation of the unique hyperfine axis is only 3.4° from this O–Si direction (Table 3.4). Simulations could be improved somewhat if the next nearest Si is also included. The hyperfine constants obtained for this second Si (Table 3.2) are close to those predicted for the next nearest neighbor Si (Table 3.4). This second Si, however, gives rise to much weaker (the ESEEM intensity decreases roughly as $\mathbf{r^{-3}}$) spectra with narrower width, hence larger uncertainty in the fitted values.

Unlike the case for ^{29}Si, proton ESEEM gives rise to complex and asymmetric patterns (Figure 3.6 and 3.7). This can be attributed to a number of things. First, there are two nonequivalent protons associated with each nearest neighbor water molecule. Second, simulation shows that there are two slightly different subpopulations for each

of the two water protons (Figure 3.6). Finally, the expected distances for the nearest neighbor protons are much larger than that seen for the nearest neighbor Si's and as such contributions from the protons in the next, next-next, and next-next-next nearest shells are much more pronounced. To minimize the problems of the latter, we fixed the hyperfine matrices for H6, H7, and H8 to the values calculated from the point-dipole model and the ideal hydroxylapophyllite structure. The hyperfine matrices were varied for H3, H4, and H5 but restricted to being axial and traceless. This approach allowed good fits for the nearest sets of protons, H1 and H2. Distances calculated using the pointdipole model are 4.35 Å and 4.41 Å for H1a and H1b, respectively, which are slightly smaller (~0.2 Å) than those from X-ray and neutron diffraction experiments (Table 3.4). The values of 4.84 Å and 4.94 Å for H2a and H2b are within experimental uncertainty of those from X-ray and neutron diffraction (Table 3.4). It should be noted that the unit-cell parameters and atom positions at 25 K (ESEEM experiments) may be slightly different from those determined from room-temperature X-ray and neutron diffraction (Prince, 1971; Rouse *et al*., 1978). The orientations of the unique hyperfine axes for H1 and H2 (Table 3.2) are also very close to those reported for X-ray and neutron diffraction but, as one would expect, are in the better agreement with those from the latter technique (Table 3.4). The distances obtained by fitting H3, H4, and H5 are also close to those determined from X-ray and neutron diffraction, despite the larger uncertainty in fitting the hyperfine matrices for these protons as well as a number of assumptions made. In general, while the fits of the proton part of the ESEEM spectra are inferior to those for ^{29}Si, agreement is still

quite good, especially on the outer edges where only the nearest neighbor protons contribute (Figure 3.7). In the central region the fit is typically the poorest, but this is where overlaps from many more distant protons are expected to occur (Figure 3.6 and 3.7). Also, the spectra have a definite asymmetry, which at many orientations is well fitted by spectral simulations. This asymmetry arises from angularly dependent second-order hyperfine terms that will be differently phased for protons that have different orientations of principal hyperfine axes.

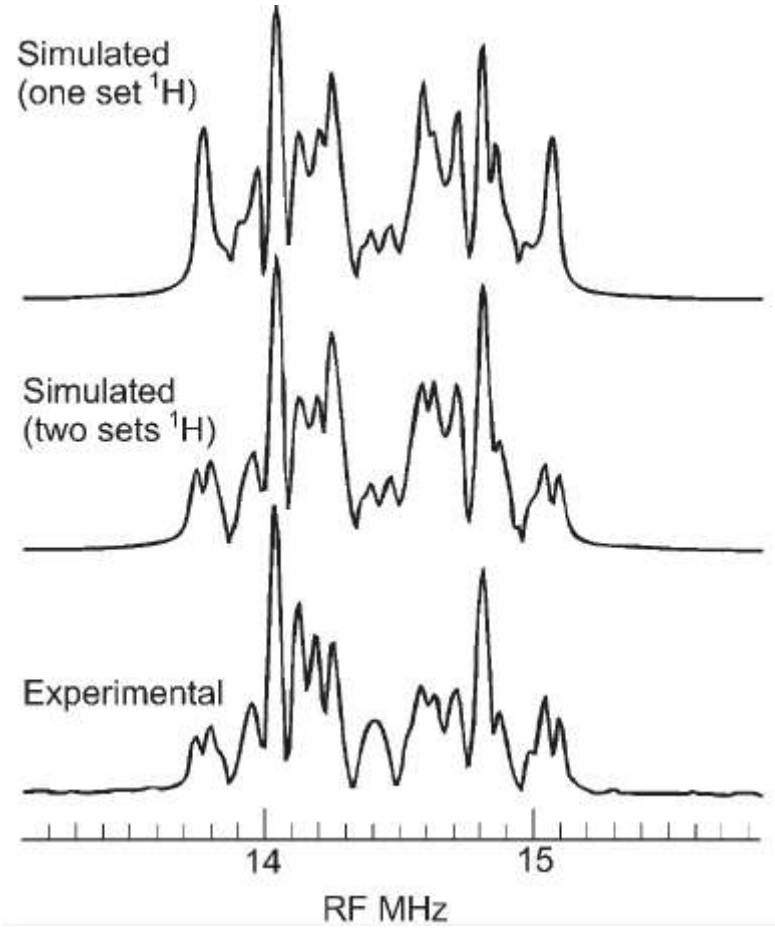

Figure 3.6 Comparison of experimental and simulated ESEEM spectra at 25 K at a rotation angle of 76° (θ = 76.1° and φ = 45.4°). The top simulation assumes a single set of two inequivalent H_2O protons while the lower simulation includes two sets for each of the two inequivalent H_2O protons.

A number of peaks centred between 0.4 and 1.0 MHz show maximum intensity 45° off axis. This is consistent with these peaks arising from a quadrupolar nucleus having its quadrupolar principal axes lying along or near a crystal axis. The most likely candidate is ^{39}K, which has a nuclear frequency of 0.69 MHz. Simulations confirm this and show the positions of the ESEEM peaks are determined almost entirely by the quadrupole tensor. For a nuclear spin of 3/2 and a quadrupole coupling much larger than the hyperfine coupling, three peaks with a separation of $\sim 3P_{zz}(3\cos^2\theta - 1)/2$ are expected to be centred around the ^{39}K nuclear frequency. Also seen are weak $\Delta m_I = \pm 2$ transitions centred around 1.2 MHz. The hyperfine coupling is expected to split each of the three peaks into two but because it is so small, it only affects the linewidth and intensity of the peaks. Another consequence of the small hyperfine coupling is that contributions from more distant ^{39}K nuclei will all add together on top of the spectra from the nearest neighbor, although the amount that they contribute decreases with increasing distance. As such, we include contributions from K2, K3, and K4 at 7.92, 11.97, and 14.20 Å, respectively (X-ray data; Table 3.4) but restrict the hyperfine matrices to those calculated using the point-dipole model [g_n is equal to 0.2606 for ^{39}K]. Using these restricted values for K2, K3, and K4, we fit the ^{39}K quadrupole tensor (and assuming the same quadrupole tensor for all K atoms) and the K1 hyperfine matrix (Table 3.2; Figure 3.8). The unique axis of the quadrupole tensor is nearly coincident with the **c**-axis and shows a small rhombic splitting. However, restricting the quadrupole tensor to be axial and having its axis exactly along the c-axis had only a small increase in RMSD. The predicted O–K1

distance from the fitted hyperfine matrix for K1 by use of the point-dipole model is 6.32 Å (Table 3.2), which agrees well with the experimental value of 6.35 Å determined from X-ray diffraction data (Table 3.4). The unique axis of the hyperfine matrix is found to be only 1.4° away from the O–K1 direction as well (Tables 2 and 4).

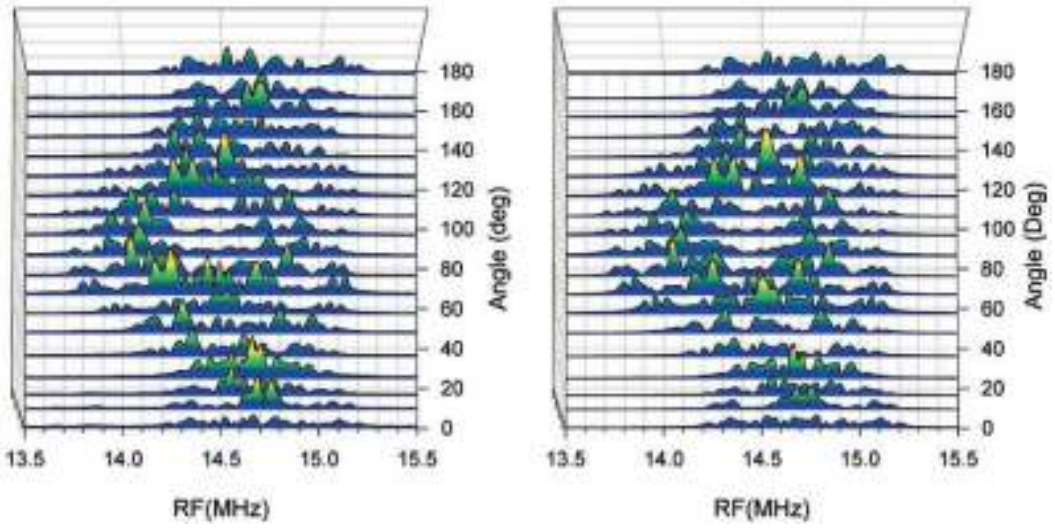

Figure 3.7 Stacked plots of the ^{1}H portion of the experimental and simulated three-pulse ESEEM spectra as a function of rotation angles. Intensity in the vertical axis unlabelled (arbitrary unit).

Figure 8 also shows the presence of a number of peaks below 0.4 MHz. They may be attributable to other quadrupolar nuclei with small magnetic moments (*e.g.* ^{41}K) and/or can arise as artifacts due to the imperfect subtraction of the decay of the spin echo.

3.4 Discussion

Marfunin (1979) classified O^- centres into two groups on the basis of the location of the unpaired electron: 1) in the σ orbital, yielding $g_{//} \leq g_e$ and $g_{\perp} > g_e$ and 2) in the π nonbonding orbitals, resulting in $g_{//}$ and $g_{\perp}$ switching places (relative to those of the first group), and $g_{//}$ usually close to a bond direction. Marfunin (1979) noted that the former group includes those formed from an impurity oxygen ion substituting for a halogen ion and one oxygen ion nearest to a cation vacancy in oxides of the MgO type. The second group includes a bridging oxygen trapping a hole to compensate for the positive charge deficiency arising from one of the cations being replaced by a lower-charged cation (*e.g.*, the $[AlO_4]^0$ centre in quartz; Nuttall& Weil, 1981; Walsby *et al*., 2003) and free radicals XO_m^{n-} , such as CO_3^-, SO_4^-, PO_4^{2-}, SiO_4^{3-}, WO_4^-, VO_4^{2-} and AsO_4^{2-}. We caution that inclusion of free radicals XO_m^{n-} as O^- centres is debatable owing to the fact that the unpaired electron in some of them (*e.g.*, CO_3^-) is not localised on a single oxygen ion.

3.4.1 O^- centres in apophyllites

Bershov & Marfunin (1967) reported an unknown holelike centre (g_1 = 2.0041, g_2 = 2.0106, g_3 = 2.0451) in apophyllites, without any other details such as experimental techniques or principal axis directions. Their g_1 and g_3 values are closely comparable to $g_{\perp}$ and $g_{//}$ of this study. It is unclear whether this hole-like centre in Bershov & Marfunin (1967) is the O^- centre of this study or not.

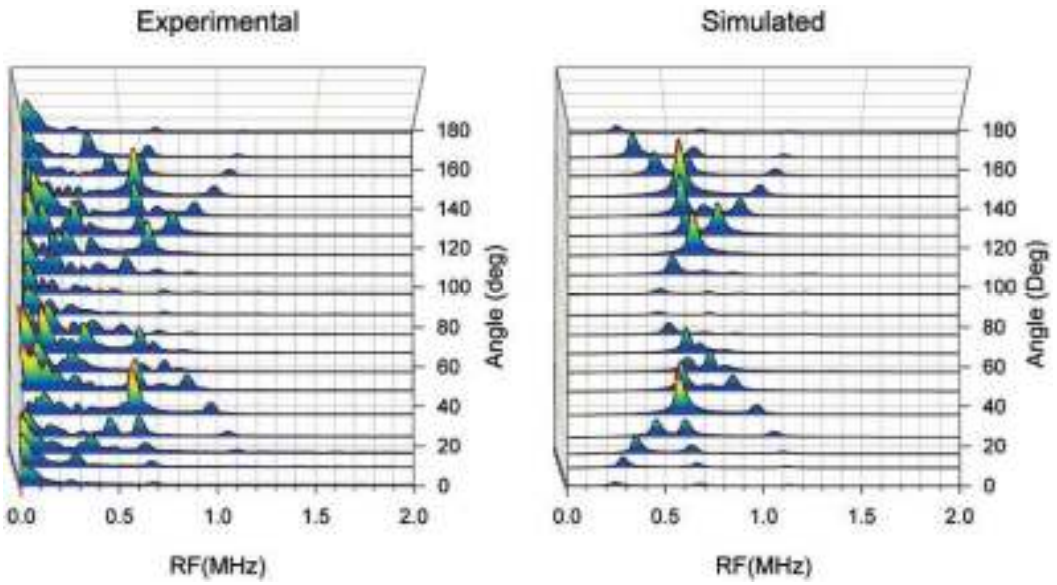

Figure 3.8 Stacked plots of the ^{39}K portion of the experimental and simulated three-pulse ESEEM spectra as a function of rotation angles. Note that intensity in the vertical axis (unlabelled, arbitrary units) has been reduced five times (relative to those in Figure 3.5 and 3.7) to show the strong ^{39}K spectra.

Table 3.4 Orientations and distances from the OH group to selected Si, H and K atoms in hydroxylapophyllite.

	X-ray diffraction			Neutron diffraction		
	Orientation		Distance	Orientation		Distance
Atoms	θ (°)	φ (°)	r (Å)	θ (°)	φ (°)	r (Å)
Si1	35.9	20.9	3.71	36.1	20.9	3.70
Si2	42.2	33.5	6.63	42.2	33.5	6.61
H1	68.4	16.6	4.56	72.0	21.1	4.54
H2	63.9	63.7	4.82	61.6	62.2	4.90
H3	71.7	346.1	5.33	74.9	342.6	5.36
H4	68.7	290.6	5.85	67.1	291.3	6.00
H5	24.5	13.4	6.37	24.8	15.1	6.11
H6	27.9	82.7	7.06	24.6	81.1	7.13
H7	42.5	85.8	8.46	49.6	84.1	8.57
H8	48.0	95.4	8.66	43.0	94.3	8.87
K1	90	45	6.35	90	45	6.34
K2	0	0	7.92	0	0	7.88
K3	48.6	0	11.97	48.7	0	11.94
K4	90	18.4	14.20	90	18.4	14.17

X-ray diffraction data from Rouse *et al*. (1978); Neutron diffraction data from Prince (1971).

The $g_{//}$ and $g_{\perp}$ values suggest the O^- centres in apophyllites to belong to Marfunin's (1979) first group. In particular, they are closely comparable to the well established O^- centres in apatites (Piper *et al*., 1965; Mengeot *et al*., 1975; Nokhrin *et al*., 2005). For example, the O^- centre in fluorapatite [$g_{\perp}$ = 2.0522(2) and $g_{//}$ = 2.0018(2)] has been proposed to arise from trapping of a hole by an O^{2-} ion substituting for an F^- ion, which is coordinated to $3Ca^{2+}$ ions in the same plane and 2 F-ions at 3.44 Å in the c-axis column. The presence of the two equivalent F^- ions in the F^--O^--F^- configuration has been confirmed by the observed ^{19}F hyperfine structure with an intensity ratio of 1:2:1 (Piper *et al.*, 1965). Similarly, Mengeot *et al*. (1975) reported an OH^--O^--OH^- centre in hydroxylapatite [$g_{\perp}$ = 2.0683(2) and $g_{//}$ = 2.0018(2)] and confirmed this configuration by the observed hyperfine structure [$A_{//}$ = 0.56(2) mT and $A_{\perp}$ = 0.59(8) mT] arising from the nearest proton at ~2.48 Å. The O^- centre in apophyllites, similar to its counterpart in fluorapatite, is surrounded by four Ca^{2+} ions in the same plane (Figure 3.1). However, the eight nearest F^- ions to the O^- centre in fluorapophyllite are 10.15 Å away and the two F^- ions along the c-axis are at 15.83 Å, which can account for the absence of any detectable ^{19}F hyperfine structures. Similarly, the nearest protons to the O^- centre in hydroxylapophyllite are at ~4.56 Å, which is expected by the point-dipole model to yield a hyperfine splitting of 0.1 mT (*i.e*., narrower than the main absorption line, hence not detectable in CW-EPR spectra either; Figure 3.2). By analogy with its counterpart in hydroxylapatite (Mengeot *et al*., 1975), the unpaired electron of the O^- centre in hydroxylapophyllite is expected to be localized primarily on the $2p_z$ orbital parallel to the **c**-axis.

Internuclear distances and directions calculated from ^{29}Si, ^{1}H and ^{39}K hyperfine matrices are consistent with the centre lying at or very near the 0,0,0 position (Tables 3.2 and 3.4), confirming its formation from the OH^- group. This location is best revealed by the nearest neighbour ^{29}Si hyperfine data. For example, the unique A(^{29}Si) axis at $\theta = 38.8$ and $\varphi = 20.4$ is nearly along the OH–Si direction (35.9, 20.9) (Tables 3.2 and 3.4). The calculated distance of 3.71 Å from the ^{29}Si hyperfine splitting is in excellent agreement with the OH-Si distance of 3.71 Å from X-ray diffraction (Rouse *et al.*, 1978).

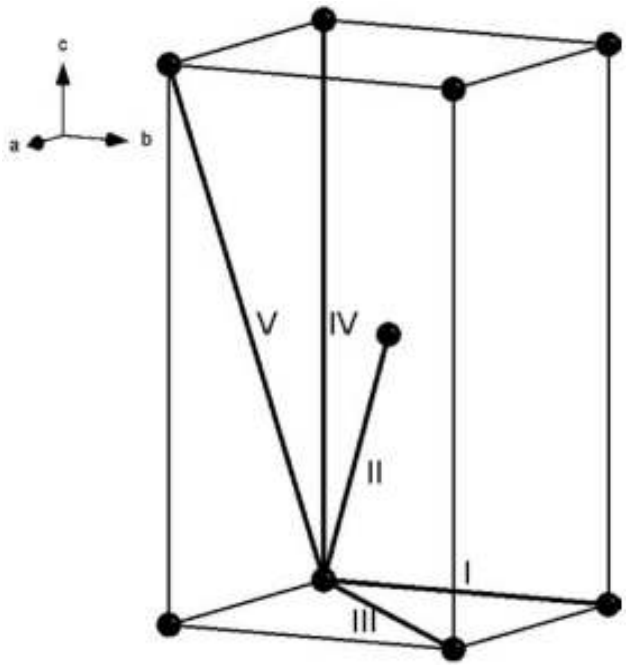

Figure 3.9 The positions of the hydroxyl oxygen atoms in the hydroxylapophyllite structure (*cf.* Rouse *et al.*, 1978) illustrating five possible O^--O^- pairs: I, II, III and IV correspond to those in **Tables 3.3** and **3.5** V is predicted to have a smaller splitting (**Table 3.5**), which is not detectable in EPR spectra.

While the anisotropic part of the ^{29}Si hyperfine coupling for Si1 can be predicted quite well using the point-dipole model, one must evoke spin polarisation and the resultant negative spin density to account for the isotropic part of the ^{29}Si hyperfine coupling (+0.36 MHz). Si2 is much farther away and as expected the isotropic ^{29}Si hyperfine is close to zero and can be neglected. For H1a/H1b a small isotropic hyperfine is also observed (–0.15 MHz), which corresponds to a spin density of -1.0×10^{-4} (*i.e.*, slightly larger than that for Si1 at -0.8×10^{-4}). For H2a/H2b the isotropic hyperfine is essentially zero and can be neglected. While the H2 proton is slightly farther away than H1, the difference in isotropic hyperfine could also be attributable to the fact that the O(4)-H1 bond is slightly longer than the O(4)-H2 bond (Chao, 1971; Prince, 1971; Rouse *et al.*, 1978) and as such more polarisable.

The reason for two sets of slightly different proton splittings (H1a and H1b, and H2a and H2b; Table 3.2) remains uncertain. The primary difference between the two pairs of protons is a very slightly smaller anisotropic hyperfine implying a very slightly longer distance (0.06 Å and 0.10 Å for H1 and H2, respectively). No such extra splitting is observed in the ^{29}Si spectra, but the smaller magnetic moment of ^{29}Si may preclude this. One possible mechanism may be symmetry reduction related to positional disorder of the OH group (Rouse *et al*., 1978). D_4 symmetry was used in the analysis of the proton ESEEM spectra, while simulations using lower symmetries (C_4, D_2 and C_2) yielded poor fittings. Because the EPR spin Hamiltonian is invariant to inversion, a symmetry reduction from D_{4h} (*P4/mnc*) to D_4 is possible and could explain nonequivalent protons. Another possibility is that lower symmetry (C_4 or D_{2h})

domains exist but on average the site symmetry is D_4 or D_{4h}. For example, partial dehydration of fluorapophyllite is known to result in the loss of one of the water molecules and loss of D_{4h} symmetry at the K site, yet because the choice of which of the eight waters is lost is random, the overall *P4/mnc* symmetry is retained (Ståhl, 1993).

The O^- centre in fluorapophyllite obviously formed during gamma-ray irradiation (Mao & Pan, 2009). It is plausible that this centre in hydroxylapophyllite without any artificial irradiation formed from natural radiation. Unfortunately, the source of natural radiation for this sample from an unknown locality can not be deduced. Nevertheless, a radiation-induced origin is supported by the fact that this centre can be enhanced by gamma-ray irradiation and can be restored by gamma-ray irradiation after a complete thermal bleaching at 300 °C (Figure 3.4). Following Mengeot *et al*. (1975), irradiation resulting in ionization of some OH groups and removal of their hydrogen atoms is a potential mechanism for the formation of the O^- centre in hydroxylapophyllite. We note that paramagnetic atomic H^0 expected from this process has not been detected in our EPR spectra, although protons disassociated by irradiation might have aggregated to form H_2 or other diamagnetic species.

3.4.2 O^--O^- pairs in hydroxylapophyllite

The four sets of well-resolved satellite peaks (I, II, III and IV) have been successfully fitted as pairs of O^- centres (Table 3.3). The unique axis direction of $^{I}\mathbf{D}$ for I (90, 90) is along the b-axis [and its symmetrically related directions at (90, 0),

(90, 180) and (90, 270)]. The $\mathbf{D}_3$-axis of II at (39, 45) corresponds to a diagonal vector from the origin through the centre of the unit cell (Figure 3.9). The $\mathbf{D}_3$-axis of III at (90, 45) is along the [110] direction, and that of IV is along the **c**-axis (Figure 3.9). These directions obviously correspond very well to those of the four pairs of neighboring OH^- ions in hydroxylapophyllite (Figure 3.9), or more accurately the four pairs of O^- centres derived from these OH^- ions (*cf*. Mengeot *et al*., 1975). Moreover, the fitted $^{I}\mathbf{D}$ values from the four sets of satellite peaks in EPR spectra agree very well with those predicted from the distances of these four OH^--OH^- pairs by assuming an entirely dipolar interaction between two positively charged holes (Table 3.5; *cf*. Abraham *et al*., 1987):

$$D = -(\mu_0/4\pi)(2g_{//}^2 + g_{\perp}^2)\beta_e^2/(2r^3) \quad \text{.....(3.5)}$$

Such agreements between the fitted and predicted **D** value for all four sets of satellite peaks confirm that they arise from the four geometrically distinct pairs of well separated, weakly interacting O^- centres (Figure 3.9). These results also provide further support for the identification of the O^- centre and its location at the hydroxyl oxygen site. It should also be noted that because **g** is anisotropic, $^{I}\mathbf{D}$ is expected to have a small rhombic component except in the case of biradical IV for which the internuclear axis is parallel to the symmetry axis (Table 3.3).

Figure 3.9 includes a fifth O^--O^- pair (V) with a separation of 18.2 Å , corresponding to a D value of 0.476 mT (Table 3.5). This pair with an orientation of (29.6, 0) is expected to have the largest splitting of 0.6 mT in spectra with **B**//**c**, where is not resolved owing to overlapping with the main absorption line (Figure 3.2a).

Similarly, another possible O^--O^- pair separated by a normal OH^- ion along **a**-axis has a distance of 17.95 Å . The maximum splitting of ~1 mT for this pair is expected in spectra with **B**//**a**, where it overlaps with II, III and IV, hence not resolved either (Figure 3.2b).

Table 3.5 Distances and orientations of O^--O^- pairs in hydroxylapophyllite.

O^-–O^-	Distance (r) (Å)	Orientation		$D/g_e\beta_e$(mT) [a]	$D/g_e\beta_e$(mT) [b]
		θ (°)	φ (°)		
I	8.978	90	90	–3.962	–3.959
II	10.15	38.7	45	–2.745	–2.767
III	12.70	90	45	–1.401	–1.411
IV	15.83	0	0	–0.723	–0.745
V	18.20	29.6	90	–0.476	[c]

[a] calculated from $D = -(\mu_0/4\pi)(2g_{//}^2 + g_{\perp}^2)\beta_e^2/(2r^3)$ (Abraham *et al.*, 1987),

[b] experimental D for I, II, III and IV ($=3/2D_3$ in Table 3.3),

[c] not resolved.

The detection of these biradicals in the natural hydroxylapophyllite is probably attributable to a high concentration of the O^- centre in this sample, resulting in the presence of statistically significant O^--O^- pairs detectable by EPR. These biradicals, which are not detectable in the gamma-ray-irradiated fluorapophyllite with a very weak O^- centre (Mao & Pan, 2009), are detectable but weaker in the two apophyllite samples (*i.e.*, Gaspé, Quebec and Wasson's Bluff, Nova Scotia) with an O^- centre of intermediate intensities. The presence of these biradicals at both 90 K and 290 K distinguishes them from other biradicals associated with cation and anion vacancies. For example, the V^0 centres (or O^--□-O^-, where □ denotes a cation vacancy) in MgO, CaO and SrO have been shown to be stable only at cryogenic temperatures and decay to the V^- centres (O^--□) at room temperature (Abraham *et al.*, 1975, 1987; Rubio *et al.*,

1976). Similarly, Mashkovtsev *et al.* (2007) noted that their E_1 centre [with one unpaired electron each on two silicon cations on the opposite sides of an oxygen (O^0) vacancy] in quartz is unstable at room temperature.

3.4.3 Comparison with O^- centres in other layer silicates

The original purpose of our single-crystal EPR studies of apophyllites was to provide structural models for oxygen-associated radiation-induced defects in layer silicates (*e.g.*, kaolinite, dickite, illite, and montmorillonite; Clozel *et al.*, 1994; Sorieul *et al.*, 2005; Morichon *et al.*, 2008). Oxygen-associated radiation-induced defects in layer silicates have attracted considerable interests, because they are sensitive dosimeters for determining and monitoring the migration of radionuclides in Earth's surface environments and have direct relevance to long-term nuclear waste disposal (*e.g.*, Clozel *et al.*, 1994; Allard & Muller, 1998; Allard *et al.*, 2003, 2007; Sorieul *et al.*, 2005; Morichon *et al.*, 2008). However, the structural models of all radiation-induced defects in layer silicates are generally not well understood owing to the fact that these minerals almost invariably occur in ''clay'' sizes and do not permit quantitative single-crystal EPR studies. For example, powder EPR studies suggested three O^- centres in kaolinite: A and A' interpreted to represent trapped holes on apical oxygen from Si–O bonds, and B as a hole trapped on an oxygen linked to one or two ^{27}Al nuclei (Clozel *et al.*, 1994; Köksal *et al.*, 2004). Confirmation of these structural models requires additional data such as: 1) localisation of the unpaired spin on a single oxygen atom, 2) detection and quantitative analysis of the hyperfine structures

arising from interaction with a ^{29}Si nucleus (*i.e.*, A and A') and one or two ^{27}Al nuclei (B), and 3) defect orientations and their relationships to specific bonds and other symmetrical directions in the ideal structures.

All proposed O^- centres in kaolinite, dickite, illite and montmorillonite (Clozel *et al.*, 1994; Sorieul *et al.*, 2005; Morichon *et al.*, 2008) have principal g values consistent with Marfunin's (1979) second group. Therefore, the O^- centres in apophyllites can not be considered as direct analogues. Their difference arises from the fact that the O^{2-} and OH^- ions for the formation of the O^- centres in common layer silicates are coordinated to cations in tetrahedral and/or octahedral sheets, unlike its counterpart surrounded by interlayer Ca^{2+} ions in apophyllites. The characteristic feature of the first-group O^- centres in apophyllites and other minerals is their relatively weak crystal field effects (Marfunin, 1979). The O^- centres originated from O^{2-} and OH^- ions in common layer silicates, on the other hand, form stronger bonds with the octahedral or tetrahedral cations, resulting in the unpaired electron in the π nonbonding orbitals (Marfunin, 1979). This explains the general absence of the first group O^- centres in common layer silicates. One notable exception is a proposed O^- centre in irradiated, synthetic fluorphlogopite, which is characterized by g values [$g_{//}$ = 2.004(1) and $g_{\perp}$ = 2.045(5)] of Marfunin's (1979) first group and has been interpreted to represent an O^- ion replacing an F^- ion linked to an octahedrally coordinated Mg^{2+} cation (Novozhilov *et al.*, 1969).

3.5 Conclusions

Single-crystal EPR spectra reveal an O^- center and its biradical pairs in hydroxylapophyllite, and single-crystal ESEEM spectra allow the identification and location of multiple neighboring nuclei of the O^- center. The best-fit spin-Hamiltonian parameters suggest that the O^- center forms from the hydroxyl oxygen ion after the removal of its proton. This defect model is further confirmed by excellent agreements between the best-fit directions and calculated distances of the O^--O^- biradical pairs with those of the corresponding OH^--OH^- pairs. The O^- center is bleached out at 300 °C but can be readily restored by γ-ray irradiation.

3.6 References

ABRAHAM, M.M., BOLDU, O. & CHEN, Y. (1987): EPR and ENDOR of trapped-hole centers in alkaline-earth oxides. In: Electronic Magnetic Resonance of the Solid State (Weil, J.A., ed.). *Canadian Society for Chemistry*, 427-448.

ABRAHAM, M.M., CHEN, Y., BOATNER, L.A. & REYNOLDS, R.W. (1975): V^- and V^0 centers in CaO single crystals. *Solid State Commun*. **16**, 1209-1213.

ALLARD, T. & MULLER, J.P. (1998): Kaolinite as an in situ dosimeter for past radionuclide migration at the Earth's surface. *Appl. Geochem.* **13**, 751–765.

ALLARD, T., ILDEFONSE, P., PEREZ DEL VILLARD, L., SORIEUL, S., PELAYO, M., BOIZOT, B., BALAN, E. & CALAS, G. (2003): Radiation-induced defects in dickites from the El Berrocal granitic system (Spain): relation with past occurrence of natural radioelements. *Eur. J. Mineral.* **15**, 629–640.

ALLARD, T., CALAS, G. & ILDEFONSE, P. (2007): Reconstruction of past U migration in a sedimentary deposit (Coutras, France): Implications for a radwaste repository. *Chem. Geol.* **239**, 50-63.

BARTL, H. & PFEIFER G. (1976): Neutronenbeugungsanalyse des apophyllit $KCa_4(Si_4O_{10})_2(F/OH).8H_2O$. *Neues Jahrb. Mineral Monatsh*, 58-65.

BERSHOV, L.V. & MARFUNIN, (1967): Electron-spin resonance of electron-hole centres in minerals. *Dokl. Akad. Nauk SSSR*, **173**, 410–412.

CHAO, G.Y. (1971): The refinement of the crystal structure of apophyllite. II. Determination of the hydrogen positions by X-ray diffraction. *Amer. Mineral*. **56**, 1234-1242.

CHE, M., TENCH, A.J. (1983): Characterization and reactivity of molecular oxygen species on oxide surfaces. *Advan. Catalysis* **32**, 1-148.

CLOZEL, B., ALLARD, T. & MULLER, J.P. (1994): Nature and stability of radiation-induced defects in natural kaolinites: new results and reappraisal of published works. *Clays Clay Minerals* **42**, 657-666.

COLVILLE, A.A., ANDERSON, C.P. & BLACK, P.M. (1971): Refinement of the crystal structure of apophyllite: I. X-ray diffraction and physical properties. *Amer. Mineral.* **56**, 1222-1233.

DUNN, P.J., ROUSE, R.C. & NORBERG, J.A. (1978): Hydroxyapophyllite, a new mineral, and a redefinition of the apophyllites group. Part I. Description, occurrence, and nomenclature. *Amer. Mineral*. **63**, 196-199.

KEIJZERS, C. P., REIJERSE, E. J., STAM, P., DUMONT, M. F. & GRIBNAU, M. C. M. (1987) "MAGRES: A General Program for Electron Spin Resonance, ENDOR and ESEEM," *J. Chem. Soc., Faraday Trans. I,* **83**, 3493-3503.

KÖKSAL, F., KÖSEOĞLU, R., ŞAKA, I., BAŞARAN, E. & ŞENER, F. (2004): Electron paramagnetic resonance of natural and γ –irradiated alunite and kaolin mineral powders. *Radiation Effects Defects Solids*, **159**, 393-398.

MAO, M. & PAN, Y. (2009): Radiation-induced defects in apophyllites. I. The NH_2 free radical in fluorapophyllite. *Eur. J. Mineral*., **21**,317-324.

MARFUNIN, A.S. (1979): Spectroscopy, luminescence and radiation centers in minerals. Springer-verlag berlin Heidelberg New York.

MASHKOVTSEV, R.I., HOWARTH, D.F. & WEIL, J.A. (2007): Biradical states of oxygen-vacancy defects in α-quartz. *Phys. Rev. B* **76**, 214114-1-11.

MENGEOT, M., BARTRAM, R.H. & GILLIAM, O.R. (1975): Paramagnetic hole-like defect in irradiated calcium hydroxyapatite single crystals. *Phys. Rev. B* **11**, 4110-4124.

MOMBOURQUETTE, M.J., WEIL, J.A. & MCGAVIN, D.G. (1996): EPR-NMR (Users' Manual). Department of Chemistry, University of Saskatchewan, Saskatoon, SK., Canada.

MORICHON, E., ALLARD, T., BEAUFORT, D. & PATRIER, P. (2008): Evidence of native radiation-induced paramagnetic defects in natural illite from unconformity-type uranium deposits. *Phys. Chem. Minerals* **35**, 339-346.

MURPHY, D.M. & CHIESA, M. (2004): EPR of paramagnetic centres on solid surfaces. *Electron. Paramag. Reson*. **19**, 279-317.

NILGES, M.J., PAN, Y. & MASHKOVTSEV, R.I. (2009): Radiation-induced defects in quartz. III. W-band EPR, ENDOR and ESEEM study of a peroxy radical. *Phys. Chem. Minerals* **36**, 61-73.

NOKHRIN, S.M., PAN, Y., WEIL, J.A. & NILGES, M.J. (2005): Multifrequency EPR study of radiation-induced defects in chlorapatite. *Canad. Mineral*. **43**, 1581-588.

NOVOZHILOV, A.I., SAMOILOVICH, M.I., SERGEEV-BOBR, A.A., & ANIKIN, I.N. (1969): EPR in irradiated fluorophlogopite. *Zhur. Struk. Knim.*, **10**, 45–453.

NUTTALL, R.H.D. & WEIL, J.A. (1981) The magnetic properties of the oxygen-hole aluminum centers in crystalline SiO_2. I. $[AlO_4]^0$. *Canad. J. Phys*. **59**, 1696-1708.

PECHAR, F. (1987): The X-ray diffraction refinement of the crystal structure of natural apophyllite. *Crystal. Res. Technol*. **22**, 1041-1046.

PIPER, W. W., KRAVITZ, L. C. & SWANK, R. K. (1965): Axially symmetric paramagnetic color centers in fluorapatite. *Phys. Rev. A* **138**, 1802-1814.

PRINCE, E. (1971): Refinement of the crystal structure of apophyllite. III. Determination of the hydrogen positions by neutron diffraction. *Amer. Mineral*. **56**, 124l-1251.

ROUSE, R.C., PEACOR R.D. & DUNN, P.J. (1978): Hydroxyapophyllite, a new mineral, and a redefinition of the apophyllites group II. Crystal structure. *Amer. Mineral*. **63**, 199-202.

RUBIO, J. O., TOHVER, H. T., CHEN, Y. & ABRAHAM M. M. (1976): Trapped-hole defects in SrO. *Phys. Rev. B* **14**, 5466-5472.

SORIEUL, S., ALLARD, T., MORIN, G., BOIZOT, B. & CALAS, G. (2005): Native and artificial radiation-induced defects in montmorillonite. An EPR study. *Phys Chem Minerals* **32**, 1-7.

STÄHL, K. (1993): A neutron powder diffraction study of partially dehydrated fluorapophyllite, $KCa_4(Si_8O_{20})F{\cdot}8H_2O$. *Eur. J. Mineral*. **5**, 845-849.

TAYLOR, W.H. & NÁRAY-SZABÓ, I. (1931): The structure of apophyllite. *Z. Kristallogr*. **77**, 146-158.

VAN DOORSLAER, S.,. SIERRA, G. A. & SCHWEIGER, A. (1999): Dead Time-Dependent Line Distortions in Absolute-Value Electron Spin Echo Envelope Modulation Spectra. *J. Magnet. Res.* **136**, 152–158.

WALSBY, C.J., LEES, N.S., CLARIDGE, R.F.C. &WEIL, J.A. (2003): The magnetic properties of oxygen-hole aluminum centres in crystalline SiO_2. VI: A stable AlO_4/Li centre. *Canad. J. Phys*. **81**, 583-598.

WEIL, J.A. & BOLTON J.R. (2007): Electron paramagnetic resonance, elementary theory and practical applications. *Wiley-Interscience, John Wiley & Sons Inc*.

Chapter 4

Single-crystal EPR and ENDOR study of an Al-O^- center in prehnite: implications for aluminum-associated oxyradicals in layer silicates

Single-crystal electron paramagnetic resonance (EPR) spectra of gamma-ray-irradiated prehnite (Jeffrey mine, Quebec, Canada) measured at 298 and 160 K reveal an aluminum-associated oxygen hole center (Al-O^-). Spin Hamiltonian parameters **g** and **A**(^{27}Al) fitted from the 298 K spectra suggest that this Al-O^- center represents hole trapping on an apical hydroxyl oxygen atom (after removal of the proton) coordinated to an octahedral Al^{3+} ion (*i.e.,* an [•$OAlO_4$(OH)] center from the [(OH)AlO_4(OH)] precursor, where • denotes the unpaired spin). Pulsed electron nuclear double resonance (ENDOR) spectra measured at 25 K allow the identification and quantitative analysis of two sets of ^{27}Al hyperfine structures and five proton hyperfine structures, which are all consistent with the proposed structural model. Isothermal and isochronal annealing experiments show that this center is bleached out completely at 375 °C, but can be readily restored by gamma-ray irradiation, and exhibits second-order decay kinetics. These results from the Al-O^- center in prehnite provide support for and new insights into Clozel *et al.* (1995)'s ^{VI}Al-O^--^{VI}Al model for B-centers in kaolinite.

4.1 Introduction

Aluminum-associated oxyradicals are common radiation-induced defects (RIDs) in clay minerals (Novozhilov *et al*., 1969; Angel *et al*., 1974; Jones *et al*., 1974; Meads & Malden, 1975; Hall, 1980; Clozel *et al*., 1994, 1995; Götze *et al*., 2002; Köksal *et al*., 2004). RIDs in clay minerals have recently attracted extensive studies, because they are natural dosimeters with wide applications from tracing and monitoring the migration of radionuclides in Earth's surface environments to age determination and mineral exploration, and have direct relevance to nuclear waste disposal (Ikeya, 1993; Mosser *et al*., 1996; Allard & Muller, 1998; Allard *et al*., 2003; Plötze *et al*., 2003; Morichon *et al*., 2008; Allard & Calas, 2009). RIDs, including aluminum-associated oxyradicals, in clay minerals, however, are generally not well understood with respect to their structures owing to the fact that they are usually characterized only by powder electron paramagnetic resonance (EPR) spectroscopy. Although powder EPR spectra measured with the oriented film technique have provided extremely valuable information about the orientations of RIDs in the host clay minerals (*e.g*., Clozel *et al*., 1995; Morichon *et al*., 2008), such information is usually not as unambiguous as those from the single-crystal EPR technique. Also, powder EPR spectra are generally lower in resolution and sensitivity than their single-crystal counterparts. Therefore, paramagnetic centers in clay minerals as investigated by powder EPR spectra only are usually difficult to interpret with respect to their structures. For example, all previous investigators (Angel *et al*., 1974; Jones *et al*., 1974; Meads & Malden, 1975; Hall, 1980; Clozel *et al*., 1994, 1995; Götze *et al*.,

2002; Köksal *et al*., 2004) agreed that ‘‘B-centers’’ in kaolinite represent aluminum-associated oxyradicals but disputed the structural models whether they involve hole trapping on an O^{2-} ion shared by two Al atoms or by one Al atom and one Si atom. This dispute stems from the facts that the ^{27}Al hyperfine structure observed in powder EPR spectra was not always clearly resolved and that the orientation between the hole trapping oxygen atom and its associated Al atom(s) was not known.

As part of our continuing effort to better understand RIDs in layer silicates and their analogues by single-crystal continuous-wave (CW)EPR, pulsed electron nuclear double resonance (ENDOR), and pulsed electron spin echo envelope modulation (ESEEM) spectroscopy (Mao & Pan, 2009; Mao *et al*., 2010), we have investigated prehnite ($Ca_2Al\ [AlSi_3O_{10}](OH)_2$) before and after gamma-ray irradiation (Pan *et al*., 2009). Prehnite consisting of $[AlSi_3O_{10}]$ tetrahedral and $[AlO_4(OH)_2]$ octahedral sheets (Figure 4.1) has three polymorphs (*Pncm, P2cm* and *P2/n*) owing to different Al-Si ordering schemes in the tetrahedral sites (Peng *et al*., 1959; Papike & Zoltai, 1967; Preisinger, 1965; Balic-Žunić *et al*., 1990; Baur *et al*., 1990; Zhao *et al*., 2003; Detrie *et al*., 2008). The two hydroxyl groups on the opposite apices of the Al octahedron have equivalent orientations but different Al-O bond distances in the *P2cm* polymorph (Detrie *et al*., 2008; Figure 4.1). Single-crystal EPR spectra of prehnite reported in Pan *et al*. (2009) allowed quantitative analyses of a Fe^{3+} center and a VO^{2+} radical, and suggested the presence of an aluminum-associated oxygen hole center ($Al\text{-}O^-$). The present contribution reports on results of a detailed

characterization of the Al-O^- center in prehnite by single-crystal CW-EPR and pulsed ENDOR spectroscopy, together with a series of isochronal and isothermal annealing experiments. These results are used to determine the structure and thermal stability of the Al-O^- center in prehnite and to provide new insights into aluminum-associated oxyradicals in layer silicates in general.

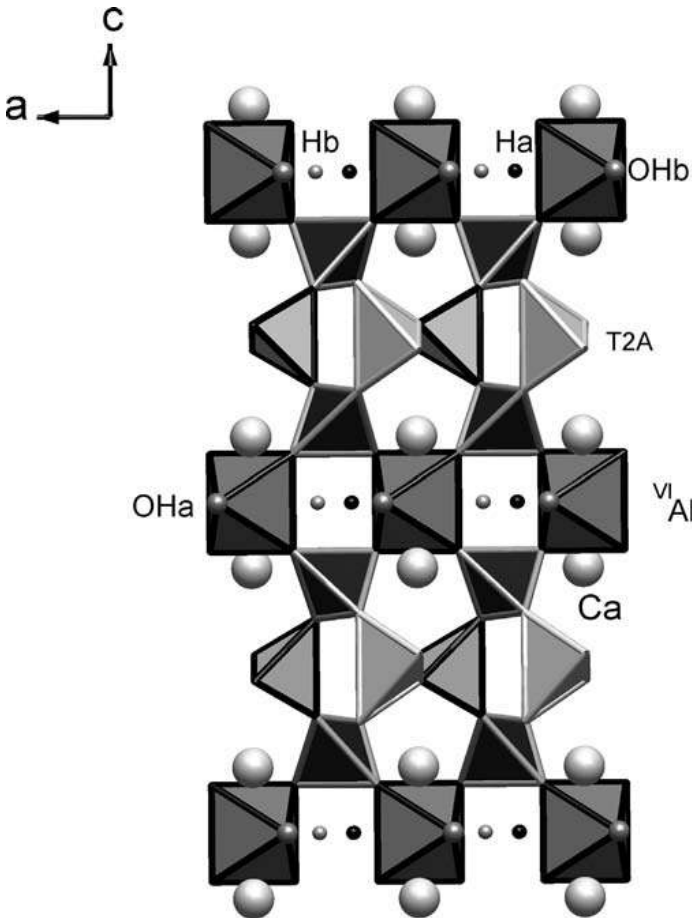

Figure 4.1 Crystal structure of *P2cm* prehnite projected to the (010) plane illustrating alternating tetrahedral and octahedral sheets (Detrie *et al*., 2008). The apical hydroxyl oxygen atoms (OHa and OHb; associated protons Ha and Hb) of Al octahedra (^{VI}Al) are marked. The tetrahedral site occupied by Al (T2A) is marked, but other tetrahedral sites occupied by Si are not labeled.

4.2 Samples and experimental techniques

4.2.1 Prehnite crystals and sample preparation

Prehnite crystals selected for this study came from the same sample (Jeffrey mine, Asbestos, Quebec, Canada) investigated in Pan *et al*. (2009). The Jeffrey mine is one of the few localities in the world where prehnite occurs as millimeter-sized crystals amenable to single-crystal EPR studies. Electron-microprobe analyses showed that prehnite in this sample contains only ~0.05(3) wt% Fe_2O_3 and trace amounts of Mn and other transition metals (Pan *et al*., 2009), also ideal for EPR studies. Single-crystal X-ray diffraction data showed that prehnite crystals in this sample are dominantly of the space group *P2cm* (Pan *et al*., 2009; *cf*. Papike & Zoltai, 1967; Detrie *et al*., 2008).

Selected crystals of prehnite are approximately 2 x 2 x 1 mm in size, have a light brownish orange color, and possess well developed {110}, {$^{-}$110}, {111} and {$^{-}$111} forms and a good {001} cleavage. They were irradiated at room temperature in a ^{60}Co cell for a dose of ~44 kGy (*i.e*., ~460 Gy/h for 96 h). One irradiated crystal was subjected to a series of step-wise, isochronal annealing experiments in the temperature range from 75 to 400 °C at a constant interval of 25 °C and a duration of 30 min. each step. This crystal after isochronal annealing to 400 °C was re-irradiated at room temperature for a dose of ~44 kGy. Four other irradiated crystals were used for isothermal annealing experiments at 250, 275, 300 and 350 °C for up to 10.6 h.

4.2.2 Single-crystal CW-EPR experiments

Single-crystal CW-EPR spectra were measured on a Bruker EMX spectrometer equipped with an ER4119 cavity, an ER218G1 goniometer with a precision of ~0.2°, and an Oxford liquid He cryostat, at the Saskatchewan Structural Science Centre, University of Saskatchewan. Conditions of single-crystal EPR measurements including the selection of rotation planes and crystal alignments are generally similar to those described in Pan *et al*. (2009). Three notable differences are: (1) experimental axes **x**, **y** and **z** are parallel to crystallographic axes **a**, **b**, and **c**, respectively; (2) measurements have been made at selected orientations for a third rotation plane parallel to the (110) face, and (3) spectra at 298 K were collected in the field of only 20 mT wide (Figure 4.2). Pan *et al*. (2009) switched the experimental axes x and y, measured only two rotation planes (*i.e*., parallel to the {001} cleavage and the ($1\bar{1}0$) face), and used wide-scan spectra to investigate the Fe^{3+} center (940 mT) and the VO^{2+} radical (140 mT). In the present study, the 298 K spectra have a resolution of ~0.019 mT (*i.e*., 1024 data points over 20 mT). Magnetic field was calibrated by use of α,γ-bis-diphenylene-β-phenyl allyl (BDPA; g = 2.0027) in benzene as an external reference material.

Single-crystal EPR measurements of prehnite after each step of isochronal and isothermal annealing were made at 298 K with the magnetic field **B**//**b**. Crystal alignment of this type was made first by use of the {001} cleavage and then adjusted on the basis of coalesce of magnetically nonequivalent sites in this orientation. Three crystals used for isothermal annealing experiments at 250, 275 and 350 °C were

measured with the cryostat installed, whereas spectral collections for the remaining crystal annealed at 300 °C were made after the cryostat was removed.

4.2.3 Pulsed ENDOR experiments

Pulsed ENDOR (Gemperle & Schweiger, 1991) spectra at 25 K were collected on a Bruker E580-10 Elexsys spectrometer at the Illinois EPR Research Center (IERC), University of Illinois at Urbana-Champaign. Samples were maintained at 25 K using a liquid He Oxford CF935 cryostat. ENDOR experiments were made using a Mims three-pulse scheme ($\pi/2 - \tau - \pi/2 - T - \pi/2 - \tau -$ echo, with the RF pulse applied during time T and the frequency of which is varied in time and with $\pi/2$ set at 16 ns). An ENIA-300 RF amplifier was used. Because Mims ENDOR gives rise to blind-spots that originate from an oscillating τ dependence, ENDOR spectra were also recorded as a function of τ and subsequently summed together.

Sets of CW-EPR and pulsed ENDOR (and ESEEM) spectra were obtained for one plane whose normal is ~30° from the a-axis (normal vector: $\theta = 94.5°$ and $\varphi = 32.6°$). Spectra were collected at 15-degree intervals. For such a plane there are two well-resolved sextets. The excited field was set at the lowest field hyperfine line of the lower field sextet and on the highest field hyperfine line of the higher field sextet. The only exception was that only one spectrum was collected on the central hyperfine line for the orientation near the c-axis, where the two sextets coalesce. Angle corrections were calculated from the fitting of the CW spectra of the two sextets using the g and ^{27}Al hyperfine matrices obtained from the three-plane CW-EPR analysis of this center

(see below). ENDOR spectra were then simulated using SIMEND, which is a version of SIMPIP that calculates a frequency swept ENDOR spectrum (Nilges *et al.*, 2009). However, the ENDOR intensity was calculated explicitly using the nuclear spin turning angle, instead of using the transition moment multiplied by a frequency factor. The ENDOR factor (Gemperle & Schweiger, 1991) is given by:

$$F_{ENDOR} = [1 - \cos(\omega_R t_{rf})]/4 \quad \text{.....(4.1)}$$

where t_{rf} is the RF pulse time and ω_R is the effective nutation frequency (given by $2\pi B_2(TM)^{1/2}$ and TM is the transition moment calculated in SIMEND). The frequency dependence of B_2 is approximated by measuring the voltage on the voltage-divided RF termination of the ENDOR probe and $B_2@\upsilon_H$ is measured by a Rabi oscillation experiment. Note that as the turning angle goes to zero, the ENDOR factor reduces to just the transition moment times B_2^2.

4.3 Results

4.3.1 Single-crystal CW-EPR spectra

Pan *et al*. (2009) noted that single-crystal EPR spectra of prehnite measured from 298 to 13 K disclose the presence of six paramagnetic defects: three Fe^{3+} centers, a Mn^{2+} center, a VO^{2+} radical and an $Al\text{-}O^-$ center. Of these, the three Fe^{3+} centers and the VO^{2+} radical have been described in detail in Pan *et al*. (2009). The Mn^{2+} center, which is indicated by the characteristic ^{55}Mn hyperfine sextet (I = 5/2 and a hyperfine constant A/h of ~250 MHz), is invariably lowing signal-to-noise ratios and is commonly obscured by the VO^{2+} radical and the $Al\text{-}O^-$ center, therefore cannot be

analyzed quantitatively. Herein, the single-crystal EPR spectra of the Al-O^- center are described in detail.

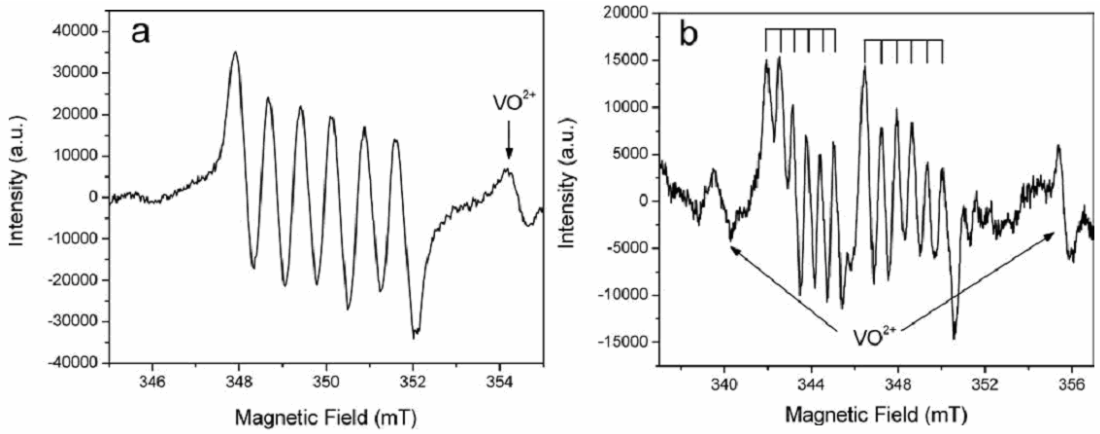

Figure 4.2 Representative 298 K single-crystal EPR spectra of γ-ray irradiated prehnite illustrating the Al-O^- center: (a) measured at ν = 9.835 GHz and **B**//**b** showing a well resolved sextet; and (b) measured at ν = 9.840 GHz and **B**^**b** = 50° showing splitting into two sets of sextet (marked). Also marked are lines from the VO^{2+} radical (Pan *et al*., 2009).

The Al-O^- center, which is visible but low in signal-to-noise ratio in the spectra of as-is prehnite, is enhanced by ~44 kGy γ-ray irradiation. The 298 K spectra of γ-irradiated prehnite, measured with B parallel to symmetry axes, show that the Al-O^- center is characterized by a sextet (*i.e*., six lines of approximately same intensities and equal distances; Figure 4.2a), indicative of the 100% naturally abundant ^{27}Al nucleus with I = 5/2. When **B** is rotated away from crystal axes, the sextet is split into at most two sets (Figure 4.2b).At a few orientations, the two sets of sextets are notably different in both linewidth and lineshape. This difference suggests that these two sets of sextets may represent either two magnetically non-equivalent

sites or two magnetically equivalent but unequally populated sites (see discussion below). The average linewidth of individual hyperfine lines are ~0.30 mT at 298 K. We note that the 160 K single-crystal EPR spectra of this center (Pan *et al*., 2009) are similar to those observed at 298 K, except for a slight reduction in average linewidth to ~0.28 mT. However, the 160K spectra were measured at a lower spectral resolution of ~0.137 mT (*i.e*., 1024 data points over 140 mT; Pan *et al*., 2009), hence not used in the analysis of this Al-O^- center.

4.3.2 Optimization of spin Hamiltonian parameters

The spin Hamiltonian parameters for this S = 1/2 center with a ^{27}Al hyperfine structure can be written as:

$$H = \beta_e \mathbf{B}^T \bullet \mathbf{g} \bullet \mathbf{S} + \mathbf{I}^T \bullet \mathbf{A} \bullet \mathbf{S} - \beta_n \mathbf{B}^T \bullet \mathbf{g_n} \bullet \mathbf{I} + \mathbf{I}^T \bullet \mathbf{P} \bullet \mathbf{I} \quad \text{.....(4.2)}$$

where β_e and β_n are electronic and nuclear magnetons, respectively, and $g_n(^{27}Al)$ is taken to have an isotropic value of 1.456601 (Weil & Bolton, 2007). The electronic Zeeman matrix **g**, the nuclear hyperfine matrix **A**, and the nuclear quadrupole tensor **P** are fitted from the experimental data (Figure 4.3). All data analyses, including angle corrections, optimization of spin Hamiltonian parameters and spectral simulations, are made by use of the software package EPR-NMR (Mombourquette *et al*., 1996). Specifically, the ideal normal directions of the {001} cleavage plane and the $(1\bar{1}0)$ and (110) faces at ($\theta = 0°$, $\varphi = 90°$), (90°, 325.2°), and (90°, 34.8°), respectively, were used for the initial optimization of spin Hamiltonian parameters. Subsequently, angle corrections were made by use of the optimized spin Hamiltonian parameters in

iterations. The actual normal directions of the three experimental planes are (4.4°, 98.2°), (83.0°, 319.8°), and (88.3°, 42.4°), respectively, indicating a small crystal misalignment for each plane. It should be noted that the final spin Hamiltonian parameters were obtained by use of the corrected orientations and, therefore, are unlikely affected significantly by crystal misalignments in data collections. Also, fitting of EPR spectra alone cannot determine the sign of the hyperfine parameter. However, the isotropic hyperfine on Al arises from spin polarization effects (Weil & Bolton, 2007) and is expected to be negative in sign (Nuttall & Weil, 1981; Adrian *et al.*, 1985). Herein we adopt a negative sign for the isotropic component of the ^{27}Al hyperfine constant (Table 4.1; *cf.* Nilges *et al*., 2009; Botis & Pan, 2010).

The appearance of two nonequivalent sets of sextets, together with the possibility of a monoclinic crystal symmetry for prehnite (Papike & Zoltai, 1965; Baur *et al*., 1990), led us to fit them separately. However, the fitted spin Hamiltonian parameters from the two sets of sextets agree within analytical uncertainties and are indistinguishable from those obtained by grouping them together as magnetically nonequivalent sites in the rotation group D_2 (Pan *et al*., 2009). Therefore, only results from the latter approach using the orthorhombic crystal symmetry (Table 4.1) are presented below. For the *P2cm* polymorph one expects two chemically unique sites, because the two hydroxyl groups on the opposite apices of the Al octahedron are nonequivalent. For the *Pncm* polymorph the two hydroxyl groups are equivalent and the corresponding centers will be equivalent. In both cases the rotation group is D_2 and there are four symmetry-related magnetically nonequivalent sites for each of the

two chemically unique sites. Fitting of the CW-EPR spectra could not differentiate between the two cases, and the two chemical sites were assumed equivalent.

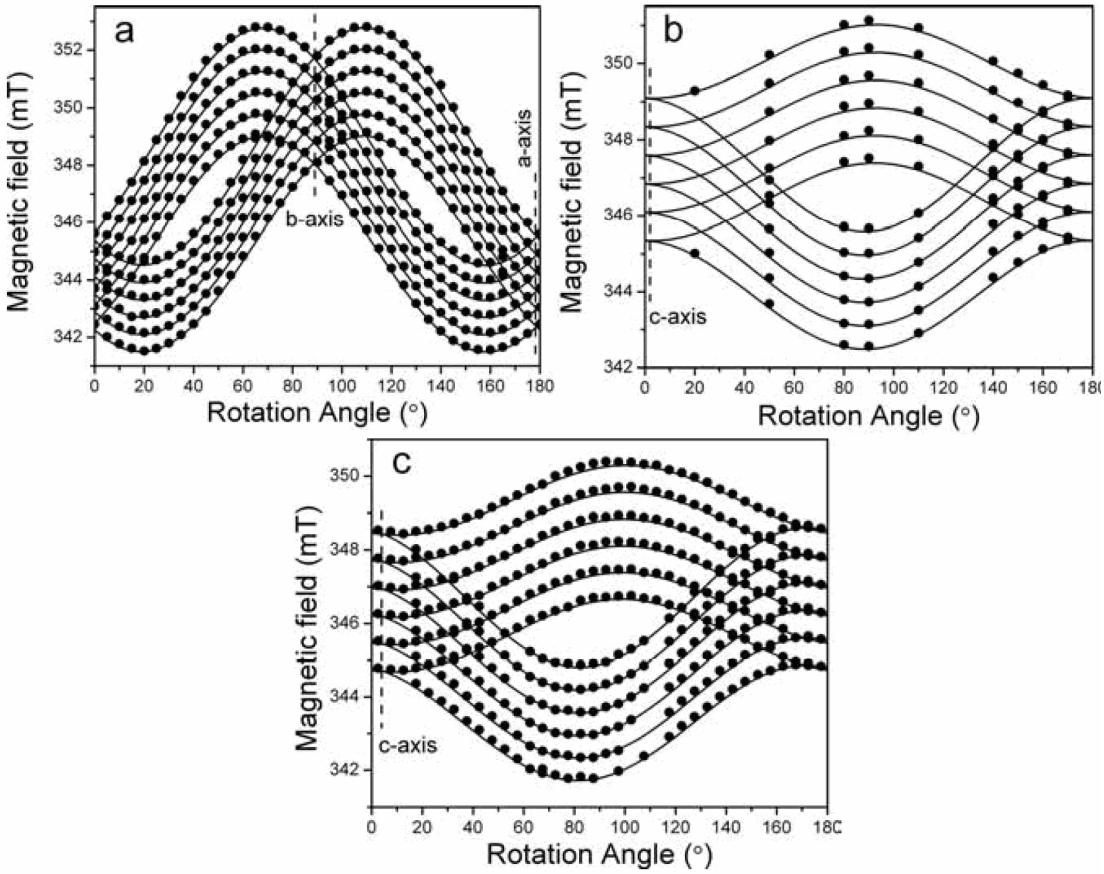

Figure 4.3 Line-position data *versus* rotation angles (roadmaps) of the Al-O^- center in prehnite in three rotation planes: (a) the {001} cleavage, (b) the (110) crystal face, and (c) the $1\bar{1}0$ crystal face. Solid circles represent experimental data points; and solid lines are predicted from spin Hamiltonian parameters in Table 4.1. Locations of crystallographic axes **a**, **b** and **c** are marked only approximately, because minor crystal misalignments are present for all three rotation planes (see text for explanation).

A total of 1920 line-position data points from the 298 K spectra were used for data fitting. However, lower weighing factors of 0.5 or 0.1 were assigned to lines that

occur in crossover regions of magnetically nonequivalent sites or are interfered by overlapping lines from the Fe^{3+} or VO^{2+} centers (Pan *et al*., 2009), resulting in a sum of weighting factors of 1738. The final value of the root-mean-squares of weighted differences (RMSD) between the calculated and observed line positions is 0.049 mT, which is only about one sixth of the average experimental linewidth.

Table 4.1 Spin Hamiltonian parameters of the Al-O^- center in prehnite.

	Matrix (**Y**)			k	Principal values	Principal directions	
g and **A**(^{27}Al) parameters from CW-EPR spectra at 298 K					(Y_k)	θ_k (°)	φ_k (°)
g	2.00813(1)	0.01521(1)	0.00000(1)	1	2.04868(1)	90.0(2)	69.4(2)
		2.04297(1)	0.00000(1)	2	2.02357(1)	179.9(2)	233*
			2.02357(1)	3	2.00242(1)	89.9(2)	159.4(2)
^{27}Al **A**/h (MHz)	–0.730(2)	0.048(1)	0.000(2)	1	–0.618(1)	89.9(7)	67.2(5)
		–0.639(2)	0.000(2)	2	–0.751(1)	91(19)	157.2(5)
			–0.757(1)	3	–0.757(1)	0(19)	160*
^{27}Al and ^{1}H hyperfine parameters from pulsed ENDOR at 25 K							
Al1a **A**/h (MHz)	–21.23	1.58	–0.01	1	–17.46	89.9	67.2
		–17.81	0.01	2	–21.24	1.6	160.6
			–21.24	3	–21.90	91.6	157.2
Al1b **A**/h (MHz)	–20.35	1.63	0.000	1	–16.47	89.9	67.2
		–17.15	0.01	2	–20.67	1.6	157.1
			–20.67	3	–21.04	91.6	157.2
Al1 **P**/h (MHz)	–0.04	0.00	0.000	1	0.04	90	89
		0.04	0.000	2	0.00	0	0
			0.000	3	–0.04	90	179
H1 **A**/h (MHz)	0.10	4.06	0.000	1	6.22	90	57
		3.52	0.000	2	–2.60	180	0
			–2.97	3	–2.97	90	300
H2 **A**/h (MHz)	–0.41	–2.01	0.000	1	3.01	90	300
		1.83	0.000	2	–1.58	0	0
			–1.58	3	–1.59	90	210
H3 **A**/h (MHz)	3.21	0.28	0.000	1	3.23	90	183
		–1.36	0.000	2	–1.38	90	93
			–1.79	3	–1.79	0	0
H4 **A**/h (MHz)	3.57	–2.39	0.000	1	5.71	90	138
		3.03	0.000	2	0.89	90	48
			–1.20	3	–1.20	0	0
H5 **A**/h (MHz)	–0.02	1.46	0.000	1	2.28	90	213
		1.35	0.000	2	–0.95	0	0
			–0.95	3	–0.95	90	123

Results reported here are for one of four symmetrically equivalent sites in the rotation group D_2 (see text for explanation). Polar angle y is relative to the crystallographic axis c, and azimuth angle φ is relative to axis a. (θ, φ) is equivalent to (180 – θ, 180 + φ). *azimuth angle is meaningless at θ ≈ 0°.

The fitted matrices **g** and **A** (Table 4.1) are rhombic and axial in symmetry, respectively. The principal axes g_{max} and $A_{//}$ are almost coaxial and are approximately along the ^{VI}Al-OH bond direction ($\theta = 90°$, $\varphi = 62°$) in the ideal prehnite structure (Detrie *et al*., 2008). The nuclear quadrupole tensor **P** is small and cannot be determined precisely with this dataset, hence not included in Table 4.1.

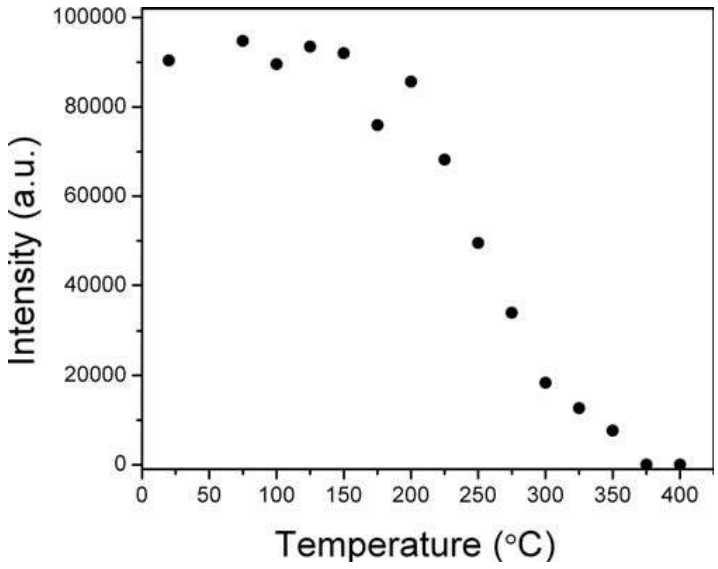

Figure 4.4 Intensity of the Al-O$^-$ center (*i.e*., peak-to-peak height of the lowest-field hyperfine line from 298 K single-crystal EPR spectra measured at **B**//**b**) as a function of isochronal annealing temperature from 75 to 400 °C.

4.3.3 Single-crystal CW-EPR spectra of annealed prehnite

Figure 4.4 shows that the Al-O$^-$ center remains unchanged after heating to at least 150 °C and then starts to decrease in intensity at 175 °C, accompanied by a fade of the brownish orange color, and is completely bleached out at 375 °C. The ~44 kGy γ-ray irradiation of the bleached crystal restores the Al-O$^-$ center to ~50 % of its original intensity, with a re-appearance of the brownish orange color. The impurity

centers such as Fe^{3+} and Mn^{2+} in prehnite are not affected by annealing in this temperature range, hence no apparent correlation with the Al-O^- center.

The four crystals selected for isothermal annealing experiments are similar in crystal size and were irradiated for the same dose. Spectra of the three crystals annealed at 250, 275, and 350 °C confirm that the Al-O^- center is broadly similar in initial concentration (Figure 4.5a). The apparently different intensity of this center in the crystal annealed at 300 °C (Figure 4.5a) is readily attributable to a different resonance condition after the cryostat was removed. These isothermal annealing experiments show that the reciprocal intensity (1/N) of the Al-O^- center *versus* the annealing time can be fitted to a second-order reaction law (Ikeya, 1993):

$$1/N = \lambda t + 1/N_0 \quad \text{.....(4.3)}$$

where N_0 is the initial intensity and λ is the specific decay constant (Figure 4.5a). Also, a plot of the fitted decay constant versus reciprocal temperature for data from crystals annealed at 250, 275, and 350 °C (Figure 4.5b) follows the Arrhenius relation:

$$\lambda = Ae^{-Ea/kT} \quad \text{.....(4.4)}$$

where A is the pre-exponential factor, Ea is the activation energy, and k is the Boltzmann constant (8.617×10^{-5} eV/K). The fitted activation energy is 1.2(1) eV. The pre-exponential factor in this case is meaningless, because the absolute concentration of the Al-O^- center has not been determined by use of well-calibrated standards.

4.3.4 Pulsed ENDOR spectra

Mims ENDOR (Gemperle & Schweiger, 1991) spectra of prehnite showed three distinct sets of peaks (Figure 4.6 and 4.7). One set of two peaks at ~6 and ~14 MHz (Figure 4.6) correspond to the ^{27}Al hyperfine structure that has been observed and analyzed already from the CW-EPR spectra. Davies ENDOR (Gemperle & Schweiger, 1991) spectra taken at a few selected orientations show only these two peaks at 6 and 14 MHz, confirming that they arise from a strongly coupled ^{27}Al nucleus. It should also be noted that the high-frequency branch of the strongly coupled ^{27}Al nucleus overlaps with the distant proton peaks in the Mims ENDOR spectra and as such is not readily seen (Figure 4.6).

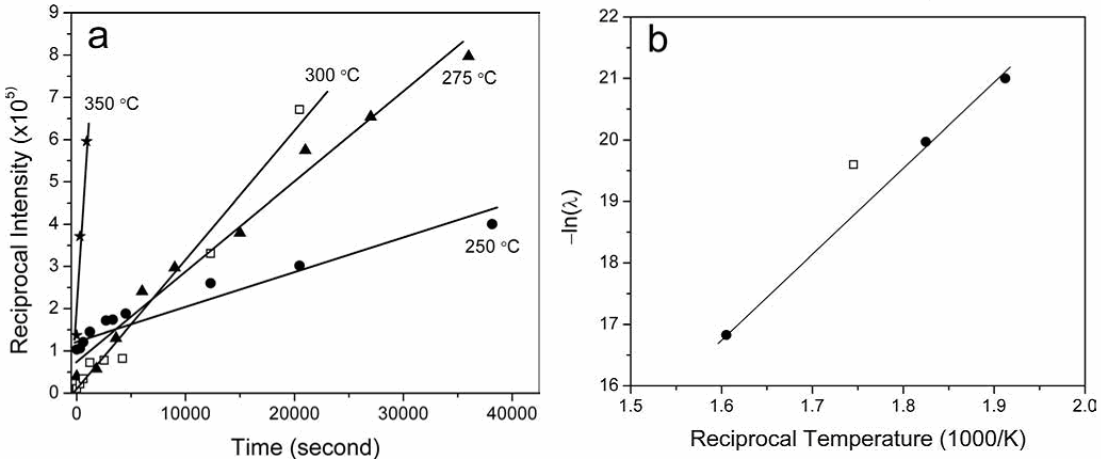

Figure 4.5 Plots of (a) reciprocal intensities (1/N) *versus* annealing time (t) illustrating the second-order decay kinetics of the Al-O$^-$ center in prehnite at 250, 275, 300, and 350 °C, and (b) decay constants (–lnλ) *versus* reciprocal temperature (1/T); note that the data point from annealing at 300 °C (open square) was not included in the regression analysis.

Closer examination of the strong ^{27}Al spectra shows that the peak at ~6 MHz is split into two at a number of orientations (Figure 4.6). These spectra are simulated best by assuming two populations with slightly different ^{27}Al hyperfine matrices. Our simulations, which assumed the two ^{27}Al hyperfine matrices to have the same orientations for their principal axes (taken from the CW-EPR spectra), show that the principal values of A differ only by two to six percent (Table 4.1), hence not observed in the CW-EPR spectra.

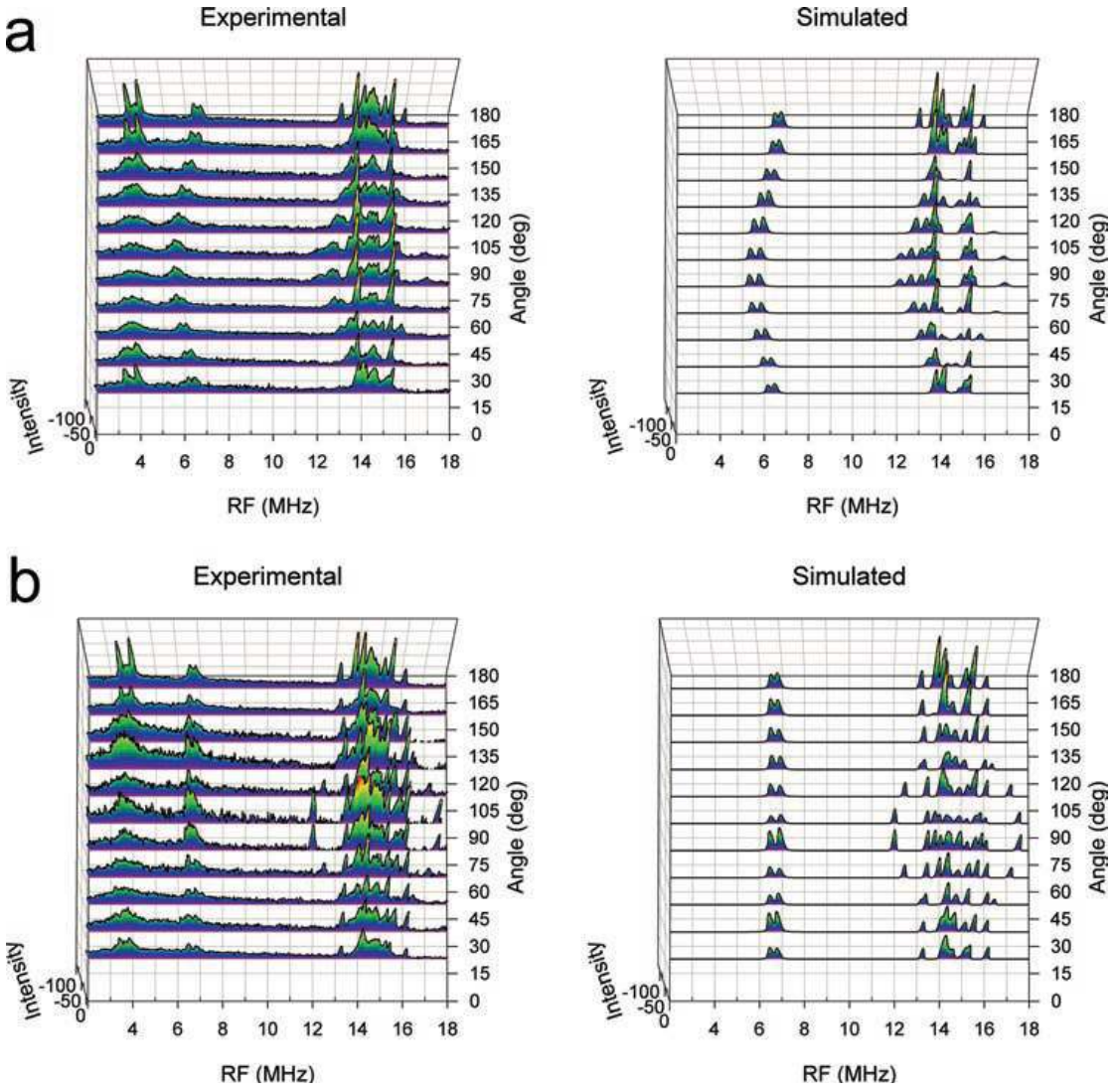

Figure 4.6 Stacked plots of the experimental and simulated ^{27}Al Mims ENDOR

spectra as a function of rotation angles: (a) the excitation field was set on the low field line of the low field sextet; and (b) the excitation field was set on the high field line of the high field sextet. Note that the peaks at ~3.8 MHz are not simulated. Also, the intensity scale has been inverted for easier viewing.

The second set of peaks at ~3.8 MHz, which give rise to a doublet splitting near the **c**-axis (Figure 4.6), is attributable to more distant ^{27}Al nuclei. Table 4.2 shows that hydroxyl oxygen atoms of octahedral Al in prehnite has four next nearest-neighbor Al atoms: two at octahedral sites at distances of 3.9 and 4.0 Å and two at the T2A sites at the same distance of 4.6 Å. The observed doublet at orientations near the c-axis is consistent with a ^{27}Al hyperfine matrix with $A_{zz} = 0.59$ MHz and a quadrupole tensor with $Q_{zz} \approx 0$. Calculations based upon the point dipole model (Weil & Bolton, 2007, p. 254) predict $A_{zz} = –0.33$ and –0.31 MHz for the two Al nuclei at the octahedral sites and $A_{zz} = +0.42$ MHz for the two Al nuclei at the T2A sites. Although the Al nuclei at the T2A sites have predicted A_{zz} values closer to the observed splitting of 0.59 MHz, the lack of resolved structures off-axis makes any definitive assignment and/or spectral fitting difficult.

The third set of peaks centered around the Lamour frequency of ~14.5 MHz (Figure 4.7) are attributable to multiple protons. For the hydroxyl oxygen atoms coordinated to an octahedral Al in *P2cm* prehnite (Detrie *et al*., 2008), there are five next-nearest-neighbor protons at distances in the range of 3–4 Å (Table 4.2). Spectral simulations using trial hyperfine matrices that were calculated on the basis of the point-dipole model show that four of these five protons (H1, H2, H3 and H5) are well accounted for, and the refined hyperfine matrices are close to those predicted by the

point-dipole model (Tables 1 and 2), although H2 shows a somewhat smaller coupling than predicted. The principal values of the hyperfine matrix for H4, however, have to be varied significantly to give a good fit. In particular, A_{max} is found to be 5.71 MHz, in comparison with the predicted value of ~3.1 MHz. Also, the fitted hyperfine matrix for H4 has a noticeable rhombic component and a significantly positive isotropic Fermi contact term of 1.8 MHz (Table 4.1).

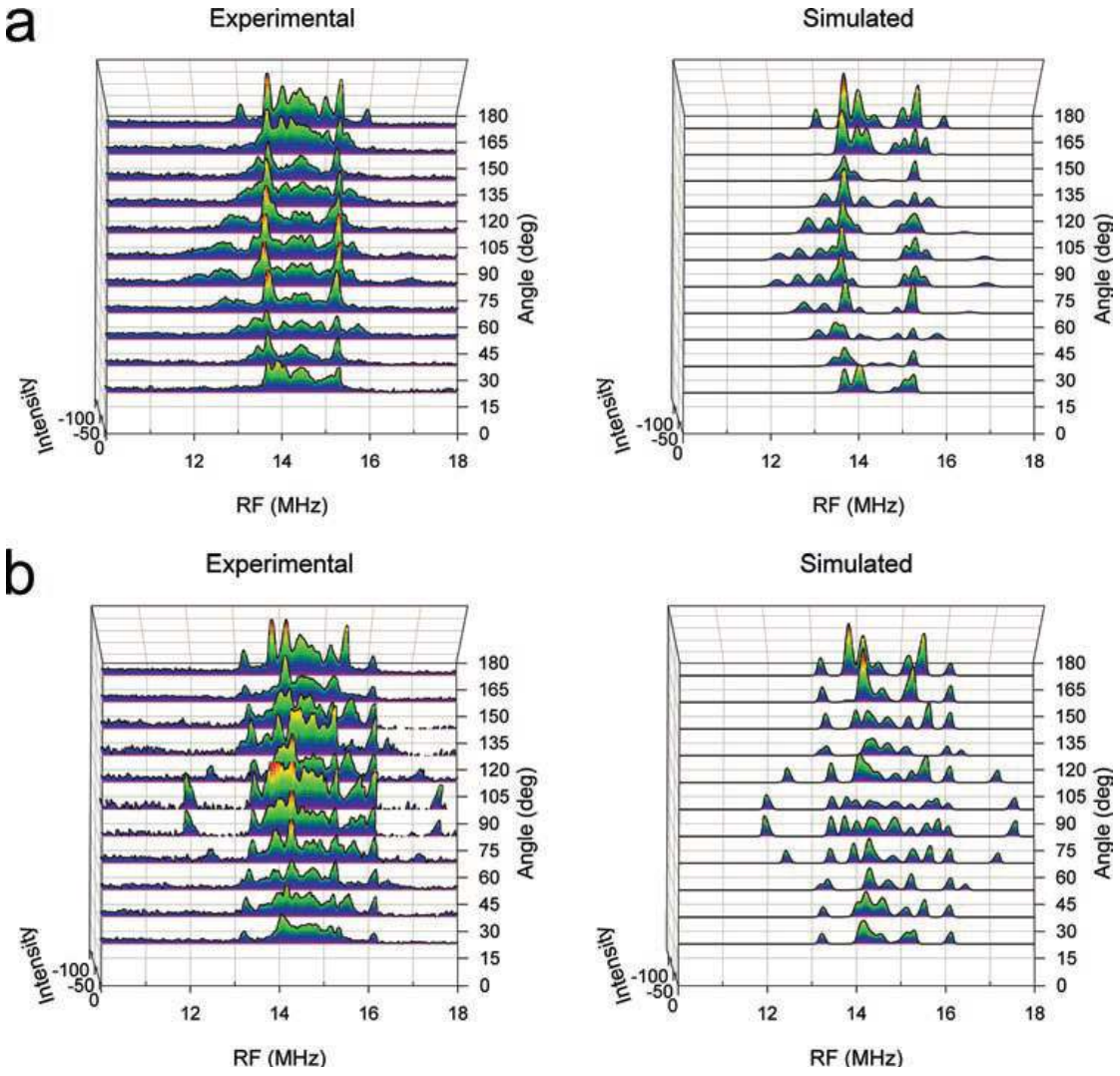

Figure 4.7 Stacked plots of the ^{1}H portion of the experimental and simulated Mims ENDOR spectra as a function of rotation angles: (a) the excitation field was set on the low field line of the low field sextet, and (b) the excitation field was set on the

high field line of the high field sextet. The intensity scale has been inverted for easier viewing.

In addition, spectral simulations for H1 show that the linewidths at orientations near A_{max} are broader than other orientations. Therefore, an increase in linewidth of 0.3 MHz, corresponding to a 5 % variance in A_{max}, was added in simulated spectra for H1 along this orientation. An isotropic linewidth of 0.14 MHz (FWHM) was used for other protons and the other two orientations of A for H1. A Gaussian lineshape, which is characteristic of an inhomogeneous system, was used in simulating the spectra.

Spectral simulations also show that the inclusion of five protons accounts for all of the resolved proton peaks (Figure 4.7). There is still an unresolved or partially resolved ‘‘matrix’’ peak at υ_H (Figure 4.7), which is attributable to more distant protons. However, addition of the sixth-nearest proton (*cf*. Detrie *et al*., 2008) yielded no appreciable improvement in the fitted spectra.

4.4 Discussion

4.4.1. Structural model and origin of the Al-O^- center in prehnite

The orientations of the g_{max} and $A_{//}$ axes at (90°, 69°) and (90°, 67°), respectively, from the CW-EPR spectra are approximately along the ^{VI}Al-OH bond direction (90°, 60°). Also, the orientations of the g_{int} axis and one $A_{\perp}$ axis are close to the c-axis, which in turn is approximately along the bisector of an O-^{VI}Al-O angle. Similarly, the g_{min} axis and another $A_{\perp}$ axis approximately coincide with the bisector

of another O-^{VI}Al-Oangle. These relationships are similar to those observed for the VO^{2+} radical in prehnite, which has been interpreted to represent hole trapping by a substitutional V atom and a hydroxyl O atom (after removal of the proton) to form V=O at an octahedral site (Pan *et al*., 2009). Similarly, the Al-O^- center most likely represents hole trapping on a hydroxyl oxygen atom linked to an octahedral Al site (*i.e*., from the [(OH)AlO_4(OH)] precursor to the [•$OAlO_4$(OH)] center, where • represents the unpaired spin).

The hydroxyl oxygen with the trapped hole can be approximated as an O^- radical center in the crystal field of the nearby AlO_4(OH) ion cluster. For the O^- radical the unpaired spin is expected to be in a 2p orbital perpendicular to the Al-O bond. The values of the **g** matrix are then expected to be approximately (Lunsford, 1973):

$g_{x'x'} = g_e$

$g_{y'y'} = g_e + 2\delta/\Delta E_1$

$g_{z'z'} = g_e + 2\delta/\Delta E_2$

where z' is defined along the Al-O direction, δ is the oxygen spin-orbit coupling (~150 cm^{-1}), and ΔE_1 and ΔE_2 are the electron excitation energies between the ground state and those formed by moving the hole from the $p_{x'}$ orbital to the $p_{z'}$ and $p_{y'}$ orbital, respectively. The value of g_{min} is close to that of the free electron and its axis is approximately perpendicular to the Al-O bond. Thus, this axis should correspond approximately to the direction of the ground state $p_{x'}$ orbital. ΔE_2 is expected to be

smaller than ΔE_1, because the $p_{z'}$ orbital is expected to have a significant sigma character. Thus, g_{max} is oriented, as expected, close to the Al-O bond direction.

The isotropic component of the strong ^{27}Al hyperfine structure as determined by CW-EPR is –19.8 MHz (comparable to –19.4 and –20.2 MHz from pulsed ENDOR, the average of which is also –19.8 MHz), indicating ~0.5% of the unpaired spin on the Al nucleus. The value of the isotropic coupling varies exponentially with the Al-O distance (Adrian *et al*., 1985), but also depends highly on the energies to excite the oxygen 2s and 2p electrons. This makes accurate theoretical calculations of the hyperfine coupling problematic. However, the approximate theory of Adrian *et al*. (1985) can still be used to estimate the difference in the two Al-O bond lengths needed to explain the difference in couplings observed in ENDOR. We calculate a difference of only 0.012 Å between the two Al-O bond lengths, which compares well with those obtained from X-ray structure studies of Detrie *et al*. (2008) for *P2cm* prehnite (0.011 and 0.006 Å depending on sample).

According to the point-dipole model, the axial component, of the strong ^{27}Al hyperfine structure would predict a distance of ~2.5 Å , which is considerably longer than the ideal Al-O bond distance of 1.92 Å (Detrie *et al*., 2008). However, at this close distance the negative contributions from spin polarization effects tend to cancel with the dipolar contributions (Adrian *et al*., 1985) and the anisotropic part of the hyperfine coupling becomes only weakly dependent on the Al-O distance. Our value of $T_{z'z'}$ (the component along the internuclear axis for the traceless, anisotropic

hyperfine coupling matrix, T) of 2.57 MHz is well within the predicted range of 1.5–3 MHz (Adrian *et al.*, 1985).

This structural model can be evaluated further by the ^{27}Al and ^{1}H hyperfine data from pulsed ENDOR (Table 4.1). The presence of two chemically nonequivalent populations for the strong ^{27}Al hyperfine structure as revealed by pulsed ENDOR is consistent with the *P2cm* symmetry (*i.e.*, symmetrically distinct OHa and OHb; Detrie *et al*., 2008). Similarly, we predict that four next-nearest-neighbor ^{27}Al nuclei are collectively responsible for the observed peaks at ~3.8 MHz (Figure 4.6; Table 4.2). Because only a single doublet is resolved for orientations at or near the **c**-axis (Figure 4.6), the hyperfine matrices for these four Al's could not be explicitly determined, but the peaks at ~3.8 MHz are not inconsistent with that expected to arise from these four Al nuclei.

Table 4.2 Next-nearest Al and H to an apical oxygen of an Al octahedron in prehnite.

	Ideal structure				Experimental			
Atom	θ (°)	φ (°)	r (Å)	$T_{z'z'}$(MHz)	θ (°)	φ (°)	r (Å)	$T_{z'z'}$(MHz)
^{VI}Al	90	103.9	3.95	0.67				
^{VI}Al	90	335.8	4.04	0.63				
^{IV}Al	3.6	257.7	4.64	0.42				
^{IV}Al	176.4	257.7	4.64	0.42				
H1	90	53.5	3.06	5.57	90	56.5	2.99	6.00
H2	90	300.9	3.53	3.61	90	300.5	3.81	3.06
H3	90	184.4	3.72	3.08	90	183	3.67	3.21
H4	90	138.9	3.74	3.05	90	138	3.44	3.91
H5	90	227.1	4.13	2.25	90	213	4.19	2.15

Data for the ideal structure of prehnite from Detrie *et al*. (2008). Note that the observed peaks at ~3.8 MHz are consistent with these nextnearest Al nuclei but are not sufficiently resolved to allow quantitative analysis (see text for explanation). $T_{z'z'}$ is the component of the anisotropic hyperfine matrix along the O-H internuclear axis.

Each of the five protons H1–H5 in the *P2cm* structure (Detrie *et al*., 2008) should exist as a pair of chemically nonequivalent protons. However, the calculated differences in proton couplings for all pairs are predicted to be only a few percent, hence only a minor line broadening is observed. Therefore, the fact that four of the five protons are well predicted by the point-dipole model provides further support for the assignment of this center to hole trapping on a hydroxyl oxygen atom coordinated to an octahedral Al atom. Although the principal values of H4 are significantly different from those predicted by the point-dipole model, the orientation of the A_{max} axis is within 1° of that predicted by the point-dipole model. For distant protons the isotropic component of the hyperfine is expected to be small. If little or no overlap of orbitals on the hydrogen and the oxygen it is usually negative, because spin polarization effects dominate. While the isotropic parts of the hyperfine for H1, H2, H3, and H5 are small (<0.2 MHz), for H4 it is both significantly larger and positive (1.8 MHz). This implies a direct orbital overlap and suggests that this proton is ‘‘hydrogen-bonded’’ to the O atom of the Al-O^- center. From the anisotropic part of the hyperfine for H4, the O. . . .H-O distance is predicted to be 3.5 Å and from the crystal structure the O-H-O angle is predicted to be 101°, which are not unreasonable values for a ‘‘hydrogen bond’’. It is noteworthy that the O-H-O angles for the other four protons are nowhere near the optimal angle of 120°.

4.4.2. Thermal stability and coloration

Aluminum-associated oxygen hole centers, which are known to involve Al at both tetrahedral and octahedral sites, are mostly detectable only at cryogenetic temperatures, because of severe line broadening related to hole hopping among equivalent oxygen atoms at elevated temperatures (Nuttall & Weil, 1981; Petrov *et al*., 1989; Claridge *et al*., 1994; Da Silva *et al*., 2005; Botis & Pan, 2010). Two notable exceptions are the proposed $[AlO_6]^0$ center in KTP ($KTiOPO_4$) and the O^- center in euclase, both of which are detectable at room temperature (Yu *et al*., 1995; Dias *et al*., 2009). This center in KTP also has similar principal g and A values (2.0464, 2.0157, 2.0027 and 17.66, 20.74, 21.02 MHz) to the Al-O^- center in prehnite. Yu *et al*. (1995) suggested this center to represent hole trapping on an oxygen atom linking a substitutional Al and a lattice Ti in the octahedral sites. Yu *et al*. (1995) also proposed two possible mechanisms for its formation: (1) substitution of Al^{3+} for Ti^{4+} resulting in a charge imbalance, and hole trapping by an O^{2-} ion to form the O^- radical during gamma-ray irradiation; and (2) OH^- impurity, which is common in KTP (Theis *et al*., 1985; Ahmed *et al*., 1986) and may occur to accompany a substitutional Al atom, may be stripped of the proton and results in hole trapping by the remaining oxygen atom during γ-ray irradiation. The latter mechanism is identical to this proposed for the [•$OAlO_4$(OH)] center in our study, except that both OH^- and Al^{3+} are lattice ions in prehnite. Similarly, the O^- center in euclase has been proposed to form from a hydroxyl group coordinated to Al in octahedral sites (Dias *et al*., 2009).

In prehnite the hydroxyl oxygen atom, after removal of its proton, is expected to remain different from the other five oxygen atoms (*i.e.*, four equatorial oxygen atoms and the other apical hydroxyl oxygen with its proton intact) coordinated to the Al octahedron. This difference may represent an energy barrier sufficient to limit hole hopping to other oxygen atoms, hence detection of the $Al\text{-}O^-$ center in prehnite at room temperature. Other thermal properties (*e.g.*, complete bleaching at 375 °C, second-order decay kinetics, and activation energy of 1.2 eV) of the $Al\text{-}O^-$ center in prehnite are similar to those of its counterparts in otherminerals (Ikeya, 1993; Pan & Hu, 2009).

Interestingly, the brownish orange color of prehnite and the $Al\text{-}O^-$ center share similar thermal properties and irradiation behavior. However, linkage between this color and the $Al\text{-}O^-$ center remains unclear. Krambrock *et al*. (2004), on the basis of optically detected magnetic resonance (ODMR) spectroscopy, showed that a yellow coloration of elbaite is related to an aluminum-associated O^- center ($Al\text{-}O^-\text{-}Al$).

4.4.3 Implications for aluminum-associated oxyradicals in layer silicates

The most common aluminum-associated oxyradicals in layer silicates are the so-called ‘‘B-centers’’ in kaolinite. Angel *et al*. (1974) first observed a ‘‘B-center’’ in X-ray irradiated kaolinite by room-temperature EPR and suggested it to be related to Al^{3+} occupying a Si^{4+} position. Meads and Malden (1975) determined its ^{27}Al hyperfine constant to be 21.3 MHz by EPR spectra at 140 K. Hall (1980) suggested that ‘‘B-centers’’ formed by an Al^{3+} ion replacing Si^{4+} with two distinct

configurations: one as ^{IV}Al-O^{-}-Si with $g_{//}$ = 2.028, $g_{\perp}$ = 1.988 and the other being ^{IV}Al-O^{-}-^{VI}Al with $g_{//}$ = 2.047 and an uncertain $g_{\perp}$ value. Clozel *et al*. (1994, 1995) and Götze *et al*. (2002) argued for a model involving two neighboring Al nuclei, whereas Köksal *et al*. (2004) favored the former model but reported somewhat different principal g and A values for ‘‘B-centers’’. ‘‘B-centers’’ are known to be stable up to ~300 °C (Angel *et al*., 1974; Jones *et al*., 1974; Meads & Malden, 1975). Clozel *et al*. (1994) also noted the stability of ‘‘B-centers’’ depends on the initial concentration and temperatures of EPR measurements.

It is noteworthy that the initial proposals of ‘‘B-centers’’ with substitutional Al at a tetrahedral site (Angel *et al*., 1974; Meads & Malden 1975; Hall, 1980) were based exclusively on similar centers in quartz and silicate glasses. Our results show that oxyradicals associated with Al at octahedral sites have similar in principal g and A values to those with Al at tetrahedral sites (see also Yu *et al*., 1995; Dias *et al*., 2009). Therefore, principal g and A values from powder EPR spectra cannot be used to discriminate aluminum-associated oxyradicals at tetrahedral or octahedral sites.

Clozel *et al*. (1995), in their comprehensive study of ‘‘B centers’’ in kaolinite, reported X- and Q-band powder spectra measured at 77 and 150 K, including those from the oriented film technique. These spectra show that the B center consists of three groups of 11 lines with intensity ratios of 1:2:3:4:5:6:5:4:3:2:1 and has one of its principal axes perpendicular to the ab plane of the kaolinite layers. Clozel *et al*. (1995) interpreted the 11-line features to represent a hyperfine structure arising from interaction with two equivalent ^{27}Al nuclei and dismissed the previously reported

^{IV}Al-O^{-}-Si and ^{IV}Al-O^{-}-^{VI}Al models. Clozel *et al*. (1995) proposed a ^{VI}Al-O^{-}-^{VI}Al model but was uncertain whether it forms from irradiation resulting in charge imbalance by the occurrence of a vacancy or impurities in the octahedral or tetrahedral layers. Also, Clozel *et al.* (1995) was unable to determine whether the hole trapping oxygen is one of the two oxygen atoms or one of the four hydroxyl oxygen atoms, all of which are coordinated to an octahedral Al atom. On the basis of the present study, we suggest that ‘‘B-centers’’ in kaolinite form from hole trapping on hydroxyl oxygen atoms after the removal of proton. Particularly, proton removal associated with ionization of hydroxyl groups makes the remaining oxygen atom an ideal candidate for hole trapping (see also Dias *et al*., 2009; Mao *et al*., 2010). Moreover, this hole-trapping oxygen atom in kaolinite is now sufficiently different from the two oxygen atoms and the three hydroxyl oxygen atoms of the Al octahedron, which is required for limited hole hopping and detection of this center at room temperature. It is noteworthy that the Al-O^{-} center in prehnite shares similarities in thermal behavior, including the second-order decay kinetics, with the ‘‘B-centers’’ in kaolinite (*e.g.*, dependence of decay on the initial concentration; Clozel *et al*., 1995). It remains unclear, however, whether one or all four of the hydroxyl oxygen atoms participate in the formation of the ‘‘B-centers’’ in kaolinite.

To the best of our knowledge, the only previous single-crystal EPR study on aluminum-associated oxyradicals in layer silicates is Novozhilov *et al*. (1969), who reported two O^{-} centers in irradiated, synthetic fluorphlogopite with a minor substitution of Al^{3+} for Mg^{2+} at the octahedral site. One of their proposed O^{-} centers is

characterized by a g_{min} value of 2.008(3) and a 10-line hyperfine structure along the crystallographic c axis. Novozhilov *et al*. (1969) interpreted the 10-line hyperfine structure to arise from interaction with an ^{27}Al and an ^{19}F nuclei and suggested this center to represent an O^- ion replacing an F^- ion linked to Al^{3+} atethe octahedral site. However, Novozhilov *et al*. (1969) were unable to quantitatively determine the **g** matrix or the ^{27}Al and ^{19}F hyperfine constants of this proposed Al-O^- center. It is plausible that the precursor in synthetic fluorphlogopite also involved a substitution of OH^- for F^- linked to Al^{3+} at the octahedral site and that the Al-O^- center formed from hole trapping on the hydroxyl oxygen after removal of the proton during irradiation.

4.5 Conclusions

Combined CW-EPR and pulsed ENDOR studies, together with isochronal and isothermal annealing experiments, allow a detailed characterization of a new Al-O^- center in γ-ray irradiated prehnite. This radiation-induced center has been shown to form from hole trapping on a hydroxyl oxygen atom coordinated to Al in the octahedral sites. Results from this center in prehnite provide support for Clozel *et al*. (1995)'s ^{VI}Al-O^--^{VI}Al model for radiation-induced B-centers in kaolinite and suggest them to most likely form from hole trapping on the hydroxyl oxygen atoms as well.

4.6 References

ADRIAN, F.J., JEITE, A.N., SPAETH, J.M. (1985): Theory of indirect hyperfine interactions of oxygen-aluminum defects in ionic crystals. *Phys. Rev. B*, **31**, 3923–3931.

AHMED, F., BELT, R. F., AND GASHUROV, G. (1986): Infrared study of $KTiOPO_4$ single crystals hydrothermally grown in H_2O and D_2O solutions. *Journal of Applied Physics*. **60**, 839-841.

ALLARD, T. & CALAS, G. (2009): Radiation effects on clay mineral properties. *Appl. Clay Sci.*, **43**, 143–149.

ALLARD, T., ILDEFONSE, P., PEREZ DEL VILLAR, L., SORIEUL, S., PELAYO, M., BOIZOT, B., BALAN, E., & CALAS, G. (2003) Radiation-induced defects in dickites from the EL Berrocal granitic system (Spain): relation with past occurrence of natural radioelements. *European Journal of Mineralogy*. **15**, 629-640.

ALLARD, T., & MULLER J. (1998): Kaolinite as an in situ dosimeter for past radionuclide migration at the Earth's surface. *Applied Geochemistry.* **13**, 751-765.

ANGEL, B. R., JONES, J. P. E., & HALL, P. L. (1974): Electron spin resonance studies of doped synthetic kaolinite. I. *Clay Minerals*. **10**, 247-255.

BALCIC-ŽUNIĆ, T., ŠĆAVNIĆAR, S. & MOLIN, G. (1990): Crystal structure of prehnite from Komiža. *European Journal of Mineralogy.* Vol. **2**, 731-734.

BAUR, W.H., JOSWIG, W., KASSNER, D. & HOFMEISTER, W. (1990): Prehnite: structural similarity of the monoclinic and orthorhombic polymorphs and their Si/Al ordering. *Journal of Solid State Chemistry.* **86**, 330-333.

BOTIS, S. M. & PAN, Y. (2009): Theoretical modeling of the Al paramagnetic center and its precursors in stishovite. Phys. Chem. Minerals (in press; available online)

CLARIDGE, R. F. C., MACKLE, K. M., SUTTON, G. L. A., & TENNANT, W. C. (1994): 10 K EPR of an oxygen-hole aluminum center, $[AlO_4]^0$, in x-irradiated zircon, $ZrSiO_4$. *Journal of Physics: Condense Matter*. **6**, 10415-10422.

CLOZEL, B., ALLARD, T., & MULLER, J. P. (1994): Nature and stability of radiation-induced defects in natural Kaolinite: new results and a reappraisal of published works. *Clays and clay minerals*. **42**, 657-666.

CLOZEL, B., GAITE, J. M., & MULLER, J. P. (1995): Al-O^--Al paramagnetic defects in kaolinite. *Physics and chemistry in minerals*. **22**, 351-356.

DA SILVA, D. N., GUEDES, K. J., PINHEIRO, M. V. B., SPAETH, J. M., & KRAMBROCK, K. (2005): The microscopic structure of the oxygen-aluminum hole center in natural and neutron irradiated blue topaz. *Physics and chemistry of minerals*. **32**, 436-441.

DETRIE, T.A., ROSS, N.L., ANGEL, R.J., & WELCH, M.D. (2008): Crystal chemistry and location of hydrogen atoms in prehnite. *Mineral. Mag.*, **72**, 1163–1179.

DIAS, L.N., PINHEIRO, M.V.B., & KRAMBROCK, K. (2009): Radiationinduced defects in euclase: formation of O^- hole and Ti^{3+} electron centers. *Phys. Chem. Minerals*, **36**, 519–525.

GEMPERLE, C. & SCHWEIGER, A. (1991): Pulsed electron-nuclear double resonance methodology. *Chem. Rev.*, **91**, 1481–1505.

GÖTZE, J., PLÖTZE, M., GÖTTE, TH., NEUSER, R. D., & RICHTER, D. K. (2002) Cathodoluminescence and electron paramagnetic resonance studies of clay minerals. *Mineralogy and petrology*. **76**, 195-212.

HALL, P. L. (1980): The application of electron spin resonance spectroscopy to studies of clay minerals: I. isomorphous subsitutions and external surface properties. *Clay minerals*. **15**, 321-335.

IKEYA, M. (1993): New applications of electron paramagnetic resonance: ESR dating, dosimetry, and spectroscopy. World Scientific, Singapore.

JONES, J. P. E., ANGEL, B. R., & HALL, P. L. (1974): Electron spin resonance studies of doped synthetic kaolinite. II. *Clay Minerals*. **10**, 257-270.

KÖKSAL, F., KOSEOGLU, R., SAKA, I., BASARAN, E., & SENER, F. (2004): Electron paramagnetic resonance of natural and gamma-irradiated alunite and kaolin mineral powders. *Radiation effects & Defects in solids*. **159**, 393-398.

KRAMBROCK, K., PINHEIRO, M .V. B., GUEDES, K. J., MEDEIROS, S. M., SCHWEIZER, S. & SPAETH, J. -M. (2004): Correlation of irradiation-induced yellow color with the O^- hole center in tourmaline. Physics and Chemistry of Minerals, **31**: 168-175.

LUNSFORD, J.H. (1973): ESR of adsorbed oxygen species. *Catal. Rev.*, **8**, 135–157.

MAO, M. & PAN, Y. (2009): Radiation-induced defects in apophyllites. I. The NH_2 free radical in fluorapophyllite. *Eur J Mineral*. **21**, 317-324.

MAO, M., NILGES, M.J. & PAN, Y. (2010): Radiation-induced defects in apophyllites. II. An O^- centre and O^-−O^- pairs in hydroxylapophyllite. *Eur. J. Mineral.*, **22**, 89-102.

MEADS, R. E. & MALDEN P. J. (1975): Electron spin resonance in natural kaolinites containing Fe^{3+} and other transition metal ions. *Clay minerals*. **10**, 313-345.

MOMBOURQUETTE, M.J., WEIL, J.A., & MCGAVIN, D. (1996): EPR–NMR users' manual, Department of Chemistry, University of Saskatchewan, Saskatoon, Saskatchewan.

MORICHON, E., ALLARD, T., BEAUFORT, D., & PATRIER, P. (2008): Evidence of native radiation-induced paramagnetic defects in natural illites from unconformity-type uranium deposits. *Physics and chemistry of minerals*. **35**, 339-346.

MOSSER, C., BOUDEULLE, M., WEBER, F., & PACQUET, A. (1996): Ferriferous and vanadiferous kaolinites from the hydrothermal alteration halo of the cigar lake uranium deposit (Canada). *Clay Minerals*. **31**, 291-299.

NOVOZHILOV, A.I., SAMOILOVICH, M.I., SERGEEV-BOBR, A.A. & ANIKIN, I.N. (1969): EPR in irradiated fluorphlogopite. *Zhur. Struk. Knim*. **10**, 45-453.

NUTTALL, R.H.D. & WEIL, J.A. (1981): The magnetic properties of the oxygen-hole aluminum centers in crystalline SiO_2. I. $[AlO_4]^0$. *Can. J. Phys.*, **59**, 1696–1708.

PAN, Y. & HU, B. (2009): Radiation-induced defects in quartz. IV. Thermal properties and implications. *Phys. Chem. Minerals*, **36**, 421-430.

PAN, Y., MAO, M. & LIN, J. (2009): Single-crystal EPR study of Fe^{3+} and VO^{2+} in prehnite from the Jeffrey mine, asbestos, Quebec. *Can. Mineral*., **47**, 1013-1025.

PAPIKE, J.J. & ZOLTAI, T. (1965): Ordering of tetrahedral aluminum in prehnite $Ca_2(Al,Fe^{+3})[Si_3AlO_{10}](OH)_2$. *Am. Mineral*. **52**, 974-984.

PENG, S.-T., CHOU, K.-D. & TANG, Y.-C. (1959): The structure of prehnite. *Acta Chim. Sinica* **25**, 56-63.

PETROV, I, AGEL, A, & HAFNER, S. S. (1989): Distinct defect centers at oxygen positions in albite. *Am. Mineral.* **74**, 1130-1141.

PLÖTZE, M., KAHR, G., & HERMANNS STENGELE, R. (2003): Alteration of clay minerals – gamma-irradiation effects on physicochemical properties. *Appl. Clay Sci.*, **23**, 195–202.

PREISINGER, A. (1965): Prehnit – ein neuer Schichtsilikattyp. *Tschermaks Mineral. Petrogr. Mitt.*, **10**, 491–504.

THEIS, W. M., NORRIS, G. B., & PORTER, M. D. (1985): High resolution infrared measurements of the OH- bands in KTiOPO4. *Applied Physics Letters*. **46**, 1033-1035.

WEIL, J.A. & BOLTON J.R. (2007): Electron paramagnetic resonance: elementary theory and practical applications. Wiley-Interscience, John Wiley & Sons Inc., New York, 664 p.

YU, J., LEE, C., LIU, K., LIU, C., HUANG, Y., PAYNE, D. A., & LII, K. (1995): Electron paramagnetic resonance study of an Al-associated oxygen hole center in $KTiOPO_4$: Al crystals. *Journal of Physics and Chemistry in Solids*. **56**, 233-240.

ZHAO, W.-Y., LIU, X.-W., WANG, Q.-Y. & ZHANG, Q.-J. (2003): Space symmetry of prehnite, $Ca_2Al^{[6]}[Si_3AlO_{10}](OH)_2$, from the Tieshan iron mineral deposit, *Central China. Mineral. Mag.*, **67**, 73–77.

Chapter 5

Hemimorphite as a natural sink for arsenic in zinc deposits and related mine tailings: Evidence from single-crystal EPR spectroscopy and hydrothermal synthesis

Hemimorphite is a refractory mineral in surface environments and occurs commonly in supergene non-sulfide Zn deposits and Zn mine tailings. Single-crystal electron paramagnetic resonance (EPR) spectra of gamma-ray-irradiated hemimorphite from Mapimi (Durango, Mexico) reveal two arsenic-associated oxyradicals: $[AsO_4]^{4-}$ and $[AsO_4]^{2-}$. Inductively coupled plasma mass spectrometry analyses confirm this sample to contain 270 ppm As and that hemimorphite from other Zn deposits has appreciable amounts of arsenic as well. Spin Hamiltonian parameters, including matrices **g**, **A**(^{75}As) and **P**(^{75}As), show that the $[AsO_4]^{4-}$ radical formed from electron trapping by a locally uncompensated $[AsO_4]^{3-}$ ion substituting for $[SiO_4]^{4-}$. Matrices **g**, **A**(^{75}As) and **P**(^{75}As) of the $[AsO_4]^{2-}$ radical show it to have the unpaired spin on the bridging oxygen of an $[AsO_4]^{3-}$ ion at a Si site and linked to a monovalent impurity ion. This structural model for the $[AsO_4]^{2-}$ radical is further supported by observed ^{29}Si and ^{1}H superhyperfine structures arising from interactions with a single Si atom and two equivalent H atoms, respectively. Hydrothermal

experiments at 200 °C and ~9.5 MPa show that hemimorphite contains up to ~2.5 wt% As_2O_5 and suggest that both the arsenate concentration and the pH value in the solution affect the As content in hemimorphite. These results demonstrate that hemimorphite is capable of sequestering arsenate in its crystal lattice, hence is a natural sink for attenuating As in supergene non-sulfide Zn deposits and Zn mine tailings. Moreover, results from hemimorphite potentially have more far-reaching implications for major silicates such as zeolites in the immobilization and removal of arsenic in surface environments.

5.1 Introduction

Arsenic has long been the subject of intense research, because it is one of the most common and highly toxic contaminants in surface environments, including those associated with mining activities and metallurgical processes (Nriagu, 1994; Foster *et al*., 1998; Courtin-Nomade *et al*., 2009; Walker *et al*., 2009). Numerous studies have demonstrated that the mobility and bioavailability of As are usually closely related to its host phases (*i.e*., minerals in many cases; Foster *et al*., 1998; Courtin-Nomade *et al*., 2009; Walker *et al*., 2009). Therefore, significant efforts have been devoted to the identification and development of minerals (or their synthetic equivalents) that are capable of fixing or minimizing the mobility and bioavailability of As in the environment (*e.g*., Bothe and Brown, 1999; Di Benedetto *et al*., 2006; Blanchard *et al*., 2007; Fernández- Martínez *et al*., 2008; Lee *et al*., 2009; Drahota & Filipi, 2009).

As part of our ongoing study on radiation-induced defects in silicates (Mao & Pan, 2009; Pan *et al*., 2009; Mao *et al*., 2010), we have investigated gamma-ray irradiated hemimorphite by electron paramagnetic resonance (EPR) spectroscopy. EPR spectroscopy is a powerful and well-established technique for structural characterization of dilute paramagnetic species (*i.e*., those with at least one unpaired electron; Calas, 1988; Pan *et al*., 2002; Weil & Bolton, 2007). Hemimorphite, $Zn_4(Si_2O_7)(OH)_2{\bullet}H_2O$, is a common mineral (and often important ore) in the oxidized parts of zinc deposits (*i.e*., non-sulfide Zn deposits; Takahashi, 1960; Boni & Large, 2003; Hitzman *et al*., 2003; Coppola *et al*., 2008) and has been reported to occur in Zn mine tailings as well (Walder & Chavez, 1995; Day & Bowell, 2005;

Espiari *et al*., 2006; Schaider *et al*., 2007; Cabala *et al*., 2009). EPR spectra presented herein show for the first time that natural hemimorphite contains lattice-bound arsenate. This result is supported by compositional data of natural and synthetic hemimorphite from inductively coupled plasma mass spectrometry (ICPMS) and electron-microprobe analyses, respectively. These new structural, chemical and experimental results collectively demonstrate hemimorphite as a natural sink for As in Zn deposits and related mine tailings, and potentially have far-reaching implications for other silicates in the immobilization and removal of arsenic in surface environments.

Hemimorphite has attracted a large number of recent studies stemming from not only interesting features associated with its zeolite-like crystal structure containing a confined water molecule in the channel (Figure 5.1a; Libowitzky and Rossman, 1997; Libowitzky *et al*., 1997, 1998; Kolesov, 2006; Frost *et al*., 2007; Geiger & Dachs, 2009; Dachs & Geiger, 2009) but also its catalytic applications (Breuer *et al*., 1999; Yurieva *et al*., 2001; Catillon-Mucherie *et al*., 2007). The structure of hemimorphite (space group *Imm2*) consists of corner-sharing $Zn(OH)O_3$ and SiO_4 tetrahedra that have all of their apices aligned approximately along the crystallographic axis **c**, giving rise to its characteristic polar structure (Barclay & Cox, 1960; McDonald & Cruickshank, 1967; Hill *et al*., 1977; Takeuchi *et al*., 1978; Cooper *et al*., 1981; Libowitzky *et al*., 1998). Two zinc and one silicon tetrahedra are first linked to form rings, which in turn are linked in infinite sheets parallel to the (010) plane (McDonald & Cruickshank, 1967). Two neighboring SiO_4 tetrahedra are

linked by sharing the O4 atom to form the Si_2O_7 group (Figure 5.1b). The other three oxygen atoms (two O1 and one O2) of a SiO_4 tetrahedron are linked to two zinc atoms each (Figure 5.1b). The three basal Si–O bonds have approximately equal distances, whereas the apical Si–O2 bond is slightly longer, forming a somewhat elongated SiO_4 tetrahedron (McDonald & Cruickshank, 1967). One of the three pseudo-tetrad axes of this SiO_4 "quasi-tetrahedron" is oriented along $\theta = \sim 55°$ and $\varphi = \sim 90°$, where θ and φ are tilting angles relative to crystallographic axes **c** and **a**, respectively. The direction of the apical Si–O2 bond is ($\theta = 7.9°$, $\varphi = 270°$). The basal bonds Si–O1 and Si–O4 are oriented at (65°, 25°) and (75°, 270°), respectively (*cf*., Hill *et al*., 1977). The silicon atoms are located in mirror planes, whereas the zinc atoms are at general positions.

5.2 Samples and experimental techniques

5.2.1. Samples and trace element analyses

Ten samples of hemimorphite from the University of Saskatchewan reference mineral collection (Table 5.1) were first examined by reconnaissance EPR spectroscopy before and after gamma-ray irradiation. Gamma-ray irradiations of these samples were made at room temperature in a ^{60}Co cell, for doses ranging from 200 to 20,000 Gray (*i.e*., 0.2 to 20 kGy). The sample from the Mapimi Ag–Pb–Zn mine (Durango, Mexico; #1 in Table 5.1) was selected for detailed single-crystal EPR measurements, because its reconnaissance spectra had the best signal-to-noise ratios. All ten samples (Table 5.1) were also analyzed for trace elements by inductively

coupled plasma mass spectrometry (ICPMS), using the HF–HNO_3 dissolution method, at the Department of Geological Sciences, University of Saskatchewan.

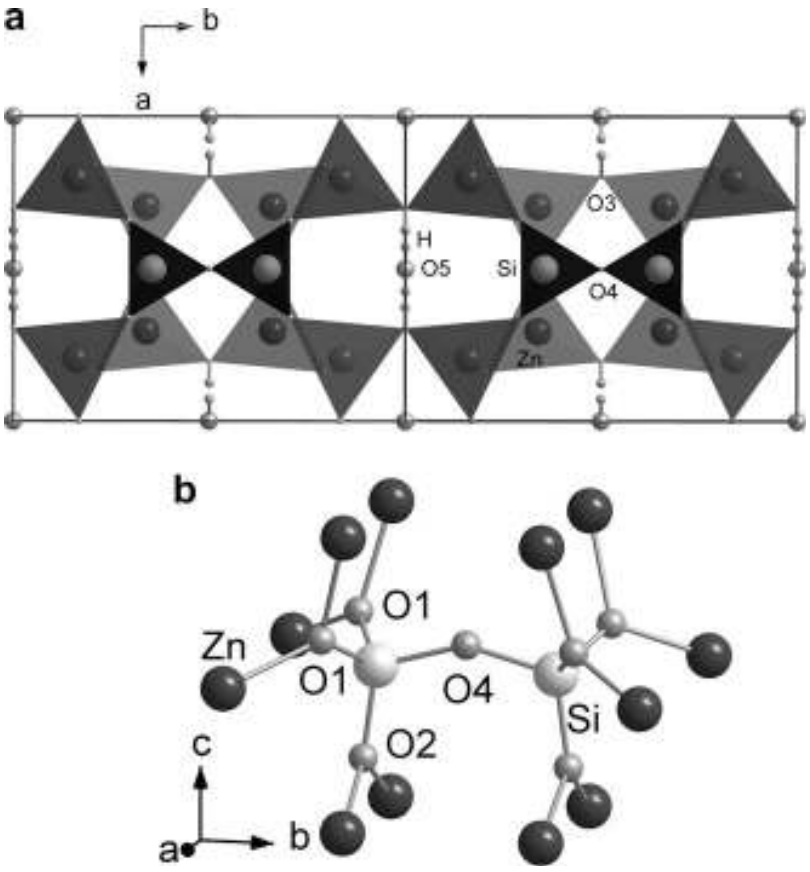

Figure 5.1 (a) Crystal structure of hemimorphite projected to the (001) plane; (b) linkage of the Si_2O_7 group and its neighboring Zn atoms; also included is the molecular H_2O in the channel. Labels of the oxygen atoms after Hill *et al*. (1977).

5.2.2 EPR measurements

All EPR spectra were measured on a Bruker EMX spectrometer at the Saskatchewan Structure Sciences Centre, which is equipped with an automatic frequency controller, a high-sensitivity ER4119 cavity, and a home-made goniometer. The coordinate system selected for single-crystal EPR spectral measurements and

analyses has the experimental axes **x**, **y** and **z** parallel to the crystallographic axes **a**, **b** and **c**, respectively. Reconnaissance single-crystal EPR spectra were made for each crystal before and after gamma-ray irradiation, with the magnetic field B parallel to **c** (Figure 5.2a). Two crystals irradiated at ~1 and ~20 kGy were then chosen for detailed single-crystal EPR measurements in three orthogonal rotation planes [*i.e.*, plane xz approximately parallel to the {010} cleavage, and yz and xy parallel to the (100) and (001) crystal faces; see results of angle corrections below]. This crystal irradiated to a total dose of ~1 kGy was taken out of the ^{60}Co cell for measurements at intermediate doses of ~0.2, 0.4 and 0.6 kGy. Also, this crystal was re-measured after storage at room temperature for 18 days.

Experimental conditions for single-crystal EPR measurements at room temperature (~290 K; Table 5.2) included a microwave frequency of ~9.36 GHz and ~9.61 GHz and a microwave power of ~20 mW and 63 mW for wide and narrow scans (see below), respectively, a modulation frequency of 100 kHz, and a modulation amplitude of 0.06 mT. Both crystals irradiated at ~1 and 20 kGy were measured in a wide magnetic field range from 80 to 520 mT and a resolution of ~0.107 mT (*i.e.*, 4096 data points over 440 mT), while the crystal having a dose of ~1 kGy was also measured in a narrow range from 334 to 348 mT and a resolution of ~0.014 mT (1024 points over 14 mT). Calibration of the magnetic field was made by use of α,γ-bis-diphenylene-β-phenyl allyl (BDPA) in benzene (g = 2.0027) as a standard.

5.2.3 Hydrothermal synthesis

Natural hemimorphite in laterites generally occurs as extremely fine-grained aggregates (*e.g.*, McPhail *et al*., 2004; Coppola *et al*., 2008), whereas its epigenetic counterpart is known to form millimeter-sized or larger crystals. Accordingly, we conducted our synthesis experiments of hemimorphite at 200 °C and ~9.5 MPa to produce suitable crystals for electron-microprobe analysis to investigate factors controlling the incorporation of As in this mineral.

Three series of hydrothermal syntheses were made using Zn powder from Alfar Aesar, natural quartz and $NaH_2AsO_4 \cdot 7H_2O$ (Alfar Aesar) as starting materials (Table 5.3). These materials were used without further purification. Series I had a constant initial pH value of 12 but variable Zn:Si:As atomic ratios from 2:1:1 to 64:32:1. Series II used a constant Zn:Si:As atomic ratio of 2:1:1 but variable initial pH values from 0 to 14. Series III had the same range of initial pH values from 0 to 14 but a uniform Zn:Si:As atomic ratio of 16:8:1. These mixtures in ~10 mL deionized water, after their initial pH values were adjusted by use of KOH and HNO_3, were loaded into 23 mL acid digestion bombs (Parr Instrument Company). These bombs were heated to 200 °C and held there for 48 h. The water volume of 10 mL in these 23 mL bombs at 200 °C corresponds to a pressure of ~9.5 MPa. In addition, reconnaissance experiments using the same starting materials, Zn:Si atomic ratios from 16:1 to 1:1 and initial pH values from 2 to 12 have been attempted at room temperature and atmospheric pressure for durations up to one month, but were not successful in producing hemimorphite.

Solid products from each experiment were recovered by washing in deionized water and air dried. They were first examined on a petrographic microscope and then measured for powder X-ray diffraction (PXRD) patterns by using a Rigaku R200 diffractometer with CuKα1 radiation (k = 1.54056 Å) at 40 kV and 30 mA. Subsequently, the solid products were embedded in epoxy and polished for back-scattered electron imaging and quantitative wavelength-dispersive-spectrometry analysis on a JEOL JXA-8600 superprobe at the Department of Geological Sciences, University of Saskatchewan. Analytical conditions included 15 kV accelerating voltage, 10 nA beam current, 1–2 μm beam size, counting times of 30 s (Zn and Si) and 90 s (As), and Zn metal (Zn), GaAs (As) and quartz (Si) as standards.

5.3 Results

5.3.1 Crystals and compositions of natural hemimorphite

Selected crystals of hemimorphite from Mapimi are approximately 3 x 3 x 1 mm in dimension and are characterized by a perfect {010} cleavage and well-developed (100) and (001) faces. They are colorless both before and after gamma-ray irradiation. Duplicate ICPMS analyses yielded closely comparable abundances for all elements analyzed for, including Al (728 and 756 ppm), As (269 and 271), Ca (7250 and 7020), Cd (26 and 26), Cu (357 and 351), Fe (67 and 63), Ga (82 and 81), Mg (27 and 30), Pb (1.9 and 2.0), Sb (9.1 and 9.2), Ti (36 and 32) and W (4.1 and 3.9). Other trace elements analyzed for (Li, Rb, Cs, Ba, Sr, Mn, Cr, Co, Ni,

Sc, V, Be, Bi, Ge, Sn, P,Y, Zr, Hf, Nb, Ta, Tl, Mo, Th, U and rare-earth elements) are below 1 ppm.

Other samples of hemimorphite investigated in this study also contain millimeter-sized crystals, except that sample #8 is composed of fine-grained aggregates as encrustation (Table 5.1). These samples were chosen not only to represent hemimorphite from diverse Zn deposits but also allow easy mineral separation for ICPMS analyses. Crystals in samples #2 and #3 are similar in appearance to those in sample #1 but have notably lower contents of As (Table 5.1). Two samples from the El Potosi Ag–Pb–Zn mine (Chihuahua, Mexico) also have different As contents. Samples of hemimorphite from other Zn and Zn–Pb–Cu deposits (Franklin and Sterling Hill, New Jersey; Evelyn Mine, Pine Creek, Australia; M'Fouati, Reneville, Congo) all contain appreciable amounts of arsenic as well (Table 5.1). Other notable trace elements in these samples are Cu, Pb and Cd (up to 1295, 1280 and 51 ppm, respectively; Table 5.1).

Table 5.1 Summary of hemimorphite samples investigated in this study.

No.	Location	As (ppm)	Cu (ppm)	Pb (ppm)	Cd (ppm)
1	Mapimi, Durango, Mexico	269 (271)	357 (351)	1.9 (2.0)	26 (26)
2	Durango, Mexico	6	765	1280	51
3	Durango, Mexico	127	936	36	<0.11
4	El Potosi, Chihuahua, Mexico	36	1200	390	4.39
5	El Potosi, Chihuahua, Mexico	18	1030	89	0.49
6	Evelyn Mine, Pine Creek, Australia	39	1000	70	11
7	Franklin, New Jersey, USA	200	760	3.7	1.59
8	Sterling Hill, New Jersey, USA	275	570	31	4.68
9	79 Mine, Gila Co., Arizona, USA	79	1295	163	39
10	M'Fouati, Reneville, Congo	338	669	436	2.59

5.3.2 Single-crystal EPR spectra of natural hemimorphite

Two previous EPR studies of natural hemimorphite reported the following paramagnetic centers: Cu^{2+}, Mn^{2+}, Fe^{3+} and E' (Vassilikou-Dova and Eftaxias, 1991; Gallegos *et al*., 2009). These centers, except for E', have been observed in samples of hemimorphite examined by our reconnaissance EPR measurements. Single-crystal EPR spectra of the as-is hemimorphite from Mapimi (not shown), however, contain only a broad Fe^{3+} peak at the effective g value of ~4.28.

Single-crystal EPR spectra of gamma-ray irradiated hemimorphite from Mapimi, measured at **B**//**c** and 290 K, reveal the presence of two quartets (*i.e*., each with four peaks of approximately equal intensities), in addition to the broad Fe^{3+} peak at the effective g value of ~4.28 (Figure 5.2a). One quartet is characterized by large and unequal separations from ~80 to 200 mT (Figure 5.2a), whereas the other has small separations of ~2 mT (Figure 5.2a and b). Measurements of one crystal immediately after each step of gamma-ray irradiation show that these quartets are well resolved with a dose of as little as 0.2 kGy and grow in intensity almost linearly with increasing dose to 1 kGy, whereas the Fe^{3+} center is unaffected by irradiation (Figure 5.3). Re-measurements of this crystal after storage at room temperature for 18 days show that both quartets exhibit significant degrees of decay, but the Fe^{3+} center remains the same (Figure 5.3). Step-wise irradiation of another crystal yielded similar trends up to ~2 kGy, where the narrow quartet reaches saturation and starts to decrease with further irradiation. Assuming a steady-state rate of decay, the half

lives for the wide- and narrow-quartets are estimated to be ~21 and 29 days, respectively.

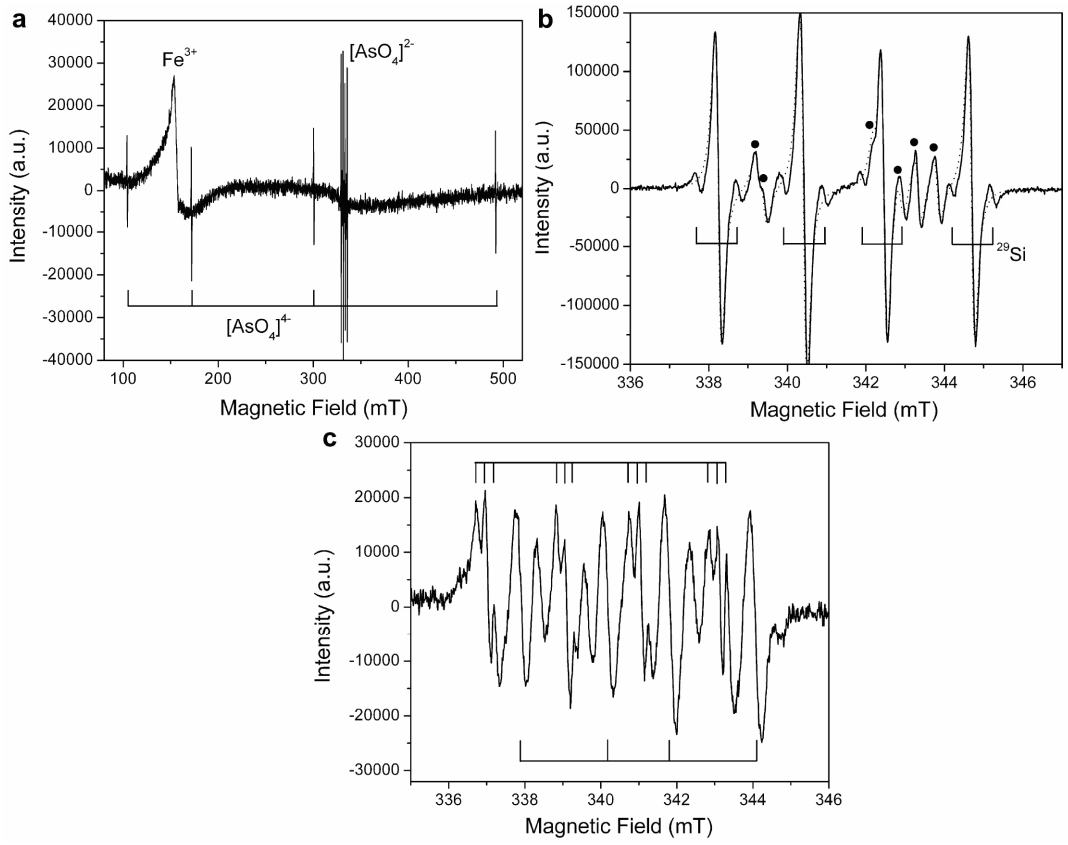

Figure 5.2 Representative single-crystal EPR spectra of γ-ray irradiated hemimorphite: (a) a wide-scan spectrum at **B**//**c** and microwave frequency v = 9.36 GHz illustrating the presence of a broad Fe^{3+} peak at g = ~4.28 and the two quartets belonging to the $[AsO_4]^{4-}$ and $[AsO_4]^{2-}$ radicals; (b) a narrow-scan spectrum at **B**//**c** and v = 9.61 GHz illustrating the $[AsO_4]^{2-}$ radical; also shown for comparison is a simulated spectrum (dotted) including lines of "forbidden transitions" (marked by black circles) in excellent agreement with the observed spectrum (solid). A pair of satellite peaks (marked) accompanying each of the four main absorptions lines belongs to a ^{29}Si superhyperfine structure; (c) a narrow-scan spectrum at **B**^**b** = 10° and v = 9.61 GHz illustrating that the $[AsO_4]^{2-}$ radical is resolved into two magnetically nonequivalent sites (marked) and that one set of the quartet is further split into three lines each with an intensity ratio of ~1:2:1. Additional lines present

are attributable to “forbidden transitions”.

The quartet with large and unequal separations is attributable to a center with an electron spin S = 1/2 interacting with a nucleus of I = 3/2 and a natural isotope abundance of ~100%, and a large hyperfine constant. This quartet is resolved into four sets in both (001) and (010) planes but only two sets in the (100) plane (Figure 5.4), indicative of four magnetically nonequivalent sites (*i.e.*, a triclinic site symmetry in the orthorhombic hemimorphite; Rae, 1969). The average linewidth of this quartet is ~0.3 mT. The presence of As from ICPMS analyses, together with the fitted spin Hamiltonian parameters (see below), allows us to identify this quartet to represent the $[AsO_4]^{4-}$ radical (*cf.*, Dalal *et al.*, 1972, 1977).

The narrow quartet is also attributable to a simple spin S = 1/2 interacting with an ~100% naturally abundant nucleus of I = 3/2. This quartet, which has an average linewidth of ~0.3 mT as well, is resolved in to a maximum of only two sets in the (010) plane (Figure 5.5), indicating a monoclinic site symmetry (Rae, 1969). We interpret this quartet to represent the $[AsO_4]^{2-}$ radical (*i.e.*, an arsenic-associated hole center; Edwards *et al.*, 1968; Subramanian *et al.*, 1977). Interestingly, this $[AsO_4]^{2-}$ radical in hemimorphite is characterized by the common presence of extra weak lines. For example, a pair of weak satellite peaks with a separation of ~1 mT accompanying each of the main absorption lines are clearly resolved at **B**//**c** (Figure 5.2b). Spectral simulations confirm that these satellite peaks have almost uniform intensities of ~2.5% of their respective main lines and, hence, are best explained by a ^{29}Si superhyperfine structure (*i.e.*, interaction with a single ^{29}Si nucleus with I = 1/2 and

natural isotope abundance of 4.7%). Roadmaps (Figure 5.5) show that separations of the main lines vary significantly, indicative of a considerable nuclear quadrupole effect. Some weak lines (*e.g.*, Figure 5.2b) are attributable to this nuclear quadrupole effect (see below). In addition, each of four main lines for two magnetically equivalent sites of this radical at **B^b** ≈ 10° in the xz plane is resolved into three lines with an intensity ratio of ~1:2:1 (Figure 5.2c), which are interpreted to represent a ^{1}H superhyperfine arising from interaction with two equivalent (or nearly equivalent) hydrogen atoms (see below).

5.3.3 Spin Hamiltonian parameters of the $[AsO_4]^{4-}$ and $[AsO_4]^{2-}$ radicals

The numbers of line-position data for the ^{29}Si and ^{1}H superhyperfine structures of the $[AsO_4]^{2-}$ radical (Figure 5.2b and c), unfortunately, are inadequate for quantitative analyses. Therefore, the spin Hamiltonian for both $[AsO_4]^{4-}$ and $[AsO_4]^{2-}$ radicals, which involve a single unpaired electron (S = 1/2) and a ^{75}As hyperfine structure (I = 3/2), can be written as:

$$H = \beta_e \mathbf{B}^T \bullet \mathbf{g} \bullet \mathbf{S} + \mathbf{I}^T \bullet \mathbf{A} \bullet \mathbf{S} - \beta_n \mathbf{B}^T \bullet g_n \bullet \mathbf{I} + \mathbf{I}^T \bullet \mathbf{P} \bullet \mathbf{I} \quad \text{.....(5.1)}$$

where β_e and β_n are the electronic (Bohr) and nuclear magneton, respectively; and an isotropic g_n value of 0.959647 is adopted for ^{75}As (Weil and Bolton, 2007). The parameters to be optimized are matrices **g**, **A** and **P**. Iterative fittings for both radicals, using the software package EPR–NMR (Mombourquette *et al.*, 1996), were made first by inclusion of only matrices **g** and **A**, and were accompanied by steps of

angle corrections. Matrix **P** was added in the final stage and was fitted together with **g** and **A**.

Table 5.2 Spin Hamiltonian parameters of $[AsO_4]^{4-}$ and $[AsO_4]^{2-}$ in hemimorphite at 290 K.

	Matrix **Y**			k	Principal value (Y_k) Y_k	Principal direction θ (˚)	φ (˚)	RMSD (mT)
				$[AsO_4]^{4-}$				
g	2.00489(4)	−0.00021(6)	0.00007(4)	1	2.00490(4)	90.2(5)	357.5(8)	
		1.99959(4)	0.00259(4)	2	2.00130(4)	56.3(3)	88(1)	
			1.99740(3)	3	1.99568(4)	33.6(3)	267.9(6)	0.074
$\mathbf{A}/g_e\beta_e$ (mT)	121.89(1)	0.20(1)	0.22(1)	1	131.43(1)	51.2(2)	87.7(2)	
		126.92(1)	5.57(1)	2	121.88(1)	89.9(2)	357.6(2)	
			124.44(1)	3	119.97(1)	141.2(2)	87.4(4)	
$\mathbf{P}/g_e\beta_e$ (mT)	0.13(1)	−0.01(2)	0.02(1)	1	0.35(1)	135.0(9)	100(7)	
		−0.07(1)	−0.42(1)	2	0.13(1)	85(4)	185(3)	
			−0.06(1)	3	−0.48(1)	45.4(6)	90(2)	
				$[AsO_4]^{2-}$				
g	2.00982(1)	0.00000(1)	0.00000(1)	1	2.02407(1)	52.6(2)	270.0(2)	
		2.01641(1)	–0.01003(1)	2	2.00982(1)	89.9(2)	180.0(2)	
			2.01092(1)	3	2.00326(1)	142.6(2)	270.0(2)	0.026
$\mathbf{A}/g_e\beta_e$ (mT)	1.678(1)	0.000(1)	0.000(1)	1	2.158(1)	42.0(2)	270.0(3)	
		1.994(1)	–0.147(1)	2	1.861(1)	132.1(2)	270(1)	
			2.025(1)	3	1.678(1)	89.9(5)	0.0(5)	
$\mathbf{P}/g_e\beta_e$ (mT)	0.142(1)	0.000(1)	0.000(2)	1	0.142(1)	90(4)	360(1)	
		–0.229(1)	0.110(1)	2	0.121(1)	17.8(2)	90(16)	
			0.086(1)	3	–0.263(1)	72.1(2)	270.0(3)	

Results reported here are for one of four symmetrically equivalent sites in the rotation group D_2. Polar angle θ is relative to the crystallographic axis **c**, and azimuth angle φ is relative to axis **a**. (θ, φ) is equivalent to (180-θ, 180+φ).

A total of 1361 line-position data points from the widescan spectra were used for fitting the $[AsO_4]^{4-}$ radical. Of these, a few points from peaks that occur in the crossover regions of magnetically nonequivalent sites or overlap with those of other centers were assigned a weighing factor of 0.5, resulting in a sum of weighted factors of 1351. The final value of the root-mean-squares of weighted differences (RMSD) between the calculated and observed line positions is 0.074 mT, which is

only one third of the average linewidth of this radical. The calculated normals of the experimental yz and xy planes at (90.01°, 0.02°) and (0.8°, 168.5°), respectively, are close to the ideal normal directions of the (100) and (001) faces at (90°, 0°) and (0°, 180°), suggesting excellent crystal alignments for these two planes. The calculated normal of the xz plane at (86.5°, 88.1°), on the other hand, is ~4° away from the normal of the {010} cleavage at (90°, 90°). This misalignment makes the experimental "xz" plane essentially a general plane, where all four magnetically nonequivalent sites are resolved (Figure 5.4c). We emphasize that crystal misalignment has been corrected for during data analysis and, therefore, is not expected to contribute significant errors to the fitted spin Hamiltonian parameters (Table 5.2).

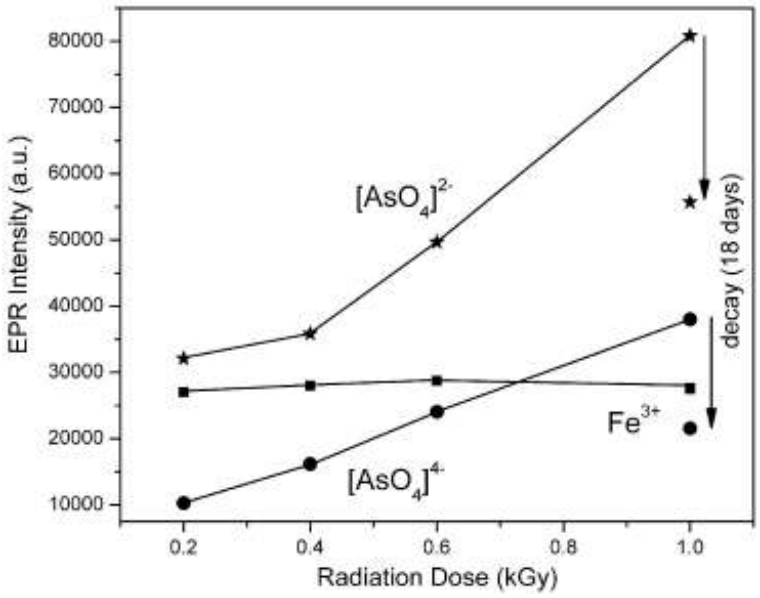

Figure 5.3 Intensities of the Fe^{3+} center and the $[AsO_4]^{4-}$ and $[AsO_4]^{2-}$ radicals as a function of gamma-ray radiation dose. Also shown are the intensities of these centers after 1 kGy irradiation and then storage at room temperature for 18 days.

The most salient feature of the fitted matrix **g** for the $[AsO_4]^{4-}$ radical is that it deviates only slightly from an axial symmetry (Table 5.2). Matrix **A** is axial in symmetry as well, with the unique A_{max} axis at (51.3°, 87.7°) approximately coaxial with the g_{int} axis (Table 5.2). The nuclear quadrupole tensor P is two orders of magnitude smaller than the hyperfine constants and, therefore, is difficult to determine precisely. Nevertheless, one principal P axis oriented at (45.4°, 90°) is approximately coaxial with the g_{int} and A_{max} axes (Table 5.2).

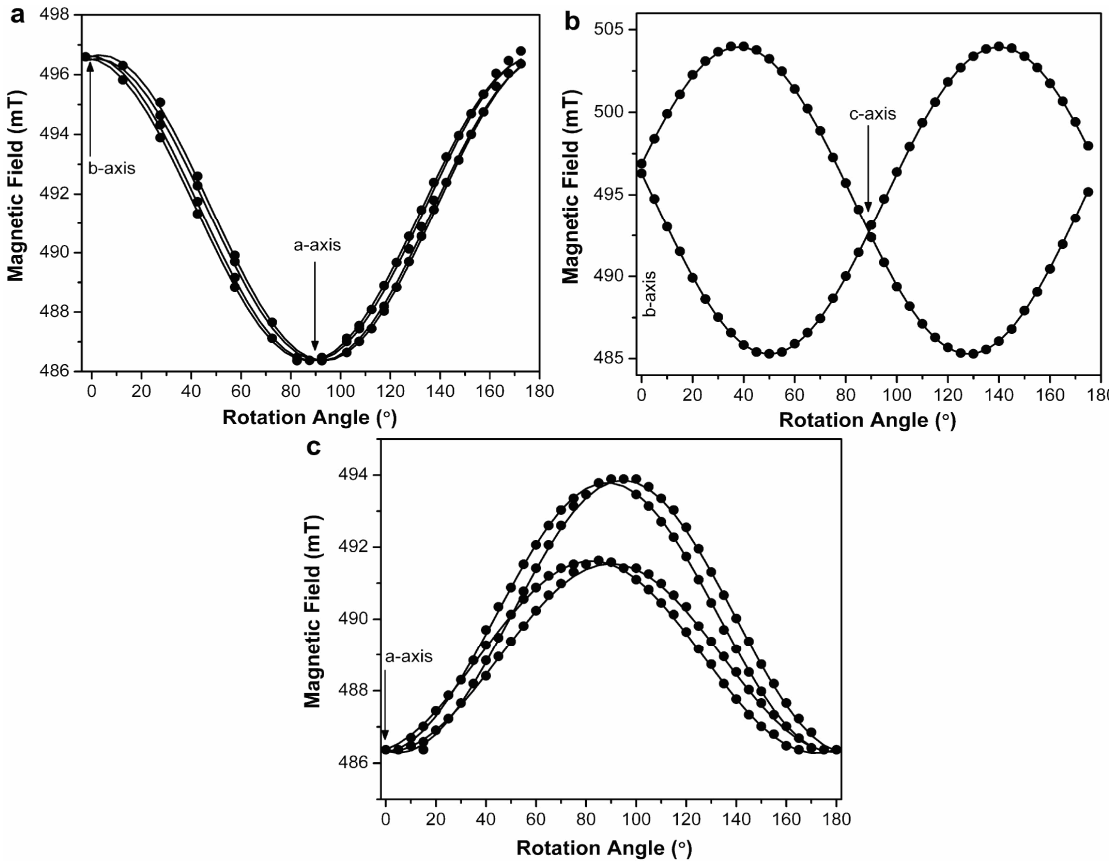

Figure 5.4 Line-position data points of the $[AsO_4]^{4-}$ radical (the highest-field hyperfine transition only) in hemimorphite as a function of rotation angles (*i.e.*, roadmaps; at a microwave frequency of 9.36 GHz): (a) experimental *xy* plane: **B**//(001), (b) *yz* plane: **B**//(100) and (c) *xz* plane: **B**//{010}; note that this plane has a crystal misalignment of ~4°.

A total of 1776 line-position data points from the main absorption lines in the narrow-scan spectra were used for fitting the $[AsO_4]^{2-}$ radical. Again, data points for lines that occur in the crossover regions of magnetically nonequivalent sites or overlap with those of other centers were assigned a weighing factor of 0.5, yielding a sum of weighted factors of 1759. Angle corrections yielded the normals of the experimental yz, xz and xy planes at (89.99°, 0.02°), (89.99°, 90.00°) and (0.00°, 17.58°), respectively, all close to perfect crystal alignments. The final RMSD value between calculated and measured line-position data is 0.026 mT (Table 5.2).

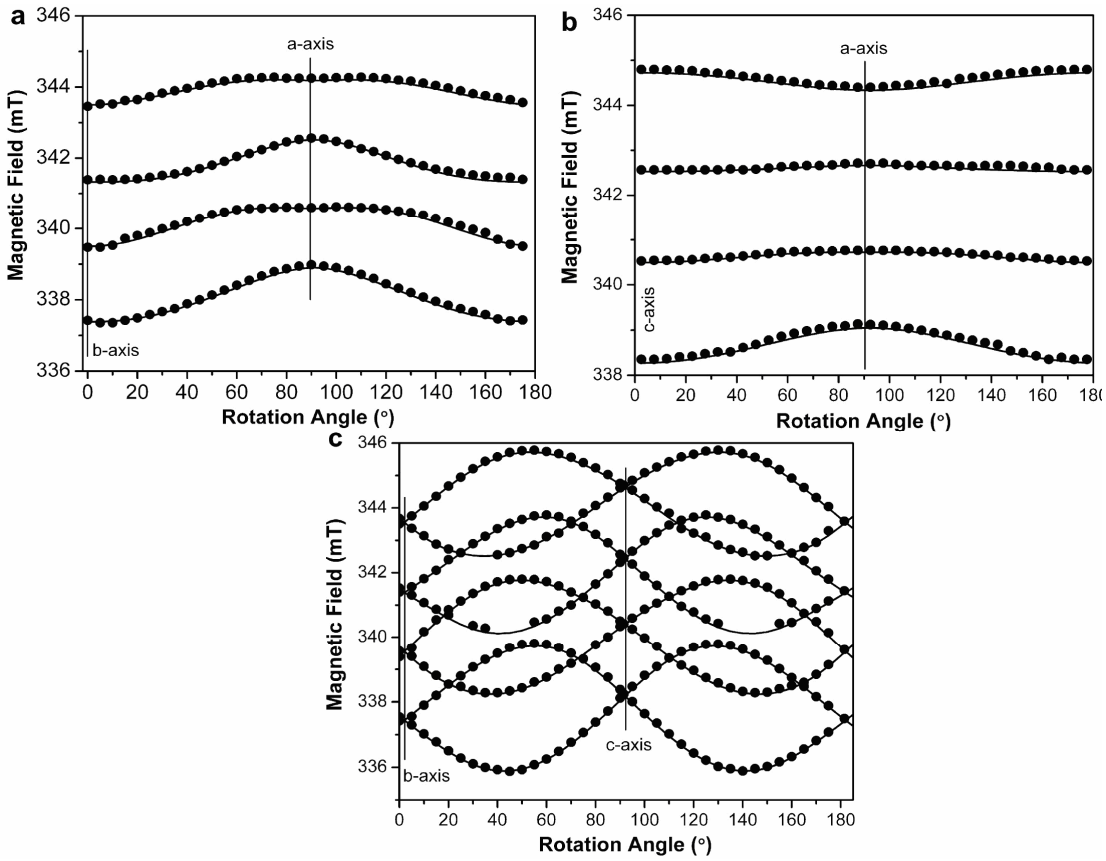

Figure 5.5 Line-position data points of the $[AsO_4]^{2-}$ radical (the main absorption lines only) in hemimorphite as a function of rotation angles (*i.e.*, roadmaps; at a microwave frequency of 9.61 GHz): (a) experimental *xy* plane: **B**//(001), (b) *xz* plane: **B**//{010} and (c) *yz* plane: **B**//(100).

Matrices **g** and **A** of the $[AsO_4]^{2-}$ radical are characterized by approximately coaxial g_{max} and A_{max} axes (Table 5.2). The fitted principle P values of this radical (Table 5.1) are ~10% of the hyperfine constants (Table 5.2). The unique P_{min} axis is also in the same plane with the g_{max} and A_{max} axes (Table 5.2) and is only 3° away from the Si–O4 bond direction in the hemimorphite structure. Spectral simulations confirm that these spin Hamiltonian parameters (including the nuclear quadrupole tensor), fitted from the main absorption lines, make excellent predictions for the "forbidden transitions" ($m_I \neq 1$) in the observed spectra (*e.g.*, Figure 5.2b).

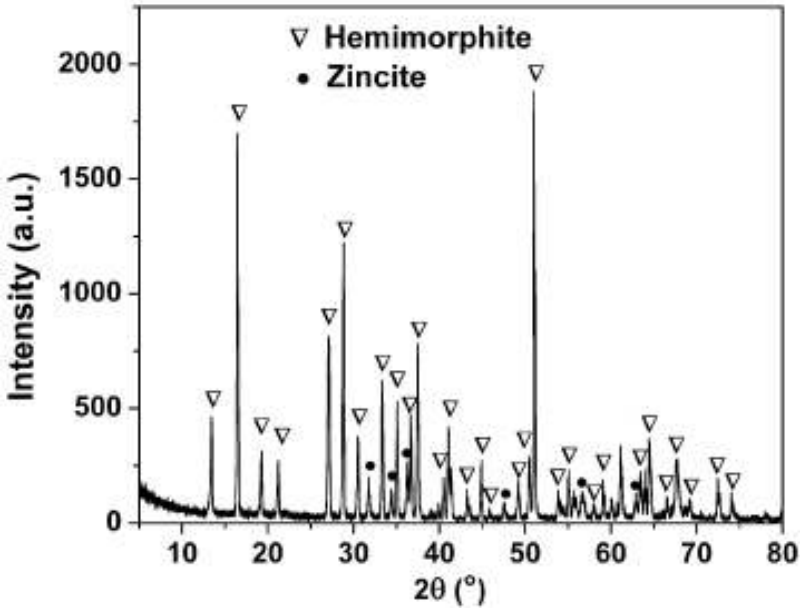

Figure 5.6 Representative PXRD pattern of solid products from synthesis experiments at 200 °C and ~9.5 MPa (run #14; Table 5.3).

5.3.4 Synthetic hemimorphite

Powder X-ray diffraction (PXRD) patterns (Figure 5.6) confirm optical examinations that the solid products from Series I experiments all contain

hemimorphite and zincite (plus unreacted quartz in low-As runs; Table 5.3). Series II experiments produced hemimorphite and zincite at initial pH values ≥ 8, a mixture of adamite [$Zn_2AsO_4(OH)$], hemimorphite and zincite at the initial pH value of 6, but only adamite and zincite at initial pH values ≤ 4 (Table 5.3). Similarly, hemimorphite appears only in Series III at initial pH values ≥ 4 (Table 5.3). It is noteworthy that the final pH values of all experiments are higher than their respective initial values (Table 5.3).

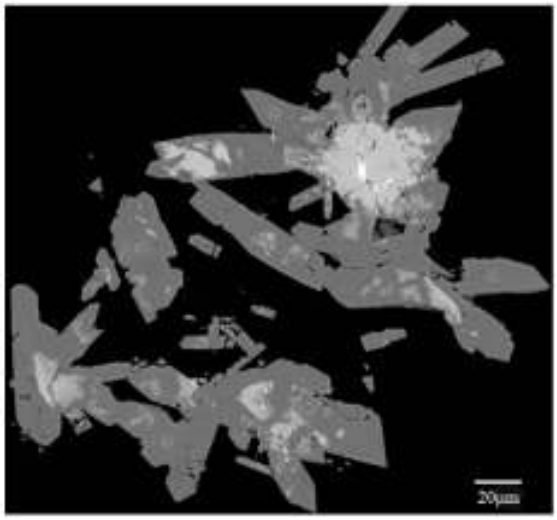

Figure 5.7 Representative back-scattered electron image illustrating euhedral hemimorphite crystals with zincite (light grey) and unreacted Zn (white) from run #4 (Table 5.3).

Hemimorphite occurs as euhedral platy crystals that sometimes contain zincite as inclusions (occasionally unreacted Zn as well; Figure 5.7). Individual crystals of hemimorphite from the As-rich runs are only ~10–30 μm in the maximum dimension, but up to 120 μm in the As-poor runs. Notable exceptions are

runs #10 of Series II and #17 and #18 of Series III (Table 5.3), in which hemimorphite crystals are invariably smaller than 1 μm in width, making them difficult for quantitative electron-microprobe analysis.

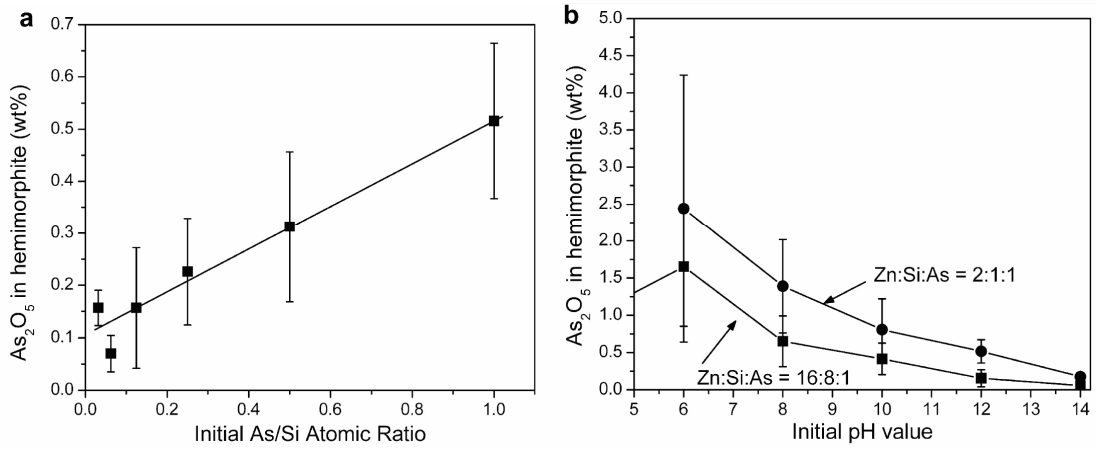

Figure 5.8 As contents in synthetic hemimorphite: (a) as a function of the Si/As atomic ratio in the starting materials from Series I experiments and (b) as a function of the initial pH values from Series I, II and III experiments. Error bars represent standard deviations.

Electron-microprobe analyses show that the As contents in hemimorphite from Series I experiments vary considerably in a given run (*i.e.*, standard deviation as large as 70% of the average value; Table 5.3). This variation is unlikely to be an analytical artifact, because analyses using a defocused beam (~10 μm) to minimize dehydration related to beam damage yielded similar ranges of As values. It is noteworthy that the measured As content in hemimorphite of Series I correlates positively with the As/Si value in the starting materials (Figure 5.8a). Similarly, the measured As contents in hemimorphite from Series II and III experiments show large variations as well, which are at least partly attributable to analytical difficulties related to small crystal sizes in

runs #10, #17 and #18. For example, one analysis of hemimorphite from run #10 yielded an anomalous value of 5.11 wt% As_2O_5, whereas other analyses from this same run gave 1–2 wt% As_2O_5. Generally, the measured As contents in hemimorphite from Series II show a negative correlation with the initial pH values (Figure 5.8b). A similar trend is also apparent for hemimorphite from Series III, except for that from run #18 (Figure 5.8b).

Table 5.3 Hydrothermal synthesis of hemimorphite at 200 °C and ~9.5 MPa.

Run#	Starting materials (g)			pH		Solid product	Composition*
	Zn	SiO2	$NaH_2AsO_4•7H_2O$	Before	After		
Series I (Zn:Si:As atomic ratio from 2:1:1 to 64:32:1 and initial pH = 12)							
1	0.1307	0.0608	0.312	12	13	Hem+Zct	0.516 ± 0.148
2	0.1307	0.0604	0.156	12	13	Hem+Zct	0.312 ± 0.144
3	0.1307	0.0613	0.078	12	13	Hem+Zct+Qtz	0.227 ± 0.102
4	0.1307	0.0611	0.039	12	13	Hem+Zct+Qtz+Zn	0.157 ± 0.115
5	0.1307	0.0610	0.0195	12	13	Hem+Zct+Qtz	0.069 ± 0.034
6	0.1307	0.0610	0.0098	12	13	Hem+Zct+Qtz	0.157 ± 0.034
Series II (Zn:Si:As atomic ratio = 2:1:1 and initial pH from 14 to 0)							
7	0.1307	0.0600	0.312	14	≥14	Hem+Zct	0.175 ± 0.055
8	0.1307	0.0611	0.312	10	11	Hem+Zct+Qtz	0.807 ± 0.414
9	0.1307	0.0609	0.312	8	11	Hem+Zct+Qtz	1.39 ± 0.62
10	0.1307	0.0604	0.312	6	9	Adm+Hem+Zct+Qtz	2.44 ± 1.83
11	0.1307	0.0607	0.312	4	6.8	Adm+Zct+Qtz	
12	0.1307	0.0598	0.312	2	5.5	Adm+Zct+Qtz	
13	0.1307	0.0604	0.312	0	3	Adm+Qtz	
Series III (Zn:Si:As atomic ratio = 16:8:1 and initial pH from 14 to 0)							
14	0.1307	0.0606	0.0390	14	≥14	Hem+Zct	0.056 ± 0.036
15	0.1307	0.0610	0.0390	10	13	Hem+Zct+Qtz	0.415 ± 0.211
16	0.1307	0.0610	0.0390	8	12	Hem+Zct+Qtz	0.65 ± 0.34
17	0.1307	0.0605	0.0390	6	12	Hem+Zct+Qtz	1.65 ± 0.80
18	0.1307	0.0600	0.0390	4	12	Hem+Zct+Qtz	0.95 ± 0.51
19	0.1307	0.0611	0.0390	2	5	Adm+Zct+Qtz	
20	0.1307	0.0609	0.0390	0	2	Qtz	

* The As content in hemimorphite (average ± standard deviation) on the basis of 3–10 spot analyses in each run. *Abbreviations*: Hem, hemimorphite; Adm, adamite; Zct, zincite; Qtz, residual quartz and Zn, residual Zn.

5.4 Discussion

5.4.1 Structures and formation of the $[AsO_4]^{4-}$ and $[AsO_4]^{2-}$ radicals in hemimorphite

The $[AsO_4]^{4-}$ radical in hemimorphite is similar in principal g and A values to its well-established counterparts in other crystalline hosts (*e.g.*, Dalal *et al.*, 1972, 1977; Murty *et al.*, 1977). This radical has been shown to have the un-paired spin localized largely on the central As atom, resulting in its large ^{75}As hyperfine constants (Table 5.2). The reported matrices **g** and **A** of the $[AsO_4]^{4-}$ radicals are also known to have approximately axial symmetry, with their unique g and A axes being coaxial along a pseudo-symmetry axis of the $[AsO_4]^{4-}$ polyhedron. The g_{int}, A_{max} and P_{min} axes of the $[AsO_4]^{4-}$ radical at (60°, 90°), (50°, 90°) and (45°, 90°), respectively, are all close to one pseudo-tetrad axis of the SiO_4 tetrahedron in hemimorphite at (55°, 90°), supporting a location of this radical at a Si site. Indeed, a locally uncompensated $[AsO_4]^{3-}$ ion substituting for a $[SiO_4]^{4-}$ group results in one positive net charge, hence is an excellent trap for an electron during gamma-ray irradiation. The observed triclinic symmetry of this radical in hemimorphite suggests that the As atom, unlike the original Si site, is not in a mirror plane. This distortion is probably attributable to differences between the $[AsO_4]^{3-}$ and $[SiO_4]^{4-}$ groups, with or without the effect of a charge-compensating ion. Alternatively, this observed symmetry reduction may be related to trapping of the unpaired electron, which is known to cause local structural distortion relative to the diamagnetic precursors (Botis & Pan, 2009).

Similarly, the fitted principal g and A values for the arsenic-associated hole center are closely comparable to those of the $[AsO_4]^{2-}$ radical in $CaWO_4$, which has been interpreted to have the unpaired electron largely on an oxygen atom (Edwards *et al*., 1968; Subramanian *et al*., 1977). The $[AsO_4]^{2-}$ radical in hemimorphite is most likely associated with $[AsO_4]^{3-}$ ions at the Si site as well, because they are unlikely to substitute for the $[ZnO_3(OH)]^{5-}$ groups owing to differences in both valence states and ionic radii between As^{5+} and Zn^{2+}. In addition, the fitted g_{max} and A_{max} axes (Table 5.2) are all in the same plane with the Si, O2 and O4 atoms and are approximately along the Si–O4 bond direction, suggesting that the unpaired electron is localized on the O4 atom (Figure 5.2). Moreover, the observed monoclinic symmetry of this radical suggests that distortion must have occurred largely on the O4 and the As atoms and can account for the angles between the g_{max} and A_{max} axes (Table 5.2) and the Si–O4 bond. Similarly, the $[AsO_4]^{2-}$ radical in $(NH_4)_2HPO_4$, which has more orthorhombic ^{75}As hyperfine constants, has been reported to involve a significant distortion and hence no correlation between principal g axes and the P–O bond directions in the host lattice (Subramanian *et al*., 1977).

The large nuclear quadrupole effect exhibited by the $[AsO_4]^{2-}$ radical in hemimorphite (Table 5.2) has not been reported for this radical in the literature. The nuclear quadrupole coupling tensor P, which is a sensitive measure of the electric field gradients about the ^{75}As nucleus, provides further evidence that the $[AsO_4]^{2-}$ radical in hemimorphite involves a localization of the unpaired spin on the O4 atom and the location of the As atom in a symmetry plane.

This structural model for the $[AsO_4]^{2-}$ radical in hemimorphite is further supported by the observed ^{29}Si and ^{1}H superhyperfine structures (Figure 5.2b and c). For example, the observed magnitude of ^{29}Si superhyperfine splitting at ~1 mT (Figure 5.2b) is similar to that reported for the well-established $[AlO_4]^0$ center in quartz (Nuttall & Weil, 1981) and supports the presence of a nearest-neighbor Si atom (Figure 5.1). Also, the O4 atom has two equivalent hydrogen atoms at ~3.5 Å (Figure 5.1). On the basis of the dipole–dipole model (Mao *et al*., 2010), this distance is consistent with the observed 1H superhyperfine splitting of ~0.3 mT (Figure 5.2c).

The formation of the $[AsO_4]^{2-}$ radical in $CaWO_4$ has been attributed to hole trapping by an $[AsO_4]^{3-}$ ion substituting for the $[WO_4]^{2-}$ group (Edwards *et al*., 1968). Our experiments show clearly that the $[AsO_4]^{2-}$ radical in hemimorphite is induced by irradiation as well. As mentioned above, however, a locally uncompensated $[AsO_4]^{3-}$ ion substituting for $[SiO_4]^{4-}$ is an electron trap and, therefore, is unlikely to form the $[AsO_4]^{2-}$ radical by itself. Also, the $[AsO_4]^{2-}$ radical in hemimorphite is unlikely to be a V_k type center (*i.e*., hole trapping on an oxygen atom of an $[AsO_4]^{3-}$ ion next to a cation vacancy) for the following three reasons. First, the $[AsO_4]^{2-}$ radical has a nearestneighbor Si atom as indicated by the observed ^{29}Si superhy-perfine structure (Figure 5.2b). Second, a Zn vacancy results in the O1(x2), O2 and O3 atoms with a dangling bond each and, therefore, can not explain the apparent hole trap on the O4 atom. Third, Subramanian *et al*. (1977) and Murty *et al*. (1977) reported V_k type centers $[AsO_4. \ . \ .PO_4]^{5-}$ in irradiated arsenate-doped

phosphates $Na_2HPO_4 \bullet 7H_2O$ and KH_2PO_4, which have the unpaired spin shared by the AsO_4 and PO_4 groups and are characterized by significantly different ^{75}As hyperfine constants.

A more plausible explanation for the formation of the $[AsO_4]^{2-}$ radical in hemimorphite involves an $[AsO_4]^{3-}$ ion next to a monovalent cation substituting for Zn^{2+}. For example, ICPMS data suggest a coupled substitution of the type:

$$Cu^{+} + As^{5+} = Zn^{2+} + Si^{4+} \quad \text{.....(5.2)}$$

This substitution yields a neutral entity $[CuO_3(OH)][AsO_4][SiO_4]$, which may then lead to hole trapping on the O4 atom during gamma-ray irradiation. In this type of configurations, ^{63}Cu (I = 3/2 and 69.2%) and ^{65}Cu (I = 3/2 and 30.8%) superhyperfine structures are expected to be small and thus unresolved in the experimental EPR spectra. Alternatively, other unknown monovalent cations may be responsible for the above substitution.

5.4.2 Factors affecting the incorporation of As in hemimorphite

Field observations (*e.g.*, Takahashi, 1960; McPhail *et al*., 2004; Coppola *et al*., 2008) have documented the formation of hemimorphite from the weathering of Zn-bearing minerals. Thermodynamic calculations by McPhail *et al*. (2006), using data determined from dissolution experiments at 50 and 80 °C, also predicted the stability of hemimorphite at 25 °C in slightly acidic to alkaline solutions at quartz saturation and dissolved Zn concentrations of 10^{-5} m (see also Takahashi, 1960). Therefore, the failure of our synthesis experiments at ambient conditions is probably

due to the low solubility of quartz at room temperature (Rimstidt, 1997) or other unknown kinetic factors. On the other hand, experiments at 200 °C and ~9.5 MPa show that hemimorphite readily forms in a wide range of initial Zn:Si:As atomic ratios and various initial pH values (Table 5.3).

Electron-microprobe results show that the As content in synthetic hemimorphite correlates positively with the As/Si value in the starting materials (Figure 5.8a). Results of Series II experiments show that the As content in hemimorphite increases with the final pH value decreasing from 14 to 9 (Figure 5.8b; Table 5.3). The results from Series III experiments are also consistent with this trend but are not as obvious owing to the small range of final pH values from 12 to 14 (Figure 5.8b; Table 5.3). These results suggest that both As concentrations and pH values exert significant controls on the incorporation of this element in hemimorphite. However, caution must be exercised in the interpretation of these data, because equilibrium is difficult to assess in these synthesis experiments.

5.4.3 Hemimorphite as a natural sink for As in Zn deposits and related mine tailings

Mineral-based techniques for the immobilization and removal of arsenic in surface environments, including mine tailings, can be divided into two types: (1) sorption of As-species on the surfaces of minerals and (2) sequestration of As-species in the crystal lattices of minerals. The latter includes both formation of relatively insoluble arsenates (*e.g.*, johnbaumite, $Ca_5(AsO_4)_3(OH)$, Bothe & Brown, 1999; Zhu

et al., 2006; scorodite, $Fe(AsO_4)•2H_2O$, Harvey *et al*., 2006; Bluteau & Demopoulos, 2007; beudantite, $PbFe(AsO_4)(SO_4)(OH)_6$, Drahota & Filipi, 2009) and isomorphous substitutions in common minerals (*e.g*., fluorapatite and hydroxylaptite, $Ca_5(PO_4)_3(F,OH)$, Lee *et al*., 2009; calcite, $CaCO_3$, Di Benedetto *et al*., 2006; pyrite, FeS_2, Blanchard *et al*., 2007; Lowers *et al*., 2007; gypsum, $CaSiO_4•2H_2O$, Fernández-Martínez *et al*., 2008; jarosite, $KFe(SO_4)_2(OH)_6$, Savage *et al*., 2005).

Our ICPMS results show that natural hemimorphite contains significant amounts of As (Table 5.1). Moreover, our single-crystal EPR analyses show accommodation of arsenate in the hemimorphite crystal lattice. These results are supported further by data from hydrothermal syntheses. Therefore, hemimorphite adds to the growing list of minerals as natural sinks for As. Moreover, the fact that hemimorphite is a refractory mineral with limited solubility at low temperatures (Takahashi, 1960; McPhail *et al*., 2006) makes it potentially important for attenuating As in surface environments.

Particularly, hemimorphite is often a major ore mineral (up to 40 modal%) in non-sulfide Zn deposits (Takahashi, 1960; Boni & Large, 2003; Hitzman *et al*., 2003; Balassone *et al*., 2008; Coppola *et al*., 2008). Therefore, the shear volume of this mineral makes it an important sink for As in these non-sulfide Zn deposits. Moreover, many non-sulfide Zn deposits are known to have formed from primary sulfide deposits via supergene processes (Hitzman *et al*., 2003; Balassone *et al*., 2008; Coppola *et al*., 2008). It is well-known that various toxic elements including As and Pb can be remobilized during weathering of sulfide orebodies (Takahashi,

1960; Courtin-Nomade *et al*., 2009 and references therein). Our results, together with available thermodynamic data (Takahashi, 1960; McPhail *et al*., 2006), suggest that hemimorphite plays an important role in sequestering As (and Pb; Table 5.1) during supergene alteration of Zn sulfide orebodies, particularly under slightly acidic to alkaline conditions.

In this context, the role of hemimorphite for sequestering As during the formation of supergene non-sulfide Zn ores at Silvermines (Irish Midlands; Balassone *et al*., 2008) can be evaluated as an example. The Zn–Pb–Ag deposits at Silvermines contain both primary sulfide and supergene non-sulfide ores (Balassone *et al*., 2008). Geochemical analyses by Balassone *et al*. (2008) showed that the As content in two drill holes is nearly constant at ~200 ppm from primary sulfide to non-sulfide ores. Therefore, As was probably not significantly remobilized during the weathering of sulfides at Silvermines. Balassone *et al*. (2008) showed that hemimorphite and smithsonite at Silvermines are the two dominant Zn-bearing minerals and are approximately equal in abundance, with the former being more abundant than the latter in the lower part of the non-sulfide orebody. If we take an average grade of 10 wt% Zn (Balassone *et al*., 2008), the non-sulfide ores at Silvermines then contain ~10 wt% hemimorphite and smithsonite each. On the basis of the observed As contents in synthetic hemimorphite (*i.e*., ignoring possible effects of temperature), it is apparent that hemimorphite can readily account for all As contents in the non-sulfide ores and, therefore, most likely played an important role

in attenuating As during the weathering processes of the primary sulfide ores at Silvermines.

Similarly, hemimorphite has been reported to occur in Zn mine tailings (Walder & Chavez, 1995; Day & Bowell, 2005; Espiari *et al*., 2006; Schaider *et al*., 2007; Cabala *et al*., 2009). Hemimorphite in Zn mine tailings may be classified into two types on the basis of its origin: (1) "residual" from the flotation extraction of sulfide ores and (2) neocrystallization in the tailings. In either case, incorporation of As in the hemimorphite lattice attenuates its mobility and bioavailability. Similarly, hemimorphite may play important roles in the transport and bioavailability of heavy metals (Pb, Cu and Cd) in Zn mine tailings (Table 5.1; Schaider *et al*., 2007; Cabala *et al*., 2009; Chen *et al*., 2009; Gallegos et al., 2009).

Moreover, the present recognition of arsenate in the hemimorphite lattice potentially has more far-reaching implications for the applications of major silicates (*e.g*., clay minerals and zeolites) for immobilization and removal of arsenic in surface environments. The advantages of silicates over carbonates, phosphates or sulfates, which themselves may pose adverse environmental impacts, include availability of raw materials, large stability, and low solubility in aqueous solutions. However, previous studies of clay minerals and zeolites for the immobilization and removal of arsenic focused on surface sorption (*e.g*., Manning & Goldberg, 1996, 1997; Li *et al*., 2007; Ruggieri *et al*., 2008; Šiljeg *et al*., 2009). Obviously, lattice incorporation in stable silicates is preferred over surface sorption for permanent immobilization and removal of arsenic. Our confirmation of arsenate in the

zeolite-like hemimorphite lattice, together with stereochemical similarities between the $[AsO_4]^{3-}$ and $[SiO_4]^{4-}$ groups, suggests that zeolites are potential hosts of arsenate in their crystal lattices. Interestingly, wide varieties of synthetic zincoarsenate and other arsenate analogues of zeolites are known in the literature (*e.g.*, Gier & Stucky, 1991; Bu *et al*., 1998; Jensen *et al*., 1998; Feng *et al*., 2001; Johnson *et al*., 2002). Therefore, further research should be conducted to evaluate and develop silicate zeolites for immobilization and removal of arsenate (and other arsenic species) in their crystal lattices.

5.5 Conclusions

Single-crystal EPR spectra of gamma-ray-irradiated hemimorphite reveal the presence of the $[AsO_4]^{4-}$ and $[AsO_4]^{2-}$ radicals, formed from $[AsO_4]^{3-}$ ions substituting for $[SiO_4]^{4-}$ during irradiation. These single-crystal EPR data, together with compositions of natural and synthetic samples, demonstrate that hemimorphite is capable of sequestering significant amounts of arsenate in its crystal lattice, representing an important natural sink for As (and heavy metals) in supergene non-sulfide Zn deposits and Zn mine tailings. Our results also raise the interesting question whether other silicates are capable of sequestering arsenate (and other arsenic species) in their lattices for effective immobilization and removal of arsenic in surface environments.

5.6 References

BARCLAY G.A., & COX E.G. (1960) The structure of hemimorphite. *Zeit. Kristal*. **113**, 23-29.

BALASSONE G., ROSSI M., BONI M., STANLEY G., & MCDERMOTT P. (2008) Mineralogical and geochemical characterization of nonsulfide Zn–Pb mineralization at Silvermines and Galmoy (Irish Midlands). *Ore Geol. Rev*. **33**, 168-186.

BLANCHARD M., ALFREDSSON M., BRODHOLT J., WRIGHT K., & CATLOW C.R.A. (2007) Arsenic incorporation into FeS2 pyrite and its influence on dissolution: A DFT study. *Geochim. Cosmochim. Acta* **71**, 624-630.

BLUTEAU M.-C., & DEMOPOULOS G.P. (2007) The incongruent dissolution of scorodite – Solubility, kinetics and mechanism. *Hydrometallurgy* **87**, 163-177.

BONI, M., & LARGE, D. (2003) Nonsulfide zinc mineralization in Europe: An overview. *Econ. Geol.* **98**, 715-729.

BOTHE J.V., & BROWN P.W. (1999) Arsenic immobilization by calcium arsenate formation. *Environ. Sci. Tech*. **33**, 3806-3811.

BOTIS S. M. & PAN Y. (2009) First-principles calculations on the $[AlO_4/M^+]^0$ (M = H, Li, Na, K) defects in quartz and crystal-chemical controls on the uptake of Al. *Mineral. Mag.* **73**, 537–550.

BREUER K., TELES J.H., DEMUTH D., HIBST H., SCHÄFER A., BRODE S., & DOMGÖRGEN H. (1999) Zinc silicates: Very efficient heterogeneous catalysts for the addition of primary alcohols to alkynes and allenes. *Angew. Chem. Intern. Ed*. ***38***, 1401-1405.

BU X., FENG P., GIER T.E., & STUCKY G.D. (1998) Two ethylenediamine-templated zeolite-type structures in zinc arsenate and cobalt phosphate systems. *J. Solid State Chem*. **136**, 210-215.

CABALA J., KRUPA P., & MISZ-KENNAN M. (2009) Heavy metals in mycorrhizal rhizospheres contaminated by Zn-Pb mining and smelting around Olkusz in southern Poland. *Water Air Soil Pollution* **199**, 139-149.

CATILLON-MUCHERIE S., AMMARI F., KRAFFT J-M., LAURON-PERNOT H., TOUROUDE R., & LOUIS C. (2007) Preparation of coimpregnated Cu−Zn/SiO_2 catalysts: Influence of the drying step on metallic particle size and on Cu0−ZnII interactions. *J. Phys. Chem. C* **111**, 11619–11626.

CHEN A., ZHAO Z., JIA X., LONG S., HUO G., & CHEN X. (2009): Alkaline leaching Zn and its concomitant metals from refractory hemimorphite zinc oxide ore. *Hydrometallurgy* **97**, 228-232.

COOPER B.J., GIBBS G.V., & ROSS F.K. (1981) The effects of heating and dehydration on the crystal structure of hemimorphite up to 600 °C. *Zeit. Kristal*. **156**, 305–321.

COPPOLA V., BONI M., GILG H.A., BALASSONE G., & DEJONGHE L. (2008) The "calamine" nonsulfide Zn-Pb deposits of Belgium: Petrographical, mineralogical and geochemical characterization. *Ore Geol. Rev*. **33**, 187-210.

COURTIN-NOMADE A., GROSBOIS C., MARCUS M.A., FAKRA S.C., BENY J.-M., & FOSTER A.L. (2009) The weathering of a sulfide orebody: Speciation and fate of some potential contaminants. *Canad. Mineral.* **47**, 493-508.

DACHS E. & GEIGER C. A. (2009) Heat-capacity behaviour of hemimorphite, $Zn_4Si_2O_7(OH)_2 \cdot H_2O$, and its dehydrated analogue $Zn_4Si_2O_7(OH)_2$: a calorimetric and thermodynamic investigation of their phase transitions. *Eur. J. Mineral.* **21**, 971–988.

DALAL N.S., DICKSON J.R., & MCDOWELL C.A. (1972) Electron paramagnetic resonance studies of X-irradiated KH_2AsO_4, KD_2AsO_4, Rb H_2AsO_4, Rb D_2AsO_4, Cs H_2AsO_4, $NH_4H_2AsO_4$, and $ND_4D_2AsO_4$ (ferroelectrics and antiferroelectrics). *J. Chem. Phys*. **57**, 4254-4265.

DALAL N.S., HEBDEN J.A., KENNEDY D.E., & MCDOWELL C.A. (1977) An EPR and ENDOR study of the low frequency fluctuations and cluster formation in the hydrogen bonded ferroelectrics KH_2PO_4 and $KD_2PO_4$and the antiferroelectrics $NH_4H_2PO_4$, and $ND_4D_2PO_4$. *J. Chem. Phys*. **66**, 4425-4432.

DAY S.J., & BOWELL R.J. (2005) Atypical and typical zinc geochemistry in a carbonate setting, Sä Dena Hes Mine, Yukon Territory, Canada. *Geochem. Explor. Environ. Analysis* **5**, 255-266.

DI BENEDETTO F., COSTAGLIOLA P., BENVENUTI M., LATTANZI P., ROMANELLI M., & TANELLI G. (2006) Arsenic incorporation in natural calcite lattice: Evidence from electron spin echo spectroscopy. *Earth Planet. Sci. Lett*. **246**, 458–465.

DRAHOTA P. & FILIPI M. (2009) Secondary arsenic minerals in the environment: a review. *Environ. Int.* **35**, 1243–1255.

EDWARDS P.R., SUBRAMANIAN S., & SYMONS M.C.R. (1968) Electron spin resonance studies of vanadate, niobate, phosphate, and arsenate in γ-irradiated calcium molybedate and calcium tungstate. *Chem. Commun*. 799.

ESPIARI S., RASHCHI F., & SADRNEZHAAD S.K. (2006) Hydrometallurgical treatment of tailings with high zinc content. *Hydrometallurgy* **82**, 54-62.

FENG P., ZHANG T., & BU X. (2001) Arsenate zeolite analogues with 11 topological types. *J. Amer. Chem. Soc.* **123**, 8608-8609.

FERNÁNDEZ-MARTÍNEZ A., CHARLET L., CUELLO G.J., JOHNSON M.R., ROMAN-ROSS G., BARDELLI F., & TURRILLAS X. (2008) Arsenate incorporation in gypsum probed by neutron, X-ray scattering and DFT modeling. *J. Phys. Chem*. **A112**, 5159-5166.

FOSTER A.L., BROWN G.E., TINGLE T.N., & PARKS G.A. (1998) Quantitative arsenic speciation in mine tailings using X-ray absorption spectroscopy. *Amer. Mineral*. **83**, 553-568.

FROST R.L., BOUZAID J.M., & REDDY B.J. (2007) Vibrational spectroscopy of the sorosilicate mineral hemimorphite $Zn_4(OH)_2Si_2O_7.H_2O$. *Polyhedron* **26**, 2405-2412.

GALLEGOS E.A., CANO N.F., WATANABA S., & CHUBACI J.D.F. (2009) Thermoluminescence, infrared reflectivity and electron paramagnetic resonance properties of hemimorphite. *Rad. Measur*. **44**, 11-17.

GEIGER C.A., & DACHS E. (2009) Quasi-ice-like C_p behavior of molecular H_2O in hemimorphite $Zn_4Si_2O_7(OH)_2.H_2O$: C_p and entropy confined H_2O in microporous silicates. *Amer. Mineral*. **94**, 634-637.

GIER T.E., & STUCKY G.D. (1991) Low-temperature synthesis of hydrated zinco(beryllo)-phospahte and arsenate molecular sieves. *Nature* **349**, 508-510.

HARVEY M.C., SCHREIBER M.E., RIMSTIDT J.D., & GRIFFITH M.M. (2006) Scorodite dissolution kinetics: Implications for arsenic release. *Environ. Sci. Tech*. **40**, 6709-6714.

HILL R.J., GIBBS G.V., CRAIG J.R., ROSS F.K., & WILLIAMS J.M. (1977) A neutron diffraction study of hemimorphite. *Zeit. Kristal*. **146**, 241–259.

HITZMAN M.W., REYNOLDS N.A., SANGSTER D.F., ALLEN C.R., & CARMAN C.E. (2003) Classification, Genesis, and Exploration Guides for Nonsulfide Zinc Deposits. *Econ. Geol*. **98**, 685-714.

JENSEN T.R., NORBY P., NØRLUND CHRISTENSEN A., & HANSON J.C. (1998) Hydrothermal synthesis, crystal structure refinement and thermal transformation of $LiZnAsO_4 \cdot H_2O$. *Micropor. Mesopor. Materials* **26**, 77-87.

JOHNSON C.D., MACPHEE D.E., & FELDMANN J. (2002) New low temperature synthetic route to an ammonium zinc arsenate zeolite analogue with an ABW-type structure. *Inorg. Chem*. **41**, 3588-3589.

KOLESOV B. (2006) Raman investigation of H_2O molecule and hydroxyl groups in the channels of hemimorphite. *Amer. Mineral*. **91**, 1355–1362.

LEE Y.J., STEPHENS P.W., TANG Y., LI W., PHILLIPS B.L., PARISE J.B. & REEDER R.J. (2009) Arsenate substitution in hydroxylapatite: Structural characterization of the $Ca_5(P_xAs_{1-x}O_4)_3OH$ solid solution. *Amer. Mineral*. **94**, 666-675.

LI Z., BEACHNER R., MCMANAMA Z., & HONG H. (2007) Sorption of arsenic by surfactant-modified zeolite and kaolinite. *Micropor. Mesopor. Materials* **105**, 291-297.

LIBOWITZKY E., KOHLER T., ARMBRUSTER, T., & ROSSMAN G.R. (1997) Proton disorder in dehydrated hemimorphite. IR spectroscopy and x-ray structure refinement at low and ambient temperatures. *Eur. J. Mineral*. **9**, 803-810.

LIBOWITZKY E., & ROSSMAN G.R. (1997) IR spectroscopy of hemimorphite between 82 and 373 K and optical evidence for a low-temperature phase transition. *Eur. J. Mineral*. **9**, 793-802.

LIBOWITZKY E., SCHULTZ A.J., & YOUNG D.M. (1998) The low-temperature structure and phase transition of hemimorphite, $Zn_4Si_2O_7(OH)_2 \bullet H_2O$. *Zeit. Kristal*. **213**, 659-668.

LOWERS H.A., BREIT G.N., FOSTER A.L., WHITNEY J.W., YOUNT J.C., UDDIN M. N., & MUNEEM A.A. (2007) Arsenic incorporation into authigenic pyrite, Bengal Basin sediment, Bangaldesh. *Geochim. Cosmochim. Acta* **71**, 2699-2717.

MAO M., & PAN, Y. (2009) Radiation-induced defects in apophyllites. I. The NH_2 free radical in fluorapophyllite. *Eur. J. Mineral*. **21**, 317-324.

MAO M., NILGES M.J., & PAN Y. (2010) Radiation-induced defects in apophyllites. II An O^- center and related O^-–O^- pairs in hydroxylapophyllite. *Eur. J. Mineral*. **22**, 89-102.

MANNING B.A., & GOLDBERG S. (1996) Modeling arsenate competitive sorption on kaolinite, montmorillonite and illite. *Clays Clay Minerals* **44**, 609-623.

MANNING B.A., & GOLDBERG S. (1997) Adsorption and stability of arsenic(III) at the clay mineral-water interface. *Environ. Sci. Tech*. **31**, 2005-2011.

MCDONALD W.S., & CRUICKSHANK D.W.J. (1967) Refinement of the structure of hemimorphite. *Zeit. Kristal*.**124**, 180-191.

MCPHAIL D.C., SUMMERHAYES E., JAYARATNE V., & CHRISTY A. (2006) Hemimorphite solubility and stability of low-T zinc minerals. *Geochim. Cosmochim. Acta* **70**, A414.

MCPHAIL D. C., SUMMERHAYES E., WELCH S. & BRUGGER J. (2004) The geochemistry and mobility of zinc in the regolith. In Advances in Regolith. CRC LEME, Canberra, pp. 287–291.

MOMBOURQUETTE M. J., WEIL J. A. & MCGAVIN D. G. (1996) EPR–NMR User's Manual. Department of Chemistry, University of Saskatchewan, Saskatoon, Saskatchewan, Canada.

MURTY P.N., MURTY C.R.K., & SUBRAMANIAN S. (1977) Electron paramagnetic resonance study of X-irradiated arsenate-doped phosphate: KH_2AsO_4/KH_2PO_4. *Phys. Stat. Sol*. **A39**, 675-682.

NRIAGU J. O. (1994) Arsenic in the Environment. Part I: Cycling and Characterization; Wiley Series in Advances in Environmental Science and Technology, **26**.

NUTTALL R. H. D. & WEIL J. A. (1981) The magnetic properties of the oxygen-hole aluminum centers in crystalline SiO_2, I. $[AlO_4]^0$. *Canad. J. Phys.* **59**, 1696–1708.

PAN Y., MAO M., & LIN J. (2009) Single-crystal EPR study of Fe^{3+} and VO^{2+} in prehnite from the Jeffrey mine, Asbestos, Quebec. *Canad. Mineral*. **47**, 933-945.

RAE A. D. (1969) Relationship between the experimental Hamiltonian and the point symmetry of a paramagnetic species in a crystal. *J. Chem. Phys.* **50**, 2672–2685.

RIMSTIDT J. D. (1997) Quartz solubility at low temperatures. *Geochim. Cosmochim. Acta,* **61**, 2553–2558.

RUGGIERI F., MARÍN V., GIMENO D., FERNANDEZ-TURIEL J.L., GARCÍA-VALLES M., & GUTIERREZ L. (2008) Application of zeolitic volcanic rocks for arsenic removal from water. *Engineering Geol.* **101**, 245-250.

SAVAGE K. S., BIRD D. K. & O'DAY P. A. (2005) Arsenic speciation in synthetic jarosite. *Chem. Geol.* **215**, 473–498.

SCHAIDER L.A., SENN D.B., BRABANDER D.J., MCCARTHY K.D., & SHINE J.P. (2007) Characterization of zinc, lead, and cadmium mine waste: Implications for transport, exposure and bioavailability. *Environ. Sci. Tech*. **41**, 4164-4171.

ŠILJEG M., CERJAN STEFANOVIĆ Š., MAZAJ M., NOVAK TUŠAR N., ARČON I., KOVAČ J., MARGETA K., KAUČIČ V., & ZABUKOVEC LOGAR N. (2009) Structure investigation of As(III)- and As(V)-species bound to Fe-modified clinoptilolite tuffs. *Micropor. Mesopor. Materials* **118**, 408-415.

SUBRAMANIAN S., MURTY P.N., & MURTY C.R.K. (1977) Epr studies of some arsenic and phosphorus oxyradicals. *J. Phys. Chem. Solids* **38**, 825-829.

TAKAHASHI T. (1960) Supergene alteration of zinc and lead deposits in limestone. *Econ. Geol*. **55**, 1083-1115.

TAKEUCHI, Y., SASAKI, S., JISWIG, W. & FUESS, H. (1978): X-ray and neutron diffraction study of hemimorphite. *Proceedings of Japan Acad.* **54**(Series B), 577-582.

VASSILIKOU-DOVA A.B., & EFTAXIAS K. (1991) Electron spin resonance of Mn^{2+} in hemimorphite. *Crystal Res. Tech*. **27**, 117-120.

WALDER I.F., & CHAVEZ W.X. JR. (1995) Mineralogical and geochemical behavior of mill tailing material produced from lead-zinc skarn mineralization, Hanover, Grant County, New Mexico, USA. *Environ. Geol*. **26**, 1-18.

WALKER S.R., PARSONS M.B., JAMIESON H.E., & LANZIROTTI A. (2009) Arsenic mineralogy of near-surface tailings and soils: influences on arsenic mobility and bioaccessibility in the Nova Scotia gold mining districts. *Canad. Mineral*. **47**, 533-556.

WEIL J. A. & BOLTON J. R. (2007) Electron Paramagnetic Resonance: Elementary Theory and Practical Applications. John Wiley & Sons, New York.

YURIEVA T.M., KUSTOVA G.N., MINYUKOVA T.P., POELS E.K., BLIEK A., DEMESHKINA M.P., PLYASOVA L.M., KRIEGER T.K., & ZAIKOVSKII V.I. (2001) Non-hydrothermal synthesis of copper-, zinc- and copper-zinc hydrosilicates. *Material Res. Innov*. **5**, 3-11.

ZHU Y.N., ZHANG X.H., XIE Q.L., WANG D.Q., & CHENG G W. (2006) Solubility and stability of calcium arsenates at 25°C. *Water, Air and Soil Pollution* **169**, 221-238.

Chapter 6

Nature of heavy metals in hemimorphite: A cation-exchange and single-crystal EPR study

Hemimorphite, a zeolite-like mineral commonly present in supergene non-sulfide Zn deposits and Zn mine tailings, is known to contain elevated contents of As, Cd, Cu and Pb. Cation-exchange experiments of a natural hemimorphite (Mapimi, Durango, Mexico) with 0.1 M $CaCl_2$ solution at 110 °C show that As and Cu are retained, whereas Cd and Pb are readily exchanged. The retention of As is consistent with previous single-crystal electron paramagnetic resonance (EPR) results that showed its occurrence as the substitutional As^{5+} ion at the Si site. Single-crystal EPR spectra of hemimorphite from the M'Fouati Pb-Zn mine (Reneville, Congo), measured at 120 K and 295 K, show a Cu^{2+} center. The best-fit spin Hamiltonian parameters **g**, **A**(^{63}Cu), **P** (^{63}Cu) and **A**(^{1}H) of this center at 120 K demonstrate that Cu^{2+} resides at the tetrahedral Zn site, not in the channels as suggested by a previous powder EPR study. Cadmium and Pb in hemimorphite are probably present in the channels; this would account for their contrasting behavior from As and Cu during the cation-exchange experiments. However, single-crystal EPR spectra of ten samples of hemimorphite, including those after gamma-ray

irradiation for doses up to 55 kGy, from various Pb-Zn deposits did not detect any paramagnetic Cd or Pb centers.

6.1 Introduction

Hemimorphite, ideally $Zn_4Si_2O_7(OH)_2 \bullet H_2O$, is a stable mineral in surface environments and occurs commonly in supergene non-sulfide Zn deposits and Zn mine tailings (Takahashi 1960, Boni & Large 2003; Coppola *et al*. 2008). Hemimorphite has attracted a large number of studies for its catalytic applications (Breuer *et al*. 1999; Yurieva *et al*. 2001; Catillon-Mucherie *et al*. 2007) and other interesting properties associated with its zeolite-like structure containing confined H_2O molecules in the channels (Libowitzky & Rossman, 1997; Libowitzky *et al*. 1997, 1998; Kolesov 2006; Frost *et al*. 2007; Geiger & Dachs 2009; Dachs & Geiger 2009; Cano *et al*. 2009; Bissengaliyeva *et al*. 2010; Seryotkin & Bakakin 2011). Another source of interest stems from the recognition of hemimorphite as a sink for As and heavy metals (Cd, Cu and Pb) in mine tailings and soils surrounding smelters (Walder & Chavez 1995; Day & Bowell 2005; Espiari *et al*. 2006; Schaider *et al*. 2007; Cabala *et al*. 2009; Mao *et al*. 2010).

Mao *et al*. (2010) reported that a suite of 10 samples of hemimorphite from Zn-Pb-Cu deposits contains 6 to 338 ppm As, <0.11 to 39 ppm Cd, 357 to 1200 ppm Cu and 1.9 to 1280 ppm Pb, whereas synthetic hemimorphite can contain up to 2.5 wt% As_2O_5. Single-crystal electron paramagnetic resonance (EPR) spectra of gamma-ray-irradiated hemimorphite revealed the presence of two arsenic-associated oxygen radicals $[AsO_4]^{4-}$ and $[AsO_4]^{2-}$, derived from substitutional $[AsO_4]^{3-}$ groups at the Si site, and provided unambiguous evidence for the sequestration of arsenate in its structure. Similarly, using powder EPR data, Gallegos *et al*. (2009) reported

paramagnetic Cu^{2+} and Pb^{3+} ions in natural and gamma-ray-irradiated hemimorphite, respectively, and interpreted them to reside at interstitial sites in the crystal structure on the basis of their ionic radii.

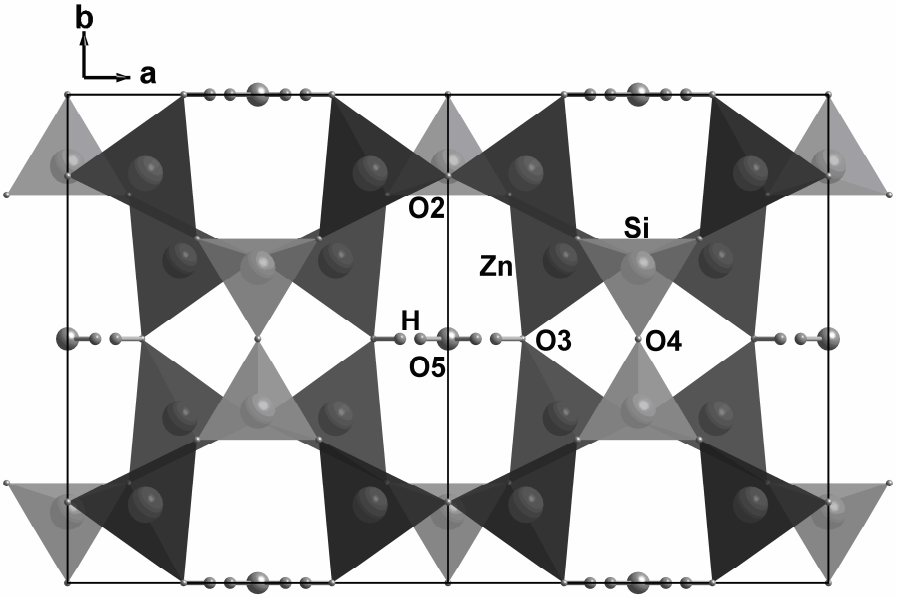

Figure 6.1 Crystal structure of hemimorphite projected to the (001) plane (data from Hill *et al*. 1977).

In the present study, we follow upon our previous EPR study of As (Mao *et al*. 2010) and investigate Cu, Cd and Pb in hemimorphite by use of combined cation-exchange and single-crystal EPR experiments. Specifically, cation-exchange experiments were intended to test whether Cu, Cd and Pb reside at the channel sites, as proposed by Gallegos *et al*. (2009). Single-crystal EPR measurements were made for identification and quantitative analysis of paramagnetic Cu, Cd and Pb centers (Gallegos *et al*. 2009). These data are then compared to provide new insights into the

oxidation states and structural environments of these heavy-metal ions in hemimorphite, with implications for the remediation of heavy-metal contamination.

6.2 Background information on the structure of hemimorphite

The crystal structure of hemimorphite (space group *Imm2*) consists of corner-sharing $Zn(OH)O_3$ and SiO_4 tetrahedra that have all of their apices aligned approximately along the crystallographic axis **c**, giving rise to its characteristic polar structure (Hill *et al*. 1977; Libowitzky *et al*. 1998). These tetrahedra are first linked to form three-membered rings, which in turn are joined together to build infinite sheets parallel to (010). The H_2O molecules occupy the center of large channels between the tetrahedral sheets and are held together by hydrogen bonds to the OH groups (Figure 6.1; Hill *et al*. 1977). Two neighboring SiO_4 tetrahedra, with Si atoms located in mirror planes, are linked by sharing the O4 atom to form the Si_2O_7 group (Figure 6.1). The $Zn(OH)O_3$ group, with the Zn atom at general positions (Figure 6.1), has non-equivalent Zn-O bonds and deviates significantly from an ideal tetrahedron (Hill *et al.* 1977; Libowitzky *et al.* 1998; Seryotkin & Bakakin 2011). Libowitzky *et al.* (1998) reported that hemimorphite undergoes a reversible second-order phase transition at 98(2) K to a low-temperature structure in the space group *Abm2*. These authors noted that room-temperature hemimorphite contains dynamically disordered OH and H_2O groups, whereas the low-temperature structure is characterized by an ordered arrangement of non-equivalent OH groups and rotated H_2O molecules in the channels. Also, Seryotkin & Bakakin (2011) noted that hemimorphite undergoes a

pressure-induced phase transition from *Imm2* to *Pnn2* under hydrostatic conditions at ~2.5 GPa.

6.3 Samples and Experimental Methodology

Mao *et al*. (2010) investigated a suite of 10 hemimorphite samples from various Zn-Pb deposits worldwide by use of single-crystal EPR spectroscopy and inductively coupled plasma-mass spectrometry (ICP-MS). These same samples were used in this study. In particular, the sample from Mapimi, Durango, Mexico (#1 in Mao *et al*. 2010) was selected for cation-exchange experiments at 110 °C for durations of 3, 5, 7 and 10 days. For each experiment, ~100 mg of hemimorphite powder mixed with ~10 mL of 0.1 M $CaCl_2$ solution was loaded into 23 mL acid digestion bombs (Parr Instrument Company). The solids were extracted after each exchange experiment by centrifuge and were dissolved in HF-HNO_3 for trace-element analysis by ICP-MS, at the Department of Geological Sciences, University of Saskatchewan.

Mao *et al*. (2010) measured reconnaissance single-crystal EPR spectra for all 10 samples, before and after gamma-ray irradiations at doses from 0.8 to 50 kGy. In this study, the sample from the M'Fouati Pb-Zn mine (#10 in Mao *et al*. 2010) was selected for detailed EPR and UV-Vis-NIR analyses. The UV-Vis-NIR measurements on a doubly polished crystal of ~1 mm thick were made on a Perkin Elmer Lambda 900 spectrometer in the wavelength range from 200 to 2800 nm with a resolution of 1 nm.

All EPR spectra were collected on a Bruker EMX spectrometer at the Saskatchewan Structure Sciences Centre, which is equipped with an automatic microwave bridge controller, a high-sensitivity ER-4119 cavity, and an ER-218G1 goniometer with a precision of 0.2º. Detailed spectral measurements at 295 K of an as-is crystal from M'Fouati were made in three rotational planes parallel to the (010), (100) and (001) faces at an interval of every 5°. Spectral measurements of this crystal at 120 K and microwave frequencies of ~9.389 GHz were made in the same three rotational planes, except that the interval in the plane parallel to the (001) face was increased to 10° or 15°. Other experimental parameters included a modulation frequency of 100 kHz, a modulation amplitude of 0.09 mT, a microwave power of 20 mW, and spectral resolutions from 0.0244 mT (*i.e.*, 2,048 data points over 50 mT) to ~0.039 mT (2,048 data points over 80 mT). Magnetic field calibration was made by using α,γ-bis-diphenylene-β-phenyl allyl (BDPA) in benzene as a standard (g = 2.0027).

6.4 Results

6.4.1 Cation-exchange experiments and UV-Vis-NIR spectrum

The salient feature of the cation-exchange experiments is that the contents of As and Cu in the exchanged hemimorphite are not reduced relative to those in the original sample, where the progressive increase in Cu with time may represent an uptake of this element from the impurity of $CaCl_2$ solution (Table 6.1). However, Cd is completely exchanged after three days (Table 6.1). The increased Pb contents in

experiments 1-3 and 5 may represent either a heterogeneous distribution of Pb or an analytical problem with this element. The Pb contents in experiments 1-7 and 10 are notably lower than that in the original sample (Table 6.1).

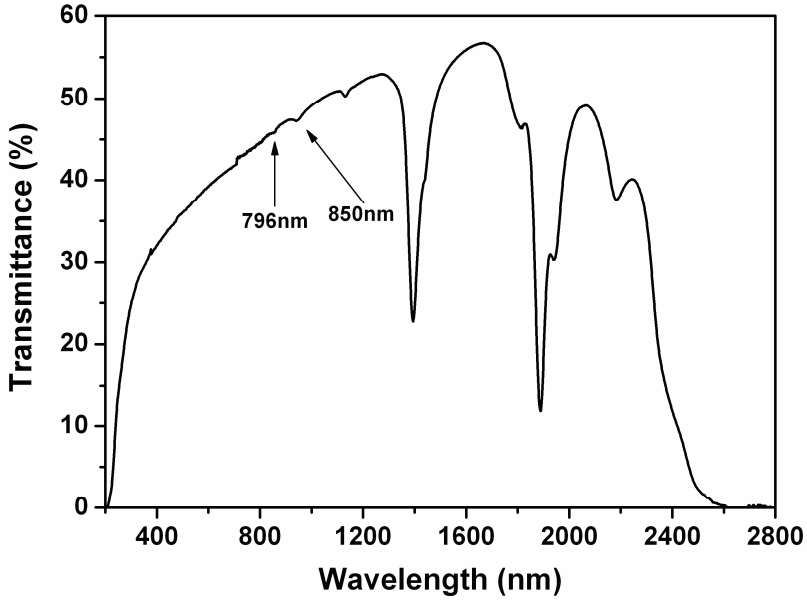

Figure 6.2 UV-Vis-NIR spectrum of hemimorphite from the M'Fouati Pb-Zn mine.

Table 6.1 Heavy metals in hemimorphite after exchange experiments

Runs	As (ppm)	Cu (ppm)	Cd (ppm)	Pb (ppm)
#1*	269(271)	357(351)	26(26)	1.9(2.0)
#1–3	276	380	nd	4.20
#1–5	268	413	0.18	8.63
#1–7	265	426	0.05	1.40
#1–10	270	445	nd	0.58
Solution	0.09	0.04	nd	nd

* duplicate analyses of Sample #1 in Mao *et al*. (2010);
Runs #1–3, 5, 7 and 10 are for 3, 5, 7 and 10 days, respectively;
Solution is the 0.1 M $CaCl_2$ solution; nd, not detectable.

The UV-Vis-NIR spectrum of hemimorphite from the M'Fouati Pb-Zn mine shows two strong absorptions around 1400 nm and 1900 nm and two weak

absorptions at 940 nm and 1126 nm, which have been assigned to various combinations of bending and stretching vibration (v_2+v_3), (v_1+v_3) and ($v_1+v_2+v_3$), ($v_1+2v_2+v_3$) of the H_2O molecule (Libowitzky & Rossman, 1997; Gallegos *et al*. 2009). Two additional weak peaks at 796 nm and 850 nm (Figure 6.2) are probably attributable to Cu^{2+} (see below).

6.4.2 Single-crystal EPR spectra

Previous EPR studies (Vassilikou-Dova & Eftaxias 1991; Gallegos *et al*. 2009; Mao *et al*. 2010) reported the presence of Cu^{2+}, Fe^{3+}, E', Mn^{2+}, $[AsO_4]^{4-}$, $[AsO_4]^{2-}$, and Pb^{3+} centers in hemimorphite. Our reconnaissance EPR measurements of both as-is and gamma-ray-irradiated hemimorphite from the 10 samples confirmed the common presence of the Fe^{3+}, Mn^{2+}, Cu^{2+}, $[AsO_4]^{4-}$, $[AsO_4]^{2-}$ and several unknown centers (see also Gallegos *et al*. 2009). However, paramagnetic Cd and Pb centers were not found in samples examined in this study. Interestingly, our EPR spectra of a sample labeled as "hemimorphite from Bleiberg, Austria" contain well-resolved Cd^{+}, Pb^{3+} and Zn^{+} centers (Popescu & Grecu 1973, 1975; Nistor *et al*. 1994, 1995). However, powder X-ray diffraction analysis shows this sample to be "botryoidal" calcite. The well-resolved Cu^{2+} EPR spectra measured on the sample from M'Fouati (Figure 6.3) are described herein.

The 295 K spectra of the S=1/2 Cu^{2+} center in the as-is hemimorphite crystal from M'Fouati, measured with the magnetic field **B** parallel to a crystallographic axis (Figure 6.3a), consist of a quartet (*i.e*. four lines of approximately equal intensity and

equal distance), corresponding to the characteristic ^{63}Cu hyperfine structure (I = 3/2, natural isotope abundance of 69.15% and g_n = 1.4849). The Cu^{2+} spectra, as **B** is rotated away from crystallographic axes, are resolved into four magnetically nonequivalent sites, indicative of its location at a general position in hemimorphite. At some crystal orientations, the hyperfine structure arising from the less abundant ^{65}Cu isotope (I = 3/2, natural isotope abundance of 30.85% and g_n = 1.5877) is resolved from the ^{63}Cu hyperfine structure in two of the four sites. Also, additional quartets of lower intensities are present and are attributable to the same Cu^{2+} center (see below). The average linewidths of the Cu^{2+} center in the 295 K spectra is ~0.59 mT. Gamma-ray irradiations with doses up to 50 kGy do not affect the intensity or the line position of the Cu^{2+} center.

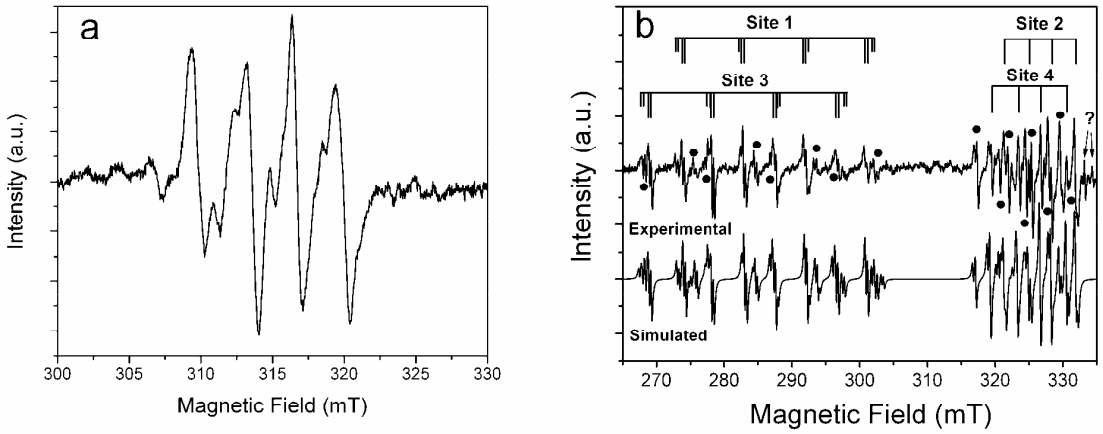

Figure 6.3 Representative single-crystal EPR spectra of as-is hemimorphite from the M'Fouati Pb-Zn mine: a) **B**//**c** and 295 K; and b) **B**^**a** = 37.5° and 120 K illustrating four magnetically non-equivalent sites of the Cu^{2+} center, where the short and long ticks mark the ^{63}Cu and ^{65}Cu hyperfine lines, respectively. Note that the ^{63}Cu hyperfine lines at sites 1 and 3 are further split into two of approximately intensities. Also, solid circles mark additional lines belonging to the Cu^{2+} center in a small

fragment or domains.

The 120 K EPR spectra of the Cu^{2+} center have the average linewidth reduced to ~0.31 mT, resulting in better resolution of the ^{63}Cu and ^{65}Cu hyperfine structures (Figure 6.3b). In particular, individual lines of the ^{63}Cu and ^{65}Cu hyperfine structures at some orientations are further resolved into doublets with separations up to ~0.4 mT (Figure 6.3b), suggesting a superhyperfine interaction with a next-nearest-neighbor hydrogen nucleus (see below). Also, the weak set of quartets is now better resolved than its counterpart in the 295 K spectra. Spectral simulations confirm that the weak set of quartets represents the same Cu^{2+} center and arises from a small fragment (or domains) related to the host by a rotation of ~3° about the axis **c**. Attempts to physically remove the small fragment or domains were not successful. In any case, these weak lines are readily distinguishable in most spectra and, therefore, do not adversely affect our analysis of the Cu^{2+} center.

6.4.3 Spin Hamiltonian parameters of Cu^{2+}

The general spin Hamiltonian of the S=1/2 Cu^{2+} center, with the ^{63}Cu and ^{65}Cu hyperfine structures and the ^{1}H hyperfine structure (Figure 6.3), can be written as:

$$H = \beta_e \mathbf{B}^T \mathbf{g} \mathbf{S} + \sum(\mathbf{I}^T \mathbf{A}_i \mathbf{S} + \mathbf{I}^T \mathbf{P}_i \mathbf{I} - \beta_n \mathbf{B}^T g_{ni} \mathbf{I}) \quad \text{.....(6.1)}$$

where β_e and β_n are the electronic (Bohr) and nuclear magneton, respectively. Iterative fittings for matrices **g**, **A** and **P**, using the software package EPR–NMR (Brown *et al*. 2003), were made for data from both the 295 K and 120 K spectra, in a coordination

system with its axes **X**, **Y** and **Z** along the crystallographic axes **a**, **b** and **c**, respectively. Fittings for data from the 295 K spectra included **g** and **A**(^{63}Cu) only, because the ^{65}Cu hyperfine structure and the ^{1}H superhyperfine structure are generally not resolved at this temperature (Figure 6.3a). The total number of line-position datapoints from three rotation planes was 1367, which is reduced to 1301 after those points from the crossover regions were assigned a weighing factor of 0.5. The final value of the root-mean-squares of weighted differences (RMSD) between the calculated and observed line-positions is 0.572 mT (Table 6.2), which is approximately equal to the average linewidth. The calculated normals of the three rotation planes in the (001) face, the (100) face and the {010} cleavage are (1.7º, 0.6º), (83.5º, 358.1º), and (92.0º, 89.4º), respectively, indicating small misalignments from the ideal directions of (0º, 0º), (90º, 0º), and (90º, 90º).

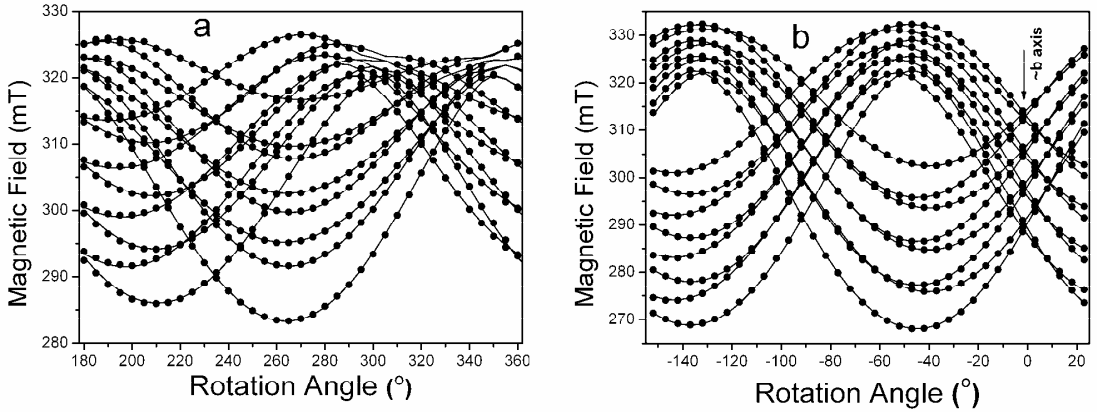

Figure 6.4. Line-position datapoints of the Cu^{2+} center in hemimorphite as a function of rotation angles (*i.e.*, roadmaps) at 120 K: (a) the (010) face and ν = 9.399 GHz and (b) the (100) face and ν = 9.392 GHz. Solid circles represent experimental data points, and solid lines are calculated from the best-fit spin Hamiltonian parameters in Table 6.2.

Initial fittings for data from the 120 K spectra included matrices **g**, **A**(^{63}Cu) and **P**(^{63}Cu). Matrices **A**(^{65}Cu) and **P**(^{65}Cu) were assumed to be proportional to **A**(^{63}Cu) and **P**(^{63}Cu) according to the g_n values. This assumption has been confirmed to be valid, because spectral simulations using the assumed **A**(^{65}Cu) and **P**(^{65}Cu) reproduce the observed ^{65}Cu hyperfine structure well (Figure 6.3b). The total number of line-position datapoints for the ^{63}Cu hyperfine structure was 1391, which is reduced to 1281 after those from crossover regions were assigned a weighing factor of 0.5 each. The final RMSD value is 0.124 mT (Table 6.2), which is smaller than half of the average linewidth. The calculated normals of the three rotation planes are (5.5º, 359.9º), (78.8º, 358.2º), and (95.5º, 93.6º), again showing notable misalignments in the crystal. Figure 6.4 demonstrates that the calculated and observed roadmaps at 120 K are in excellent agreement. Further support for the best-fitted spin Hamiltonian parameters comes from agreement between experimental and simulated powder EPR spectra (Figure 6.5).

The best-fit matrices **g** and **A**(^{63}Cu) from the 295 K and 120 K spectra are similar (Table 6.2). Therefore, only those from the 120 K spectra will be considered here. **g** is approximately axial in symmetry and has its principal values similar to other Cu^{2+} centers (Sharnoff 1965; Kuska *et al*. 1967; Parker 1971; Cozar & Ardelean 1987; Cozar *et al*. 1999; Biyik *et al*. 2007). However, **A**(^{63}Cu) and **P**(^{63}Cu) are highly rhombic in symmetry (Table 6.2). The most salient feature is that the orientations of g_{max}, A_{max} and P_{max} at (θ=128.0º, φ=243.1º), (130.8º, 248.3º) and (133º, 248º), respectively, are almost co-axial and are approximately along the direction of the

O1a–Zn–O1b bisector (123°, 236°) in the ZnO_4 pseudotetrahedron (Figure 6.6). Similarly, the orientations of g_{int}, A_{min} and P_{int} at (65.8º, 173.8º), (67.4º, 179.4º) and (69º, 180º) are close to the directions of the O1a–Zn–O3 and the O1b–Zn–O2 bisectors (Figure 6.6). Likewise, the orientations of g_{min}, A_{int} and P_{min} at (47.8º, 287.9º), (49.3º, 290.3º) and (50º, 288º) match approximately the directions of the O1a–Zn–O2 and O1b–Zn–O3 bisectors (Figure 6.6).

Table 6.2 Spin Hamiltonian parameters of the Cu^{2+} center in hemimorphite

	Matrix **Y**			k	Principal value (Y_k)	Principal direction θ_k (˚)	Principal direction φ_k (˚)	RMSD (mT)
				295 K				
g	2.01210(3)	0.0845(2)	0.0629(2)	1	2.4008(3)	52.5(2)	63.7(2)	
		2.2285(3)	0.1523(3)	2	2.0835(3)	65.6(3)	174.0(3)	
			2.1867(2)	3	2.0518(4)	47.4(2)	288.7(5)	
$\mathbf{A}(^{63}Cu)/g_e\beta_e$	1.5(1)	1.36(5)	2.16(9)	1	10.63(3)	49.4(2)	69.9(2)	0.572
(mT)		7.02(4)	3.40(5)	2	0.7(2)	68(1)	180(1)	
			6.04(5)	3	3.30(7)	48.7(8)	291(1)	
				120 K				
g	2.1200(1)	0.0836(1)	0.0636(1)	1	2.3949(1)	52.0(2)	63.1(2)	
		2.2202(1)	0.1510(1)	2	2.0820(1)	65.8(2)	173.8(2)	
			2.1859(1)	3	2.0492(1)	47.8(2)	287.9(2)	
$\mathbf{A}(^{63}Cu)/g_e\beta_e$	1.59(3)	1.55(2)	2.37(2)	1	11.04(1)	49.2(2)	68.3(2)	
(mT)		7.12(1)	3.56(1)	2	0.59(4)	67.4(2)	179.4(3)	0.124
			6.20(1)	3	3.29(1)	49.3(2)	290.3(4)	
$\mathbf{P}(^{63}Cu)/g_e\beta_e$	–0.07(1)	0.10(2)	0.05(1)	1	0.30(1)	47(1)	68(2)	
(mT)		0.03(1)	0.24(1)	2	–0.09(1)	69(6)	180(6)	
			0.04(1)	3	–0.21(1)	50(4)	288(9)	
$\mathbf{A}(^{1}H)/g_e\beta_e$	0.05(11)	0.03(8)	–0.08(7)	1	0.42(2)	52(3)	96(9)	
(mT)		0.23(4)	0.25(6)	2	0.09(5)	73(21)	200(14)	0.137
			0.10(6)	3	–0.13(15)	43(13)	308(31)	

Results reported here are for one of four symmetrically equivalent sites in the rotation group D_2. Polar angle θ is relative to the crystallographic axis **c**, and azimuth angle φ is relative to axis **a**. (θ, φ) is equivalent to (180-θ, 180+φ).

The ^{1}H superhyperfine structure is resolved only in one or two magnetically nonequivalent sites at some crystal orientations in the 120 K spectra (Figure 6.3b).

Therefore, only a total of 571 datapoints (and the sum of weighing factors = 558) was available for the optimization of the matrix **A**(^{1}H). The final RMSD value of 0.137 mT is again smaller than half of the experimental linewidth. Matrix **A**(^{1}H) has a rhombic symmetry (Table 6.2) and can be decomposed into an isotropic component a = 0.13 mT, an axial component b = 0.18 mT, and a rhombic component c = 0.08 mT. The orientation of the A_1 axis at (52º, 96º; Table 6.2) is close to the Zn—H direction (66º, 120º).

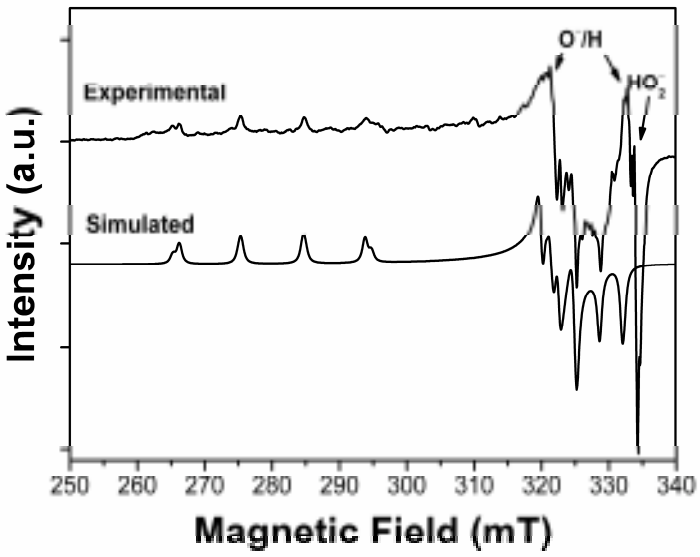

Figure 6.5 Experimental powder EPR spectrum of hemimorphite from the M'Fouati Pb-Zn mine, measured at a microwave frequency of 9.387 GHz and a temperature of 110 K, in comparison with a simulated spectrum that includes contributions from both ^{63}Cu and ^{65}Cu. Note that the experimental spectrum also contains two additional centers (*i.e.*, O^-/H and HO_2^-; authors' unpublished data).

6.5 Discussion

The orientations of the best-fit spin Hamiltonian parameters (Table 6.2) suggest that the Cu^{2+} ion resides at the Zn site. This site assignment is further supported by the observed ^{1}H superhyperfine structure that arises from interaction with the hydrogen nucleus of the hydroxyl group that links the two Zn^{2+} ions. The anisotropic component of the ^{1}H superhyperfine parameter is estimated by using the point-dipole model:

$$T_{z'} = (2\mu_0/4\pi)(g\beta_e g_n \beta_n / r^3) \quad \text{.....(6.2),}$$

where $T_{z'}$ is the traceless part of hyperfine interaction ($T_{x'} = T_{y'} = -T_{z'}/2$). The calculated Cu−H distance (r) = 2.37 Å is close to the Zn−H distance of 2.43 Å, determined by the neutron-diffraction study of Hill *et al*. (1977).

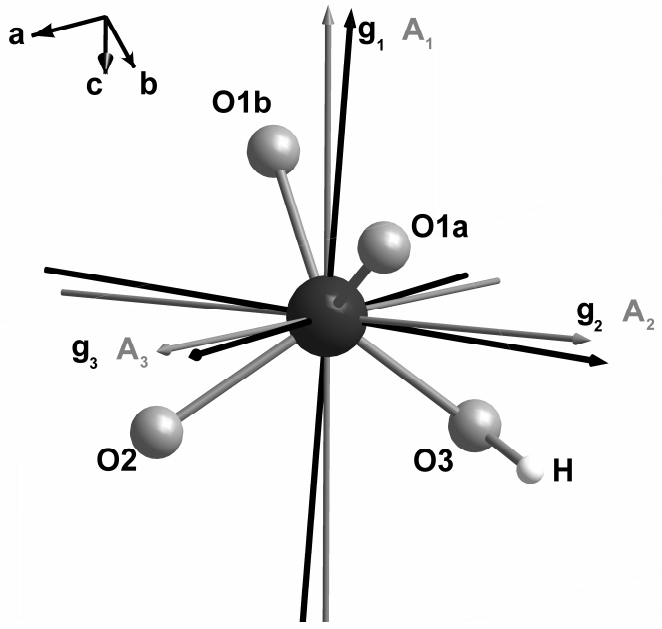

Figure 6.6 Relationships between the principal g and A(^{63}Cu) axes of the Cu^{2+} center and the ZnO_4 pseudotetrahedron in the hemimorphite structure (O1a and O1b are equivalent).

A strong Jahn-Teller effect is expected for the CuO_4 tetrahedron and is evidenced by the large rhombic character of matrices **g**, **A** and **P**, which suggests a reduction in the local symmetry of the Cu^{2+} tetrahedron from D_{2d} to approximately D_2 (Hoffmann & Goslar 1982; Reinen *et al*. 1982). Theoretical considerations on the basis of a second-order perturbation approximation (Parker 1971; Hoffmann & Goslar 1982; Pilbrow 1990) suggest that Cu^{2+} in a strongly elongate tetrahedron has $g_{\perp} > g_{//}$ and $|A_{\perp}| \approx |A_{//}|$, because its ground state is the d_z2 orbital. The Cu^{2+} ion in a weakly elongate tetrahedron has its ground state in the d_{xz} orbital, so that mixing involving the d_{xz}, d_{xy}, p_x, and p_y orbitals results in $g_{//} = 0$ and $g_{\perp}$ in a range from -2 to 4. The Cu^{2+} ion in a compressed tetrahedron has the ground state in the d_{xy} orbital, resulting in the $g_{//}$ along the direction of compression.

The contributions to principal g and A values of Cu^{2+} in a compressed tetrahedron, therefore, mainly come from the ground state d_{xy} orbital that is removed into a non-degenerated orbital by the tetragonal crystal-field. Minor contributions are known to arise from admixture of the 4*s* and 4*p* orbitals of the Cu^{2+} ion and from the effects of the oxygen ligands (Sharnoff 1965; Kuska *et al*. 1967; Abraham & Bleaney 1970; Parker 1971; Pilbrow 1990; Cozar *et al*. 1999). Successive tetrahedral and rhombic distortions reduce five energy levels into non-degenerate states. To a first approximation, the molecule orbitals in order of decreasing energy are listed below (Sharnoff, 1965; Kuska *et al*. 1967; Yokoi & Addison 1977; Cozar *et al*. 1999).

$$|xy\rangle = \alpha d_{xy} + \alpha_1 p_z + \alpha_2 \Psi(xy)_{\sigma} \quad \text{.....(6.3)}$$

$$|xz\rangle = \gamma d_{xz} + \gamma_1 p_y + \gamma_2 \Psi(xz)_{\sigma} \quad \text{.....(6.4)}$$

$$|yz\rangle = \delta d_{yz} + \delta_1 p_x + \delta_2 \Psi(yz)_\sigma \quad \text{.....(6.5)}$$

$$|x^2\text{-}y^2\rangle = \beta d_x 2_{-y} 2 + (1 - \beta^2)^{1/2} \Psi(x^2 - y^2)_\pi \quad \text{.....(6.6)}$$

$$|z^2\rangle = \varepsilon d_z 2 + (1 - \varepsilon^2)^{1/2} \Psi(z^2)_\pi \quad \text{.....(6.7)}$$

Functions (6.3), (6.4), and (6.5) belong to the ***t₂*** group, which has higher energies in the T_d symmetry, whereas Functions (6.6) and (6.7) belong to the ***e*** group with lower energies. Here,"d" and "p" represent the 3*d* and 4*p* orbitals of the Cu^{2+} ion, and Ψ denotes the oxygen ligand orbitals. Furthermore, α, β, γ, δ, and other Greek letters are all molecular orbital (MO) coefficients. The EPR parameters can be then related to those MO coefficients in different symmetries. For example, Bates *et al*. (1962) and Sharnoff (1965) proposed relationships between EPR parameters (g and A) and MO coefficients for CuO_4 with D_{2d} symmetry, and they showed a significant contribution from a large admixture (up to 11.7%; Sharnoff 1965) of energy levels from the 4*p* orbital of Cu^{2+} (see also Kokoszka *et al*. 1967; Parker 1971; Hoffmann & Goslar 1982; Cozar *et al*. 1999; Biyik *et al*. 2007). Cozar *et al*. (1999) suggested that an admixture of about 6% from the p_z character to the $3d_{xy}$ orbital leads to an increase in $g_{//}$ and a decrease in $A_{//}$ for Cu^{2+} in phosphate glasses. However, theoretical Xα calculations by Bencini & Gatteschi (1983) did not identify any mixing of *d-p* orbitals, because their calculated *p* mixing coefficient of the Xα wave function is only 0.011. These authors suggested that covalence effects, instead of the admixture of p orbitals, play a major role. Similarly, Maki & McGarvey (1958) proposed that covalence effects are the main factor affecting g and A values for Cu^{2+} with D_{4h} or D_{2h}

square-planar coordinations (see also Kivelson & Neiman 1961; Gersmann & Swalen 1962; Kuska *et al*. 1967).

Following previous studies of Cu^{2+} in pseudotetrahedral and square-planar coordinations (Gersmann & Swalen 1962; Sharnoff 1965; Kuska *et al*. 1967; Yokoi & Addison 1977; Mabbs & Collison 1992; Cozar *et al*. 1999), relations between the EPR parameters and MO coefficients for Cu^{2+} in hemimorphite can be written as follow:

$$g_z = g_e - 8\lambda_d\alpha\beta k_{\alpha\beta}/\Delta E_x{}^2{}_{-y}{}^2 \quad \text{.....(6.8)}$$

$$g_y = g_e - 2(\alpha\gamma\lambda_d - \alpha_1\gamma_1\lambda_p)(k_{\alpha\gamma} - \alpha_1\gamma_1)/\Delta E_{xz} \quad \text{.....(6.9)}$$

$$g_x = g_e - 2(\alpha\delta\lambda_d - \alpha_1\delta_1\lambda_p)(k_{\alpha\delta} - \alpha_1\delta_1)/\Delta E_{yz} \quad \text{.....(6.10)}$$

$$A_z = P_d \bullet [-\alpha^2(k_0 + 4/7) - 8\lambda_d\alpha^2\beta^2/\Delta E_x{}^2{}_{-y}{}^2 - 3/7 \bullet (\alpha\gamma\lambda_d - \alpha_1\gamma_1\lambda_p)\alpha\gamma/\Delta E_{xz} - 3/7 \bullet (\alpha\delta\lambda_d - \alpha_1\delta_1\lambda_p)\alpha\delta/\Delta E_{yz}] + P_p \bullet [4/5 \bullet \alpha_1{}^2 - k_0\alpha_1{}^2 - 3/5 \bullet (\alpha\gamma\lambda_d - \alpha_1\gamma_1\lambda_p)\ \alpha_1\gamma_1/\Delta E_{xz} - 3/5 \bullet (\alpha\delta\lambda_d - \alpha_1\delta_1\lambda_p)\alpha_1\delta_1/\Delta E_{yz}] \quad \text{.....(6.11)}$$

$$A_y = P_d \bullet [-\alpha^2(k_0 - 2/7) - 2 \bullet (\alpha\gamma\lambda_d - \alpha_1\gamma_1\lambda_p)\alpha\gamma/\Delta E_{xz} + 3/14 \bullet (\alpha\delta\lambda_d - \alpha_1\delta_1\lambda_p)\alpha\delta/\Delta E_{yz}] + P_p \bullet [-2/5 \bullet \alpha_1{}^2 - k_0\alpha_1{}^2 + 2 \bullet (\alpha\gamma\lambda_d - \alpha_1\gamma_1\lambda_p)\ \alpha_1\gamma_1/\Delta E_{xz} - 3/5 \bullet (\alpha\delta\lambda_d - \alpha_1\delta_1\lambda_p)\alpha_1\delta_1/\Delta E_{yz}] \quad \text{.....(6.12)}$$

$$A_x = P_d \bullet [-\alpha^2(k_0 - 2/7) - 2 \bullet (\alpha\delta\lambda_d - \alpha_1\delta_1\lambda_p)\alpha\delta/\Delta E_{yz} + 3/14 \bullet (\alpha\gamma\lambda_d - \alpha_1\gamma_1\lambda_p)\alpha\gamma/\Delta E_{xz}] + P_p \bullet [-2/5 \bullet \alpha_1{}^2 - k_0\alpha_1{}^2 + 2 \bullet (\alpha\delta\lambda_d - \alpha_1\delta_1\lambda_p)\alpha_1\delta_1/\Delta E_{yz} - 3/5 \bullet (\alpha\gamma\lambda_d - \alpha_1\gamma_1\lambda_p)\ \alpha_1\gamma_1/\Delta E_{xz}] \quad \text{.....(6.13)}$$

where $g_z = g_1$, $g_y = g_2$, $g_x = g_3$, $A_z = A_1$, $A_y = A_2$ and $A_x = A_3$ (Table 6.2), and

$$k_{\alpha\beta} = \alpha\beta + \beta\alpha_2 S_d + (1 - \beta^2)^{1/2}\alpha_2[T(n)]C/2$$

$$k_{\alpha\gamma} = \alpha\gamma + \gamma\alpha_2 S_d + (1 - \gamma^2)^{1/2}\alpha_2[T(n)]C/2^{1/2}$$

$$k_{\alpha\delta} = \alpha\delta + \delta\alpha_2 S_d + (1 - \delta^2)^{1/2}\alpha_2[T(n)]C/2^{1/2}$$

$$P_{d,p} = 2\gamma_n\mu_0\mu_n\langle r^{-3}\rangle_{3d,4p}$$

where μ_n and γ_n are the nuclear magneton and the gyromagnetic ratio, respectively, and $\langle r^{-3}\rangle$ is taken from the states of the Cu^{2+} ion, $P_d = 0.0360$ cm^{-1} and $P_p = 0.0402$ cm^{-1} (Sharnoff 1965; Cozar *et al*. 1999). Geometrical parameter C has a value between 1 and $(2/3)^{1/2}$ for planar and tetrahedral coordinations. Also, T(n) is an integral over the ligand functions and is equal to 0.220 for oxygen atoms; S_d is the overlap integral and is equal to 0.076 for oxygen atoms (Kivelson & Neiman 1961; Kuska *et al*. 1967). The characteristic Fermi contact term k_0 is 0.43 (Cozar *et al*. 1999), and $\lambda_d = -829$ and $\lambda_p = -925$ cm^{-1} are spin-orbital coupling constants for the free Cu^{2+} ion.

Following Bencini & Gateschi (1983), the coefficients for the admixture involving the 4*p* orbitals (α_1, γ_1, δ_1) can be assumed to be zero. Also, Kuska *et al*. (1967) proposed the following relationship between α^2 and the principal g and A values:

$$\alpha^2 = 1/(k_0 + 4/7) \bullet [-A_{//}/P_d + (g_{//} - g_e) + 3/7 \bullet (g_{\perp} - g_e)] + 0.03 \quad \text{.....(6.14).}$$

Here, the term α^2 is 0.735 if $A_{//}$ is negative. Sharnoff (1965) proposed the following equation:

$$\alpha^2 + \alpha_1^2 + \alpha_2^2 + 2(\alpha\alpha_2 S_d + \alpha_1\alpha_2 S_p) = 1 \quad \text{.....(6.15).}$$

Equation (6.15) yields $\alpha_2^2 = 0.196$ if $\alpha_1 = 0$.

In the pseudotetrahedral oxygen coordination in beryl (Solntsev *et al*. 1976; Gaite *et al*. 2001) and phosphate glasses (Cozar *et al*. 1999), the d-d transitions related

to $d_x2_{-y}2 \rightarrow d_{xy}$, $d_{xz} \rightarrow d_{xy}$, and $d_{yz} \rightarrow d_{xy}$ are in the range of 10500 – 14000 cm^{-1}. The UV-Vis-NIR spectrum of hemimorphite reveals only two weak absorptions at 845 nm (11834 cm^{-1}) and 796 nm (12562 cm^{-1}) (Figure 6.2). If we assign $\Delta E_x2_{-y}2 \approx$ 12562 cm^{-1} and $\Delta E_{xz} \approx \Delta E_{yz} \approx$11834 cm^{-1}, equations (6.7), (6.8), and (6.9) yield $\beta^2 = 0.966$, $\gamma^2 = 0.721$, and $\delta^2 = 0.411$. Following Sharnoff (1965), the $|d_{xy}>$ state contains 76.4% ($\alpha^2 + \alpha\alpha_2 S_d = 76.4\%$) $3d_{xy}$ character, and 22.2% ligand character. In comparison with previous works (Yokoi & Addison 1977), our δ^2 value is relatively small, and there is a large difference between γ^2 and δ^2. The rhombic symmetry of the spin-Hamiltonian parameters is apparently responsible for those differences in coefficients. In particular, the compressed Cu-tetrahedron shows a further distortion along the x and y axes that are close to two pseudo-diads. This distortion may cause different orbital characters at $|d_{xz}>$ and $|d_{yz}>$ states, resulting in different g_2 and g_3 and non-equal A_2 and A_3 (Table 6.2).

Zwanenburg *et al*. (1990) noted that the g values of Cu^{2+} centers vary with temperature and attributed this to a local structural distortion related to the Jahn-Teller effect. Similarly, Hoffmann *et al*. (2010) reported a temperature effect on the principal g values of Cu^{2+} in kainite and did not observe any change in the directions of the principal g axes. However, the best-fit spin Hamiltonian parameters for the Cu^{2+} center in hemimorphite are essentially constant in the temperature range from 120 K to 295 K, which is also true for the Cu^{2+} center in beryl (Solntsev *et al*. 1976).

6.5.1 Site occupancies of heavy metals in hemimorphite and implications

Our cation-exchange experiments show that As and Cu in hemimorphite are retained after exchange experiments up to 10 days, whereas Cd and probably Pb are readily exchanged. This observed retention of As is consistent with results from our previous single-crystal EPR study, which demonstrated that this element occurs as the substitutional As^{5+} ion at the Si site (Mao *et al*. 2010). Similarly, the retention of Cu in hemimorphite is consistent with its accommodation at the Zn site in the tetrahedral framework, as revealed by EPR. The readily exchangeable Cd and Pb are attributable to their locations in the channel sites. Our single-crystal EPR measurements did not detect any paramagnetic Cd or Pb centers, suggesting as the presence of diamagnetic Cd^{2+} and Pb^{2+} ions and making their site assignments impossible.

Numerous studies, including those using the EPR techniques, have been made to investigate the uptake and local structural environments of Cu in natural and synthetic zeolites, with relevance to diverse applications from enhanced catalytic properties to remediation of heavy-metal contamination (*e.g.*, Chao & Lunsford 1973; Zamadics & Kevan 1992; Kuroda *et al*. 1992; Yu *et al*. 1997; Godelitsas & Armbruster 2003; Hui *et al*. 2005; Doula & Dimirkou 2008). The general consensus is that Cu resides in the large cages in zeolites (Kuroda *et al*. 1992; Vassilikou-Dova & Eftaxias 1992; Delabie *et al*. 2000; Carl *et al*. 2002; Iacomi 2002; Godelitsas & Armbruster 2003; Hincapie *et al*. 2005). For example, single-crystal EPR studies (Chao & Lunsford 1973; Iacomi 2002) revealed six distinct sites in the cages for Cu^{2+} in chabazite (see also Zamadics & Kevan 1992). Similarly, Krishna *et al*. (2000) and

Godelitsas & Armbruster (2003) have suggested that other heavy metals, such as Co^{2+}, Pb^{2+}, and Cd^{2+}, reside in the cages in zeolites as well.

In this context, the observed accommodation of Cu^{2+} in the tetrahedral framework in hemimorphite is particularly interesting and has implications for the application of zeolites and zeolite-like materials for the remediation of heavy-metal contamination. For example, Mao *et al*. (2010) noted the accommodation of As^{5+} in the Si tetrahedral site in hemimorphite, and discussed its advantages in controlling the mobility of As during the weathering of Zn sulfide deposits. The advantage of heavy metals in the tetrahedral framework over locations in the cages is obvious, because the latter is susceptible to cation exchanges and, hence, represents a potential source for secondary contamination. In addition, numerous zeolite-type materials containing tetrahedrally coordinated Zn sites (Gier & Stucky 1991; Bu *et al*. 1998; Jensen *et al*. 1998; Johnson *et al*. 2002) are known and are potentially useful for the remediation of Cu contamination.

6.6 Conclusions

Single-crystal EPR spectra measured at 295 K and 120 K reveal the presence of a Cu^{2+} center in hemimorphite (Reneville, Congo). The best-fit spin-Hamiltonian parameters show that Cu^{2+} resides at the tetrahedral Zn site without any notable difference between 295 K and 120 K, refuting the model of Cu^{2+} in the channel suggested by a previous powder EPR study (Gallegos *et al*. 2009). Cation-exchange experiments that show Cu and As are not easily exchanged, further supporting their

locations in the tetrahedral sites. However, Cd and Pb in hemimorphite are readily exchanged and probably reside in the structural channels. These results indicate that hemimorphite is potentially useful for remediation of heavy metalloid contamination.

6.7 References

ABRAGAM, A. & BLEANEY, B. (1970): Electron paramagnetic resonance of transition ions. Clarendon Press. Oxford.

BATES, C.A., MOORE, W.S., STANDLEY, K. J. & STEVENS, K.W.H. (1962): Paramagnetic resonance of a Cu^{2+} ion in a tetrahedral crystal field. *Proc. Phys. Soc*. **79**, 73-83.

BENCINI, A. & GATTESCHI, D. (1983): Xα calculations of the EPR parameters of pseudotetrahedral copper(II) complexes. *J. Am. Chem. Soc*. **105**, 5535-5541.

BISSENGALIYEVA, M.R., BEKTURGANOV, N.S. & GOGOL, D.B. (2010): Thermodynamic characteristics of a natural zinc silicate hemimorphite. *J. Therm. Anal. Calorim*. **101**, 49-58.

BIYIK, R., TAPRAMAZ, R. & TEŞILEL, O. Z. (2007): EPR spectra of Cu^{2+} doped $[Zn(sac)_2(dmen)]$ and $[Zn(sac)_2(paen)]$ single crystals. *Spectrochim. Acta A*, **68**, 394-398.

BONI, M. & LARGE, D. (2003): Nonsulfide zinc mineralization in Europe: An overview. *Econ. Geol.* **98**, 715-729.

BREUER, K., TELES, J.H., DEMUTH, D., HIBST, H., SCHÄFER, A., BRODE, S. & DOMGÖRGEN, H. (1999): Zinc silicates: very efficient heterogeneous catalysts for the

addition of primary alcohols to alkynes and allenes. *Angew. Chem. Int. Ed*. **38**, 1401–1405.

BROWN, K., MOMBOURQUETTE, M.J. & WEIL, J.A. (2003): EPR-NMR (Users' Manual). Department of Chemistry, University of Saskatchewan, Saskatoon, SK., Canada.

BU, X., FENG, P., GIER, T.E. & STUCKY, G.D. (1998): Two ethylenediamine-templated zeolite-type structures in zinc arsenate and cobalt phosphate systems. *J. Solid State Chem*. **136**, 210-215.

CABALA, J., KRUPA, P. & MISZ-KENNAN, M. (2009): Heavy metals in mycorrhizal rhizospheres contaminated by Zn-Pb mining and smelting around Olkusz in southern Poland. *Water Air Soil Pollution* **199**, 139-149.

CANO, N.F., GALLEGOS, E.A. & WATANABE, S. (2009): Phase change and pyroelectricity in natural hemimorphite. *Rad. Effects Defects Solids*, **164**, 748-754.

CARL, P.J., VAUGHAN, E.W. & GOLDFARB, D. (2002): Interactions of Cu(II) ions with framework Al in high Si:Al zeolite Y as determined from X- and W-band pulsed EPR/ENDOR spectroscopies. *J. Phys. Chem. B* **106**, 5428-5437.

CATILLON-MUCHERIE, S., AMMARI, F., KRAFFT, J.-M., LAURON-PERNOT, H., TOUROUDE, R. & LOUIS, C. (2007): Preparation of coimpregnated Cu–Zn/SiO_2 catalysts: Influence of the drying step on metallic particle size and on Cu0–ZnII interactions. *J. Phys. Chem. C* **111**, 11619–11626.

CHAO, C.-C. & LUNSFORD, J.H. (1973): EPR spectra of Cu^{2+} in single crystals of chabazite. *J. Chem. Phys*. **59**, 3920-3925.

COPPOLA, V., BONI, M., GILG, H.A., BALASSONE, G. & DEJONGHE, L. (2008): The "calamine" nonsulfide Zn-Pb deposits of Belgium: Petrographical, mineralogical and geochemical characterization. *Ore Geol. Rev*. **33**, 187-210.

COZAR, O. & ARDELEAN, I. (1987): The local symmetry of Cu2+ ions in phosphate glasses. *J. Non-Crystal. Solids* **92**, 278-281.

COZAR, O., ARDELEAN, I., SIMON, V., DAVID, L., VEDEAN, N. & MIH, V. (1999): EPR studies of Cu^{2+} and V^{4+} ions in phosphate glasses. *Appl. Mag. Reson* **16**, 473-480.

DACHS, E. & GEIGER, C.A. (2009): Heat-capacity behaviour of hemimorphite, $Zn_4Si_2O_7(OH)_2 \bullet H_2O$, and its dehydrated analogue $Zn_4Si_2O_7(OH)_2$: a calorimetric and thermodynamic investigation of their phase transitions. *Eur. J. Mineral*. **21**, 971–988.

DAY, S.J. & BOWELL, R.J. (2005): Atypical and typical zinc geochemistry in a carbonate setting, Sä Dena Hes Mine, Yukon Territory, Canada. *Geochem. Explor. Environ. Analysis* **5**, 255-266.

DELABIE, A., PIERLOOT, K., GROOTHAERT, M.H., WECKHUYSEN, B.M. & SCHOONHEYDT, R.A. (2000): Study of the coordination of Cu^{2+} in zeolite Y: Interaction with water and ammonia. *Micropor. Mesopor. Materials* **37**, 209-222.

DOULA, M.K. & DIMIRKOU, A. (2008): An EPR study of Cu adsorption by clinoptilolite from Cl^-, NO^{3-} and SO_4^{2-} solutions. *J. Porous Mater* **15**, 457-466.

ESPIARI, S., RASHCHI, F. & SADRNEZHAAD, S.K. (2006): Hydrometallurgical treatment of tailings with high zinc content. *Hydrometall*. **82**, 54–62.

FROST, R.L., BOUZAID, J.M. & REDDY, B.J. (2007): Vibrational spectroscopy of the sorosilicate mineral hemimorphite $Zn_4(OH)_2Si_2O_7 \bullet H_2O$. *Polyhedron* **26**, 2405–2412.

GAITE, J.M., IZOTOV, V.V., NIKITIN, S.I. & PROSVIRNIN, S.Y. (2001): EPR and optical spectroscopy of impurities in two synthetic beryls. *Appl. Mag. Reson*. **20**, 307-315.

GALLEGOS, E.A., CANO, N.F., WATANABA, S. & CHUBACI, J.D.F. (2009): Thermoluminescence, infrared reflectivity and electron paramagnetic resonance properties of hemimorphite. *Rad. Measur*. **44**, 11-17.

GEIGER, C.A. & DACHS, E. (2009): Quasi-ice-like C_p behavior of molecular H_2O in hemimorphite $Zn_4Si_2O_7(OH)_2 \bullet H_2O$: C_p and entropy confined H_2O in microporous silicates. *Am. Mineral*. **94**, 634–637.

GERSMANN, H.R. & SWALEN, J.D. (1962): Electron paramagnetic resonance spectra of copper complexes. *J. Chem. Phys*. **36**, 3221-3233.

GIER, T.E. & STUCKY, G.D. (1991): Low-temperature synthesis of hydrated zinco(beryllo)-phospahte and arsenate molecular sieves. *Nature* **349**, 508-510.

GODELITSAS, A. & ARMBRUSTER, T. (2003): HEU-type zeolites modified by transition elements and lead. *Micropor. Mesopor. Materials* **61**, 3-24.

HILL, R.J., GIBBS, G.V., CRAIG, J.R., ROSS, F.K. & WILLIAMS, J.M. (1977): A neutron diffraction study of hemimorphite. *Zeit. Kristal*. **146**, 241–259.

HINCAPIE, B.O., GARCES, L.J., GOMEZ, S., GHOSH, R. & SUIB, S.L. (2005): Direct synthesis of copper faujasite. *Catalysis Today* **110**, 323-329.

HOFFMANN, S.K. & GOSLAR, J. (1982): Crystal field theory and EPR parameters in D_{2d} and C_{2v} distorted tetrahedral copper(II) complexes. *J. Solid State Chem*. **44**, 343-353.

HOFFMANN, S.K., GOSLAR, J. & TADYSZAK, K. (2010): Electronic structure and dynamics of low symmetry Cu^{2+} complexes in kainite-type crystal $KZnClSO_4 \bullet 3H_2O$: EPR and ESE studies. *J. Mag. Reson*. **205**, 293-303.

HUI, K.S., CHAO, C.Y.H. & KOT, S.C. (2005): Removal of mixed heavy metal ions in wastewater by zeolite 4A and residual products from recycled coal fly ash. *J. Hazard. Materials* **B127**, 89-101.

IACOMI, F. (2002): EPR studies of Cu^{2+} ion in chabazite. *Moldavian J. Phys. Sci*. **1**, 106-110.

JENSEN, T.R., NORBY, P., NØRLUND, C.A. & HANSON, J.C. (1998): Hydrothermal synthesis, crystal structure refinement and thermal transformation of $LiZnAsO_4 \cdot H_2O$. *Micropor. Mesopor. Materials* **26**, 77-87.

JOHNSON, C.D., MACPHEE, D.E. & FELDMANN, J. (2002) New low temperature synthetic route to an ammonium zinc arsenate zeolite analogue with an ABW-type structure. *Inorg. Chem*. **41**, 3588-3589.

KARABULUT, B., TAPRAMAZ, R. & KARADAG, A. (2008): EPR and optical absorption studies of Cu^{2+} ions in $[ZnPd(CN)_4(C_4H_{12}N_2O_2)]$ single crystals. *Appl. Mag. Reson*. **35**, 239-245.

KIVELSON, D. & NEIMAN, R. (1961): ESR studies on the bonding copper complexes. *J. Chem. Phys.* **35**, 149-155.

KOKOSZKA, G.F., REIMANN, C.W. & ALLEN, H.C.JR. (1967): The optical and magnetic spectra of copper-doped dichloro (1,10-phenanthroline) zinc. *J. Phys. Chem*. **71**, 121-126.

KOLESOV, B. (2006): Raman investigation of H_2O molecule and hydroxyl groups in the channels of hemimorphite. *Amer. Mineral*. **91**, 1355–1362.

KRISHNA, R.M., CHANG, Z., CHOO, H., RANJIT, K.T. & KEVAN, L. (2000): Electron paramagnetic resonance and diffuse reflectance spectroscopic studies of the photoionization of N-alkylphenothiazines in synthetic microporous M-clinoptilolite (M = $Na^+ + K^+$, H^+, Li^+, Na^+, K^+, Ni^{2+}, Co. *Phys. Chem. Chem. Phys*. **2**, 3335-3339.

KURODA, Y., KOTANI, A., MAEDA, H., MORIWAKI, H., MORIMATO, T. & NAGAO, M. (1992): The state of excessively ion-exchanged copper in mordenite: formation of tetragonal hydroxyl-bridged copper ion. *J. Chem. Soc. Faraday Trans*. **88**, 1583-1590.

KUSKA, H.A., ROGERS, M.T. & DRULLINGER, R.E. (1967): Effect of substituents on the anisotropic electron spin resonance parameters in copper acetylacetonates. *J. Phys. Chem*. **71**, 109-114.

LEE, J.S. & CHON, H.T. (2003): Exposure assessment of heavy metals on abandoned metal mines by ingestion of soil, crop plant and groundwater. *J. Phys. IV* **107**, 757-760.

LIBOWITZKY, E., KOHLER, T., ARMBRUSTER, T. & ROSSMAN, G.R. (1997): Proton disorder in dehydrated hemimorphite. IR spectroscopy and x-ray structure refinement at low and ambient temperatures. *Eur. J. Mineral*. **9**, 803-810.

LIBOWITZKY, E. & ROSSMAN, G.R. (1997): IR spectroscopy of hemimorphite between 82 and 373 K and optical evidence for a low-temperature phase transition. *Eur. J. Mineral*. **9**, 793-802.

LIBOWITZKY, E., SCHULTZ, A.J. & YOUNG, D.M. (1998): The low-temperature structure and phase transition of hemimorphite, $Zn_4Si_2O_7(OH)_2 \cdot H_2O$. *Zeit. Kristal*. **213**, 659-668.

MABBS, F.E. & COLLISON, D. (1992): Electron paramagnetic resonance of d transition metal compounds. Studies in Inorganic Chemistry, **16**. Elsevier.

MAKI, A.H. & MCGARVEY, B.R. (1958): Electron spin resonance in transition metal chelates. I. Copper(II) bis-acetylacetonate. *J. Chem. Phys*. **29**, 31-34.

MAO, M., LIN, J. & PAN, Y. (2010): Hemimorphite as a natural sink for arsenic in zinc deposits and related mine tailings: Evidence from single-crystal EPR spectroscopy and hydrothermal synthesis. *Geochim. Cosmochim. Acta* **74**, 2943-2956.

NISTOR, S.V., BOUWEN, A. & SCHOEMAKER, D. (1995): Cd^+ ($5s^1$) centers in Rb_2ZnCl_4 single crystals. *Phys. State Sol. B* **189**, 345-356.

NISTOR, S.V., SCHOEMAKER, D. & URSU, I. (1994): Spectroscopy of the ns^1-centers in ionic crystals. *Phys. State Sol. B* **185**, 9-76.

PARKER, I.H. (1971): Cu^{2+} in ammonium fluoride—a tetrahedral site. *J. Phys C: Solid State Phys.* **4**, 2967-2978.

POPESCU, F.F. & GRECU, V.V. (1973): EPR study of Zn^+ in calcite. *Solid State Comm*. **13**, 749-751.

POPESCU, F.F. & GRECU, V. V. (1975): Temperature dependence of Pb^{3+} EPR spectrum in irradiated calcite. *Phys. State Solidi B* **68**, 595-601.

PILBROW, J. R. (1990): Transition ion electron paramagnetic resonance. Oxford Science Publications.

REINEN, D., ATANASOV, M., NIKOLOV, G. & STEFFENS, F. (1988): Local and cooperative Jahn-Teller distortions of Ni^{2+} and Cu^{2+} in tetrahedral. *Inorg. Chem*. **27**, 1678-1686.

RODRIGUEZ, L., RUIZ, E., ALONSO-AZCARATE, J. & RINCON, J. (2009): Heavy metal distribution and chemical speciation in tailings and soils around a Pb-Zn mine in Spain. *J. Environ. Manag*. **90**, 1106-1116.

SCHAIDER, L.A., SENN, D.B., BRABANDER, D.J., MCCARTHY, K.D. & SHINE, J. P. (2007): Characterization of zinc, lead, and cadmium mine waste: implications for transport, exposure and bioavailability. *Environ. Sci. Technol*. **41**, 4164–4171.

SERYOTKIN, Y.V. & BAKAKIN, V.V. (2011): Structural evolution of hemimorphite at high pressure up to 4.2 GPa. *Phys. Chem. Minerals* **38**, 679-684.

SHARNOFF, M. (1965): Electron paramagnetic resonance and the primarily 3d wave functions of the tetrachlorocuprate ion. *J. Chem. Phys*. **42**, 3383-3395.

SOLNTSEV, V.P., LEBEDEV, A.S., PAVLYUCHENKO, V.S. & KLYAKHIN, V.A. (1976): Copper centers in synthetic beryl. *Soviet Phys. Solid State* **18**, 805-806.

TAKAHASHI,T. (1960): Supergene alteration of zinc and lead deposits in limestone. *Econ. Geol*. **55**, 1083-1115.

VASSILIKOU-DOVA, A.B. & EFTAXIAS, K. (1991): Electron spin resonance of Mn^{2+} in hemimorphite. *Crystal Res. Tech*. **27**, 117-120.

VASSILIKOU-DOVA, A.B. & EFTAXIAS, K. (1992): Electron paramagnetic resonance of Cu^{2+} in descloizite mineral: an unusual electronic configuration. *J. Phys. Cond. Matter* **4**, 241-248.

WALDER, I.F. & CHAVEZ, W.X.JR. (1995): Mineralogical and geochemical behavior of mill tailing material produced from lead-zinc skarn mineralization, Hanover, Grant County, New Mexico, USA. *Environ. Geol*. **26**, 1-18.

YOKOI, H. & ADDISON, A. W. (1977): Spectroscopic and redox properties of pseudotetrahedral copper(II) complexes. Their relationship to copper proteins. *Inorg. Chem*. **16**, 1341-1349.

YU, J.S., RYOO, J.W., LEE, C.W., KIM, S.J., HONG, S.B. & KEVAN, L. (1997): Copper(II) ionic species in Cu^{II}-exchanged K-offretite gallosilicate determined by electron paramagnetic resonance and electron spin echo modulation spectroscopies. *J. Chem. Soc. Faraday Trans*. **93**, 1225-1231.

YURIEVA, T.M., KUSTOVA, G.N., MINYUKOVA, T.P., POELS, E.K., BLIEK, A., DEMESHKINA, M.P., PLYASOVA, L.M., KRIEGER, T.K. & ZAIKOVSKII, V. I. (2001): Non-hydrothermal synthesis of copper-, zinc- and copper–zinc hydrosilicates. *Mater. Res. Innov*. **5**, 3–11.

ZAMADICS, M. & KEVAN, L. (1992): Electron spin resonance and electron spin echo modulation studies of copper(II) ions in the aluminosilicate chabazite: acomparison of copper(II) cation location and adsorbate interaction with isostructural silicoaluminophosphate-34. *J. Phys. Chem*. **96**, 8989-8993.

ZWANENBURG, G., MICHIELS, J.J.M. & DE BOER, E. (1990): EPR study of K_2SeO_4: Cu^{2+} in the high temperature phase and in the in commensurate phase. *Phys. Rev. B* **42**, 7783-7789.

Chapter 7

Phase transitions and proton ordering in hemimorphite: New insights from single-crystal EPR experiments and DFT calculations

Single-crystal electron paramagnetic resonance (EPR) spectra of gamma-ray-irradiated hemimorphite (Mapimi, Durango, Mexico) after storage at room temperature for three months, measured from 4 K to 275 K reveal a hydroperoxy radical HO_2 derived from the water molecule in the channel. The EPR spectra of the HO_2 radical confirm that hemimorphite undergoes two reversible phase transitions at ~98 K and ~21 K, and allow determinations of its spin-Hamiltonian parameters, including superhyperfine coupling constants of two more-distant protons from the nearest hydroxyl groups, at 110 K, 85 K, 40 K and 7 K. These EPR results show that the HO_2 radical changes in site symmetry from monoclinic to triclinic related to the ordering and rotation of its precursor water molecule in the channel at <98 K. The monoclinic structure of hemimorphite with completely ordered O−H systems at low temperature has been evaluated by both the EPR spectra of the HO_2 radical at <21 K and periodic density functional theory (DFT) calculations.

7.1 Introduction

Hemimorphite of the ideal formula $Zn_4Si_2O_7(OH)_2 \bullet H_2O$, an important ore mineral in non-sulfide Zn deposits and a common constituent in Zn mine tailings, has attracted considerable attention, because of its complex phase transitions (Libowitzky & Rossman, 1997; Libowitzky *et al*. 1998; Kolesov, 2006; Frost *et al*., 2007; Geiger & Dachs, 2009; Dachs & Geiger, 2009; Cano *et al*., 2009; Bissengaliyeva *et al*., 2010; Seryotkin & Bakakin, 2011) and interesting properties for catalytical (Breuer *et al*. 1999, Yurieva *et al*. 2001, Catillon-Mucherie *et al*. 2007) and environmental applications (Walder & Chavez 1995, Day & Bowell 2005, Espiari *et al*. 2006, Schaider *et al*. 2007, Cabala *et al*. 2009, Mao *et al*., 2010; Mao & Pan, 2012).

The zeolite-like structure of hemimorphite at room temperature (RT) and atmospheric pressure belongs to the space group *Imm2* and consists of SiO_4 and $Zn(OH)O_3$ tetrahedra sharing corners to form a framework with confined H_2O molecules in channels along [001] (Barclay & Cox, 1960; McDonald & Cruickshank, 1967; Hill *et al*., 1977; Takéuchi *et al*., 1978; Cooper *et al*., 1981; Libowitzky *et al*., 1998; Figure 7.1a). The H_2O molecule in the center of the channels lies in the (010) plane with the rotation axis along [001], and is held together by the OH groups via four co-planar hydrogen bonds (*i.e.*, "two-dimensional ice", Figure 7.1b; Hill *et al*., 1977; Takéuchi *et al*., 1978; Libowitzky *et al*., 1998; Kolesov, 2006).

Libowitzky & Rossman (1997), on the basis of Fourier-transform infrared (FTIR) and optical measurements, reported that hemimorphite undergoes a reversible second-order phase transition at 98(2) K. Subsequently, Kolesov (2006) observed

another phase transition at ~20-30 K in a polarized Raman spectroscopic study. Seryotkin & Bakakin (2011) noted that hemimorphite undergoes a phase transition from *Imm2* to *Pnn2* at a hydrostatic pressure of ~2.5 GPa.

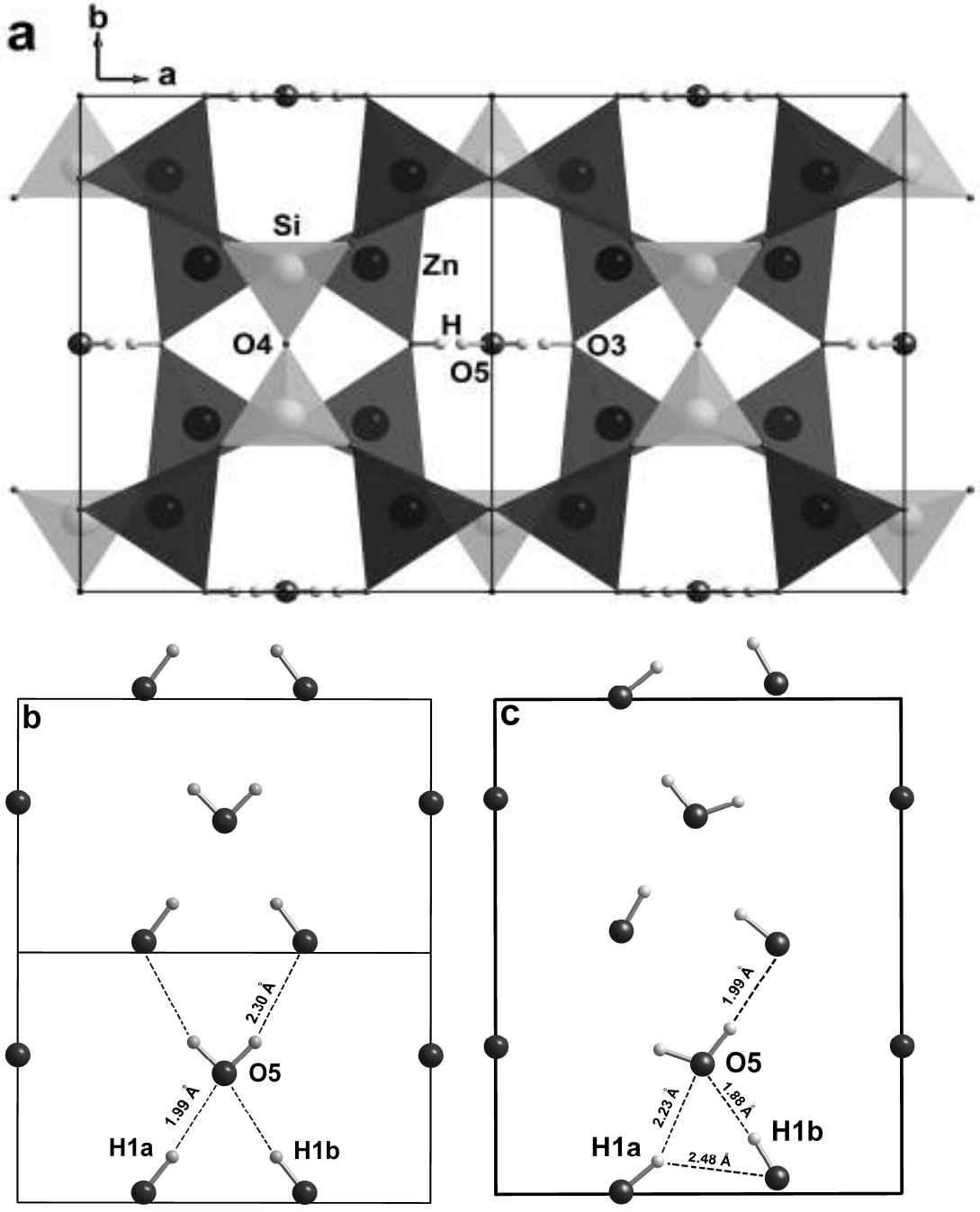

Figure 7.1 a) Crystal structure of hemimorphite at room temperature projected to the (001) plane (data from Takéuchi *et al.*, 1978); and b) and c) comparison of the

positions and orientations of the water molecule and the hydroxyl groups in the (010) plane at RT (Hill *et al*. 1977) and 20 K (Libowizky *et al*., 1998). Distance of hydrogen bonds (dashed lines) are marked.

A neutron diffraction study by Libowitzky *et al*. (1998) showed that the structure of hemimorphite at 20 K belongs to the space group *Abm*2. These authors noted that, while hemimorphite at RT contains dynamically disordered OH and H_2O groups, the *Abm*2 structure is characterized by an ordered arrangement of nonequivalent OH groups and rotated H_2O molecules in the channels. In particular, the H_2O molecule at 20 K is displaced from the center of the channels and the <HOH> bond angle increases from 90.5° at RT to 108(2)° at 20 K. Although all OH groups at 20 K remain in the (010) plane, the symmetrically related O3–H3 hydroxyl groups at RT are rotated into two different positions with different O–H vectors at 20 K (Figure 7.1c). Libowitzky *et al.* (1998) recognized that the *Abm*2 structure contains a sequence of ordered and apparently disordered channels in the same unit cell and proposed two monoclinic structures with ordered O–H systems in the channels at low temperature.

As part of our single-crystal EPR study of hemimorphite (Mao *et al*., 2010; Mao & Pan, 2012), we observed a proton-associated oxyradical in gamma-ray-irradiated crystals. The single-crystal EPR spectra of this proton-associated oxyradical measured from 4 K to 275 K clearly show that hemimorphite undergoes two phase transitions at ~21 K and ~98 K, confirming the observations of Libowitzky & Rossman (1997) and Kolesov (2006). Moreover, quantitative determinations of spin

Hamiltonian parameters of this oxyradical, including proton hyperfine coupling constants, at 110 K, 85 K, 40 K and 7 K, provide new insights into proton ordering associated with the two phase transitions. In addition, the monoclinic structures proposed by Libowitzky *et al.* (1998) have been evaluated by both periodic density functional theory (DFT) calculations and the EPR results at <21 K.

7.2 Sample and experimental methodology

7.2.1 Single-crystal EPR measurements

The hemimorphite crystal (~1 mm x 2.5 mm x 3 mm) of Sample #1 (Mapimi, Durango, Mexico) investigated in Mao *et al*. (2010) was used in this study. Mao *et al*. (2010) did single-crystal EPR measurements immediately after this crystal was irradiated at RT in a ^{60}Co cell for a dose of ~50 kGy.

In this study, all EPR spectra of the gamma-ray-irradiated hemimorphite, after storage at RT for three months, were collected on a Bruker EMX spectrometer at the Saskatchewan Structural Sciences Centre, University of Saskatchewan. The spectrometer is equipped with an automatic microwave controller, a high-sensitivity ER-4119 cavity, an ER-218G1 goniometer with a precision of 0.2°, and an Oxford Instrument liquid-helium cryostat.

Detailed spectral measurements in three rotation planes approximately parallel to the (010), (100) and (001) crystal faces, at a constant interval of 5° in each plane, were made at 110 K, 85 K, 40 K and 7 K. Experimental conditions included microwave frequencies of ~9.387 GHz, a modulation frequency of 100 kHz, a

modulation amplitude of 0.05 mT, a microwave power of 20 mW or 2 mW, and spectral resolutions from 0.0039 mT (*i.e*., 2,048 data points over 8 mT) to ~0.0078 mT (2,048 data points over 16 mT). Calibration of the magnetic field was made by using a Bruker strong pitch with g = 2.0028 as an external standard.

Additional single-crystal spectral measurements were made with **B**//**a** in the temperature range from 4 K to 275 K and **B**//**b** from 4 K to 110 K, using variable intervals from 1 K to 25 K (Figure 7.2a,b). At each temperature, the crystal in the cavity was allowed to equilibrate for at least an hour before measurements. Experimental conditions for these measurements were similar to those above, except for spectral resolutions of 0.0049 mT (*i.e*., 2,048 data points over 10 mT) for those with **B**//**b**.

7.2.2 DFT computation methodology

All periodical calculations were performed using the supercell approach (Pisani, 1996) and the parameter free hybrid DFT method PBE0 (Adamo & Barone, 1999) as implemented in the package CRYSTAL06 (Dovesi *et al*., 2006). Here PBE stands for both Perdew, Burke and Ernzerhof GGA exchange and correlation functionals that contain no empirical parameters (Perdew *et al*., 1996). All-electron basis sets used in this study are those known to be well suitable for periodic calculations (Li & Pan, 2011), and include the 86-411d31G of Jaffe & Hess (1993) for Zn, standard 6-31G* for O and H, and Pisani's (1992) 8-41G**, [1s3sp2d] from primitives (20s13p2d) for Si.

The thresholds for the overlap and penetration Coulomb integrals, the overlap for Hartree-Fock (HF) exchange integrals, and the two pseudo-overlaps for HF series were set to 10^{-8}, 10^{-8}, 10^{-8}, 10^{-8}, and 10^{-18} hartree, respectively, while a tight SCF tolerance of 10^{-8} hartree was chosen. Also, the extra-large grid (XLGRID) that employs the pruned (75,974) grid for each atom was used, which is much more accurate than the default (55,434) grid in the description of the optimized charge densities (Li & Pan, 2011). The Pack-Monkhorst shrink factor was set to 6 for the unit-cell geometry optimizations. The same shrink factor was doubled for the Gilat net to describe the Fermi surface of the system (Dovesi *et al*., 2006).

7.3 Results and discussion

7.3.1 Single-crystal EPR spectra

Single-crystal EPR measurements of the gamma-ray-irradiated hemimorphite after storage at RT for three months show that the $[AsO_4]^{4-}$ and $[AsO_4]^{2-}$ radicals observed in Mao *et al*. (2010) have faded completely and that two new resonance signals (denoted I and II in Figure 7.2) are now resolved at <275 K. It should be noted, however, that Centers I and II are present in the crystal immediately after gamma-ray irradiation but commonly overlap with the $[AsO_4]^{2-}$ radical, making them difficult to investigate before the latter is completely decayed. Figure 7.2 also shows an electron-like center E' of Cano *et al.* (2009) and Gallegos *et al*. (2009), which does not have any detectable hyperfine structure and has not been investigated further in this study.

The 110 K spectra of Center I consist of two strong lines and three weak satellites at **B**//**a** (Figure 7.2a), and two sets of three lines with the intensity ratio of ~1:2:1 at **B**//**b** (Figure 7.2b). These spectra features suggest that Center I arises from an unpaired electron (S = ½) interacting with one close proton (I = 1/2 and natural isotope abundance of ~100%) and two more-distant and equivalent protons. The spectrum of Center I at **B**//**c** contains one broad (~0.2 mT) multiplet (Figure 7.2c). Away from crystallographic axes, the signals are resolved to at most two sets, indicative of a monoclinic site symmetry (Rae 1969). The average linewidth of Center I at 110 K is ~0.25 mT.

Below 98 K the EPR spectra of Center I at random orientations consist of four magnetically nonequivalent sets (Figure 7.2d), indicative of a triclinic site symmetry (Rae 1969). The average linewidths of Center I at 85 K and 40 K are 0.14 mT and ~0.12 mT, respectively, which are significantly narrower than that at 110 K and result in better resolved superhyperfine splittings arising from the two more-distant protons in the 40 K spectra (Figure 7.2).

The spectra of Center I at <21 K are closely comparable to these above 98 K but differ markedly from those between 22 and 98 K (Figure 7.2a,b), providing clear evidence for another phase transition at ~21 K. Repeated EPR measurements showed that this phase transition at ~21 K, similar to that at ~98 K (Libowitzky & Rossman, 1997), is reversible. Moreover, the linewidth of Center I increases significantly close to the phase transition at ~21 K (Figure 2a,b). Lang *et al*. (1977) reported a similar increase in the EPR linewidth of the substitutional Fe^{3+} center $[FeO_4]^0$ in quartz and

the isostructural berlinite ($AlPO_4$) near the α↔β phase transition and interpreted it to originate from fluctuations at the phase transition.

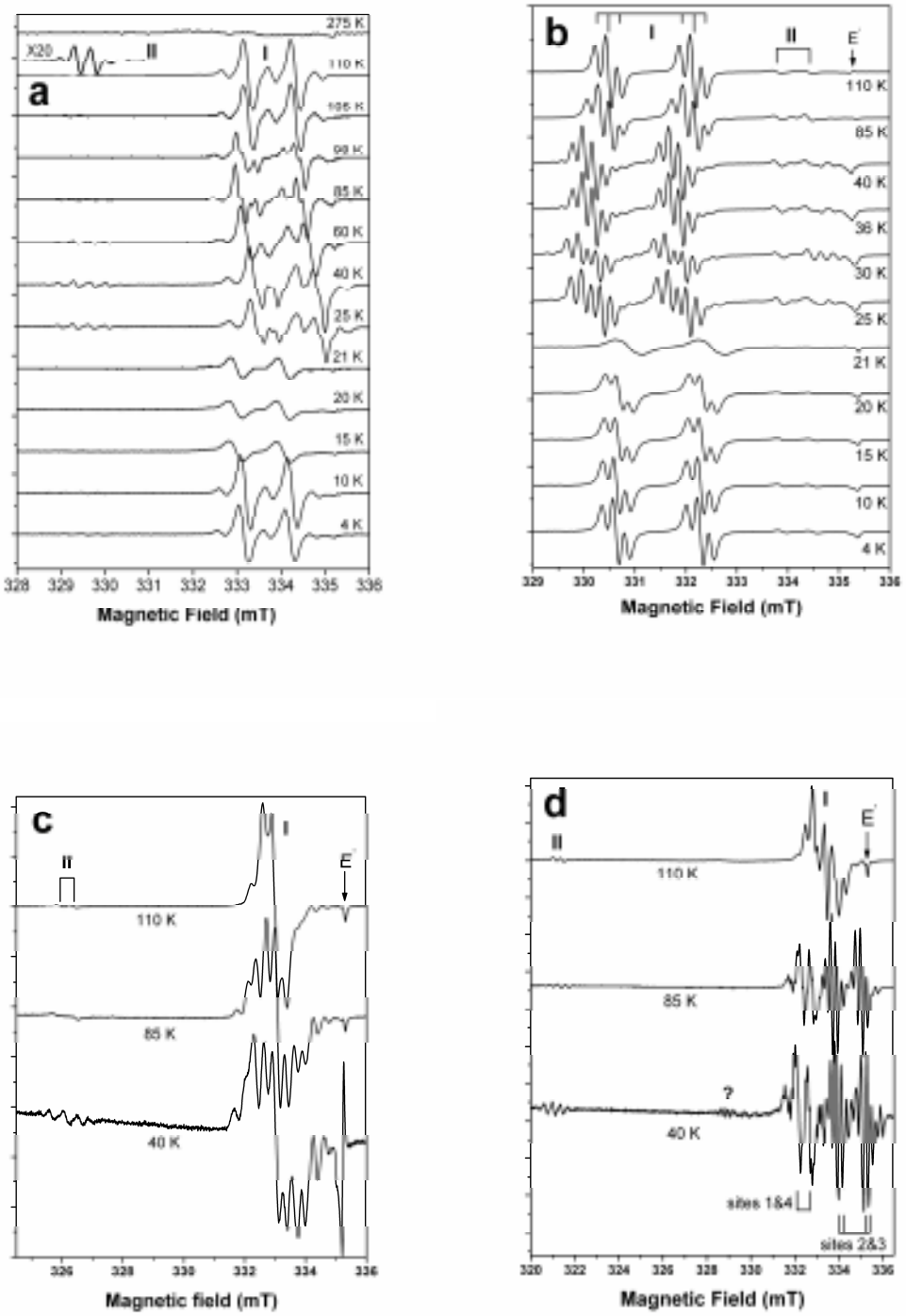

Figure 7.2 Representative single-crystal EPR spectra of gamma-ray-irradiated hemimorphite as a function of temperature: a) **B**//~**a** and microwave frequency ν =

9.395 GHz; b) **B**//~**b** and ν = 9.386 GHz; c) **B**//~**c** and ν = 9.385 GHz; and d) **B**^**a** = ~45° and ν = 9.395 GHz. Three centers (I, II and E') are marked. Question mark notes an unknown center in d). Four magnetically nonequivalent sites of Center I in d) are also labeled.

The 110 K EPR spectrum of Center II at **B**//**a** consists of two strong lines and two weak satellites (Figure 7.2a), with an average linewidth of ~0.16 mT. The satellites decrease in intensity when **B** is rotated away from **a** and are not resolved at **B**//**b** or **B**//**c**. This center is resolved into at most two sets in all three rotation planes, indicating a monoclinic site symmetry (Rae, 1969). These features suggest that Center II arises from an unpaired electron (S = ½) interacting with one proton. The doublet and the weak satellites represent the "allowed" and "forbidden" proton nuclear transitions, respectively. The EPR spectra of Center II also show clear evidence for the phase transition at ~98 K but become too weak to be detected below 21 K. Also, Center II is invariably lower in intensity than Center I (Figure 2a,b) and is obscured completely by the latter where they overlap with each other. Therefore, quantitative determinations of the spin Hamiltonian parameters of Center II are not possible, owing to insufficient data points.

7.3.2 Optimization of spin Hamiltonian parameters

The spin Hamiltonian used for the description of Center I having hyperfine interactions with three protons (i = 1, 2, 3) takes the form:

$$\mathbf{H} = \beta_e \mathbf{B}^T \mathbf{g} \mathbf{S} + \Sigma(\mathbf{I}^T \mathbf{A}_i \mathbf{S} - \beta_n \mathbf{B}^T g_{ni} \mathbf{I}) \quad \text{.....(7.1),}$$

where β_e and β_n are the electronic (Bohr) and nuclear magnetons, respectively; **S** and **I** are the electron-spin and nuclear-spin operatoers, respectively; T denotes transpose; and the scalar g_n value of 5.5856912 is adopted for ^{1}H. Iterative fittings for the Zeeman electron matrix **g** and the nuclear hyperfine matrices **A** were made by using of the software package EPR-NMR (Brown *et al*., 2003). The experimental axes x, y, and z were set along the crystallographic axes **a**, **b** and **c**, respectively.

The total number of line-position data points for the fitting of Center I at 110 K is 5800, which is reduced to 5782 after assigning those at crossover regions to a weighing factor of 0.5. The final value of the root-mean-squares of weighted differences (RMSD) is 0.030 mT (Table 7.1), which is less than half of the average linewidth. The calculated normals of the three rotation planes at (θ=5.9º, ϕ=124.7º), (91.2º, 356.0º), and (87.7º, 87.7º), in comparison with the ideal orientations at (0º, 0º), (90º, 0º), and (90º, 90º), respectively, indicate minor crystal misalignments. Here, θ and ϕ denote the polar and azimuth angles from **c** and **a**, respectively. Spectral simulations confirm that the best-fit spin-Hamiltonian parameters at 110 K (Table 7.1) reproduce the experimental spectra very well (Figure 7.3a).

The total numbers of line-position data points for the fittings of Center I at 85 K and 40 K are 2270 and 4395, respectively, which are reduced to 2260 and 4338.5 after assigning a weighing factor of 0.5 to those at the crossover regions. The relatively smaller number of data points at 85 K is due to the fact that some spectra from (100) and (001) planes at this temperature were not included owing to low signal-to-noise ratios. The final RMSD values for 85 K and 40 K are 0.069, and 0.062

mT, respectively (Table 7.1), again less than half of the average linewidths in the corresponding spectra. The calculated normals of the three rotation planes are (4.0º, 90.7º), (89.3º, 353.9º), and (91.1º, 90.8º) at 85 K, and (1.3º, 175.9º), (91.3º, 359.1º), and (90.0º, 90.0º) at 40 K. The small differences in the calculated normals of a given rotation plane among the experiments at different temperatures are expected from the fact that crystal alignment was adjusted after measurements at each temperature. Spectral simulations confirm that the best-fit spin Hamiltonian parameters at 85 and 40 K (Table 7.1) also reproduce their respective experimental spectra very well (Figure 7.3b).

The apparent similarity in the EPR spectra of Center I below 21 K to those above 98 K led us to use the spin Hamiltonian parameters and crystal orientations obtained from the 110 K spectra as the starting point. The final RMSD value of 0.059 mT (Table 7.1) is also smaller than half of the experimental linewidth. Spectral simulations show that the EPR spectra measured at 7 K are well reproduced by the best-fit spin Hamiltonian parameters of Center I at this temperature (Figure 7.3c).

Table 7.1 Spin Hamiltonian parameters of the HO_2 radical at different temperatures

	Matrix **Y**			k	Principal value (Y_k)	Principal direction θ (˚)	φ (˚)	RMSD (mT)
110 K								
g	2.0092(1)	0	0	1	2.0241(1)	90.0(1)	270.0(1)	
		2.0242(3)	0	2	2.0141(1)	180.0(1)	164*	
			2.0141(2)	3	2.0092(1)	90.0(1)	0.0(1)	
^1H_c	−1.074(2)	0	0	1	0.038(1)	180.0(1)	250*	0.030
$\mathbf{A}/g_e\beta_e$ (mT)		−1.670(1)	0	2	−1.074(2)	90.0(1)	0.0(1)	
			0.038(1)	3	−1.670(1)	90.0(1)	270.0(1)	
$^1H_{d1}$	−0.056(1)	0	−0.263(1)	1	−0.207(1)	90(4)	269(8)	
$\mathbf{A}/g_e\beta_e$ (mT)		−0.207(1)	0	2	−0.194(2)	62.4(1)	359(11)	

			0.309(1)	3	0.447(2)	152.4(1)	0(1)	
$^1H_{d2}$	–0.056(1)	0	0.263(1)	1	–0.207(1)	90(4)	90(8)	
$\mathbf{A}/g_e\beta_e$ (mT)		–0.207(1)	0	2	–0.194(2)	62.4(1)	180(11)	
			0.309(1)	3	0.447(2)	152.4(1)	180(1)	
				85 K				
g	2.0091(1)	0.0033(1)	0.0055(1)	1	2.0272(1)	69.9(1)	73.2(1)	
		2.0248(1)	0.0036(1)	2	2.0148(1)	40.6(1)	317.8(2)	
			2.0134(1)	3	2.0053(1)	56.4(1)	177.2(2)	
^1H_c	–1.06(1)	–0.30(1)	0.52(1)	1	–0.08(1)	36.6(6)	330(1)	0.069
$\mathbf{A}/g_e\beta_e$ (mT)		–1.58(1)	–0.34(2)	2	–1.37(1)	54.4(6)	166(2)	
			–0.55(1)	3	–1.74(1)	82(1)	70(1)	
$^1H_{d1}$	–0.09(1)	0.01 (1)	–0.18(1)	1	–0.16(1)	90(14)	93(37)	
$\mathbf{A}/g_e\beta_e$ (mT)		–0.18(1)	–0.01(1)	2	–0.16(1)	69(1)	3(42)	
			0.32(1)	3	0.39(1)	159.1(6)	4(4)	
$^1H_{d2}$	–0.04(1)	–0.04(1)	0.30(1)	1	–0.24(1)	98(10)	66(17)	
$\mathbf{A}/g_e\beta_e$ (mT)		–0.23(1)	–0.04(1)	2	–0.21(1)	60(3)	151(23)	
			0.29(1)	3	0.48(1)	149(5)	171(2)	
				40 K				
g	2.0077(1)	0.0080(1)	0.0066(1)	1	2.0359(1)	61.1(1)	67.1(1)	
		2.0262(1)	0.0011(1)	2	2.0083(1)	42.5(1)	300.0(1)	
			2.0136(1)	3	2.0034(1)	61.8(1)	174.2(1)	
^1H_c	–1.11(1)	–0.07(1)	0.54(1)	1	–0.03(1)	27.5(2)	348.8(1)	0.062
$\mathbf{A}/g_e\beta_e$ (mT)		–1.72(1)	–0.13(1)	2	–1.38(1)	62.9(6)	179.4(2)	
			–0.32(1)	3	–1.74(1)	85.7(1)	87.2(1)	
$^1H_{d1}$	–0.17(1)	0.02(1)	–0.23(1)	1	–0.28(1)	64.5(3)	23(1)	
$\mathbf{A}/g_e\beta_e$ (mT)		–0.20(1)	–0.11(1)	2	–0.21(1)	89.4(5)	113(1)	
			0.26(1)	3	0.38(1)	154.5(3)	24.5(4)	
$^1H_{d2}$	–0.12(1)	0.02(1)	0.33(1)	1	–0.34(1)	63.1(1)	143.7(9)	
$\mathbf{A}/g_e\beta_e$ (mT)		–0.22(1)	–0.10(1)	2	–0.19(1)	80.3(4)	238.6(7)	
			0.30(1)	3	0.49(1)	151.2(2)	166.6(2)	
				7 K				
g	2.0095(1)	0	0	1	2.0237(1)	90.0(1)	270.0(1)	
		2.0237(1)	0	2	2.0137(1)	180.0(1)	180*	
			2.0137(1)	3	2.0095(1)	90.0(1)	0.0(1)	0.059
^1H_c	–1.102(7)	0	0	1	0.015(9)	180.0(4)	34*	
$\mathbf{A}/g_e\beta_e$ (mT)		–1.690(8)	0	2	–1.102(7)	90.0(4)	0 (1)	
			0.015(9)	3	–1.690(8)	90.0(3)	270(1)	
$^1H_{d1}$	–0.051(5)	0	–0.254(6)	1	–0.199(10)	87(20)	275(39)	
$\mathbf{A}/g_e\beta_e$ (mT)		–0.199(9)	0	2	–0.188(6)	62 (2)	7(49)	
			0.281(8)	3	0.418(8)	151.6(5)	0.1(9)	
$^1H_{d2}$	–0.051(5)	0	0.254(6)	1	–0.199(10)	87(20)	95 (39)	
$\mathbf{A}/g_e\beta_e$ (mT)		–0.199(9)	0	2	–0.188(6)	62 (2)	187(49)	
			0.281(8)	3	0.418(8)	151.6(1)	180.1(9)	

^1H_c, $^1H_{d1}$ and $^1H_{d2}$ denote the close proton and two more-distant protons. *Tilting angles relate to axis a (φ) are meaningless when the tilting angle relative to axis c (θ) is close to zero. The sets of (θ, φ) and (180° – θ, 180° + φ) are equivalent.

Table 7.2 Spin Hamiltonian parameters of the HO_2 radical in selected hosts

Host	g1	g2	g3	A1/geβe (mT)	A2/geβe (mT)	$A_3/g_e\beta_e$ (mT)	Ref.
Argon	2.0393	2.0044	2.0044	1.35	0.86	0.86	1
$BaCl_2•H_2O$	2.02	2.007	2.007	1.6	0.8	0.8	2
Glassy hydrogen peroxide	2.0356	2.0082	2.0043	–20.1	8.7	–5.3	3
$SrCl_2•6H_2O$	2.0355	2.008	2.003	–1.72	–0.6	–1.27	4
Hydrogen peroxide	2.0353	2.0086	2.0042	1.38	0.35	1.55	5
Ice I_h	2.0376	2.0117	2.0025	–0.8	–1.6	–1.3	6
Ice I_h	2.0443	2.0081	2.0022	–0.5	–1.5	–1.1	6
Ice I_h	2.0455	2.0105	2.0023	–0.3	–1.4	–1.0	6

Reference 1 is Adrian *et al*., 1967; 2, Radhakrishna *et al*., 1976; 3, Chumakova *et al*., 2008; 4, Catton & Symons, 1969; 5, Wyard *et al*., 1968; and 6, Bednarek & Plonka, 1987.

The best-fit matrices **g** and **A**(^{1}H for the close proton) of Center I at 110 K (Table 7.1) are both close to axial in symmetry and are similar to those of the hydroperoxy radical HO_2 in various hosts (Table 2; Adrian *et al*., 1967; Wyard *et al*., 1968; Catton & Symons, 1969; Radhakrishna *et al*., 1976; Bednarek & Plonka, 1987; Chumakova *et al*., 2008). Following Chumakova *et al*. (2008), the unique g_1 and A_1 axes of the HO_2 radical are along the O=O and O−H bond directions, respectively, whereas the g_3 and A_2 axes are usually coaxial and normal to the radical plane. Therefore, the orientations of the g_3 and A_2 axes (Table 7.1) suggest that the HO_2 radical in hemimorphite at 110 K lies in the (100) mirror plane, hence explaining its monoclinic site symmetry, and those of the unique g_1 and A_1 axes indicate the O=O and O−H bonds along **b** and **c**, respectively. Also, the best-fit matrices **A** for the two more-distant protons are axial in symmetry as well and have their unique axes opposite in direction at (152.4, 180) and (152.4, 0), consistent with those from the oxygen atom of the water molecule to the protons of the two nearest hydroxyl groups (Figure 7.1b). Therefore, the most plausible model for Center I in hemimorphite at

110 K involves hole trapping on an O=O–H group formed from the water molecule and interacting with two equivalent protons of two nearest hydroxyl groups (Figure 7.1b). The anisotropic components of **A** for these two more-distant protons (Table 7.1), using the point-dipole model

$$T_z = (2\mu_0/4\pi)(g\beta_e g_n \beta_n / r^3) \quad (7.2),$$

where T_z is the traceless part ($T_x = T_y = -T_z/2$), predict a hole-nucleus distance of 2.33 Å, which is in reasonable agreement with the O−H1a and O−H1b distances of 1.99 Å at 110 K (Figure 7.1b). This agreement is even better, if one considers the fact that the isotropic component of the hyperfine coupling constant a = −0.9 mT (Table 7.1) indicates a small portion of the unpaired spin on the proton, and therefore provides further support for the formation of the HO_2 radical from the water molecule in the channel.

The orientations of the g_3 axis (56.4, 177.2) and the close-proton A_2 axis (54.4, 166) of Center I at 85 K suggest that the HO_2 radical is now inclined to the (100) plane. Also, the unique g_1 and A_1 axes are not along **b** or **c**, explaining the triclinic site symmetry at this temperature. Moreover, the two protons from the nearest hydroxyl groups (Figure 7.1c) are not equivalent either (Table 7.1). The best-fit spin Hamiltonian parameters of Center I at 40 K also suggest an inclined HO_2 radical relative to the (010) plane but differ significantly in both principal values and principal axis directions from those of its counterpart at 85 K (Table 1), indicating a marked thermal effect in this temperature range.

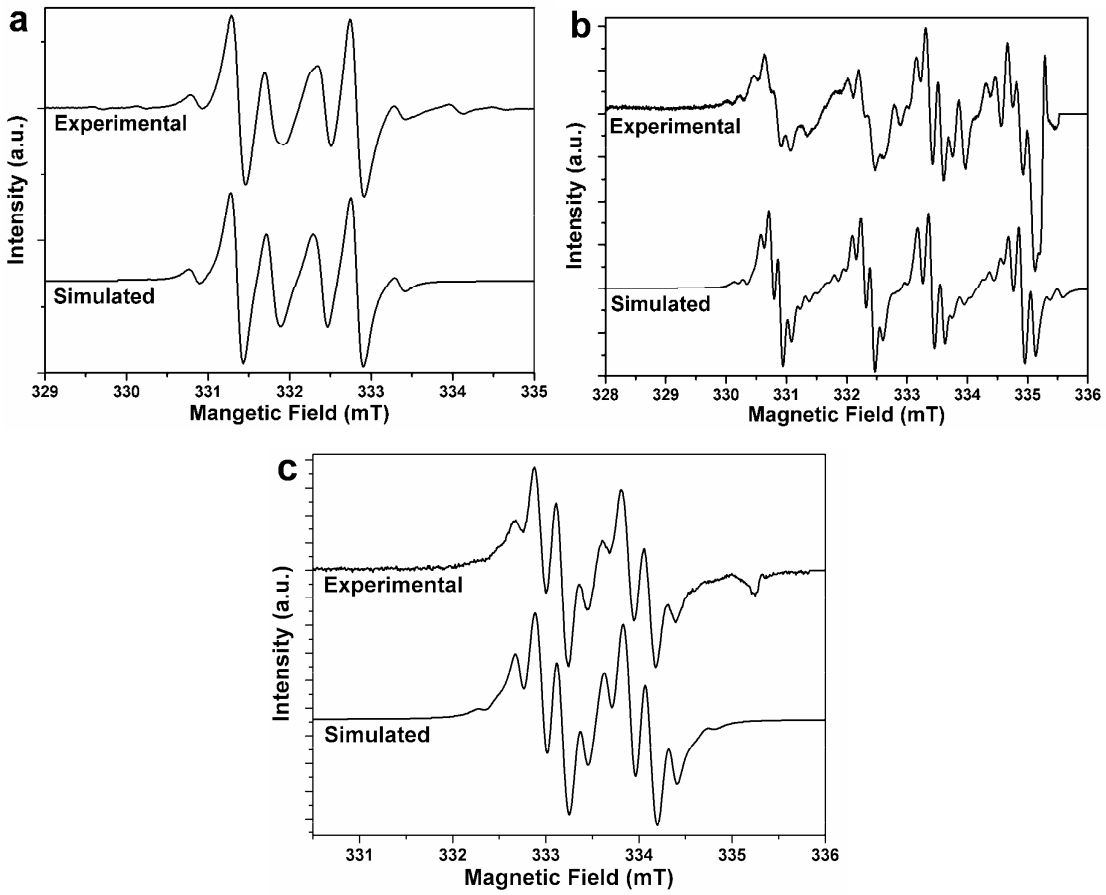

Figure 7.3 Comparison of experimental and simulated EPR spectra of Center I: a) **B**^**b** = ~42° in the (100) plane and v = 9.387 GHz at 110 K; b) **B**^**b** = ~50° in the (001) plane and v = 9.386 GHz at 40 K, and c) **B**^**a** = ~35° in the (010) plane and v = 9.386 GHz at 7 K.

The best-fit spin-Hamiltonian parameters of HO_2 radical at 7 K are closely comparable to those at 110 K, except that the superhyperfine coupling constants of the the two more-distant protons at 7 K are notably smaller than those at 110 K (Table 1).

Attempts to determine hyperfine structures of the HO_2 radical from additional protons expected in the hemirmorphite structure (Figure 7.1) have been made by use of pulsed electron nuclear double resonance (ENDOR) and electron spin echo

envelope modulation (ESEEM) measurements at temperatures from 4 K to 40 K but were not successful, presumably owing to a short spin-relaxation time of this center.

7.3.3 Monoclinic structures optimized by DFT calculations

The two monoclinic structures of space groups *Cc* and *Ic* with completed ordered O-H systems suggested by Libowitzky *et al*. (1998) differ only in the choice of the origin. Our DFT calculations for these two monoclinic space groups started with their unit-cell parameters and atomic fractional coordinates transformed from those of the *Abm2* structure by using the relationships described in Libowitzky *et al*. (1998). Our calculations show that both monoclinic structures converged readily and are, as expected, almost identical in the calculated energies. These structures are characterized by an angle of 29° between the water molecule and the (010) plane, and have two non-equivalent hydroxyl groups to the water molecule (r = 1.67 Å vs 2.48 Å).

Another monoclinic structure with completely ordered O-H systems evaluated by DFT calculations was derived from the orthorhombic one of space group *Imm2* (Hill *et al.* 1977) by the matrix (1, 0, 0 / 0, 1, 0.5 / 0, 0, 0.5). The resulting structure of space group *Im* converged readily as well but is energetically slightly less favorable than its *Cc* and *Ic* counterparts (*i.e.*, ΔE = 2.8 kcal/mol). The most salient feature of the *Im* structure are that its water molecule is parallel to the (010) plane and has two equivalent protons from the nearest hydroxyl groups (r = 2.06 Å).

7.3.4 Phase transitions and proton ordering in hemimorphite

Our single-crystal EPR spectra of the HO_2 radical, measured in the temperature range from 4 K to 275 K (Figure 7.2), provide unambiguous evidence that hemimorphite undergoes two reversible phase transitions at ~98 K and ~21 K (Libowitzky & Rossman, 1997; Libowitzky *et al.*, 1998; Kolesov, 2006). Moreover, quantitatively determined proton hyperfine and superhyperfine coupling constants of this radical at 110 K, 85 K, 40 K and 7 K provide detailed information about the locations and orientations of the water molecule and hydroxyl groups in hemimorphite at these temperatures.

Specifically, the observed EPR spectra and the best-fit spin Hamiltonian parameters of the HO_2 radical at 110 K are consistent with the location of the water molecule at the center of the channel and the presence of two equivalent protons from the nearest hydroxyl groups (Figure 7.1b). The reduction in the observed site symmetry of the HO_2 radical below ~98 K supports the suggestion of Libowitzky *et al*. (1998) that the precursor water molecule is displaced (and rotated) away from the center of the channel. In particular, the angles of the inclined HO_2 radical relative to the **c** axis at ~34° and 29° from EPR data at 85 K and 40 K, respectively, are closely comparable to the magnitude of rotation for the water molecule in the *Abm*2 structure from the neutron diffraction experiment of Libowitzky *et al*. (1998). In addition, the distinct superhyperfine coupling constants for the two distant protons confirm that the two nearest hydroxyl groups are symmetrically nonequivalent below the ~98 K phase transition (Figure 7.1c; Libowitzky *et al*., 1998). Moreover, the notable differences in

both the experimental spectra (Figure 7.2) and the best-fit spin Hamiltonian parameters at 85 K and 40 K (Table 7.1) suggest a significant thermal effect on the ordering and rotation of the water molecule in the channel in this temperature range.

Table 7.3 Unit-cell parameters and fractional coordinates of atoms in monoclinic hemimorphite optimized by DFT calculations.

	Im a = 8.448 Å, b = 11.899 Å, c =10.132 Å, α =115.2°			*Ic* a = 8.154 Å, b = 12.004 Å, c = 10.262 Å, α = 115.3°		
	x/a	y/b	z/c	x/a	y/b	z/c
Zn1	0.29558	−0.33931	0.09284	0.29162	−0.3375	0.09524
Zn2	0.20481	−0.16003	−0.06742	−0.28996	−0.3477	0.09517
Zn3	0.29506	0.33990	−0.06718	0.21325	−0.15566	−0.06358
Zn4	0.20495	0.16016	0.09260	−0.20987	−0.15814	−0.05854
Si1	0	−0.14528	−0.30633	0.00026	−0.14470	0.20020
Si2	0	0.14531	−0.16100	0.00548	0.14129	0.34207
Si3	0	0.14542	0.33871	–	–	–
Si4	0	−0.14541	0.19367	–	–	–
O1	0.16031	−0.20514	−0.27413	0.16274	−0.20818	−0.27021
O2	0.16039	0.20512	−0.06902	0.15027	0.21237	−0.05863
O3	0	−0.16095	−0.47322	0.16571	−0.20139	0.23665
O4	0	0.16131	0.18760	−0.17930	0.19033	−0.07350
O5	0	0.00002	−0.18457	0.00527	−0.15897	0.03556
O6	0.16032	−0.20511	0.22607	0.00257	0.15298	0.19048
O7	0	0.00007	0.31473	0.00875	−0.00135	−0.17811
O8	0	0.16090	−0.31226	0.32293	−0.00327	−0.45083
O9	0	−0.16173	0.02645	0.32301	0.00424	0.01062
O10	0.16043	0.20514	0.43070	0.48306	−0.01262	−0.23138
O11	0.30969	0.00031	−0.47327	–	–	–
O12	−0.50000	0.00212	−0.22159	–	–	–
O13	0.31052	0.00002	0.02667	–	–	–
O14	−0.50000	−0.00554	0.27671	–	–	–
H1	0.38375	0.00161	−0.39978	0.36951	−0.00253	−0.36139
H2	0.41136	0.00093	−0.16132	0.06619	−0.49789	0.04438
H3	0.38230	−0.00030	0.10110	0.41653	−0.00412	−0.14801
H4	0.41138	−0.00142	0.33949	0.41765	0.03281	0.30771

Note that all atoms, including symmetrically equivalent ones, are included for comparison.

The EPR spectra of the HO_2 radical below the ~21 K phase transition and the best-fit spin-Hamiltonian parameters at 7 K (Table 7.1) confirm the suggestion of Libowitzky *et al*. (1998) that the hemimorphite structure with completed ordered O−H system at low temperature is monoclinic. However, our EPR data do not support the *Cc* or *Ic* structures proposed by Libowitzky *et al*. (1998). Specifically, the HO_2 radical in the *Cc* and *Ic* structures is expected to be located at a general position, which gives rise to four-fold splittings from both the monoclinic crystal symmetry and the (010) crystal twinning (*cf*. Libowitzky *et al*. 1998). Also, the two protons from the nearest hydroxyl groups for a HO_2 radical in these structures are magnetically nonequivalent. Therefore, the *Cc* and *Ic* structures are incompatible with the observed EPR spectra of the HO_2 radical at <21 K (Figure 7.2). The *Im* structure (Table 7.3), on the other hand, predicts that the HO_2 radical in the (100) mirror plane has no magnetic site splitting but can account for the observed splittings in the EPR spectra at <21 K (Figure 7.2) by the (010) crystal twinning. Also, the two protons from the nearest hydroxyl groups are equivalent to the HO_2 radical in the (100) mirror plane. Moreover, the increased distance from the water molecule to the protons of the nearest hydroxyl groups in the optimized *Im* structure can explain the smaller proton superhyperfine coupling constants at 7 K relative to those at 110 K (Table 7.1).

7.4 Conclusions

Single-crystal EPR spectra of gamma-ray-irradiated hemimorphite, measured from 275 K to 4 K, disclose a HO_2 radical. The spectral variations of this HO_2 radical

show that hemimorphite undergoes two reversible phase transitions at ~98 K and ~21 K. The best-fit spin-Hamiltonian parameters, including ^{1}H superhyperfine coupling constants, at 110 K show that the HO_2 radical takes the position of the H_2O molecule in the structural channel and interacts with two equivalent protons of the closest hydroxyl groups. Data-fitting results of spectra at 85 K and 40 K confirm the structural model of Libowitzky *et al*. (1998), which suggests that the water molecule is displaced (and rotated) from the center of the channel, while the two hydroxyal groups are not equivalent to the H_2O molecule. Spin-Hamiltonian parameters fitted from spectra collected at 7 K confirm that hemimorphite has a monoclinic structure with completely ordered O-H systems below the phase transition at ~21 K.

7.5 References

ADAMO, C., & BARONE, V. (1999): Toward reliable density functional methods without adjustable parameters: the PBE0 model. *J. Chem. Phys.*, **110**, 6158–6170

ADRIAN F. J., COCHRAN E. L., & BOWERS, V. A. (1967): ESR spectrum of HO2 in argon at 4.2 K. *J. Chem. Phys.*, **47**, 5441-5442.

BARCLAY, G. A. & COX, E. G. (1960): The structure of hemimorphite. *Z. Kristallogr.*, **113**, 23-29.

BEDNAREK, J. & PLONKA, A. (1987): Single-crystal electron spin resonance studies on radiation-produced species in ice I_h. Part 2 – The HO_2 radical. *J. Chem. Soc., Faraday Trans.1*, **83(12)**, 3737-3747.

BISSENGALIYEVA, M.R., BEKTURGANOV, N.S. & GOGOL, D.B. (2010): Thermodynamic characteristics of a natural zinc silicate hemimorphite. *J. Therm. Anal. Calorim*. **101**, 49-58.

BREUER, K., TELES, J.H., DEMUTH, D., HIBST, H., SCHÄFER, A., BRODE, S. & DOMGÖRGEN, H. (1999): Zinc silicates: very efficient heterogeneous catalysts for the addition of primary alcohols to alkynes and allenes. *Angew. Chem. Int. Ed*. **38**, 1401–1405.

BROWN, K., MOMBOURQUETTE, M.J. & WEIL, J.A. (2003): EPR-NMR (Users' Manual). Department of Chemistry, University of Saskatchewan, Saskatoon, SK., Canada.

CABALA, J., KRUPA, P. & MISZ-KENNAN, M. (2009): Heavy metals in mycorrhizal rhizospheres contaminated by Zn-Pb mining and smelting around Olkusz in southern Poland. *Water Air Soil Pollution* **199**, 139-149.

CANO, N.F., GALLEGOS, E.A. & WATANABE, S. (2009): Phase change and pyroelectricity in natural hemimorphite. *Rad. Effects Defects Solids*, **164**, 748-754.

CATILLON-MUCHERIE, S., AMMARI, F., KRAFFT, J.-M., LAURON-PERNOT, H., TOUROUDE, R. & LOUIS, C. (2007): Preparation of coimpregnated Cu–Zn/SiO_2 catalysts: Influence of the drying step on metallic particle size and on Cu0–ZnII interactions. *J. Phys. Chem. C* **111**, 11619–11626.

CATTON, R. C. & SYMONS, M. C. R. (1969): Unstable intermediates. Part LX. HO_2 radical in γ-irradiated strontium chloride hexahydrate. *J. Chem. Soc. A*, 1393-1395.

CHUMAKOVA, N. A., & YANKOVA, T. S., & VOROBIEV, A. Kh. (2008): EPR study of the orientation distribution function of HO2 radicals ordered by light irradiation. *Appl. Magn. Reson.*, **33**, 117-126.

COOPER, B. J. & GIBBS, G. V. (1981): The effects of heating and dehydration on the crystal structure of hemimorphite up to 600°C. *Z. Kristallogr.*, **156**, 305-321.

DACHS, E. & GEIGER, C.A. (2009): Heat-capacity behaviour of hemimorphite, $Zn_4Si_2O_7(OH)_2 \cdot H_2O$, and its dehydrated analogue $Zn_4Si_2O_7(OH)_2$: a calorimetric and thermodynamic investigation of their phase transitions. *Eur. J. Mineral*. **21**, 971–988.

DAY, S.J. & BOWELL, R.J. (2005): Atypical and typical zinc geochemistry in a carbonate setting, Sä Dena Hes Mine, Yukon Territory, Canada. *Geochem. Explor. Environ. Analysis* **5**, 255-266.

DOVESI, R., SAUNDERS, V.R., ROETTI, C., ORLANDO, R., ZICOVICH-WILSON, C.M., PASCALE, F., CIVALLERI, B., DOLL, K., HARRISON, N.M., BUSH, I.J., D'ARCO, P., LLUNNELL, M. (2006): CRYSTAL 2006, User's manual. University of Torino, Torino. http://www.crystal.unito.it

ESPIARI, S., RASHCHI, F. & SADRNEZHAAD, S.K. (2006): Hydrometallurgical treatment of tailings with high zinc content. *Hydrometall*. **82**, 54–62.

FROST, R.L., BOUZAID, J.M. & REDDY, B.J. (2007): Vibrational spectroscopy of the sorosilicate mineral hemimorphite $Zn_4(OH)_2Si_2O_7 \cdot H_2O$. *Polyhedron* **26**, 2405–2412.

GALLEGOS E.A., CANO N.F., WATANABA S., & CHUBACI J.D.F. (2009): Thermoluminescence, infrared reflectivity and electron paramagnetic resonance properties of hemimorphite. *Rad. Measur*. **44**, 11-17.

GEIGER, C.A. & DACHS, E. (2009): Quasi-ice-like C_p behavior of molecular H_2O in hemimorphite $Zn_4Si_2O_7(OH)_2 \bullet H_2O$: C_p and entropy confined H_2O in microporous silicates. *Am. Mineral*. **94**, 634–637.

HILL, R.J., GIBBS, G.V., CRAIG, J.R., ROSS, F.K. & WILLIAMS, J.M. (1977): A neutron diffraction study of hemimorphite. *Zeit. Kristal*. **146**, 241–259.

JAFFE, J.E., & HESS, A.C. (1993): Hartree-Fock study of phase changes in ZnO at high pressure. *Phys. Rev.* B **48**, 7903-7909.

KOLESOV, B. (2006): Raman investigation of H_2O molecule and hydroxyl groups in the channels of hemimorphite. *Amer. Mineral*. **91**, 1355–1362.

Lang R, Calvo C, Datars WR (1977) Phase transformation in $AlPO_4$ and quartz studied by electron paramagnetic resonance of Fe^{3+}. *Can. J. Phys.* **55**:1613-1620.

Li, Z. & Pan, Y. (2012) First-principles calculations of the E'_1 center in quratz: Structural models, ^{29}Si hyperfine parameters and association with Al impurity. In J. Goetze and R. Mockel, eds., *Quartz: Deposits, Mineralogy and Analytics, Springer-Verlag, Berlin*, 161-175.

LIBOWITZKY, E. & ROSSMAN, G.R. (1997): IR spectroscopy of hemimorphite between 82 and 373 K and optical evidence for a low-temperature phase transition. *Eur. J. Mineral*. **9**, 793-802.

MAO, M., LIN, J. & PAN, Y. (2010): Hemimorphite as a natural sink for arsenic in zinc deposits and related mine tailings: Evidence from single-crystal EPR spectroscopy and hydrothermal synthesis. *Geochim. Cosmochim. Acta* **74**, 2943-2956.

MAO, M. & PAN, Y. (2012): Nature of heavy metals in hemimorphite: A cation-exchange and single-crystal EPR study. *Can. Mineral.* **49**, 31-43.

MCDONALD, W. S. & CRUICKSHANK D. W. J. (1967): Refinement of the structure of hemimorphite. *Z. Kristallogr.*, **124**, 180-191.

PERDEW, J. P., BURKE, K., & WANG, Y. (1996): Generalized gradient approximation for the exchange-correlation hole of a many electron system. *Phys. Rev.* B **54**, 16533-16539.

Pisani, C. (1996): Quantum-mechanical ab-initio calculation of the properties of crystalline materials. Springer.

Pisani, C., Dovesi, R., Orlando, R. (1992): Near-Hartree-Fock wave functions for solids: the case of crystalline silicon. *Int. J. Quant. Chem.* **42**, 5–33.

RAE, A. D. (1969): Relationship between the experimental Hamiltonian and the point symmetry of a paramagnetic species in a crystal. *J.Chem.Phys.*, **50**, 2672-2685.

RADHAKRISHNA, S., CHOWDARI, B. V. R., & KASIVISWANATH, A. (1976): EPR studies of the hydroperoxy radical in X-irradiated single crystals of $BaCl_2 \bullet H_2O$. *Chem. Phys. Lett.*, **40**, 134-138.

SCHAIDER, L.A., SENN, D.B., BRABANDER, D.J., MCCARTHY, K.D. & SHINE, J. P. (2007): Characterization of zinc, lead, and cadmium mine waste: implications for transport, exposure and bioavailability. *Environ. Sci. Technol*. **41**, 4164–4171.

SERYOTKIN, Y.V. & BAKAKIN, V.V. (2011): Structural evolution of hemimorphite at high pressure up to 4.2 GPa. *Phys. Chem. Minerals* **38**, 679-684.

TAKÉUCHI, Y., SASAKI, S., & JOSWIG, W. (1978): X-ray and neutron diffraction study of hemimorphite. *Proc. Japan Acad.*, **54B**, 577-582.

WALDER, I.F. & CHAVEZ, W.X.Jr. (1995): Mineralogical and geochemical behavior of mill tailing material produced from lead-zinc skarn mineralization, Hanover, Grant County, New Mexico, USA. *Environ. Geol*. **26**, 1-18.

WYARD, S. J., SMITH, R. C., & ADRIAN F. J. (1968): ESR spectrum of HO_2 in solutions of hydrogen peroxide in water at 77 K. *J. Chem.. Phys.*, **49**, 2780-2783.

YURIEVA, T.M., KUSTOVA, G.N., MINYUKOVA, T.P., POELS, E.K., BLIEK, A., DEMESHKINA, M.P., PLYASOVA, L.M., KRIEGER, T.K. & ZAIKOVSKII, V. I. (2001): Non-hydrothermal synthesis of copper-, zinc- and copper–zinc hydrosilicates. *Mater. Res. Innov*. **5**, 3–11.

CHAPTER 8

Conclusions

This single-crystal EPR spectroscopic study, supplemented by data from other analytical techniques (FTIR, EMPA, and ICPMS), hydrothermal experiments, and first-principles theoretical calculations, provides detailed structural models for several important radiation-induced defects in apophyllites, prehnite, and hemimorphite, with direct relevance and potential applications to remediation of heavy metalloid contamination and nuclear waste disposal. Major findings of this study can be summarized as follow:

1) EPR spectra reveal a NH_2 radical in γ-ray irradiated fluorapophyllite. The best-fit spin-Hamiltonian parameters show that the NH_2 radical in fluorapophyllite at room temperature resides at the K site and spins rapidly along the molecule C_2 axis, which coincides with the crystallographic **c** axis. These results, together with data from FTIR and electron-microprobe analyses, suggest that the NH_2 radical is most likely formed from the radiolysis of NH_4^+ ion. This is the first-ever report of the NH_2 radical in the mineral lattice.

2) Single-crystal EPR and ESEEM spectra reveal a radiation-induced O^- center

and its biradical pairs in hydroxylapophyllite. The best-fit spin-Hamiltonian parameters suggest that the O^- center represents electron trapping on the hydroxyl oxygen atom after removal of its proton. This model is further supported by excellent agreements between the best-fit directions and calculated distances of the O^--O^- biradical pairs with those of the corresponding OH^--OH^- pairs. This O^- center is bleached out at 300°C but can be restored by γ-ray irradiation.

3) Single-crystal CW-EPR and pulsed ENDOR spectroscopic measurements, along with isothermal and isochronal annealing experiments, allow a detailed study of an Al-O^- center in gamma-ray-irradiated prehnite. The best-fit spin-Hamiltonian parameters show that this center corresponds to hole trapping on the apical hydroxyl oxygen atom coordinated to Al at an octahedral site. These results support the ^{VI}Al-O^--^{VI}Al model of Clozel *et al.* (1995) for the radiation-induced B center in kaolinite.

4) Single-crystal EPR spectra of gamma-ray-irradiated hemimorphite (Mapimi, Durango, Mexico) reveal the presence of $[AsO_4]^{4-}$ and $[AsO_4]^{2-}$ centers. These EPR results along with data from hydrothermal experiments show that hemimorphite is capable of sequestering significant amounts of arsenate in its crystal lattice, representing an important natural sink for As (and other heavy metalloids) in supergene non-sulfide Zn deposits and Zn mine tailings.

5) Spin-Hamiltonian parameters from single-crystal EPR spectra of

hemimorphite (Reneville, Congo) at 295 K and 120 K show that Cu^{2+} resides at the tetrahedral Zn site, not in the channels as previously suggested by the powder EPR study of Gallegos *et al*. (2009). This result is consistent with cation-exchange experiments that show Cu and As are not readily exchanged. Cd and Pb in hemimorphite, on the other hand, are readily exchanged and probably reside in the structural channels. These results suggest that hemimorphite is potentially useful for remediation of heavy metalloid contamination.

6) Single-crystal EPR spectra of gamma-ray-irradiated hemimorphite, measured from 275 K to 4 K, reveal a hydroperoxy radical HO_2. The EPR spectra of this radical show that hemimorphite undergoes two reversible phase transitions at ~98 K and ~21 K. The best-fit spin-Hamiltonian parameters show that the HO_2 radical occupies the position of the H_2O molecule and interacts with two protons from the closest hydroxyl groups. Spin-Hamiltonian parameters obtained from spectra measured at 85 K and 40 K confirm the suggestion of Libowitzky *et al*. (1998) that the water molecule is displaced (and rotated) from the center of the channel. Spin-Hamiltonian parameters fitted from spectra measured at 7 K confirm that hemimorphite has a monoclinic structure with completely ordered O-H systems below the phase transition at ~21 K.

Appendix A

A review of EPR, ENDOR, and ESEEM techniques

A.1 Electron Paramagnetic Resonance Spectroscopy

Electron Paramagnetic Resonance (EPR) Spectroscopy, which is also called Electron Spin Resonance (ESR) Spectroscopy, is a method to record the microwave absorption of a sample in a magnetic field. EPR spectroscopy is widely used in biochemistry, chemistry, geology, and physics.

The most remarkable feature of EPR is its capability to detect and distinguish paramagnetic centers in very low concentration (0.1%-0.0001%; Marfunin 1979). Therefore, EPR has been used for studying systems such as:

a) Free radicals in solid, liquid or aqueous phases;

b) Transition metal ions;

c) Various point defects in crystals

d) Systems with more than one unpaired electron (biradicals or triplet-state systems); and

e) Systems with conducting electrons (metals and semiconductors; Weil & Bolton, 2007).

A.1.1 Fundamental Principles

Atoms and molecules both have electrons that surround their nuclei with specific orbitals; these electrons also spin. Commonly, according to the Pauli Exclusion Principle, if two electrons occupy the same sub-orbital, the energy of their spins would counteract each other. So, when there is only one electron occupying the electron sub-orbital, the spin is ½, producing a magnetic moment that can be oriented in an external magnetic field. Here, the interaction between the magnetic moment from an unpaired electron and the external magnetic field is called the Zeeman effect.

The orientation of the magnetic moment will be either similar or opposite to the direction of the external magnetic field. Thus, two energy levels occur, designated as m_s= 1/2 and m_s= -1/2.

When there is no external magnetic field, the two spin energy levels are degenerated. Once the magnetic field is applied, the two energy levels start splitting, and with the magnetic field rising, the splitting becomes larger and larger. If a microwave of specific energy enters the system, it will be absorbed when the gap between two energy levels is equal to the energy of the microwave emitted (Fig. A.1).

Here, the microwave energy $\Delta E = h\nu = E_{1/2}-E_{-1/2}$, "ν" is the microwave frequency. Since the $E_s = g\mu_0 B_0 M_s$, $\Delta E = h\nu = E_{1/2}-E_{-1/2} = 1/2g\mu_0 B_0-(-1/2)g\mu_0 B_0 = g\beta B_0$.

$h\nu = g\beta B_0$ .....(A.1)

Where "g" is the Zeeman splitting factor and it is a dimensionless parameter; "β" is the Bohr magneton and B_0 is the external magnetic field.

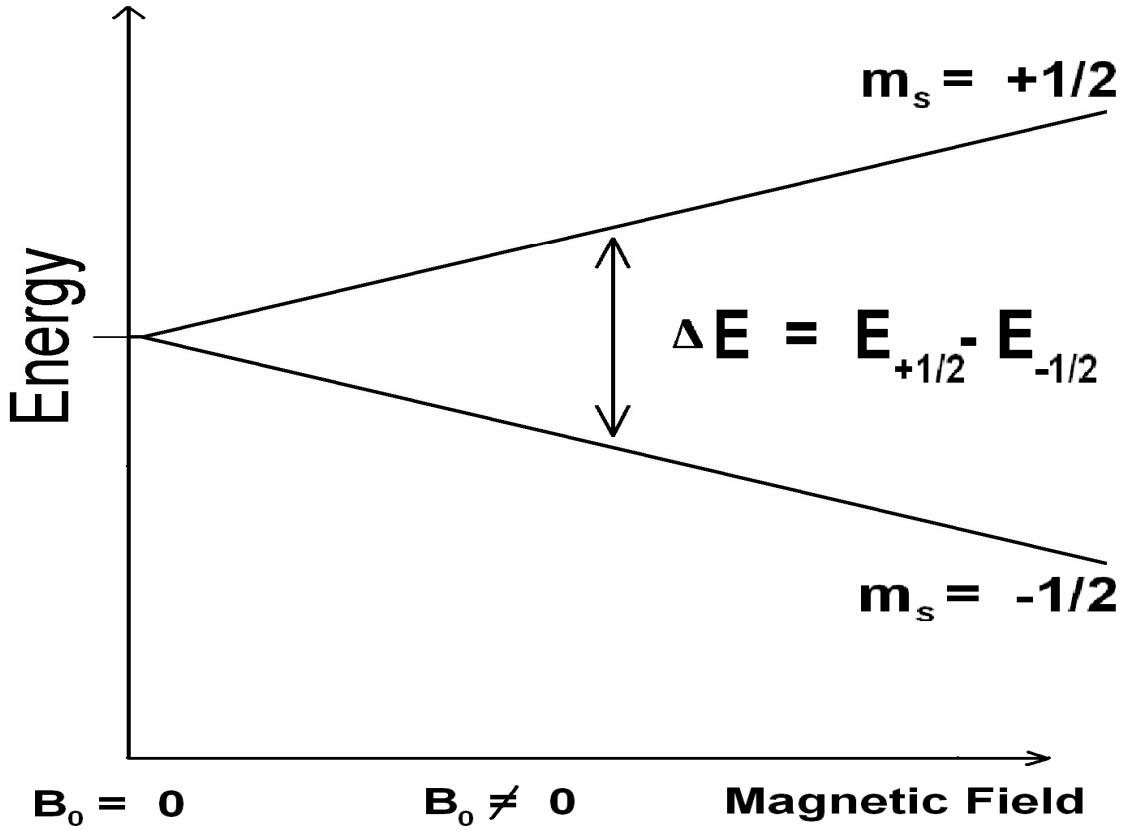

Figure A.1 The scheme of the spin energy levels for EPR.

Usually, the unpaired electrons in some orbitals of paramagnetic defects will be quenched by the orbital angular momentum and/or the crystal field (if in a solid). Therefore, different "g" values reflect the orbital that the unpaired electron occupies, or the symmetry of the crystal. If the unpaired electron stays on the ground state as a free electron, the "g" value for that is called "g_e", which is equal to 2.0023.

Due to the influence of the orbital angular momentum and the crystal field, the "g" values are useful for providing information about the nature, location and local

symmetry of paramagnetic defects. Because of the 3-dimensional structure of paramagnetic defects, a “g” matrix is required to describe the Zeeman energy.

A.1.2 The spin Hamiltonian and g tensor

Besides the Zeeman Effect, there are several other factors that influence EPR spectra, including the nuclear spin parameter “A”, electron quadrupole interaction parameter “D”, and the nuclear quadrupole interaction parameter “P”; spin Hamiltonian is used to describe the EPR spectra. In the spin-Hamiltonian, each parameter has its own term, and all the factors in one center are summed together. For example, for the atomic hydrogen (H^0) system, there is only one unpaired electron and a single nucleus with a nuclear spin number I =1/2, so the spin-Hamiltonian is: $H = g_e\beta_e B_0 S + SAI - g_n\beta_n B_0 I$.

The “A” parameter arises from interaction between the unpaired electron(s) and a nucleus with non-zero nuclear spin. The nuclear spin splits the energy level(s) from the unpaired electron into (2I+1) levels with the external magnetic field. That makes the fine structure absorption line(s) also split into 2I+1 lines. This splitting is also called the hyperfine splitting, and the lines are called the hyperfine structures.

When a center contains more than one unpaired electron (S>1/2), the interaction between unpaired electrons will occur. This electronic quadrupole interaction leads the energy levels to split without any external magnetic field, called the initial splitting or zero-field splitting. Here, we use the “D” parameter to describe the perturbation on the energy levels.

When nuclei have nuclear spin I>1/2, another parameter "P", describing the nuclear quadrupole interaction, is used in the spin-Hamiltonian. Just like the "D" parameter, the "P" parameter also produces an initial splitting before an external magnetic field is applied.

Besides the parameters mentioned above, other parameters such as the fourth-degree parameters S^4 and I^4, and higher-order parameters may occur, but are very small or not relevant to this work, and will not be discussed here.

For a single crystal, the paramagnetic centers could be isotropic or anisotropic in local symmetry, so a tensor is involved in some parameters to describe the spin Hamiltonian.

When an EPR measurement is taken to determine the local structural information of paramagnetic defects in a single crystal, an experimental coordinate system must be chosen. Commonly the X, Y, and Z axes are used in the orthogonal coordinate system and these axes are not necessarily coincident with the crystallographic axes. So, the external magnetic field B is $B\cos\theta_x$, $B\cos\theta_y$, $B\cos\theta_z$, corresponding to the experimental X, Y, Z axes. If one uses the "g" term as an example and there is only the Zeeman term in a spin Hamiltonian, it will become:

$$H=\beta_e[B\cos\theta_x, B\cos\theta_y, B\cos\theta_z]\hat{g}\begin{vmatrix} S_x \\ S_y \\ S_z \end{vmatrix} \quad \text{.....(A.2)}$$

Here,

$$\hat{g}=\begin{vmatrix} g_{xx} & g_{xy} & g_{xz} \\ g_{yx} & g_{yy} & g_{yz} \\ g_{zx} & g_{yz} & g_{zz} \end{vmatrix}$$

Equation 1.2 also can be written as:

$H= H=\beta_e \mathbf{B}^T \hat{g} \mathbf{S}$ .....(A.3)

Now, an effective magnetic field vector B_{eff} is involved.

$\mathbf{B}_{eff}=[B\cos\theta_x, B\cos\theta_y, B\cos\theta_z]\hat{g}$ .....(A.4)

and

$H= \beta_e \mathbf{S} \mathbf{B}_{eff}$ .....(A.5)

The "$\mathbf{B}_{eff}$" factor includes the relationship between the orientation of the external magnetic field B, and that of the experimental coordinate system and the "g" tensor. From the "$\mathbf{B}_{eff}$", the orientation of the external magnetic field to the experimental coordinate system for single crystals can be calculated. The "g" matrix also can be calculated. After diagonalization of the "g" matrix, the principal values and principal axis orientations corresponding to the experimental coordinate system can be established for the center, and local structural information can then be obtained (Weil & Bolton, 2007).

A.1.3 EPR Spectrometers

A basic magnetic-field-sweep EPR spectrometer requires a microwave bridge, a variable magnetic field, a resonant cavity, a solid-state diode detector, and a computer for data acquisition (Fig. 2). Usually, commercial EPR spectrometers

produced are operated in the X band (ν = ~9.3 GHz), K band (ν = ~24 GHz), Q band (ν = ~36 GHz), and W band (ν = ~95 GHz) frequencies.

Following Figure A.2, a microwave of a specific frequency is produced from the klystron, and enters through the isolator that makes the microwaves all vibrate in the same orientation. The energy of microwave would be adjusted after it goes through the attenuator. When the microwave reaches the directional coupler, it will be divided into two parts: one is sent to the monitoring detector to record as a standard for comparison, and another is sent to the resonant cavity. Once the microwave reaches the detector, the detector can record the signal, and compare with the signal from the monitoring detector to analysis the quantity of absorption. Finally, the signal is amplified by the amplifier and recorded by the computer. During this process, the intensity of the magnetic field is rising linearly in a specific range, and resonances will happen in some magnetic field intensities depending on the sample in the cavity. Therefore, in the final spectrum, the x-coordinate would be the intensity of magnetic field in a range and the y-coordinate would be the intensity of absorption for the invariable microwave. The EPR spectrum usually is differentiated once to make it analysis convenient.

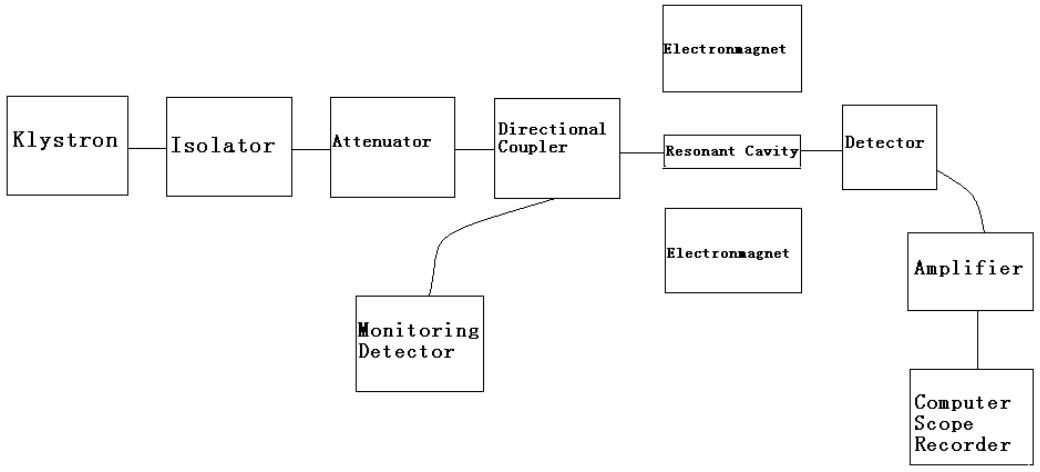

Figure A.2 Block diagram illustrating the basic components of an EPR spectrometer.

A.2 Electron-Nuclear double resonance spectroscopy

The electron-nuclear double resonance (ENDOR) spectroscopy is an advanced EPR technique, and has been widely applied in chemistry, biochemistry, and crystallography. Basically, the principle of ENDOR includes two steps: (1) an EPR transition is saturated by an intense microwave (mw) field and (2) a radio frequency (rf) induces nuclear spin transitions altering the populations of some of energy levels. Because ENDOR can provide detailed information of nuclei that have small hyperfine splitting, it is useful for studying molecular and electronic structures of paramagnetic species (Gemperle & Schweiger, 1991; Kispert & Piekara-Sady, 2006; Kulik & Lubitz, 2009; Nilges *et al.*, 2009).

A.2.1 Fundamental Principles of CW ENDOR

In the beginning, the ENDOR experiments were run with continuous wave (Keven & Kispert, 1976). In an S = 1/2 and I = 1/2 system, the energy levels of the unpaired electron and nucleus are split by an external magnetic field, and a few absorptions of an invariable microwave will be generated according to the magnetic field (Figure A.3). If the magnetic field is fixed on a hyperfine line, the mw will saturate this EPR transition. So, if a radio frequency is swept to this system, when the rf matches to a NMR transition, the saturation of this EPR transition will be relieved. Therefore, the ENDOR signal is actually the increase of the EPR signal due to the relief of saturation (Eaton & Eaton, 2004; Kispert & Piekara-Sady, 2006).

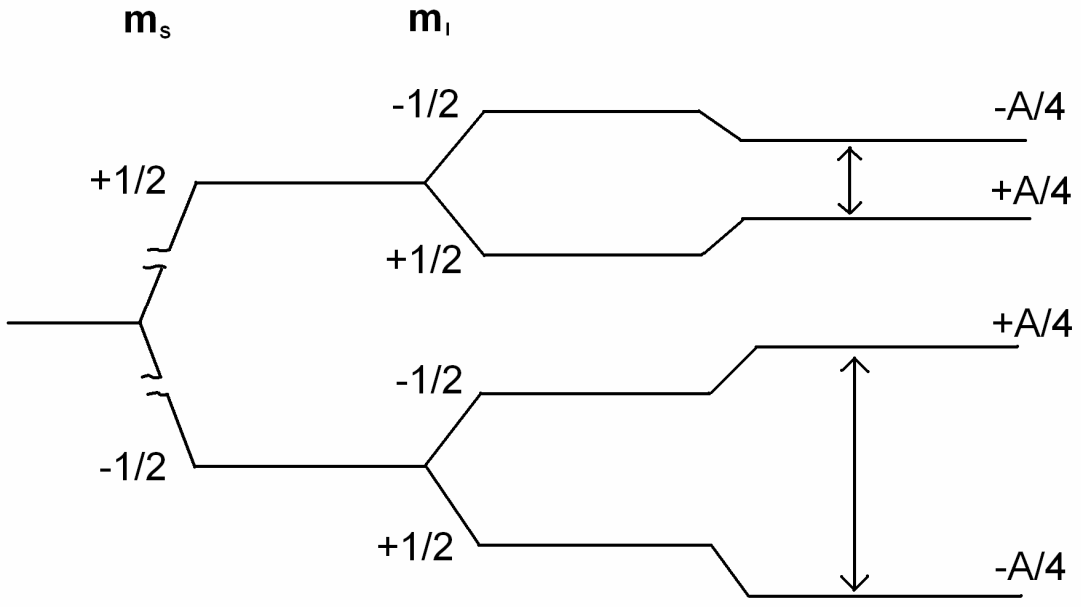

Figure A.3 Energy level diagram for the case of S = 1/2, I = 1/2, and A/2 < ν_n.

To analyze ENDOR spectra, the energy levels have to be obtained from an appropriate spin Hamiltonian. For a system with S = 1/2 and I ≥ 1/2, the spin Hamiltonian would be expressed:

$H = \beta \mathbf{B} g \mathbf{S} - g_n \beta_n \mathbf{BI} + \mathbf{SAI} + \mathbf{IPI}$ .....(A.6)

the four terms from left to right are *electronic Zeeman term*, *nuclear Zeeman term*, *hyperfine interaction term*, and *nuclear quadrupole term,* respectively. Here, the *nuclear quadrupole term* is only present when I > 1/2. According to the EPR selecting rules $\Delta m_S = \pm 1$ and $\Delta m_I = 0$, and NMR selecting rules $\Delta m_S = 0$ and $\Delta m_I = \pm 1$, if we consider I = 1/2 and A is isotropic,

$\nu_{ENDOR}^{\pm} = |\nu_n \pm A/2|$ .....(A.7)

here, the ν_n is the nuclear Larmor frequency which will decide the presence of ENDOR lines. If $|A|/2 > \nu_n$, the two ENDOR transitions are in the position of $\nu_n \pm |A|/2$, and if $|A|/2 < \nu_n$ the two ENDOR transitions will present at $|A|/2 \pm \nu_n$. When I > 1/2, the ENDOR transitions are also affected by the *nuclear quadrupole term*.

A disadvantage of CW ENDOR is that the intensity of the ENDOR transition lines is only a few percent of their corresponding EPR transitions (Gemperle & Schweiger, 1991; Kispert & Piekara-Sady, 2006), and CW ENDOR relies on a delicate balance of relaxation times, which can be difficult to achieve for some samples (Eaton & Eaton, 2004; Kispert & Piekara-Sady, 2006). However, pulsed ENDOR methods have been developed rapidly since 1960s (Mims, 1965; Gemperle & Schweiger, 1991). Unlike CW ENDOR, the entire sequence of pulsed ENDOR can be made short enough to exclude unwanted relaxation effects, and the pulsed ENDOR

efficiency can be up to 100%. Moreover, pulsed ENDOR also has more ways to manipulate the electron-nuclear spin system to simplify some complicated spectra (Gemperle & Schweiger, 1991; Chasteen & Snetsinger, 2000).

A.2.2 Fundamental Principles of pulsed ENDOR

There are two mainly used ENDOR pulse sequences, which are called "Davies ENDOR" and "Mims ENDOR". Each of them is based on the impact of rf pulses on the intensity of a spin echo that is produced by three pulses of mw frequency (Gemperle & Schweiger, 1991; Eaton & Eaton, 2004). Due to the produced electron spin echo, pulsed ENDOR can also be called ESE-ENDOR. In Davies ENDOR, an mw pulse sequence of "$\pi - T - \pi/2 - \tau - \pi - \tau -$ echo" is applied, whereas the rf is used between the first and second pulses. On the other hand, in Mims ENDOR, an mw pulse sequence of "$\pi/2 - \tau - \pi/2 - T - \pi/2 - \tau -$ echo" is applied, whereas the rf is used between the second and third pulses (Figure A.4). The Mims ENDOR is particularly effective for weakly coupled nuclei, but has some "blind" points, while the Davies ENDOR is useful for systems with large hyperfine interaction. Therefore, both pulse sequence methods have usually been used together for collecting more comprehensive data (Gemperle & Schweiger, 1991; Kispert & Piekara-Sady, 2006; Eaton & Eaton, 2004; Kulik & Lubitz, 2009).

Similarly to EPR spectroscopy, ENDOR also can be operated at X-band, Q-band, K-band, W-band, and so on. Because Larmor frequency increases proportionally to the external magnetic field but hyperfine splitting of specific nucleus

is independent of magnetic fields, the superimposed ENDOR signals of different nuclei can be resolved by running in different magnetic fields (Eaton & Eaton, 2004; Weil & Bolton, 2007; Kulik & Lubitz, 2009).

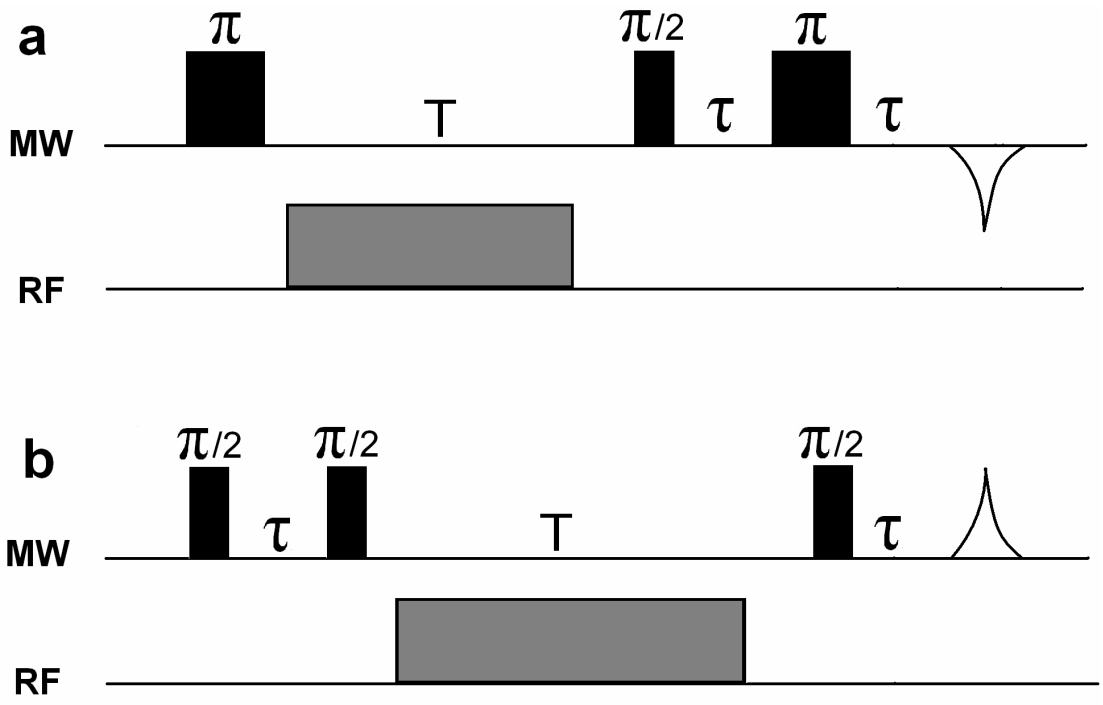

Figure A.4 The ENDOR pulse sequence: (a). Davies pulse sequence; (b). Mims pulse sequence.

A.3 Electron spin echo envelope modulation spectroscopy

Electron spin echo envelope modulation spectroscopy (ESEEM) is a pulsed EPR technique based on electron spin echo. Because the decay of primary electron spin echoes are modulated with frequencies that correspond to nuclear frequencies and their combinations, ESEEM is able to provide detailed nuclear structural information of the neighboring unpaired electron, so it becomes very useful in

investigating hyperfine and nuclear quadrupole coupling in solids (Chasteen & Snetsinger, 2000; Schweiger & Jeschke, 2001).

Fundamentally, an electron spin echo spectroscopy is formed from an echo as a function of the pulse-interval time. The simplest electron spin echo requires two mw pulses, and it is also known as a Hahn echo (Eaton & Eaton, 2004; Chasteen & Snetsinger, 2000). In Hahn echo, the pulse sequence is "$\pi/2 - T - \pi - T -$ echo" (Figure A.5). Before the first pulse starts, the selected external magnetic field arranges unpaired electrons precessing about the direction of the external magnetic field (z axis). Here, these electrons can be seen as vectors. Then, a short microwave pulse will be applied along the direction perpendicular to the external magnetic field. This microwave will cause these vectors to rotate 90° (x axis). Because different spins have slightly different Larmor frequencies, these spins are all precessing at different frequencies and diverge from average. After a specific time *t*, another microwave pulse will flip these vectors (i.e., spins) into 180°, so the faster and slower processing spins will be interchanged, and through the same time *t*, the vectors will reconverge and form echo which usually contains much electron and nuclear structural information. At last, the echo intensity will be recorded as a function of *t*. After Fourier transformation, the modulated echo decay curve becomes the spectrum of the nuclear modulation frequencies (Eaton & Eaton, 2004; Chasteen & Snetsinger, 2000; Schweiger & Jeschke, 2001).

For the two-pulse ESEEM, the linewidth of spectra is related to the phase memory time T_m of the electron spins which is usually larger than that of the

homogeneous EPR. Furthermore, the phase memory time $T_m^{(n)}$ of nuclear spins is commonly much longer than T_m. Therefore, the linewidth of two-pulse ESEEM spectrum is commonly larger than that of EPR, and the resolution in two-pulse ESEEM spectra may be inferior compared to ENDOR spectra. However, this disadvantage could be overcome by the three-pulse ESEEM spectroscopy (Eaton & Eaton, 2004; Schweiger & Jeschke, 2001).

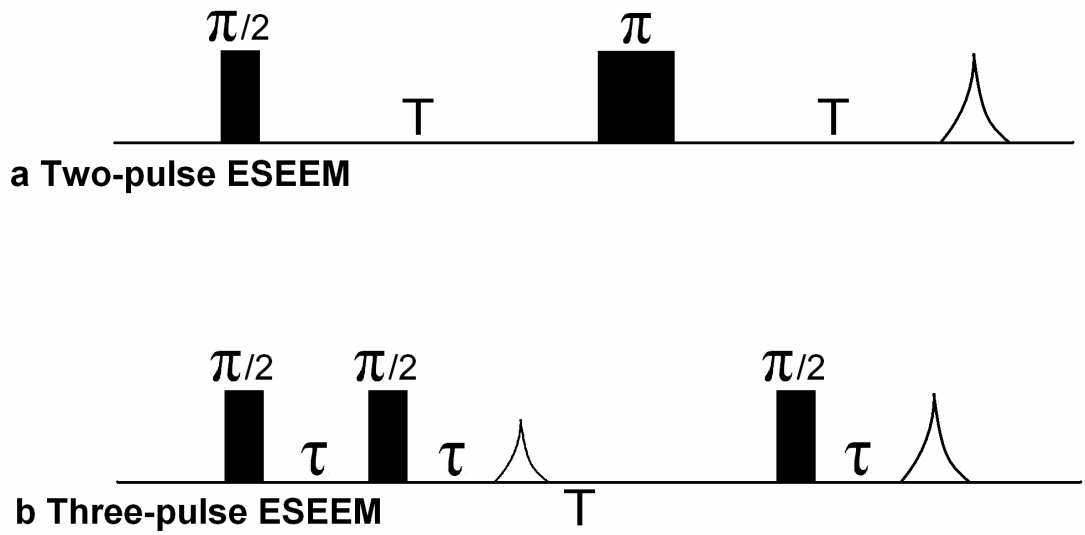

Figure A.5 The ESEEM pulse sequence: (a). Hahn pulse sequence; (b). Mims pulse sequence.

The sequence of three-pulse ESEEM is "π/2 − τ − π/2 − T − π/2 − τ − echo". Similarly with two-pulse ESEEM, the first pulse of three-pulse ESEEM has same effect as that of two-pulse ESEEM. During the free evolution of the first time τ, the electron coherence has evolved on a given electron transition, and then the second pulse of π/2 is applied, which creates nuclear coherence and causes a coherence branching. After another time interval of τ, a spin echo forms. Through an evolution

time T, the third $\pi/2$ pulse leads the nuclear coherence back to electron coherence which may evolve on any electron transition during the third time interval τ. And, finally, a stimulated echo forms, which is recorded as a function of τ (Eaton & Eaton, 2004; Chasteen & Snetsinger, 2000; Schweiger & Jeschke, 2001).

A main advantage of three-pulse ESEEM over two-pulse ESEEM is that the decay of the spin echo is no longer governed by the phase memory time T_m ($\approx T_{2e}$), and is actually related to the spin-lattice or longitudinal relaxation time of the electron spin (T_{1e}). Due to $T_{1e} \geq T_{2e}$, the envelope decays more slowly in three-pulse ESEEM than in two-pulse ESEEM, so spectra of three-pulse ESEEM give a better resolution in general. However, the time τ between the first and second pulses has to be added as "dead time" of the instrument. Therefore, some rapidly decaying modulation can be missed. To investigate these kinds of modulations, two-pulse sequence is used (Chasteen & Snetsinger, 2000).

A.4 References.

CHASTEEN, N. D. & SNETSINGER, P. A. (2000) ESEEM and ENDOR spectroscopy. *Physical Methods in Bioinorganic Chemistry Spectroscopy and Magnetism*, 187-231.

EATON, G. R. & EATON, S. S. (2004) Electron-nuclear double resonance spectroscopy and electron spin echo envelope modulation spectroscopy. *Comprehensive coordination chemistry II*, **2**, 49-55.

GEMPELE, C. & SCHWEIGER, A. (1991) Pulsed electron-nuclear double resonance methodology. *Chem. Rev.*, **91**, 1481-1505.

KISPERT, L. D. & PIEKARA-SADY, L. (2006) ENDOR spectroscopy. *Handbook of Applied Solid State Spectroscopy*, 151-199.

KULIK, L. & LUBITZ, W. (2009) Electron-nuclear double resonance. *Photosynth. Res.*, **102**, 391-401.

MARFUNIN, A. S. (1979) Spectroscopy, luminescence and radiation centers in minerals. *Springer-verlag berlin Heidelberg New York*.

MIMS, W. B. (1965) Pulsed ENDOR experiments. *Proc. R. Soc. Lond. A*, **283**, 452–457

NILGES, M. J., PAN, Y., AND MASHKOVTSEV, R. I. (2009) Radiation-induced defects in quartz III. Single-crystal EPR, ENDOR, and ESEEM study of a peroxy radical. *Phy. Chem. Minerals*, **36**, 61-73.

SCHWEIGER, A. & JESCHKE, G. (2001) Principles of pulse electron paramagnetic resonance. *Oxford Univerisity Press*.

WEIL, J. A., & BOLTON, J. R. (2007): Electron paramagnetic resonance, elementary theory and practical applications. *Wiley Interscience*.

Appendix B

Summary of EPR sample preparation, experimental methods, EPR spectra, data-fitting input, and output files.

This appendix summarizes data about the sample preparations for EPR analyses, experimental methods, and a list of all EPR spectra, as well as a list of input and output files for fitting spin-Hamiltonian parameters in this thesis. My purpose is to provide detailed experimental procedures as a reference for further single-crystal EPR experiments.

B.1 Sample preparation.

For single-crystal EPR experiments in this thesis, all mineral samples were measured in NMR or EPR tubes, which have been shown to contain no paramagnetic signals at RT. Therefore, samples have been cut to fit into NMR tubes (5 mm in diameter) or EPR tubes (3 mm in diameter). Because of the sealing issues at cryostat temperatures, NMR tubes were used only for room temperature experiments, whereas EPR tubes were used for both room- and cryostat-temperature experiments.

To select the best crystal for EPR experiments, a few crystals with appropriate sizes (usually less than 5 mm or 3 mm in diameter) were first manually removed from a hand specimen. These crystals were then been examined carefully under a petrologic

microscope to avoid twinning, cracking, and visible inclusions, which could all influence the EPR signal. The selected crystals were then fit in a NMR or EPR tube in different orientations. Sand paper may be used to grind down some large crystals.

Mineral powders were obtained by grinding in a ceramic mortar for about 15 minutes and weighed for ~0.15 gram for collecting EPR spectra. The selected crystals for produce powder samples were also usually examined for purity under a binocular microscopy.

B.2 EPR experiments

To obtain sufficient data for fitting spin-Hamiltonian parameters, the single-crystal EPR spectra usually have to be collected on more than one experimental plane, and three experimental planes would be the most desirable.

In a single-crystal EPR experiment, the selected crystal is glued by vacuum grease on the top of a plastic rod that is inserted into a NMR/EPR tube. Between the rod and the tube, suitable adhesive tape is glued on the rod to avoid movement of the rod and the tube. The top part of the tube is attached to a goniometer (a home-made goniometer for NMR tubes and the Bruker ER218G1 goniometer for EPR tubes), and the bottom part (i.e. where the crystal lies) is located at the center of the resonance cavity for achieving the strongest signal. For experiments at room temperature, the crystal is glued on different faces/cleavage planes for collecting spectra. For most planes, an angle interval of 5° is used for a rotation of 180°, except for a case where

angle intervals from 1° to 20° are required due to analytical requirements or experimental issues (e.g., sample frozen, cavity unbalanced, etc.).

At cryogenic temperatures, the data collection of single-crystal EPR experiments is the same with that at room temperature, but the experimental system is much more complicated and requires a cryostat inside the resonant cavity. The tube, which is sealed by parafilm, is inserted into the cryostat, while an O ring seals the connection between the tube and the goniometer. Below the bottom of the tube, there is a thermometer connected to a wire heater. The nitrogen/helium gas flows from the bottom of the cryostat. Through manipulating the flowing volume of liquid nitrogen/helium and the power of the wire heater, the temperature inside the resonant cavity can be controlled. The nitrogen/helium gas is sucked through a pipe on the other side of the cryostat. Depending on the flowing volume of liquid nitrogen/helium, the internal pressure of the cryostat is about 200 to 500 mbar (Figure B.1). Commonly, it takes approximately one hour for the crystal to cool down to (and equilibrate) the desired temperature, and then spectral collection can start.

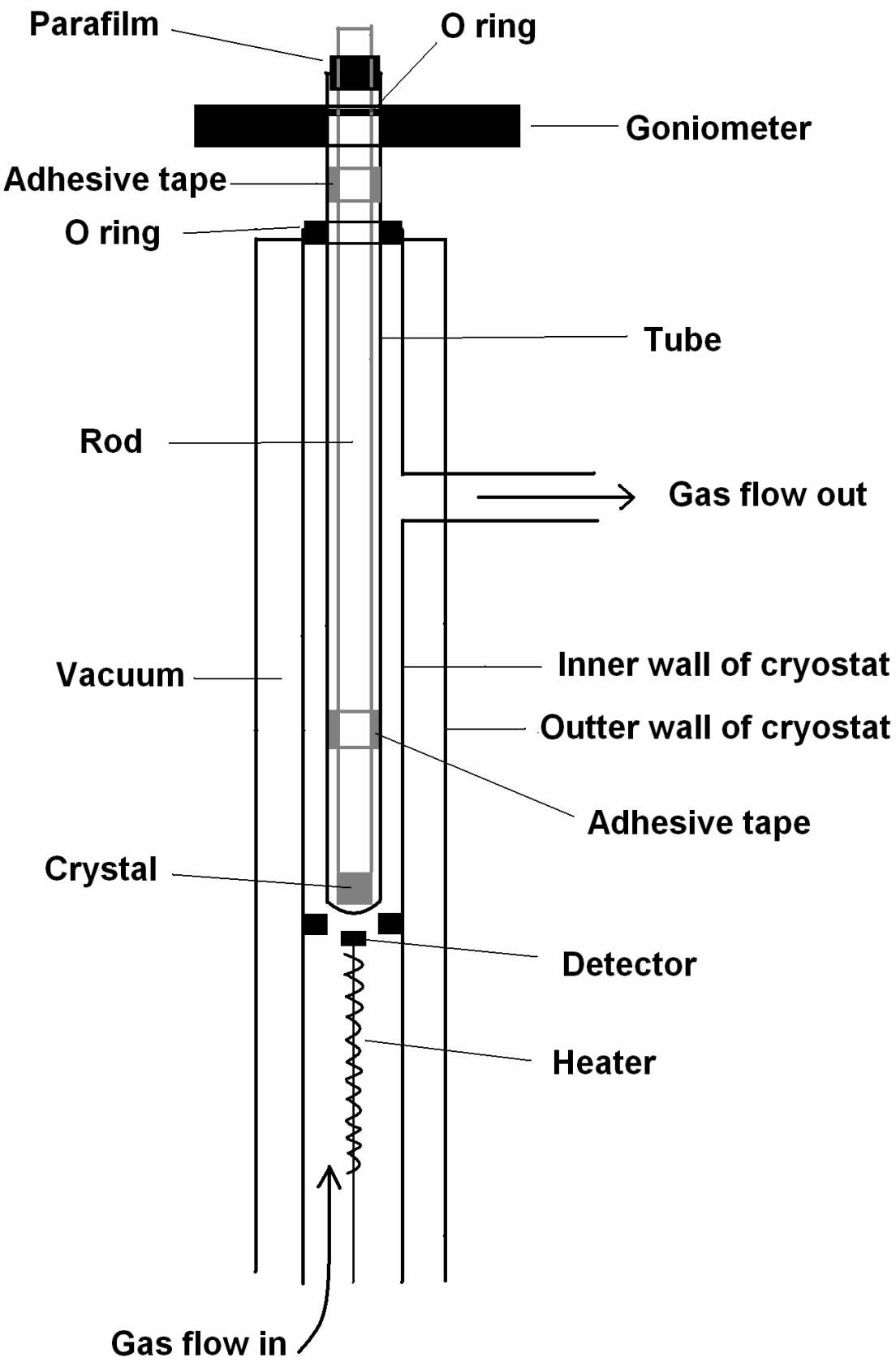

Figure B.1 The cryostat system of EPR experiments.

B.3 Radiation and Annealing procedures

To produce or enhance the paramagnetic centers in minerals, artificial radiation experiments at room temperature were made in a ^{60}Co source (γ-ray) that has a dose rate of ~7.49 Gy/min. Mineral samples for γ-ray irradiation are loaded in a glass vial. For specific radiation doses, the radiation time varies from 1 hour to 5 days or longer. After γ-ray irradiation, samples were immediately transferred to the EPR cavity for analysis (and a few cases kept in dark), because some centers decay quickly when they are exposed to light.

All annealing experiments were made in a Muffle furnace (Thermolyne model 47900). Samples in ceramic or platinum crucibles were put into the Muffle furnace after the set temperature stabilized. Depending on different research purposes, the annealing time varies from 1 minute to a few hours at different temperatures.

B.4 List of EPR spectra and data-fitting files

In this thesis, single-crystal EPR spectra of apophyllites have been collected in two orthogonal planes (Figure B.2a), and single-crystal EPR spectra of prehnite and hemimorphite have been collected in three orthogonal planes (Figure B.2b,c). The EPR spectra and their corresponding data-fitting files have been listed in Table B.1, and saved in a supplementary file.

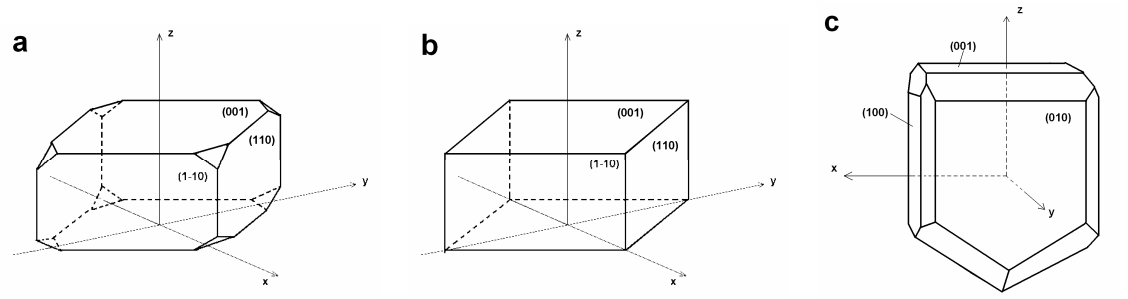

Figure B.2 Sketches of selected crystals measured in this thesis: (a) apophyllites; (b) prehnite; and (c) hemimorphite.

Table B.1 List of experiments, spectra, and data-fitting files in this thesis.

Mineral and locality	Experimental Temperature	Measured plane	Number of spectra	Name of spectra folder	Name of input file	Fitted center
Fluorapophyllite (North Bohemia, Czech)	RT	(001)	37	001 RT	NH2 RT	NH_2 radical
		(110)	37	110 RT		
Hydroxylapophyllite (Unknown)	RT	(001)	39	001 RT	Main line RT	O^- center
		(110)	39	110 RT		
Hydroxylapophyllite (Unknown)	90 K	(001)	37	001 90K	Main line 90K, BP I Dg, BP II Dg, BP III Dg, BP IV Dg	O^- center, and O^--O^- biradical I,II,III,IV.
		(110)	37	110 90K		
Prehnite (Jeffery mine, Asbestos, Quebec, Canada)	RT	(001)	37	001 RT	Al-O- RT1, Al-O-RT2	Al-O^- center
		(110)	37	110 RT		
		(1-10)	9	1-10 RT		
Hemimorphite (Mapimi, Durango, Mexico)	RT	(001)	36	001L	AsO44- RT	$[AsO_4]^{4-}$ center
		(010)	37	010L		
		(100)	37	100L		
Hemimorphite (Mapimi, Durango, Mexico)	RT	(001)	37	001N1	AsO42- RT	$[AsO_4]^{2-}$ center
		(010)	37	010N1		
		(100)	39	100N1		
Hemimorphite (M'Fouati, Reneville, Congo)	RT	(001)	37	001 RT	Cu63 RT	Cu^{2+} center
		(010)	38	010 RT		
		(100)	20	100 RT		
Hemimorphite (M'Fouati, Reneville, Congo)	120 K	(001)	14	001 120K	Cu63 C1 120K, Cu63 C2 120K, Cu63H1 C1 120K	Cu^{2+} - H^+ center
		(010)	38	010RC 120K		
		(100)	36	100 120K		
Hemimorphite (Mapimi, Durango, Mexico)	110 K	(001)	37	001 110K	110K	HO_2-2H radical
		(010)	37	010 110K		
		(100)	37	100 110K		

Hemimorphite (Mapimi, Durango, Mexico)	85 K	(001)	37	001 85K	85K	HO_2-2H radical
		(010)	43	010 85K		
		(100)	37	100 85K		
Hemimorphite (Mapimi, Durango, Mexico)	40 K	(001)	36	001 40K	40K	HO_2-2H radical
		(010)	37	010 40K		
		(100)	38	100 40K		
Hemimorphite (Mapimi, Durango, Mexico)	4 K	(001)	10	001 4K	7K	HO_2-2H radical
	6 K	(010)	6	010 6K		
	8 K	(010)	8	010 8K		
	9 K	(010)	6	010 9K		
	3 K	(100)	16	100 3K		
	11 K	(100)	4	100 11K		

Appendix C

Summary of EMPA and ICPMS data

Electron microprobe analysis (EMPA) and inductively coupled plasma mass spectrometry (ICPMS) were used to determine the major, minor and trace elements of selected minerals. As a supplement of compositiobal data in this thesis, this appendix also includes detection limits and uncertainties for EMPA and ICP-MS data.

C. 1 EMPA data

Electron microprobe analyses were preformed on a JEOL JXA-8600 Superprobe electron microprobe analyzer in the Department of Geological Science, University of Saskatchewan, which is equipped with three wavelength dispersive spectrometers (WDS). Analytical conditions included an accelerating voltage of 15 kV, beam current of 10 nA, beam diameter of ~ 5 μm and the following standards: quartz (Si), jadeite (Na), magnetite (Fe), diopside (Ca), sanidine (K), fluorite (F), γ-Al garnet (Al), and tugtapite (Cl).

Tables C.1 and C.2 include the raw data of EMPA analyses of fluorapophyllite, hydroxylapophyllite, and prehnite. Table C.3 reports the detection limit of each element analyzed, which is the minimal peak to background ratio that is measurable, and depends on x-ray counting times (usually longer is better), the standard sample

(*i.e.*, the mean atomic number of the matrix and the quality of the standard), and the spectral background of each element and mineral itself.

Table C.1 EMPA results of apophyllites.

Apophyllite #1	Oxide wt%								
Point #,	SiO_2	Al_2O_3	Fe_2O_3	CaO	Na_2O	K_2O	Cl	F	Total
1	52.1	0.08	0.00	24.60	0.07	4.00	0.00	0.00	80.95
2,	51.8	0.06	0.00	25.77	0.07	4.06	0.00	0.00	81.81
3,	52.6	0.03	0.01	25.58	0.08	4.00	0.00	0.00	82.32
4,	54.6	0.04	0.00	25.78	0.07	4.27	0.02	0.00	84.77
5,	52.9	0.07	0.00	26.21	0.00	1.70	0.00	0.00	80.95
6,	52.6	0.04	0.03	25.61	0.04	4.16	0.01	0.00	82.51
7,	52.4	0.03	0.01	25.37	0.06	4.01	0.00	0.00	81.97
8,	54.8	0.04	0.03	25.59	0.02	4.04	0.00	0.00	84.55
9,	52.0	0.06	0.00	25.81	0.04	4.15	0.00	0.03	82.16
10,	53.1	0.01	0.00	25.43	0.04	4.11	0.00	0.00	82.73
11,	53.6	0.02	0.02	25.51	0.04	4.18	0.01	0.00	83.48
12,	52.7	0.00	0.01	25.29	0.08	4.08	0.01	0.00	82.24
13,	54.1	0.04	0.00	25.79	0.03	4.14	0.00	0.00	84.13
14,	55.1	0.10	0.01	26.91	0.31	4.26	0.00	0.00	86.76
15,	53.1	0.01	0.00	25.40	0.04	3.95	0.00	0.00	82.55
Average	53.2	0.04	0.01	25.64	0.07	3.94	0.00	0.00	82.92
Std	1.0	0.02	0.01	0.47	0.06	0.60	0.01	0.01	1.51

Apophyllite #2	Oxide wt%								
Point #,	SiO_2	Al_2O_3	Fe_2O_3	CaO	Na_2O	K_2O	Cl	F	Total
1,	53.9	0.06	0.00	24.67	0.06	3.83	0.01	0	82.57
2,	54.4	0.02	0.00	24.49	0.03	3.87	0.00	0	82.85
3,	54.5	0.03	0.02	24.34	0.04	3.82	0.00	0	82.84
4,	54.2	0.04	0.00	24.59	0.03	3.89	0.04	0	82.79
5,	54.5	0.13	0.00	24.52	0.05	3.78	0.02	0	83.06
6,	55.4	0.05	0.00	25.28	0.04	4.03	0.01	0	84.87
Average	54.5	0.05	0.00	24.64	0.04	3.87	0.01	0	83.16
Std	0.5	0.03	0.01	0.29	0.01	0.08	0.01	0	0.77

Apophyllite #3	Oxide wt%								
Point #,	SiO_2	Al_2O_3	Fe_2O_3	CaO	Na_2O	K_2O	Cl	F	Total
7,	54.0	0.17	0.00	24.60	0.07	3.21	0.00	2.09	84.23
8,	54.6	0.22	0.02	24.78	0.10	3.13	0.00	2.16	85.10
9,	55.1	0.19	0.00	24.56	0.09	3.22	0.00	2.13	85.37

10,	54.8	0.19	0.00	24.51	0.09	3.16	0.01	2.08	84.93
11,	54.9	0.19	0.01	24.56	0.10	3.20	0.01	2.12	85.12
12,	54.0	0.10	0.00	24.60	0.06	3.27	0.01	2.09	84.21
Average	54.6	0.18	0.01	24.60	0.09	3.19	0.00	2.11	84.82
Std	0.4	0.04	0.01	0.08	0.01	0.04	0.01	0.03	0.44

Table C.2 EMPA results of prehnite.

Prehnite #1	Oxide wt%								
Point #,	SiO_2	Al_2O_3	Fe_2O_3	CaO	Na_2O	K_2O	Cl	F	Total
1,	41.7	23.17	0.07	26.98	0.00	0.00	0.03	0.00	91.97
2,	43.1	24.51	0.06	26.28	0.09	0.04	0.01	0.00	94.10
3,	44.3	24.26	0.04	27.38	0.08	0.01	0.02	0.01	96.17
4,	44.1	24.19	0.07	26.17	0.03	0.01	0.01	0.00	94.68
5,	43.8	24.30	0.01	27.10	0.05	0.01	0.01	0.00	95.37
6,	42.9	24.57	0.03	25.78	0.05	0.03	0.00	0.00	93.40
7,	43.3	24.24	0.00	27.25	0.00	0.20	0.00	0.15	95.18
8,	43.7	24.75	0.08	26.58	0.05	0.00	0.02	0.00	95.19
9,	42.7	25.02	0.05	26.35	0.05	0.00	0.02	0.00	94.24
10,	43.5	24.87	0.11	26.68	0.06	0.00	0.00	0.00	95.27
Average	43.3	24.38	0.05	26.65	0.05	0.03	0.01	0.01	94.55
Std	0.7	0.49	0.03	0.56	0.03	0.06	0.01	0.04	1.19

Table C.3 Detection limits of EMPA analyses.

Element	Standard	MDL(wt%)	MDL(ppm)
Si	quartz	0.0093	93
F	fluorite	0.0652	652
Cl	tugtapite	0.0124	124
K	sanidine	0.0104	104
Na	jadeite	0.0113	113
Al	γ-Al garnet	0.0094	94
Fe	magnetite	0.0315	315
Ca	diopside	0.0113	113

C. 2 ICP-MS data

All ICP-MS analyses were made by using a Perkin-Elmer Sciex Elan 5000 instrument in the Department of Geological Science, University of Saskatchewan. The

crystals used for ICP-MS analyses were first examined with a binocular microscope to minimize impurities, and then grinded into powder in a ceramic mortar. The HF-HNO_3 method was used to dissolve samples for ICP-MS analyses.

Trace elements of hydroxylapophyllite, hemimorphite, and solution and minerals from cation-exchange experiments are given in this appendix. BCR-2 (Basalt, Columbia River) was used as a standard during ICPMS analyses. The detection limit of each element from ICPMS is calculated from the following equation:

Det.Lmt. = 3 • STD(BK) • C(std A,B)/I(std A,B) • DilF.....(C.1)

where the STD(BK) is the relative standard deviation of blank, C(std A,B) is the concentration of calibration standard, I(std A,B) is the intensity of calibration standard, and DilF is the dilution factor.

Table C.4 ICP-MS data of hydroxylapophyllite (analyzed on 12th Oct. 2007).

Element	Hydroxla-pophyllite	BCR-2	BCR-2	BCR-2, reference value	BCR-2/rec	BCR-2/rec	DilF	Det. lmt. (ppm)
Li	0.28	7.9	11	9	88%	123%	Li 7	0.002
Be	ud	ud	ud	-	-	-	B 11	0.83
Sc	16.4	42	35	33	128%	107%	Sc 45	0.002
V	3.3	523	453	416	126%	109%	V 51	0.001
Rb	164	48.8	47	48	102%	98%	Rb 85	0.0002
Sr	8.6	361	342	346	105%	99%	Sr 88	0.006
Y	0.38	36	33	37	99%	91%	Y 89	0.0001
Zr	1.7	200	189	188	107%	101%	Zr 90	0.0001
Nb	0.41	14.3	13	14	102%	94%	Nb 93	0.0001
Mo	0.41	286	273	248	115%	110%	Mo 95	0.0006
Cs	0.93	1.09	1.08	1.1	99%	98%	Cs 133	0.0001
Ba	2.2	692	672	683	101%	98%	Ba 137	0.0008
La	2.4	25.9	24.8	25	104%	99%	La 139	0.0001
Ce	2.1	57.4	54.3	53	108%	102%	Ce 140	0.0001
Pr	0.17	7.0	7.0	6.8	104%	104%	Pr 141	0.0001

Nd	0.61	29.5	27.7	28	106%	99%	Nd 145	0.0003
Sm	0.10	6.8	6.2	6.7	102%	93%	Sm 147	0.0002
Eu	0.13	2.08	1.92	2	104%	96%	Eu 151	0.0001
Gd	0.17	7.5	6.9	6.8	111%	102%	Gd 157	0.0004
Tb	0.02	1.14	1.09	1.07	107%	102%	Tb 159	0.0001
Dy	0.11	6.5	6.4	6.3	104%	102%	Dy 163	0.0001
Ho	0.01	1.29	1.31	1.33	97%	98%	Ho 165	0.0001
Er	0.01	3.95	3.76	3.8	104%	99%	Er 167	0.0001
Tm	0.00	0.53	0.51	0.54	98%	95%	Tm 169	0.0001
Yb	0.01	3.46	3.28	3.5	99%	94%	Yb 173	0.0001
Lu	0.01	0.52	0.48	0.51	101%	95%	Lu 175	0.0001
Hf	0.50	4.7	5.0	4.8	99%	106%	Hf 178	0.0001
Ta	0.03	0.78	0.78	0.81	96%	96%	Ta 181	0.0001
Tl	0.02	0.26	0.26	-	-	-	Tl 205	0.0002
Pb	2.68	9.7	10.2	11	89%	93%	Pb 208	0.004
Bi	0.02	0.05	0.05	0.047	97%	98%	Bi 209	0.0001
Th	0.12	6.19	6.5	6.2	100%	106%	Th 232	0.0001
U	0.16	1.60	1.73	1.69	95%	102%	U 238	0.0001
Mg	27	28723	21706	21600	133%	100%	Mg 26	0.01
P	26	1808	1588	1527.4	118%	104%	P 31	0.10
Ti	28	16603	13789	13548.7	123%	102%	Ti 47	0.007
Cr	12	19.25	17.25	18	107%	96%	Cr 52	0.001
Mn	2.11	1713	1521	1520	113%	100%	Mn 55	0.002
Fe	209	105154	93676	96521	109%	97%	Fe 54	0.10
Co	0.93	38.3	36.4	37	104%	98%	Co 59	0.0004
Ni	7.8	17.2	15.4	13	133%	118%	Ni 60	0.13
Cu	1.8	20.7	18.1	19	109%	96%	Cu 65	0.003
Zn	17.6	134	131	127	106%	103%	Zn 66	0.001
Ga	0.33	25.3	19.3	23	110%	84%	Ga 69	0.0003
Ge	ud	ud	ud	-	-	-	Ge 74	0.006
As	1.0	1.8	1.5	0.65	280%	240%	As 75	0.006
Se	ud	ud	0.49	0.088		556%	Se 77	0.02
Ag	0.38	ud	ud	-	-	-	Ag 107	0.0001
Cd	0.14	0.20	0.13	-	-	-	Cd 111	0.0006
Sn	0.68	5.2	5.8	2.7	195%	216%	Sn 118	0.002
Sb	0.04	0.39	0.48	0.62	62%	78%	Sb 121	0.0005
W	0.10	0.48	0.44	0.44	109%	101%	W 182	0.0003

Table C.5 ICP-MS data of hemimorphite (analyzed on 30th, Jun. 2009).

Element	Hemi Maxico Sample #1	Hemi Maxico,dupl.	BCR-2	BCR-2, reference value	BCR-2/rec	DilF	Det. lmt. (ppm)
Li	ud	ud	10	9	112%	Li 7	0.90
Be	ud	ud	-	1.6	-	Be 9	0.88
Sc	ud	ud	36	33	112%	Sc 45	2.55
V	0.50	0.63	462	416	111%	V 51	0.16
Rb	0.53	0.54	48.3	48	101%	Rb 85	0.02
Sr	2.2	2.1	352	346	102%	Sr 88	0.16
Y	0.09	0.10	32.8	37	89%	Y 89	0.01
Zr	1.2	1.30	186.6	188	99%	Zr 90	0.03
Nb	0.28	0.30	14.9	14	107%	Nb 93	0.04
Mo	ud	ud	255	248	103%	Mo 95	0.14
Cs	0.02	0.03	1.2	1.1	109%	Cs 133	0.02
Ba	0.87	0.90	685	683	100%	Ba 137	0.05
La	0.22	0.21	24.8	25	99%	La 139	0.02
Ce	0.39	0.39	52.6	53	99%	Ce 140	0.02
Pr	0.04	0.04	6.96	6.8	102%	Pr 141	0.003
Nd	0.37	0.44	30	28	107%	Nd 145	0.15
Sm	ud	0.04	6.4	6.7	96%	Sm 147	0.009
Eu	ud	ud	2.1	2	107%	Eu 151	0.01
Gd	ud	0.12	7.7	6.8	114%	Gd 157	0.05
Tb	0.00	0.02	1.14	1.07	107%	Tb 159	0.01
Dy	0.04	0.08	6.36	6.3	101%	Dy 163	0.02
Ho	ud	0.02	1.33	1.33	100%	Ho 165	0.02
Er	ud	ud	3.6	3.8	95%	Er 167	0.08
Tm	ud	ud	0.49	0.54	90%	Tm 169	0.01
Yb	0.03	0.03	3.3	3.5	95%	Yb 173	0.008
Lu	ud	ud	0.39	0.51	77%	Lu 175	0.001
Hf	0.07	0.08	5.6	4.8	118%	Hf 178	0.02
Ta	0.02	0.03	0.90	0.81	114%	Ta 181	0.01
Tl	ud	ud	0.3	0.3	106%	Tl 205	0.0001
Pb	1.88	2.04	9.8	11	87%	Pb 208	0.11
Bi	ud	ud	-	0.047	-	Bi 209	0.01
Th	0.31	0.29	6.1	6.2	99%	Th 232	0.02
U	0.06	0.04	1.70	1.69	100%	U 238	0.003
Mg	27	30	21469	21600	101%	Mg 26	2.32
Al	727	756	73188	71400	106%	Al 27	7.64
P	ud	ud	1561	1527.4	103%	P 31	70.6
Ca	7245	7016	45124	50900	66%	Ca 44	366.8
Ti	36	32	14878	13548.7	114%	Ti 47	7.9
Cr	ud	ud	15.8	18	88%	Cr 52	0.56

Mn	0.98	0.98	1454	1520	110%	Mn 55	0.06
Fe	67	62	93226	96521	97%	Fe 54	6.41
Co	0.18	0.18	41	37	113%	Co 59	0.07
Ni	ud	ud	12.6	13	98%	Ni 60	0.48
Cu	357	350	23	19	128%	Cu 65	0.64
Ga	81.91	80.96	23.6	23	103%	Ga 69	0.27
Ge	0.28	0.26	-	1.5	-	Ge 74	0.03
As	271	269	1.6	0.65	257%	As 75	0.05
Ag	0.41	0.42	-	0.027	-	Ag 107	0.01
Cd	26	26	-	0.13	-	Cd 111	0.14
Sn	0.07	0.05	2.3	2.7	83%	Sn 118	0.04
Sb	9.1	9.1	0.41	0.62	60%	Sb 121	0.05
W	4.1	3.9	3.7	0.44	854%	W 182	0.0001

Table C.6 ICP-MS data of hemimorphite (analyzed on 26th, Aug. 2009).

Element	Hemi-Chiwana Sample #4	Hemi-Durango2 Sample #2	Hemi-Durango3 Sample #3	Hemi-Elpotosi Sample #5	Hemi-Pine Creek Sample #6	Hemi-Unknown	BCR-2	BCR-2	BCR-2	BCR-2, reference value	BCR-2/rec	BCR-2/rec	BCR-2/rec		Det. lmt. (ppm)
Li	ud	2.8	ud	3.1	ud	ud	10.8	5.9	ud	9	121%	66%	-	Li 7	2.22
Be	ud	ud	ud	2.1	ud	ud	ud	ud	ud	2	-	-	-	Be 9	0.57
Sc	4.8	0.61	ud	ud	5.5	8.9	36.4	36.6	36.9	33	111%	111%	112%	Sc 45	0.66
V	2.7	0.36	0.53	0.29	0.42	0.51	454	473	457	416	109%	114%	110%	V 51	0.12
Rb	0.35	0.25	0.23	0.09	0.61	0.49	45.8	46.6	47.5	48	95%	97%	99%	Rb 85	0.02
Sr	0.30	6.7	ud	ud	0.43	0.65	335	334	340	346	97%	97%	98%	Sr 88	0.21
Y	0.14	0.26	0.07	0.06	0.13	0.14	34.4	34.1	34.5	37	93%	92%	93%	Y 89	0.01
Zr	0.27	0.11	0.08	0.06	0.05	0.37	188	190	189	188	100%	102%	101%	Zr 90	0.05
Nb	0.07	0.02	0.01	0.02	0.05	0.04	14.7	14.2	13.4	14	105%	102%	96%	Nb 93	0.03
Mo	ud	0.22	ud	0.24	ud	0.12	265	265	256	248	107%	107%	103%	Mo 95	0.11
Cs	0.11	0.09	ud	ud	0.04	0.02	1.04	1.15	0.99	1.1	94%	104%	90%	Cs 133	0.02
Ba	0.98	10.8	0.62	0.94	0.80	18.2	665	678	668	683	97%	99%	98%	Ba 137	0.32
La	0.17	0.20	0.07	0.06	0.15	0.16	25.3	26.3	25.7	25	101%	105%	103%	La 139	0.02
Ce	0.26	0.16	0.13	0.10	0.26	0.25	53.8	57.5	54.3	53	102%	109%	103%	Ce 140	0.01
Pr	0.03	0.05	0.02	0.01	0.03	0.04	6.9	7.5	7.1	6.8	102%	110%	104%	Pr 141	0.01
Nd	0.08	0.19	0.05	0.05	0.09	0.11	29.5	28.5	30.9	28	106%	102%	110%	Nd 145	0.10
Sm	0.57	0.14	ud	0.29	0.25	0.14	7.7	6.8	7.1	6.7	116%	102%	106%	Sm 147	0.10
Eu	ud	0.05	ud	ud	ud	ud	1.86	2.13	1.87	2	93%	106%	94%	Eu 151	0.02
Gd	0.25	0.04	ud	ud	0.03	ud	6.9	8.1	8.0	6.8	103%	120%	118%	Gd 157	0.20
Tb	0.01	0.00	ud	ud	ud	ud	1.11	1.16	1.22	1.07	104%	109%	114%	Tb 159	0.02
Dy	ud	ud	ud	ud	ud	ud	6.6	6.2	6.9	6.3	106%	99%	110%	Dy 163	0.04

Ho	0.01	0.00	ud	ud	0.00	0.01	1.19	1.5	1.33	1.33	90%	112%	100%	Ho 165	0.01
Er	0.02	0.02	0.00	0.01	0.00	0.00	3.9	3.3	4.0	3.8	104%	87%	106%	Er 167	0.10
Tm	0.02	ud	ud	ud	ud	ud	0.52	0.54	0.52	0.54	97%	101%	97%	Tm 169	0.02
Yb	0.33	0.15	0.29	0.07	0.22	0.07	3.3	3.2	3.7	3.5	94%	93%	108%	Yb 173	0.04
Lu	ud	ud	ud	ud	ud	ud	0.53	0.57	0.61	0.51	105%	113%	119%	Lu 175	0.04
Hf	ud	0.06	0.01	ud	ud	0.01	5.06	4.88	4.77	4.8	105%	102%	99%	Hf 178	0.04
Ta	0.05	0.02	ud	0.02	ud	ud	0.84	0.85	0.75	0.81	103%	105%	93%	Ta 181	0.01
Tl	ud	9.4	ud	0.06	ud	ud	0.1	0.31	0.26	0.3	33%	104%	86%	Tl 205	0.03
Pb	389	1283	35	89	69	56	10.2	9.5	9.8	11	93%	86%	90%	Pb 208	0.19
Bi	0.03	0.01	ud	ud	ud	ud	ud	ud	ud	0.047	-	-	-	Bi 209	0.01
Th	0.04	0.03	0.03	0.02	0.07	0.07	6.0	5.8	5.8	6.2	97%	93%	94%	Th 232	0.02
U	1.0	1.1	0.26	0.26	0.20	0.11	1.70	1.55	1.68	1.69	100%	92%	99%	U 238	0.03
Mg	29	14	32	ud	ud	26	25087	24392	22122	21600	116%	113%	102%	Mg 26	29.1
Al	663	328	373	242	654	473	79627	78290	70559	71400	112%	110%	99%	Al 27	4.8
P	47	ud	ud	ud	120	123	1544	1511	1495	1527.4	101%	99%	98%	P 31	37.1
Ca	644	38687	ud	269	ud	418.71	43579	48320	53318	50900	86%	95%	105%	Ca 44	186.3
Ti	50	23	23	13	39	32.35	14264	14758	14483	13548.7	105%	109%	107%	Ti 47	1.33
Cr	1.5	0.59	0.49	0.44	0.52	1.70	17.3	17.2	13.9	18	96%	96%	77%	Cr 52	0.31
Mn	3.2	6.2	7	38	5.3	1.2	1688	1678	1607	1520	111%	110%	106%	Mn 55	0.27
Fe	62	333	ud	ud	ud	ud	99375	98417	95329	96521	103%	102%	99%	Fe 54	46.7
Co	ud	0.27	ud	0.23	0.11	ud	38.8	39.3	38.6	37	105%	106%	104%	Co 59	0.08
Ni	ud	1.8	1.3	ud	1.2	ud	12.3	9.7	10.8	13	95%	75%	83%	Ni 60	1.17
Cu	1199	764	936	1031	1001	805	19.9	19.8	17.6	19	105%	104%	93%	Cu 65	0.56
Ga	110	114	124	125	23	27	23.0	24.1	22.7	23	100%	105%	99%	Ga 69	0.03
Ge	ud	1.1	ud	ud	0.14	3.7	ud	ud	ud	1.5	-	-	-	Ge 74	0.13
As	36	6.0	127	18	38	3.3	0.86	0.46	0.57	0.65	132%	71%	88%	As 75	0.32

Se	ud	ud	ud	ud	ud	ud	ud	ud	ud	0.088	-	-	-	Se 77	8.4
Ag	7.2	0.25	0.49	0.41	0.23	0.43	ud	ud	0.18	0.027	-	-	682%	Ag 107	0.05
Cd	4.4	50.6	ud	0.49	11	5.3	ud	ud	ud	0.13	-	-	-	Cd 111	0.11
Sb	4.3	0.83	10	0.99	6.8	0.31	0.4	0.69	0.3	0.62	68%	111%	43%	Sb 121	0.03

Table C.7 ICP-MS data of hemimorphite (analyzed on 22nd, Dec. 2009).

Element	Hemi, 79 Arizona Sample #9	Hemi, Bleiberg	Hemi, Franklin Sample #7	Hemi, Reneville Sample#10	Hemi, Sterling Sample #8	BCR-2	BCR-2, reference value	BCR-2/rec	DilF	Det. lmt. (ppm)
Li	0.24	ud	ud	0.44	1.2	11	9	122%	Li 7	0.20
Be	ud	ud	ud	ud	1.3	1	2	48%	Be 9	0.39
Sc	ud	ud	0.35	ud	1.8	35.2	33	107%	Sc 45	0.29
V	11	0.05	2.3	0.38	5.3	478	416	115%	V 51	0.02
Rb	0.26	0.10	0.13	0.25	2.6	48.5	48	101%	Rb 85	0.08
Sr	23	20	17	21	28	330	346	97%	Sr 88	0.02
Y	6.1	8.6	0.34	0.26	3.3	32.6	37	91%	Y 89	0.02
Zr	0.75	0.20	0.12	0.18	1.9	175	188	95%	Zr 90	0.01
Nb	0.23	0.09	0.19	0.24	0.45	12.2	14	89%	Nb 93	0.01
Mo	ud	ud	ud	ud	ud	253	248	102%	Mo 95	0.42
Cs	0.06	ud	ud	ud	0.06	1.3	1.1	121%	Cs 133	0.05
Ba	3.5	7.6	3.8	12	37	670	683	97%	Ba 137	0.03
La	0.67	1.3	0.17	0.43	10	24.4	25	98%	La 139	0.006
Ce	0.86	0.13	0.14	0.29	7.6	52.8	53	100%	Ce 140	0.0005
Pr	0.18	0.25	0.03	0.05	1.5	6.9	6.8	106%	Pr 141	0.002
Nd	0.87	1.1	0.14	0.19	5.9	31.3	28	109%	Nd 145	0.001
Sm	0.23	0.16	0.01	ud	0.89	7.0	6.7	100%	Sm 147	0.01
Eu	0.05	ud	ud	ud	0.18	2.1	2	106%	Eu 151	0.05
Gd	0.56	0.33	0.04	0.03	0.79	7.0	6.8	107%	Gd 157	0.02
Tb	0.08	0.06	ud	ud	0.09	1.03	1.07	98%	Tb 159	0.007
Dy	0.56	0.43	0.05	0.02	0.59	6.7	6.3	113%	Dy 163	0.007
Ho	0.12	0.11	0.00	0.00	0.10	1.32	1.33	101%	Ho 165	0.0001
Er	0.35	0.38	0.01	0.01	0.30	3.9	3.8	122%	Er 167	0.006
Tm	0.03	0.05	ud	ud	0.05	0.59	0.54	108%	Tm 169	0.006
Yb	0.17	0.24	ud	ud	0.26	3.9	3.5	109%	Yb 173	0.02
Lu	ud	0.02	ud	ud	ud	0.53	0.51	105%	Lu 175	0.02
Hf	0.04	ud	ud	ud	0.03	5.0	4.8	109%	Hf 178	0.02
Ta	0.01	ud	ud	0.01	0.01	0.77	0.81	98%	Ta 181	0.004
Tl	0.05	0.10	ud	0.11	0.07	ud	0.3	-	Tl 205	0.03
Pb	163	347	3.7	435	31	11.3	11	103%	Pb 208	0.01
Bi	0.39	ud	0.08	0.05	0.10	0.05	0.047	111%	Bi 209	0.03
Th	0.12	0.04	0.02	0.04	0.29	5.8	6.2	93%	Th 232	0.01
U	1.2	0.17	0.12	0.11	0.78	1.79	1.69	106%	U 238	0.02
Mg	107	163	ud	49	199	23461	21600	109%	Mg 26	19.4
Al	589	88	351	402	1777	77118	71400	108%	Al 27	1.15
P	289	47	776	547	315	1348	1527.4	88%	P 31	45.6
Ti	33	9.6	8.5	14	85	14845	13548.7	110%	Ti 47	0.79
Cr	1.4	ud	ud	0.35	2.1	15.2	18	84%	Cr 52	0.34
Mn	57	20	5.8	15	314	1676	1520	110%	Mn 55	0.15

Fe	466	ud	48	83	1236	96351	96521	100%	Fe 54	35.2
Co	3.1	1.0	ud	0.03	0.27	38.8	37	105%	Co 59	0.01
Ni	11	4.6	ud	ud	2.8	16.2	13	125%	Ni 60	0.95
Cu	1293	152	761	668	570	22	19	116%	Cu 65	1.03
Zn	547958	26217	534541	546036	518035	134	127	106%	Zn 66	6.43
Ga	116	8.8	139	113	110	21.7	23	94%	Ga 69	0.08
Ge	0.34	ud	2.4	11	1.4	ud	1.5	-	Ge 74	0.11
As	78	ud	200	338	275	ud	0.65	-	As 75	2.24
Ag	2.1	0.07	0.17	0.31	0.36	ud	0.088	-	Ag 107	0.02
Cd	38	336	1.6	4.6	2.6	ud	0.027	-	Cd 111	0.16
Sn	0.26	0.20	0.23	0.21	0.38	3.56	2.69	132%	Sn 118	0.13
Sb	0.28	0.09	0.50	0.26	7.4	0.18	0.62	29%	Sb 121	0.03
W	0.12	ud	ud	ud	0.17	0.55	0.44	126%	W 182	0.12

Table C.8 ICP-MS data of cation-exchange experiments (analyzed on 15th, Jun. 2011).

Element	0.1M/L $CaCl_2$ solution	BCR-2	BCR-2, reference value	BCR-2/rec	DilF	Det. lmt. (ppm)
Li	1.5	10	9	113%	Li 7	0.002
Mg	0.74	22709	21600	105%	Mg 26	0.00001
Al	0.01	73227	71400	103%	Al 27	0.002
P	ud	1501	1527.4	98%	P 31	0.05
Ca	3000	45210	50900	89%	Ca 44	0.005
Sc	0.01	39.5	33	120%	Sc 45	0.0003
Ti	0.08	14510	13548.7	107%	Ti 47	0.0007
V	0.02	459	416	110%	V 51	0.001
Cr	0.02	11	18	64%	Cr 52	0.002
Mn	0.01	1631	1520	107%	Mn 55	0.0003
Fe	0.19	104729	96521	109%	Fe 54	0.04
Co	0.01	37.5	37	101%	Co 59	0.0003
Ni	0.05	10.6	13	82%	Ni 60	0.0006
Cu	0.04	20.7	19	109%	Cu 65	0.001
Zn	0.00	137	127	108%	Zn 66	0.002
Ga	0.00	22.1	23	96%	Ga 69	0.0002
Ge	0.00	ud	1.5	-	Ge 74	0.0004
As	0.09	5.	0.65	781%	As 75	0.0013
Rb	0.20	50	48	104%	Rb 85	0.00002
Sr	55	363	346	105%	Sr 88	0.0005
Y	0.18	37.6	37	102%	Y 89	0.00004
Zr	0.00	193	188	103%	Zr 90	0.0002

Nb	ud	12.6	14	90%	Nb 93	0.00001
Mo	ud	251	248	101%	Mo 95	0.0002
Ag	ud	ud	0.027	-	Ag 107	0.00005
Cd	0.00	2.5	0.13	1987%	Cd 111	0.0005
Sn	0.00	ud	2.7	-	Sn 118	0.0002
Sb	0.00	0.34	0.62	55%	Sb 121	0.0001
Cs	0.01	1	1.1	92%	Cs 133	0.00002
Ba	0.02	717	683	105%	Ba 137	0.00005
La	0.00	26.3	25	105%	La 139	0.00004
Ce	ud	53.8	53	102%	Ce 140	0.00004
Pr	ud	7.2	6.8	106%	Pr 141	0.00004
Nd	0.00	30.4	28	109%	Nd 145	0.00007
Sm	0.00	7	6.7	104%	Sm 147	0.00007
Eu	ud	1.9	2	95%	Eu 151	0.00004
Gd	0.00	7.2	6.8	107%	Gd 157	0.00004
Dy	ud	6.22	6.3	99%	Dy 163	0.0002
Ho	0.00	1.42	1.33	107%	Ho 165	0.00001
Er	ud	3.5	3.8	92%	Er 167	0.00009
Tm	ud	0.47	0.54	87%	Tm 169	0.00001
Yb	ud	4	3.5	116%	Yb 173	0.0002
Lu	ud	0.43	0.51	85%	Lu 175	0.00005
Hf	ud	5.3	4.8	110%	Hf 178	0.00003
Ta	0.00	0.78	0.81	96%	Ta 181	0.00003
W	0.00	ud	0.44	-	W 182	0.00009
Tl	0.00	ud	0.3	-	Tl 205	0.00001
Pb	0.00	11.3	11	103%	Pb 208	0.0002
Th	ud	7.3	6.2	117%	Th 232	0.00005
U	0.00	1.82	1.69	108%	U 238	0.00006

Table C.9 ICP-MS data of cation-exchange experiments (analyzed on 28th, Jun. 2011).

Element	S1-3	S1-5	S1-7	S1-10	BCR-2	BCR-2, reference value	BCR-2/rec	DilF	Det. lmt. (ppm)
Li	0.08	ud	0.50	ud	13	9	148%	Li 7	0.002
Mg	11.6	7.6	1.8	6.1	20023	21600	93%	Mg 26	0.005
Al	557	396	65	61	69137	71400	97%	Al 27	0.001
P	3.0	11	2.6	8.1	1364	1527.4	89%	P 31	0.05
Ca	3863	124	ud	ud	58225	50900	114%	Ca 44	9.3
Sc	0.00	ud	ud	ud	35	33	107%	Sc 45	0.0007
Ti	25	16	2.1	4.8	13153	13548.7	97%	Ti 47	0.005

V	0.13	0.04	0.03	ud	481	416	116%	V 51	0.0003
Cr	1.3	2.3	0.32	5.7	18.2	18	101%	Cr 52	0.003
Mn	8.7	8.2	1.3	1.5	1678	1520	110%	Mn 55	0.0002
Fe	29	29	7.9	24	107984	96521	112%	Fe 54	0.04
Co	0.04	0.04	0.06	0.10	45	37	122%	Co 59	0.0002
Ni	1.8	4.4	0.71	3.9	20	13	157%	Ni 60	0.0004
Cu	380	413	426	445	34	19	179%	Cu 65	0.0006
Zn	-	-	-	-	160	127	126%	Zn 66	0.59
Ga	92	85	90	102	21.7	23	95%	Ga 69	0.0004
Ge	0.26	0.37	0.20	0.18	ud	1.5	-	Ge 74	0.0004
As	275	267	264	269	ud	0.65	-	As 75	0.001
Rb	0.19	0.07	0.02	0.02	48	48	100%	Rb 85	0.0002
Sr	0.70	1.1	ud	0.31	364	346	105%	Sr 88	0.0003
Y	0.11	0.06	0.04	0.04	34	37	94%	Y 89	0.00003
Zr	77	63	13	15	207	188	111%	Zr 90	0.00004
Nb	0.23	0.20	0.08	0.07	14.6	14	104%	Nb 93	0.00005
Mo	0.28	0.09	ud	0.09	266	248	107%	Mo 95	0.0004
Ag	0.46	0.36	0.26	0.19	ud	0.027	916%	Ag 107	0.00015
Cd	ud	0.18	0.05	ud	0.35	0.13	270%	Cd 111	0.0004
Sn	0.10	1.0	2.8	0.02	4.3	2.7	160%	Sn 118	0.0002
Sb	4.6	4.7	4.1	4.6	2	0.62	320%	Sb 121	0.0001
Cs	0.03	0.01	0.00	ud	0.96	1.1	87%	Cs 133	0.00006
Ba	0.64	0.28	0.03	ud	701	683	103%	Ba 137	0.00009
La	0.12	0.06	0.03	0.01	25.8	25	103%	La 139	0.00001
Ce	0.28	0.17	0.03	0.03	55	53	104%	Ce 140	0.00008
Pr	0.01	0.03	ud	ud	6.9	6.8	103%	Pr 141	0.00003
Nd	0.07	0.04	ud	ud	30.3	28	108%	Nd 145	0.0003
Sm	ud	0.02	ud	ud	5	6.7	74%	Sm 147	0.00008
Eu	ud	ud	ud	ud	2.07	2	103%	Eu 151	0.00007
Gd	ud	0.00	ud	ud	6.6	6.8	97%	Gd 157	0.0001
Dy	ud	0.03	0.01	0.00	6.2	6.3	98%	Dy 163	0.00004
Ho	ud	0.00	ud	ud	1.39	1.33	105%	Ho 165	0.00003
Er	ud	0.01	0.02	ud	4.6	3.8	122%	Er 167	0.00004
Tm	ud	ud	ud	0.00	0.57	0.54	105%	Tm 169	0.00003
Yb	ud	0.01	ud	ud	3	3.5	86%	Yb 173	0.0002
Lu	ud	ud	0.00	ud	0.53	0.51	103%	Lu 175	0.00002
Hf	1.9	1.3	0.34	0.41	4.6	4.8	96%	Hf 178	0.00001
Ta	0.02	0.01	0.00	ud	0.75	0.81	93%	Ta 181	0.00002
W	0.11	ud	ud	ud	0.72	0.44	164%	W 182	0.00005
Tl	0.01	0.01	0.01	ud	0.24	0.3	81%	Tl 205	0.00004
Pb	4.2	8.6	1.4	0.58	11.7	11	107%	Pb 208	0.0002
Th	0.12	0.06	ud	ud	6.6	6.2	107%	Th 232	0.00003
U	0.06	0.06	0.02	0.00	2.5	1.69	147%	U 238	0.00002